AAV-mediated expression of Secreted Klotho as a therapeutic strategy for Alzheimer's disease

Rebeca Blanch García

Universitat Autònoma de Barcelona

Department of Biochemistry, Molecular Biology and Biomedicine

PhD Program in Biochemistry, Molecular Biology and Biomedicine

DOCTORAL THESIS

AAV-mediated expression of Secreted Klotho as a therapeutic strategy for Alzheimer's disease

Rebeca Blanch García

January 2023

Supervisor: Miguel Chillón Rodríguez

Universitat Autònoma de Barcelona

AAV-mediated expression of Secreted Klotho as a therapeutic strategy for Alzheimer's disease

ACADEMIC DISSERTATION

Presented by

Rebeca Blanch García

To obtain the degree *of*

PhD in Biochemistry, Molecular Biology and Biomedicine

by the *Universitat Autònoma de Barcelona*.

Bellaterra, January 2023

The PhD Candidate,

REBECA BLANCH GARCÍA

The Supervisor,

Dr. MIGUEL CHILLÓN RODRÍGUEZ

The research described in this doctoral thesis was conducted in the laboratory of Gene Therapy for Diseases affecting the Central Nervous System (Department of Biochemistry and Molecular Biology, *Institut de Neurociències, Universitat Autònoma de Barcelona*), under the supervision of Dr Miguel Chillón Rodríguez.

Rebeca Blanch García was recipient of a *Formación de Profesorado Universitario* Fellowship (FPU16/03137) from the *Gobierno de España*. The PhD candidate conducted a part of this work during a 6-month research stay at University of California San Diego (USA) under the supervision of Dr. Alysson Muotri. The research stay was financially supported by an *Ayuda Complementaria para Estancias Breves* for FPU recipients (*Ministerio de Universidades*), an INc research stay grant, and an ESACT travel grant.

Index

ABBREVIATIONS

2D, 3D	two-dimensional, three-dimensional
3xTg-AD	triple-transgenic mouse model of Alzheimer's disease
6wp, 96wp	6-well plate, 96-well plate
AAP	assembly-activating protein
AAV	adeno-associated virus
Ab	antibody
Ach	acetylcholine
AChEIs	acetylcholinesterase inhibitors
AD	Alzheimer’s disease
ADAM	a disintegrin and metalloproteinase
AM	amygdala
APOE	apolipoprotein E
APP	amyloid precursor protein
Aβ	β-amyloid, beta-amyloid
BACE	β-site APP cleaving enzyme
BBB	blood-brain barrier
bp	base pairs
BSA	bovine serum albumin
CAG	cytomegalovirus enhancer fused to the chicken beta-actin promoter
cDNA	complementary DNA
CMV	cytomegalovirus
CNS	central nervous system
CP	choroid plexus
Cq	quantification cycle value (threshold cycle)
CSF	cerebrospinal fluid
CYC1	cytochrome c1
DMEM	Dulbecco’s Modified Eagle’s Medium
DMT	disease-modifying treatment
DNA	deoxyribonucleic acid
dsDNA	double-stranded DNA
EC	entorhinal cortex
ELISA	enzyme-linked immunosorbent assay
EMA	European Medicines Agency
F	females/women
FBS	fetal bovine serum
FC	frontal cortex
FDA	Food and Drug Administration
FGF	fibroblast growth factor

FOXO	forkhead transcription factor of the O class
GDS	Global Deterioration Scale
GFP	green fluorescent protein
HC	hippocampus
HEK	Human Embryonic Kidney
ICV	intracerebroventricular
IGF-1	Insulin-like growth factor 1
IL	interleukin
iPSC	induced pluripotent stem cell
ITR	inverted terminal repeat
kb	kilo base pairs
kl	*klotho* gene
KL	Klotho
KO	knockout
M	males/men
M1	activated type 1 microglia
M2	activated type 2 microglia
mAb	monoclonal antibody
MCI	mild cognitive impairment
MD	mild dementia
mKL	membrane Klotho
MRI	magnetic resonance imaging
mRNA	messenger RNA
MWM	Morris Water Maze
NFT	neurofibrillary tangle
NLRP3	NLR family pyrin domain containing 3
NMDA	N-methyl-D-aspartate
NMDAR	NMDA receptor
NNL	no neuropathological lesions
NOR	Novel Object Recognition
NPC	neural progenitor cell
NTC	non-transduced control organoids
OF	Open Field
ORF	open reading frame
P/S	Penicillin-Streptomycin
PCR	polymerase chain reaction
PEI	polyethyleneimine
PET	positron emission tomography

pKL	processed Klotho
PSEN, PS	presenilin
pTau	hyperphosphorylated tau
qPCR	real-time quantitative polymerase chain reaction
r	Pearson correlation coefficient
rAAV	recombinant AAV
RNA	ribonucleic acid
ROS	reactive oxygen species
RT	room temperature
RT-qPCR	reverse transcription-real time quantitative polymerase chain reaction
sAPP	soluble APP
scAAV	self-complementary AAV
SDS	sodium dodecyl sulphate
SETD5	SET domain containing 5
sKL	secreted Klotho
ssDNA	single-stranded DNA
TNFα	tumor necrosis factor α
TREX1	three prime repair exonuclease 1
tTau	total tau
UAB	Universitat Autònoma de Barcelona
UBE2D2	ubiquitin conjugating enzyme E2 D2
US	United States
vg	viral genomes
WT	wild type
wtAAV	wild-type AAV

SUMMARY

Alzheimer's disease (AD), the most common form of dementia, is characterized by the progressive loss of memory and cognitive capacities. The neuropathological hallmarks of AD are deposits of β-amyloid (Aβ) and Tau in the brain, accompanied by neuroinflammation, oxidative stress, impaired autophagy, and neurodegeneration. Although several therapies have been developed targeting Aβ and Tau, today there is still no treatment approved able to cure or prevent AD. The high failure rate of clinical trials may be explained by the multifactorial nature of AD and/or the low translatability of preclinical animal models. Hence, two lines of research arise: on the one hand, to test pleiotropic molecules with the potential to counteract multiple neuropathological processes of AD; on the other hand, to implement preclinical models that better recapitulate the human brain physiology.

The anti-aging and neuroprotective protein Klotho (KL) shows promise as a therapeutic candidate given its pleiotropic functions, among others, enhancing cognition, synaptic plasticity and autophagy, protecting from oxidative stress, and reducing neuroinflammation. However, it is still unclear which of the KL variants, the secreted (sKL) or the membrane (mKL), mediates those functions in the human CNS, since most of the research is focused on mKL and mouse models.

In this work, the relative gene expression of sKL and mKL was characterized in the human brain, both in healthy and AD conditions. Interestingly, sKL was the most expressed variant in frontal and entorhinal cortex, hippocampus, and amygdala, whereas mKL was predominant in choroid plexus. In mice, mKL was the most abundant, so the expression ratio sKL/mKL is inverted in the mouse brain compared to the human. Besides, during AD, the gene expression of sKL and mKL in brain appeared altered, both in AD patients and 3xTg-AD mice compared to healthy humans and WT mice, respectively. At the protein level, soluble KL in cerebrospinal fluid (CSF) was found significantly lower in AD patients with Mild Dementia (MD). We also observed a positive correlation of KL levels with age in the AD elderly, which was not found in healthy individuals. Besides, the carriers of the APOE4 allele, a major genetic risk factor of AD, presented significantly lower levels of KL in CSF.

Based on our findings in humans, we focused on exploring the potential of sKL to counteract the cognitive deficits in AD. Thus, we administered AAV9-sKL vectors into brain of two AD mouse models (3xTg-AD and APP/Tau) to express sKL and assess its effect on cognition through behavioral tests. AAV9-mediated sKL expression tended to improve the spatial learning and the reference memory in 3xTg-AD females and APP/Tau males (assessed by the MWM test), as well as the recognition and spatial memory in APP/Tau and WT females (by NOR and T-maze tests). Unfortunately, both AD mouse models lacked profound memory and cognitive deficits at the ages tested, so the effect of sKL on the behavior assessed by the tests was mild.

Finally, this work also highlights the feasibility of human brain organoids as a preclinical model for AAV-based gene therapy research. An AAV-transduction protocol was optimized and the AAV7m8 capsid variant demonstrated to be highly efficient and superior to AAV9 for transducing human brain organoids. Thus, the translatability of preclinical research in neurological diseases could be increased by using human brain organoids as a complementary model to experimental animals, particularly the development of therapeutic strategies based on AAV-mediated gene transfer.

In future studies the potential of AAV-mediated sKL expression to counteract AD-related symptoms should be explored in AD-mice developing profound cognitive deficits, while at a molecular level, the effect of AAV-mediated sKL expression remains to be analyzed *in vivo* and in human brain organoids.

INTRODUCTION

1. Alzheimer's disease

Alzheimer's disease (AD) is the most common form of dementia, accounting for 60 to 80% of the cases [1]. It is characterized by the presence of beta-amyloid (β-amyloid, Aβ) and Tau protein aggregates in the brain, and the progressive loss of memory and cognitive function, followed by deficiencies in language and visuospatial skills. These symptoms are usually accompanied by behavioral disorders like apathy, aggressiveness, and depression [2]. Over 55 million people suffer from AD or other dementias worldwide [3], and one of every 85 individuals is expected to develop AD by the year 2050 [4]. AD is a major cause of disability and dependency among older people worldwide, and it has physical, emotional, social, and economic impacts, not only for patients, but also for their families, caregivers, and society in general.

1.1. Risk factors of AD

The most important risk factor to develop AD is age [5]. For the most part, people who develop AD are older than 65 years (late onset AD) [2]. Only about 4-6% of AD patients manifest symptoms between 30 and 65 years (early onset AD). Other risk factors include genetics, positive family history, head trauma, female gender, depression, diabetes mellitus, hyperlipidemia, and vascular factors [6], [7].

Genetics is responsible for about 70% of the risk for developing AD [8]. Rare autosomal dominant mutations in the amyloid precursor protein (APP) gene and the presenilin 1 and 2 (PSEN1 and PSEN2) genes, lead to increased production of the neurotoxic form Aβ42, causing early onset of AD symptoms. The so-called familial AD, associated to those mutations, represents less than 1% of AD cases. Late onset or sporadic AD is normally associated to the apolipoprotein E (APOE) type epsilon 4 (APOE4) allele, a polymorphism in the APOE gene [9], [10]. The APOE4 constitutes a major risk factor for developing AD, since carrying one copy of the APOE4 allele increases the risk of developing AD 3-fold; and 2 copies increases it by more than 12-fold. Conversely, the APOE2 allele is believed to provide some protection against the AD, as it has shown to lower the risk by half and even alleviate the severity of familial AD cases, although it is relatively uncommon among population. The most common allele is the APOE3, thought to have a neutral role neither decreasing nor increasing risk for AD[11].

Besides, women have a higher risk of developing AD than men [12] Among the 6.5 million AD patients older than 65 years in the United States (US), 2.5 million are men and 4 million are women. In other words, around two-thirds of the American's living with AD in the US are women [13]. Moreover, studies in patients have shown that AD pathology is different in women and men, and that women are more severely affected by AD [12], [14]. Since age is the most important risk factor for AD [5], and women's life expectancy is longer than men's on average, longer lifespan in women may contribute to higher AD prevalence in women compared to men [15]–[17]. However, some experts defend that although the incidence of AD (the risk of suffering AD for men and women of the same age) is higher in women *versus (vs)* men, it cannot be simply attributed to the higher longevity in women [12]. Incidence studies performed on different populations brought some controversy in the risk of developing AD based on gender [18]–[21], which may be influenced by age and/or geographic location [22] [23].

1.2. The pathophysiology of AD

The pathology of AD was first described by the German physicist Alois Alzheimer in 1906, when he examined the brain of a patient who had experienced memory loss and change of personality before dying. During autopsy, Alzheimer noticed the presence of protein aggregates and a massive loss of neurons, especially in the cerebral cortex. This disorder was termed "Alzheimer's disease" by Emil Kraepelin in 1909 [24], and more than one century after it was described, the pathogenesis of AD is not fully understood yet.

It is commonly accepted that the causes leading to memory decline are strongly tied to deposits of misfolded protein aggregates [25]. The neuropathological hallmarks of AD are extracellular Aβ plaques and intraneuronal neurofibrillary tangles (NFTs) of hyperphosphorylated tau protein (pTau). These aggregates derive from the naturally occurring and crucial protein structures in the brain Aβ and tau [26], whose abnormal aggregation causes progressive neuronal death, memory impairment, and cognitive disturbances. The current view of AD pathogenesis hypothesizes that Aβ and pTau aggregates are accompanied by neuroinflammation, synaptic degeneration and neuronal cell death, which eventually result in cognitive impairment.

1.2.1. β-amyloid

The Aβ peptide derives from the APP, a type I membrane glycoprotein [27] whose function is not fully elucidated today. APP can be processed through two different proteolytic pathways (Figure 1).

In the **non-amyloidogenic pathway**, which occurs in non-pathological conditions, APP is cleaved by α-secretases (for instance ADAM-10, TACE or PC7) within the Aβ region, destroying the Aβ sequence and releasing a soluble fragment (sAPPα) to the extracellular space. sAPPα is an essential proliferation factor for neural and non-neural adult stem cells [28]. In the **amyloidogenic pathway** that leads to AD, APP is processed by β-secretases, including BACE1 (β-site APP cleaving enzyme). This cleavage generates a large soluble ectodomain (sAPPβ) and a membrane-bound C-terminal fragment (βCTF), which is subsequently cleaved by γ-secretases, mainly PSEN1 or PSEN2, generating the Aβ peptide. Aβ species may contain 40 to 43 amino acid residues [29], although the major form of secreted Aβ contains 40 amino acids (Aβ40). The longer Aβ isoforms, containing 42 or 43 amino acid residues (Aβ42 and Aβ43, respectively) have a higher rate of fibrillization and insolubility, so they are thought to trigger Aβ polymerization during early stages of plaque formation and are more abundant than Aβ40 within the plaques.

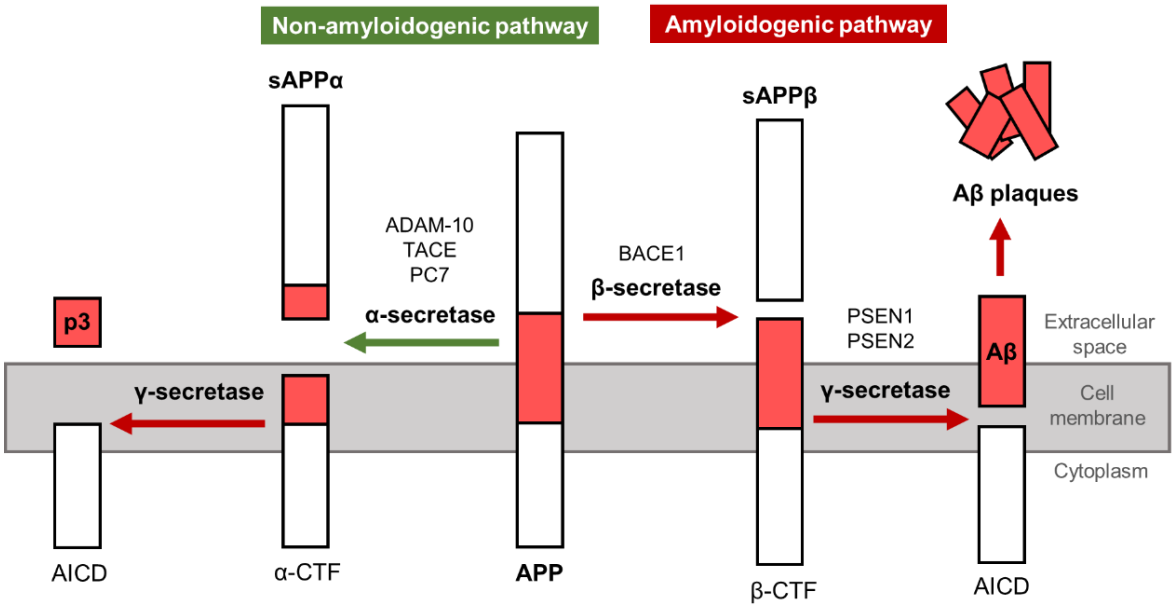

Figure 1. Proteolytic cleavage pathways of APP. Adapted from [29].

Amyloid plaques are classified according to their morphology into diffuse and dense-core [30]. Dense-core plaques consist of fibrillar Aβ deposits with compact core surrounded by dystrophic neurites (neuritic plaques) and reactive astrocytes and microglia. These plaques are associated to synaptic and neuron loss and cognitive impairment. Thus, a score of neuritic plaque can be used for the pathological diagnosis of AD [31] [32]. Diffuse plaques are amorphous Aβ deposits which are not normally neuritic nor related to glial cell activation or neuronal loss. Diffuse plaques can be found in the brain of cognitively healthy aged people, so this type of plaque is not used as pathological biomarker of AD.

The amyloid cascade hypothesis postulates that the deposition of the Aβ peptide in the brain is a central event in AD pathology. Since it was formulated in 1992 [33], Aβ oligomers have been considered the main drivers of the disease and the principal target of therapies. However, clinical examinations relying on this Aβ hypothesis have failed over the years, as well as numerous clinical trials focused on Aβ targeting. Consequently, this hypothesis has been proposed for revision, as it requires the integration of the “multi-factorial” conception of AD [34] [35].

1.2.2. Hyperphosphorylated Tau

Tau proteins belong to the family of microtubule-associated proteins and are mainly found in neurons. Six isoforms of Tau proteins identified in the adult brain play an important role in microtubule assembly and stabilization of neuronal microtubule networks, maintaining the integrity of the cytoskeleton [36].

The phosphorylation of Tau protein is developmentally regulated from fetal to adult stage. However, when Tau is abnormally hyperphosphorylated (pTau), it has a reduced affinity for microtubules and gets deposited in the cytosol. Then pTau polymerizes into paired helical filaments (PHF) and straight filaments (SF), generating NFTs. This event prevents Tau from maintaining cytoskeleton structure and leads to pathological disturbances in neurons such as loss of cytoskeletal structure, loss of dendritic spines and synaptic connectivity, axonal degeneration, and neuronal death (Figure 2). The pathological pTau is produced by genetic mutations in the *tau* gene or by dysregulation of the kinases and phosphatases that catalyze Tau phosphorylation [37] [38].

It has been suggested that pTau and Aβ are not independent mechanisms, but that they interact, and that pTau may be a downstream event of Aβ pathology [39].

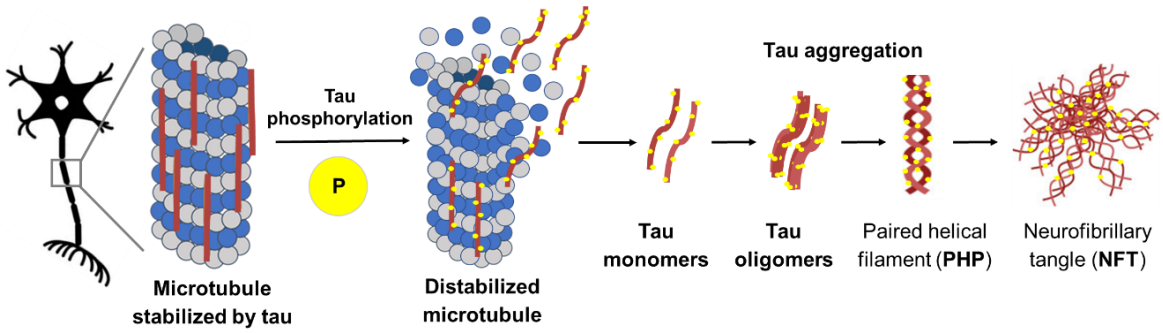

Figure 2. Tau hyperphosphorylation and aggregation leading to deposition of pathological NFTs.

1.2.3. Neuroinflammation

During AD, neuroinflammation is a complex key event driven by activated glial cells, mainly microglia and astrocytes.

Microglia and inflammasome activation

Microglia are the phagocytes of the Central Nervous System (CNS), being widely present in the brain and providing factors for the tissue maintenance, the plasticity of neuronal circuits and the protection of synapses. Microglia are also involved in the regulation of cognitive functions and memory formation, as well as in the maintenance of brain homeostasis through the clearance of dying cells, misfolded protein, and cellular debris [40].

The presence of protein aggregates or dying neurons, among other extracellular factors, can trigger the transformation of microglia from resting to activated, changing their ramified morphology to ameboid. There are two different phenotypes of activated microglia: pro-inflammatory (M1) and anti-inflammatory (M2). M1 microglia secrete pro-inflammatory cytokines and cytotoxic products that trigger inflammatory responses. Conversely, M2 microglia release anti-inflammatory cytokines and trophic factors that induce phagocytosis and increase the clearance of extracellular Aβ, thereby reducing neuroinflammation [41]

Microglia activation and accumulation are common during AD, especially around Aβ plaques [42], and inflammation has a dual role. In the early stages of AD, acute inflammation has beneficial effects because activated microglia contribute to the clearance of Aβ depositions and to maintaining brain homeostasis.

However, activated microglia can be damaging for neurons. On the one hand, the increasing Aβ accumulation cannot be removed by microglia, while they keep releasing reactive oxygen species (ROS) and pro-inflammatory cytokines, which activate the nuclear factor (NF)-kB in neurons, leading to APP synthesis and processing. Increasing Aβ peptide triggers further microglia activation and reduces their phagocytic capacity. On the other hand, Aβ activates the multiprotein complex *NLR family pyrin domain containing 3* (NLRP3) inflammasome in microglia, which stimulates caspase-1 and interleukin 1 (IL-1) activation, increasing the secretion of other pro-inflammatory cytokines and the levels of pro-inflammatory M1 microglia, further reducing Aβ clearance and aggravating AD pathogenesis[42]–[44]. The activation of NLRP3 and the pro-inflammatory environment generated by activated microglia can also induce Tau hyperphosphorylation and aggregation and in turn, neurons containing pTau further activate microglia [45], [46]. Furthermore, despite phagocytosis of dying neurons being benign for reducing inflammation, microglia can also phagocytose viable neurons (recently termed “phagoptosis”), which causes the death of these cells and contributes to the AD neurodegeneration [47].

Astrocytes

Astrocytes are large glial cells, the most abundant cells in the CNS. They were classically viewed as support cells for neurons, although they participate in several processes, such as generation and function of synapses, neurotransmitter recycling, formation and maintenance of the blood-brain barrier (BBB), immune signaling and homeostasis of ions and water [48].

In the presence of injuries in the CNS like during AD pathology, the astrocytes become reactive and tend to surround Aβ plaques and contribute to Aβ clearance [49], [50]. However, when exposed to Aβ, astrocytes release pro-inflammatory cytokines and nitric oxide, leading to detrimental feedback by exacerbating the neuroinflammation [51].

In summary, neuroinflammation in AD is not just a consequence of Aβ and pTau deposits, but it is also an event that contributes to pathogenesis as much, or even more, as protein aggregates. In fact, a study suggested that glial cells could be activated at early stages of AD, even before Aβ plaques appear. Overall, glial cells play a dual role in the pathogenesis of AD. Despite acute inflammation being a beneficial event against pathological protein

aggregates, chronic inflammation is detrimental over time, and contributes to aggravate neurodegeneration and AD pathology [42]–[44].

1.2.4. Autophagy

Autophagy is the process by which eukaryotic cells degrade and recycle dysfunctional proteins and organelles in lysosomes to maintain homeostasis. When autophagy is disrupted, cells start accumulating cellular debris, which reduces cell viability and accelerates physiological aging.

The CNS is highly dependent on autophagy to clear protein aggregates to maintain homeostasis. Neurons are especially vulnerable to dysfunctional autophagy because as they age, they tend to accumulate intracellular toxins and damaged organelles that must be cleared. Autophagy triggers the clearance of APP and plays an important role in the regulation of Aβ homeostasis. Disrupted autophagy contributes to the accumulation of toxic proteins like Aβ and Tau, leading to AD progression and worsening. Increasing evidence suggest that impaired autophagy is not only a correlative event observed during AD pathology, but also a causative factor for the development of the disease [52]. Thereby, autophagy stimulation has been proposed as a therapeutic approach to fight AD [53]

1.3. Symptomatic and Anatomical Phases of AD

AD is a progressive neurodegenerative disease characterized by different stages over time. The AD continuum refers to the progression of brain changes since they are unnoticeable to the person affected until they cause memory problems, and eventually physical disability. The three major phases on this continuum are: preclinical AD, mild cognitive impairment (MCI) due to AD and dementia due to AD, also called Alzheimer's dementia [1], [54], [55]. Alzheimer's dementia is subdivided in three stages: mild, moderate, and severe (Figure 3). The duration of each phase is variable for every individual, and may be influenced by age, genetics or sex, among other factors [56].

Clinicians use different staging methods to classify AD patients according to common patterns of symptoms. One of the most used staging systems is the Global Deterioration Scale (GDS) developed by Dr. Barry Reisberg. The GDS consists of 7 stages ranging from

no cognitive decline (stage 1: GDS1) to severe AD (stage 7: GDS7) and can be associated to the phases described in the AD continuum [57]

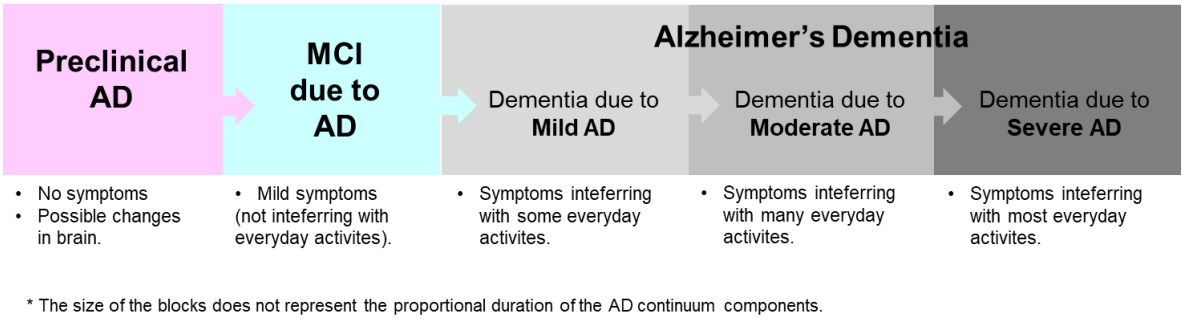

Figure 3. The Alzheimer's disease continuum. Adapted from [1].

I. Preclinical AD

Individuals have not yet developed symptoms like memory loss, but some brain changes may be measurable by biomarkers (further developed in next sections). The **GDS1** would include these preclinical AD patients, although it would also include any healthy individual with no cognitive decline. It is worth noting that not all the individuals who present AD biomarkers end up developing MCI or Alzheimer's dementia. For instance, Aβ plaques may be found in the brains of dead patients who did not experience memory loss or cognitive issues during life [58].

II. MCI due to AD

Individuals show slight memory, language and thinking impairments, but these do not interfere with their ability to perform daily activities. These patients would be classified as **GDS3**. About 15% of the patients with MCI develop dementia within two years [59] and about 30% develop Alzheimer's dementia after five years [60]. Conversely, some individuals with MCI revert to normal cognition or do not develop further cognitive decline. Identifying the patients with MCI who are more prone to develop dementia is a vital objective of ongoing research.

III. Alzheimer's dementia

Individuals experience appreciable memory, language, cognitive or behavioral symptoms that impair their ability to perform everyday activities. There are multiple symptoms that change over time as AD progresses.

III.1. Mild AD. Most patients are independent in some activities but need assistance in others to keep integrity. Difficulties may be found in handling money and completing everyday tasks. These patients showing MD match the **GDS4.**

III.2. Moderate AD. This is usually the longest stage of AD dementia. Individuals experience memory loss and language issues, and behavioral and personality alterations like suspiciousness and agitation. They also fail to recognize relatives, are prone to get confused and become incontinent at times. Multistep tasks, like bathing or dressing, are hard to be completed independently. These patients exhibiting moderate dementia match the **GDS5.**

III.3. Severe AD. Verbal communication is markedly affected, and individuals require constant surveillance. Motion is also largely diminished so the patients become bed-bound, which can trigger blood clots, skin infections and sepsis and inflammation that may lead to organ failure. Since swallowing control is also affected, eating and drinking becomes challenging, and individuals may intake food through the trachea instead of the esophagus. This leads to deposition of food particles in the lungs, which causes an infection called aspiration pneumonia, an important cause of death among AD patients. Patients exhibiting moderately severe or severe dementia match the **GDS6** and **GDS7** stages, respectively.

Anatomical progression of AD in brain

The neuropathological events provoked by Aβ and pTau lead to progressive brain atrophy. However, the temporal aggregation of Aβ plaques and NFT follow different topological patterns.

Amyloid plaque deposition starts before the cognitive decline, and it first appears in the isocortex, the most affected area, in contrast to NFTs [30]. The allocortex (entorhinal cortex, hippocampus, and subiculum) is affected by Aβ plaque later in time and to a lesser extent compared to the isocortex. Although the evolution of amyloid deposition is poorly

predictable, two staging systems have been proposed: Braak and Braak [61] and Thal et al. [62], [63] (Figure 4).

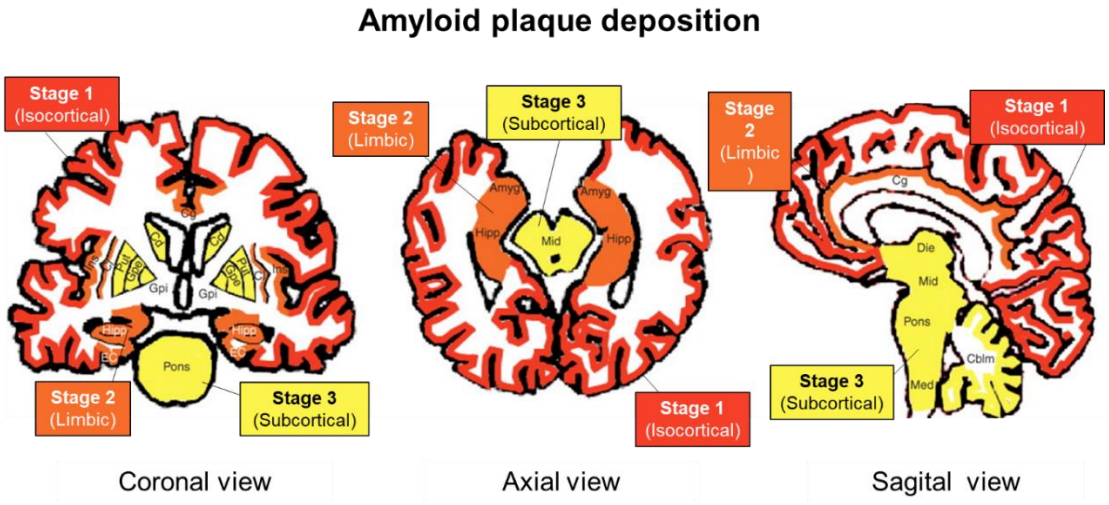

Figure 4. Spatiotemporal pattern of amyloid plaque deposition according to Thal et al. [62]. The five stages of amyloid deposition are here summarized in three stages. Stage 1 or isocortical (red); stage 2 or limbic (orange); stage 3 or subcortical (yellow). Amyg = Amygdala; EC = Entorhinal cortex; Hipp = Hippocampus; Cg = Cingulate cortex; Cd = Caudate nucleus; Put = Putamen; Gpe = Globus pallidus externus; Gpi = Globus pallidus internus; Cl = Claustrum; Ins = Insular cortex; Die = Diencephalon; Mid = Midbrain; Med = Medulla oblongata; Cblm = Cerebellum. Figure adapted from [30].

Opposite to Aβ plaque, the spatiotemporal progression of NFT follows a predictable pattern, firstly described by Braak and Braak [61]. Briefly, NFT deposition starts in the allocortex of the medial temporal lobe (entorhinal cortex and hippocampus) and then spreads to the associative isocortex. The last areas affected by NFT are the isocortical, unlike Aβ (Figure 5). The pattern of tau pathology is related to the clinical progression of AD, as studies show that the location and density of NFTs correlate to clinical symptoms of dementia [64], [65]. In fact, the topographic staging of NFT described by Braak and Braak is used for pathological diagnosis of AD.

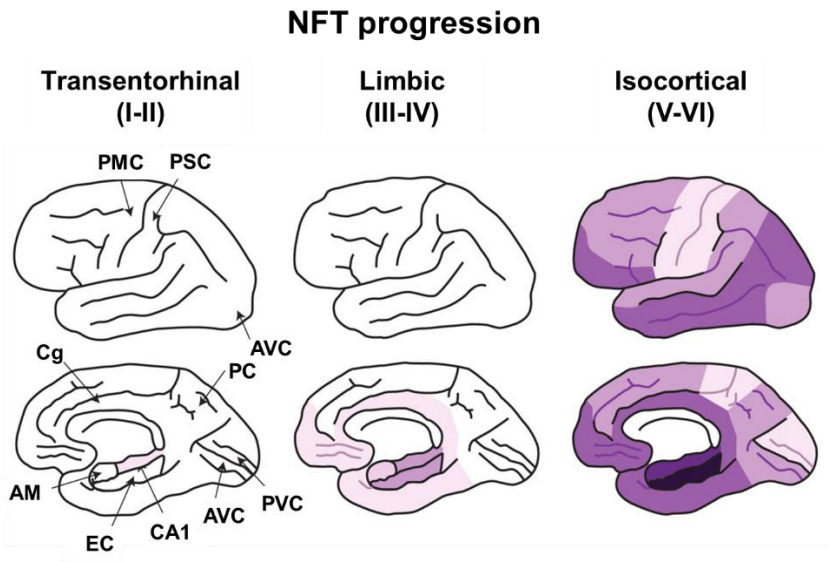

Figure 5. Spatiotemporal pattern and phases o[27] whose function is not fully elucf NFT degeneration. Adapted from [30]. Purple shading indicates the distribution of NFTs. Darker colors represent increasing densities of NFT. AM: Amygdala; EC: Entorhinal cortex; CA1: Cornus ammonis 1 hippocampal subfield; Cg: Cingulate cortex; PC: Precuneus; PMC: Primary motor cortex; PMS: Primary sensory cortex; PMV: Primary visual cortex; AVC: Associative visual cortex.

1.4. Diagnosis and biomarkers of AD

Although dementia can be detected by clinical symptoms, the only conclusive method to confirm AD diagnosis is *post mortem* autopsy of the patient's brain [66]. Thus, biomarkers are essential to confirm the AD pathology in the clinic and/or to achieve an early diagnosis.

Biomarkers are defined as characteristics (physiological, biochemical, or anatomical) that can be objectively measured *in vivo* and that indicate specific features of biological or pathogenic processes, or responses to therapeutic interventions [67]. Biomarkers not only allow to confirm an AD diagnose or a different pathology, but also to determine the stage of the disease continuum. This is of high relevance for the initiation of disease-modifying treatments (DMT), as these are only effective at early stages of the disease [66].

The most relevant biomarkers available to diagnose AD are based in brain imaging and analysis of biological fluids (Figure 6).

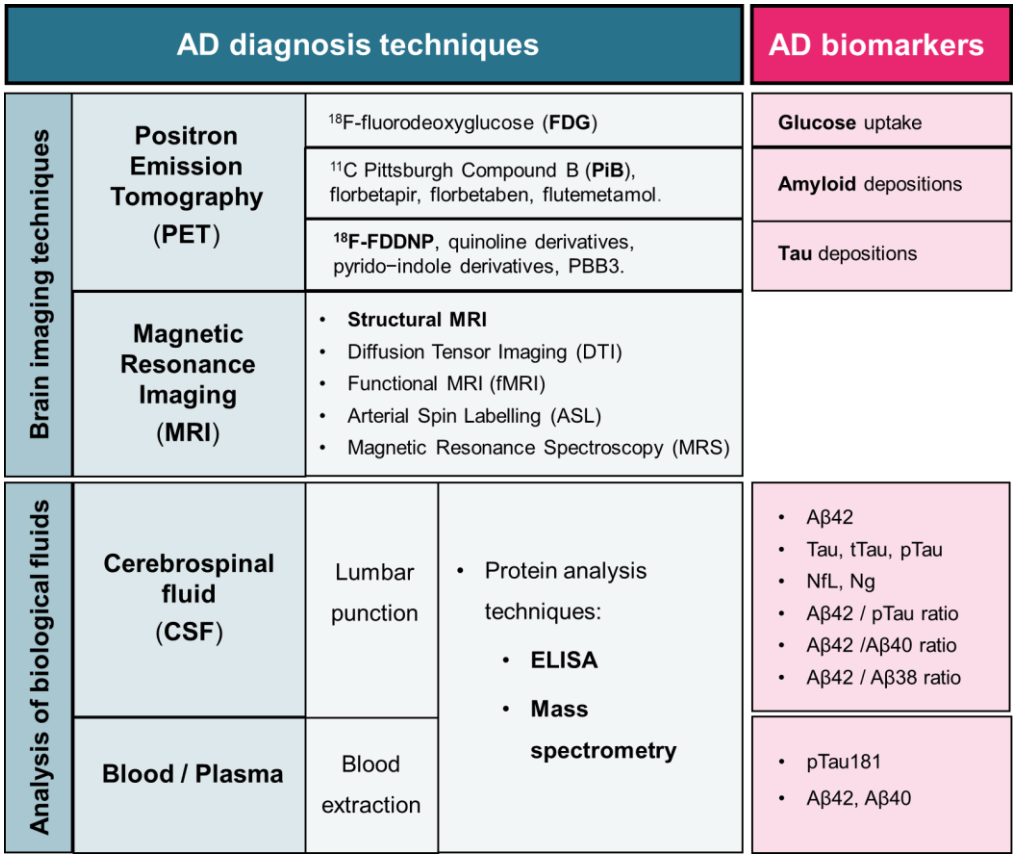

Figure 6. Summary of the most commonly used techniques for AD diagnosis in the clinic and their corresponding AD biomarkers. Data obtained from: [66], [68]–[79].

1.4.1. Brain Imaging Technologies

The changes occurring in the brain during AD can be detected through imaging techniques. Magnetic resonance imaging (MRI) and positron emission tomography (PET) are the most used techniques in the clinic to track structural or functional changes, respectively [68].

Positron Emission Tomography

PET is a molecular imaging technique that allows visualization of brain changes *in vivo*, using a suitable radiotracer for the feature of interest (metabolism, Aβ, Tau or neuroinflammation). It is highly specific and sensible and determines the AD stage of the examined patient [72]. The deficits in episodic memory that occur in AD and MCI are associated to hypometabolism (reduction in glucose uptake) in different areas of the brain. The use of the radiolabeled glucose analogue ^{18}F-fluorodeoxyglucose with PET (FDG-PET) allows measuring the glucose uptake in different brain regions, and it is considered a robust and reliable biomarker for *in vivo* diagnosis at early stages of AD [68]. The use of PET with the ^{11}C Pittsburgh Compound B (PiB), a radiotracer that binds to Aβ plaques, allows to map

Aβ deposition in the brain in vivo. However, it has a high cost and low selectivity [80]. Tau aggregates can also be mapped using PET with specific radiotracers (indicated in Figure 6) [68]. A study suggested that tau-PET is more sensitive than Aβ-PET for detecting early cognitive changes in preclinical AD [69]. Some limitations of the use of PET for clinical diagnosis are the high cost, exposure to ionizing radiation and low resolution [72].

Magnetic Resonance Imaging

MRI techniques show patterns of brain damage that lead to a diagnosis of AD by excluding other pathologies and to assess the risk of MCI conversion to AD [71]. Structural MRI, the most recommended modality for the AD diagnosis, reveals brain atrophy, whose progression follows Braak staging [61]. Visualization of the different brain regions is based on the differential release of energy of gray matter, white matter, and CSF, following magnetic field and radio frequency wave stimulation. Structural MRI provides volumetric measures of different brain regions which allows to diagnose AD and to predict cognitive decline trough a “brain atrophy score” or recently developed algorithms [66], [81]. Other MRI modalities include Diffusion Tensor Imaging (DTI), functional MRI (fMRI), Arterial Spin Labelling (ASL) and Magnetic Resonance Spectroscopy (MRS).

1.4.2. Analysis of Biological Fluids

The presence and the proportion of determined proteins (specially Aβ and tau) in CSF and plasma are considered important biomarkers to diagnose and predict the progression of AD. The detection of protein biomarkers in biological fluids is based on immunological or mass spectrometry assays [72].

Cerebrospinal Fluid

The CSF is a source of biomarkers produced in the brain, so it can indirectly reflect the biochemical changes occurring in the brain tissues. In AD patients, Aβ42 levels in CSF are decreased in early stages or even before the onset of dementia [73], probably because the Aβ deposition in brain decreases its secretion to CSF [74]. Tau levels are significantly increased in CSF of AD patients, both the total (tTau) and the pTau. The increased

concentration of tTau reflects neuronal degeneration, while the presence of pTau indicates hyperphosphorylation and likely formation of NFT. Other AD biomarkers in CSF are neurofilament light (NfL) and neurogranin (Ng), whose elevated levels reflect synaptic damage and predict brain atrophy and worsening prognostic [75], [76]. The early alteration of these biomarkers allows to diagnose AD before the onset of dementia, and to identify the patients with MCI that may progress to AD [77]. The combined analysis of different biomarkers provides greater accuracy for the AD diagnosis, for instance the ratios Aβ42 to pTau [78], Aβ42 to Aβ40 and Aβ42 to Aβ38 [82].

Despite the analysis of CSF biomarkers providing accurate and early AD diagnosis, it has some limitations such as high cost, variability in the procedures across different laboratories. Moreover, CSF collection involves an invasive intervention by lumbar puncture that causes nausea, back pain, and weakness in elder people [66].

Blood

The need for less invasive and more affordable techniques for the diagnosis of AD increases the interest for blood-based biomarkers. It is thought that in AD patients, Aβ, pTau, and NfL levels may be also altered in plasma as they are in CSF (reviewed in [83]).

Recent studies on pTau181, a specific pTau form, support that measuring its levels in plasma allows early AD detection in asymptomatic or MCI patients. In addition, measuring pTau181 would distinguish AD from other tauopathies, which is not possible by measuring other Tau forms [79], [84], [85]. A test based on high-resolution mass spectrometry to quantify Aβ42 and Aβ40 in plasma has recently been developed [86]. Nonetheless, despite plasma biomarkers having the potential to aid clinical diagnosis, they are not yet implemented in the clinic and are still being validated in research [72].

In summary, amyloid-PET neuroimaging and CSF protein analysis are the most used techniques for AD diagnosis nowadays [66]. They are sensitive and specific tools for the detection of AD biomarkers. However, they may be invasive and time-consuming, have high cost and their availability is limited. Therefore, there is still a high need for the development of accurate biomarkers that allow early detection of AD in a non-invasive way and at an affordable cost for all income countries and patients. Recently, new technologies like artificial intelligence or retinal imaging are giving rise to new AD biomarkers (summarized in [72]).

1.5. Therapeutic strategies for AD

Despite the high need and efforts to find a treatment for AD since it was described more than 100 years ago, nowadays there is still no therapy approved to cure or prevent the progression of the disease.

With the exception of Aducanumab (further discussed below) -recently approved by de Food and Drug Administration (FDA)-, all the available drugs are effective to relieve the symptoms of AD, but they do not modify the progression of the disease. These can be classified into acetylcholinesterase inhibitors (AChEIs) and N-methyl-D-aspartate (NMDA) receptor antagonists [87].

AChEIs decrease the breakdown of acetylcholine (Ach), an important neurotransmitter involved in memory whose levels are deficient during AD. AChEIs are used to improve cognitive symptoms in the patient and are effective in mild to moderate AD [66]. Commercialized AChEIs include: rivastigmine (Exelon), galantamine (Razadyne, Reminyl), donepezil (Aricept) and tacrine (Cognex). It should be noted that tacrine was withdrawn from use in 2013 due to hepatotoxicity, and analogues are currently being investigated to overcome the side effects [88].

Memantine (Namenda) is a NMDA receptor (NMDAR) antagonist approved in 2003 for the treatment of moderate to severe AD [66]. The NMDAR is involved in learning and memory together with the glutamate neurotransmitter. However, as observed in AD, elevated levels of glutamate cause excitotoxicity of neurons. Memantine reduces the glutamate induced excitotoxicity by blocking the NMDAR with moderate affinity, which allows the physiological actions of glutamate on learning and memory [89].

Since then, no therapy against AD had been approved until June 2021, when Aducanumab (aducanumab-avwa; Aduhelm) became the first DMT for MCI or mild AD approved in the US [90]. Aducanumab is a monoclonal antibody (mAb) directed against Aβ soluble and insoluble forms, reducing them in a dose- and time-dependent manner after one year of monthly intravenous infusions [91]. In the US, Aducanumab was approved using an accelerated regulatory mechanism based on the reduction in Aβ plaques, that was considered likely to predict clinical benefit [92]. However, verification of clinical benefit is still required for the continued approval of the treatment. In Europe, the European Medicines Agency (EMA) refused the market authorization of Aducanumab in December 2021 claiming that, regardless of the reduction in Aβ plaques, the clinical improvement in patients

had not been demonstrated. Besides, studies did not prove the drug to be safe enough, as brain imaging of some patients showed indicators of brain swelling and bleeding. Thus, the EMA considered that benefits of Aducanumab did not outweigh its risks [93].

By the beginning of 2022, there were 143 drug candidates in 172 ongoing clinical trials for the treatment of AD, 47 of them in phase III. Most of the candidates consist of DMT (83.2%), whose predominant targets are amyloid (20 agents), tau (13 agents), inflammation (23 agents), and synaptic plasticity (19 agents) [90].

The reduction of Aβ from the brain is a gold target of the DMT for AD. Since clinical trials based on β-secretase and γ-secretase inhibitors have failed due to severe side effects [94], immunotherapy strategies using mAb are gaining attention. For instance, Donanemab, lecanemab (BAN2401) and Gantenerumab are currently in advanced phases of clinical trials for the treatment of early AD [95]–[98].

Tau protein and NFT formation is being addressed by different strategies in clinical trials using mAb (7 trials), active vaccine (AADvac1) (1), antisense oligonucleotides (1), and small molecules (4) [90]. However, no therapeutic strategy targeting pTau has proved effective to date, and several Tau mAb have recently failed in clinical trials, including Semorinemab, Zagotenemab, Gosuranemab, and ABBV-8E12 [99].

The development of new therapies for AD is challenging with high failure rates [100]. In 2021, only one of the 49 novel drugs approved by the FDA was directed against AD, and it was the first approval for the past 18 years [101].

Most of the therapeutical strategies against AD target Aβ and pTau, although as previously mentioned, most of these drug candidates are proven ineffective. For instance, 33 drugs against Aβ have failed in phase III clinical trials [102]. Indeed, targeting amyloid to treat AD has been questioned in several perspectives [35], [98], [103], [104]. A possible explanation behind the failure of these single-target AD treatments is that therapy is started when cognitive symptoms are detectable. At this point, the accumulated damage over the years cannot be reversed, since the neuropathological alterations start years before the clinical symptoms appear. Thus, treatment should start in early stages or even before the onset of the symptoms, which requires early diagnosis tools and biomarkers.

Additionally, it is known that the pathogenesis of AD is multifactorial, and other processes besides Aβ and pTau accumulation play an important role, like neuroinflammation, oxidative

stress or synaptic impairment. This could explain why therapeutic strategies against one single target have not shown efficacy in reversing the cognitive decline and multi-targeted strategies are becoming more popular. In this respect, combination therapy aims to synergistically target different pathways to improve the multiple symptoms and causes of AD [105].

It should also be considered that AD is strongly linked to aging [5], so targeting this risk factor in a broad manner could prevent some damaging processes that are exacerbated during AD. In this regard, chronokines are a potential therapeutic approach. The term chronokine was recently coined to refer to soluble factors that drive function and change with aging [106].

In a reductionist simplification extracted from parabiosis experiments, blood of aged individuals contains increased amounts of detrimental chronokines, while young blood contains beneficial chronokines which decrease during aging [107] . Thus, it was suggested that beneficial chronokines could be administered for treating aging and age-related disorders. This innovative approach would provide a broad way to treat multi-factorial age-related diseases as AD, different from the classical pharmaceutical aim to specifically address one single target. Among other chronokines that have been identified, the anti-aging and neuroprotective Klotho shows promise as a molecular target to treat age-related neurodegenerative diseases, particularly AD.

2. Klotho

Since its discovery in 1997, α-Klotho (hereafter referred to as Klotho, KL) has gained attention in CNS disorders and aging. The *klotho* gene (*kl*) (named after the Greek goddess who spins the thread of life) was discovered during an attempt to develop a transgenic mouse model by pronuclear microinjection of a transgene. An accidental insertional mutation that disrupted *kl* led to systemic aging and shortened longevity in mice [108].

The aging-like phenotypes caused by the deficient KL expression include, among others, impaired cognition, hearing disturbance, motor neuron degeneration, arteriosclerosis, decreased bone mineral density and sarcopenia, in addition to premature death (reviewed in [109]). Conversely, KL overexpression extends the lifespan in mice [110], which supports the perception of KL as an aging-suppressor gene. KL is also considered a neuroprotective factor since KL-deficient mice have fewer dopaminergic neurons [111], neuronal degeneration in the hippocampus, hypomyelination [112], fewer synapses and lower synapse-related protein levels compared to wild-type (WT) mice [113]. They also show deficient axonal transport and increased oxidative stress in brain [114]. Moreover, behavioral studies indicate that KL-deficient mice have deficits in cognitive function [115]. In contrast, mice overexpressing KL show increased lifespan, improved cognitive abilities and resistance to oxidative stress [110], [116]–[120].

In humans, the KL-VS allele, a genetic variant of the *kl* gene, has been associated to higher levels of soluble KL [116], [121], [122]. Various studies have reported that heterozygous carriers of the KL-VS allele show improved longevity [122], enhanced cognition [116] and decreased risk of age-related heart disease [123], bigger brain volume and better function [124].

Altogether, these findings led to considering KL an anti-aging, neuroprotective and cognitive-enhancing factor, despite the molecular mechanisms behind these properties are unclear.

2.1. Klotho transcripts and protein variants

The α-*klotho gene (kl)* is composed of 5 exons. The full-length transcript codes a single pass transmembrane glycoprotein, so called transmembrane or **membrane KL (mKL)**, with

a short non-functional domain and an extracellular domain with two internal repeats (KL1+KL2) that can be proteolytically cleaved by ADAM10, ADAM17 and BACE1 secretases [125], [126]. The peptides released consisting of the extracellular domains KL1, KL2, and predominantly KL1+KL2, are referred to as shed or **processed KL (pKL)**. Within the third exon of the *kl* gene, there is an alternative splicing donor site that can originate an alternative transcript (composed of 3 exons in mouse and 5 exons in human). This transcript generated by alternative splicing contains 50 nucleotides of intronic sequence after exon 3 followed by a premature termination codon. The resulting protein is **secreted KL (sKL)**, composed of the KL1 domain and an exclusive C-terminal sequence which is not present in other KL isoforms [127], [128], and it could provide different properties. Both the pKL and sKL variants are referred to as *soluble Klotho*, since both can be found in biological fluids (serum, urine, and CSF) [129], [130]. In the past years, the variety of KL isoforms has led to confusing references and property attributions to each of the variants, so in this work, we have followed the nomenclature designated by Foster et al. [131] (Figure 7).

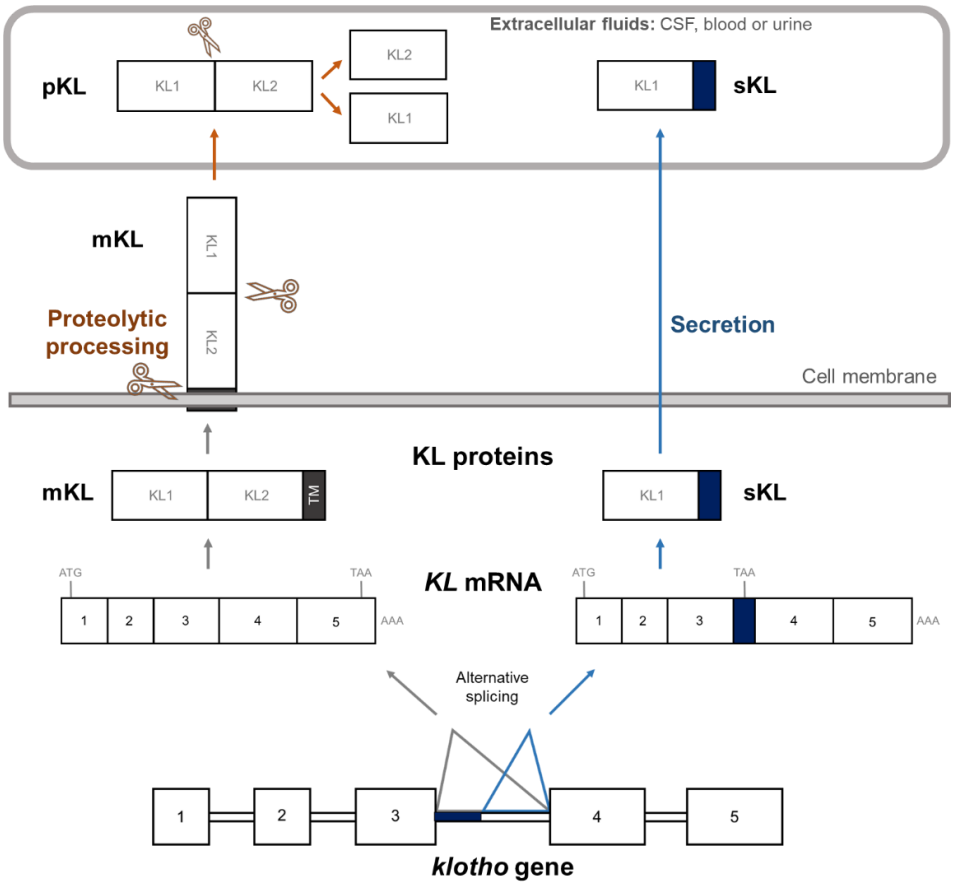

Figure 7. Human Klotho variants generated by the alternative splicing of the mRNA of *klotho* gene (mKL and sKL) and proteolytic processing of the full-length transcript variant protein by secretases (pKL). mKL: membrane KL, sKL: secreted KL, pKL: processed KL.

2.2. Klotho gene expression

Klotho gene expression is not ubiquitous, but specific of some tissues. The *kl* gene is mainly expressed in the kidney and brain. To a lesser extent, *kl* transcripts are also found in other tissues such as the skeletal muscle, urinary bladder, aorta, colon, small intestine, and endocrine organs including the thyroid gland, pituitary, placenta, pancreas, ovary, testis, and prostate [108], [127], [128]. In the kidney, *kl* is expressed in the distal convoluted tubules, and it is the source of the soluble KL proteins circulating in blood. In the brain, the highest levels of *kl* expression are found in the ependymal cells of the choroid plexus [108], which produce the soluble KL proteins for the CSF. Although at lower levels, KL mRNA has also been detected in other brain regions of mice including hippocampus, cortex, cerebellum (Purkinje cells), striatum and substantia nigra [120].

The relative expression of each KL transcript variant (mKL and sKL) is not uniform across tissues and among species. In mouse, mKL expression is predominant over sKL in all the tissues [128]. In mouse brain, sKL is more highly expressed than in other organs, although mKL mRNA is still more abundant [132]. In humans, the sKL transcript was reported to predominate over the mKL in kidney and hippocampus [127], although that work deserves further discussion in subsequent sections.

KL expression declines with age in the white matter of mammals, as observed in rhesus monkey, mice, and rats [133]. Besides, in an exhaustive mRNA analysis performed in rat brain, high *kl* expression was detected in early development, declined acutely during the second week of postnatal development, and then slowly increased to adult levels [134]. In humans, decreased levels of KL protein in CSF were found in aged subjects when compared to young adults [135].

2.3. Klotho protein distribution

High KL protein levels are detected in kidney tissue, in both human and mice. KL protein has also been detected in epithelial, endocrine, neuronal, reproductive, and arterial tissues of human and mouse [136], [137]. Soluble KL has been detected in biological fluids such as serum, CSF, and urine [129], [130]. However, the lack of antibodies able to specifically detect either sKL or pKL, hampers the possibility of differentiating between both variants.

Therefore, the extent to which each of the variants contribute to the soluble KL pool detected is still unknown.

2.4. Functions of Klotho

It is believed that the different KL protein variants exert different functions. Membrane KL is considered a component of cell surface receptor complexes, while the soluble variants are thought to act as humoral or endocrine factors. One of the reasons is because deficient *kl* expression severely affects different organs that do not express the *kl* gene, such as the lung, stomach, skin, thymus, and bones. In addition, exogenous KL overexpression in specific tissues ameliorates aging phenotypes in all organs. All this suggests that KL protein functions cell non-autonomously and acts as hormone with pleiotropic functions all over the organism [108]–[110], [138]. The most relevant systemic functions of KL are described below (Figure 8).

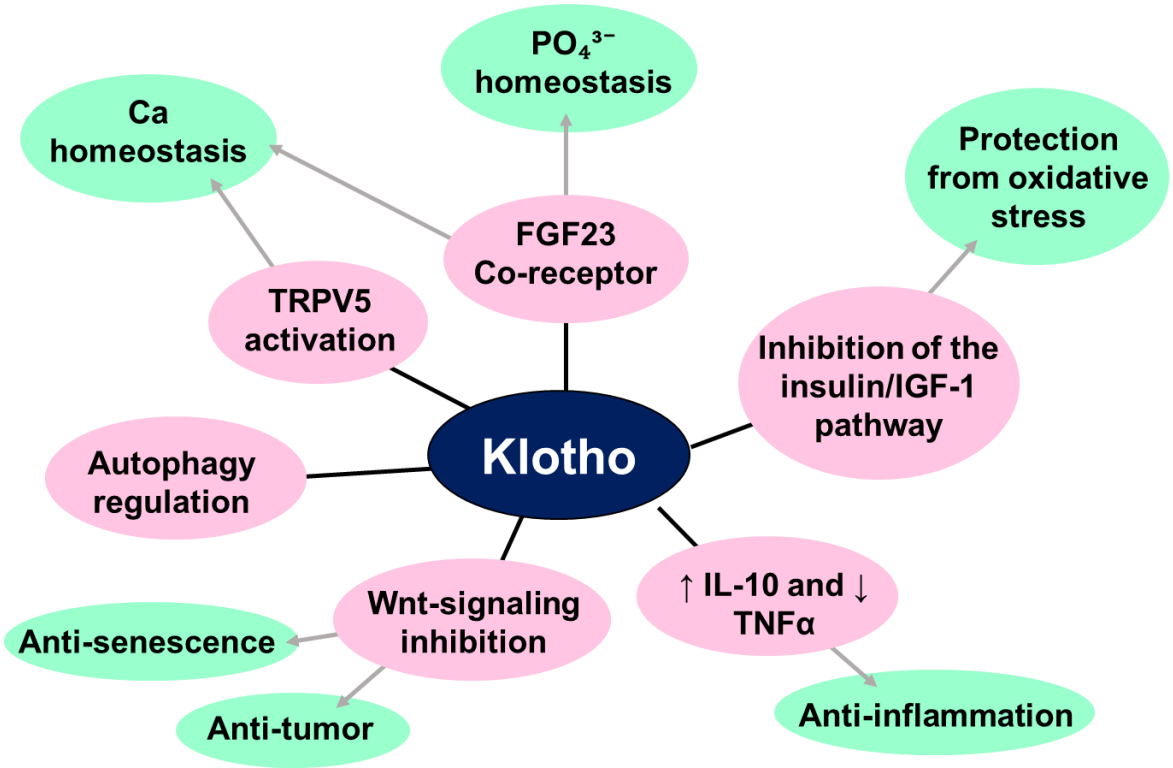

Figure 8. Summary of the main systemic functions of Klotho.

2.4.1. Regulation of phosphate and calcium homeostasis

In the kidney, mKL plays a vital role acting as a co-receptor with fibroblast growth factor (FGF) receptors, as it increases their affinity for FGF23, a bone-derived hormone whose main function is to regulate phosphate (PO_4^{3-}) excretion to urine. FGF23 is also involved in the production of the active form of D vitamin, having a key function in calcium (Ca) metabolism in kidney. The disturbance of KL and FGF23 cause premature aging and chronic diseases in mice. Conversely, the activation of the KL-FGF23 pathway in the kidney, rescues the aging phenotype in FGF23- or KL-deficient mice [139]. Therefore, KL is involved in PO_4^{3-} and Ca homeostasis by playing an important role in the FGF23 signaling pathway. Since these functions attributed to mKL are exerted by its extracellular domain (KL1), it is thought that the soluble KL variants presenting that domain could also act as humoral factors by binding to FGF23 receptors and modulating ion channels [109], [140]–[142].

KL also participates in the regulation of Ca homeostasis by activating the transient receptor potential vanilloid-5 (TRPV5), a channel that enables transcellular Ca reabsorption in the distal convoluted tubule of the kidney [143]convoluted tubule of the kidney [143]. The maintenance of Ca homeostasis is of high relevance given the physiological processes in which Ca plays a crucial role, for instance muscle contraction, neuronal excitability, enzymatic activity, bone formation, cell membrane formation, and exocytosis [144].

2.4.2. Protection from oxidative stress

Soluble KL suppresses phosphorylation of insulin and the IGF-1 receptor, inhibiting the signaling pathway of the insulin/insulin-like growth factor-1 (IGF-1) and leading to the phosphorylation and activation of forkhead transcription factors of the O class (FOXOs) such as FOXO1, FOXO3a and FOXO4. Phosphorylated FOXO3a induces transcription of antioxidative enzymes such as manganese superoxide dismutase (MnSOD) and catalase, which remove reactive oxygen species (ROS), and thus, protect from oxidative damage [145], [146]. The inhibition of the insulin/IGF-1 signaling is a mechanism conserved in evolution known to suppress aging and extend lifespan [147]. Therefore, KL potentially exerts its anti-aging effects by inhibiting the insulin/IGF-1 pathway and consequently increasing resistance to oxidative stress [110], [146], [148], [149].

2.4.3. Anti-inflammatory properties

Klotho stimulates the production of the anti-inflammatory cytokine IL-10, which inhibits the expression of pro-inflammatory cytokines such as the tumor necrosis factor α (TNFα) [150]. The TNFα has a central role in the production of pro-inflammatory cytokines and the cytokine cascade that triggers inflammation [151], so high levels of TNFα generate a pro-inflammatory environment. Therefore, by stimulating IL-10 and inhibiting TNFα, KL can reduce the inflammatory environment.

2.4.4. Anti-senescence and anti-tumor properties

Wnt signaling activation is essential for stem cell proliferation and survival. However, persistent Wnt signaling causes stem cell dysfunction and depletion, leading to cell senescence [152], [153]. Stem cell dysfunction prevents tissues from regenerating and accelerates aging processes. Soluble KL is thought to bind Wnt ligands and prevent Wnt binding to its cell-surface receptors, thus inhibiting Wnt signaling [154]. This property could contribute to the anti-aging function of KL.

Apart from this, aberrant activation of Wnt signaling is related to the development of melanoma, hepatocellular and colorectal cancers, among others [155]–[157]. In several tumorigenic processes, downregulation of KL is associated with tumor malignancy, whereas KL overexpression has shown anti-tumorigenic effects in solid tumors and hematological malignancies (reviewed in [158]). Thereby, KL is also considered an anti-tumorigenic target and a biomarker of cancer prognosis. However, the exact mechanism by which it exerts tumor-suppressor effects is not entirely described yet.

2.4.5. Regulation of autophagy

Autophagy is the process by which cells self-degrade dysfunctional proteins or damaged organelles, and it is crucial for maintaining homeostasis. Abnormal autophagy, either insufficient or excessive, leads to the development of diseases, including, cancer, kidney injury, AD, cardiovascular disease, chronic obstructive pulmonary disease (COPD), diabetes and muscular dystrophy. In all these diseases, KL has been reported to be involved in regulating autophagy. Decreased KL expression is associated with worsening of abnormal autophagy, whereas higher expression correlates with amelioration of

abnormal autophagy (reviewed in [159]). Therefore, KL seems to have a dual role inducing or inhibiting autophagy, depending on the pathological condition. KL is thought to regulate autophagy through its influence in Beclin-1 and aldosterone level [160] and the IGF-1/PI3K/Akt/mTOR signaling pathway [110], [161], [162], resulting in the restoration of normal autophagy to reach beneficial effects. Thus, KL could be a potential therapeutic target for diseases in which autophagy is impaired (Figure 9).

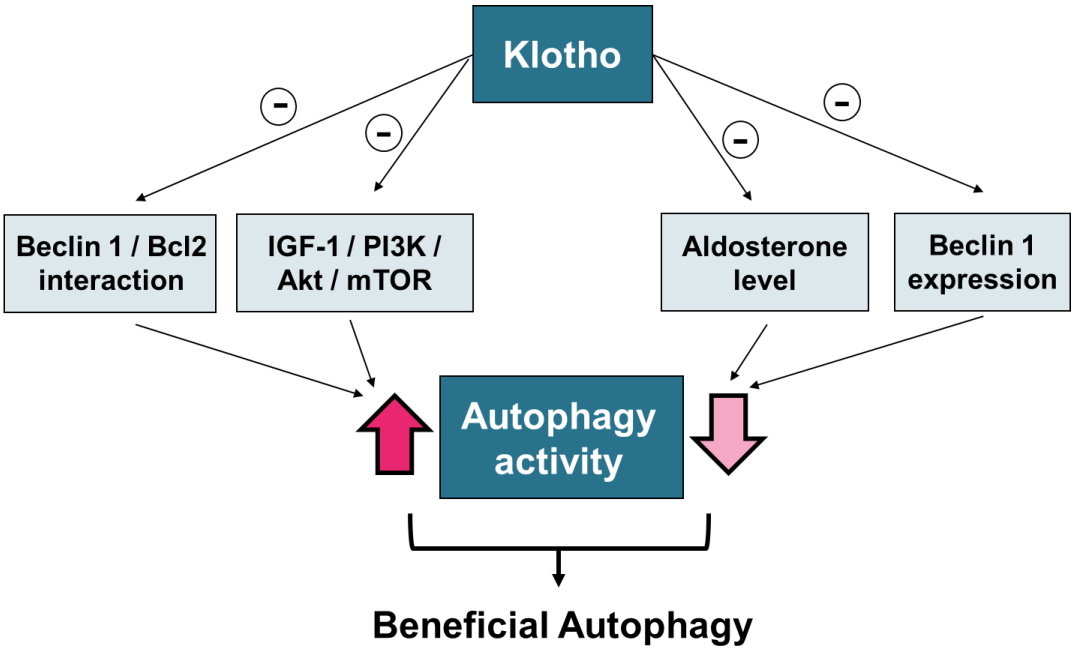

Figure 9. Klotho influence in the regulation of autophagy by its induction or inhibition, leading to a beneficial effect (adapted from [159]).

2.5. Klotho in the Central Nervous System

Increasing evidence supports the relevance of KL in the CNS and its influence on the development of age-related neurodegenerative diseases, as AD. However, the molecular pathways by which KL acts in the brain are unknown, and no putative receptor has been identified yet. Thus, the neuroprotective properties of KL have been discovered from the effects of its deficiency or overexpression.

2.5.1. KL expression is decreased in aging and neurodegenerative diseases

Decreased *kl* expression during aging has been reported in the brain of rhesus monkey, mouse, and rat, and in the CSF of humans [132], [133], [135].

Lower KL levels are also found under neuropathological conditions. Human patients of AD and multiple sclerosis show decreased soluble KL in CSF [135], [163], and *kl* mRNA levels are lower in hippocampi of epilepsy patients [164]. In different AD mouse models, diminished KL expression has been reported in brain as well: in the hAPP, KL protein levels are reduced in hippocampus [165]; in the APP/PS1, both mRNA and protein are decreased in choroid plexus [162]; and in the 3xTg-AD, *kl* mRNA levels decayed more rapidly with age than in healthy mice [132].

In summary, decreased KL levels are associated to aging and neurodegenerative diseases like AD, and it may be related to the cognitive decline as we will discuss in the following sections.

2.5.2. KL enhances cognition and memory

In humans, the heterozygous carriers of the KL-VS allele associated to higher levels of soluble KL, have shown better cognitive performance, not only in older adults, but also in AD patients [116], [121], [122], [124], [166], [167]. However, the KL-VS allele in homozygosity is related to reduced lifespan and decreased cognitive function [122], [124]. A recent study caused controversy reporting that elderly heterozygous of the KL-VS showed lower cognitive performance [168]. Herein, it seems that the positive effect of KL on cognition may be related to the protein levels.

In mice, increasing KL levels have also been associated with improved cognitive functions. For instance, transgenic mice overexpressing *kl* perform better in learning and memory tests, and AAV-mediated sKL expression in brain improved memory in old mice [116], [118], [169]. In addition, peripheral administration of the soluble pKL protein acutely improved cognitive performance in young and aging mice [170], although the mechanism by which this protein interacts with brain function is controversial, since soluble KL is not known to cross the BBB. Conversely, klotho-deficient mice show impaired recognition and associative memory [115].

In mouse models resembling AD pathology, KL augmentation ameliorates cognitive performance as well. Lentivirus-mediated expression of full-length KL in brain attenuated cognitive dysfunction in APP/PS1 mice [161], [171]. Increasing full-length KL expression in the hAPP transgenic mice by crossing with transgenic mice overexpressing *kl*, enhanced spatial learning and memory in hAPP mice [165]. In hAPP transgenic mice, increasing KL expression by crossing with transgenic mice overexpressing full-length *kl* enhanced spatial learning and memory [165]. Moreover, KL upregulation following lingustilide administration reduced the memory deficits in SAMP8 mice.

Altogether, this data indicates that increasing KL levels improves cognitive capacities, both in normal aging and AD pathology. The beneficial effects of KL in the cognitive performance could be explained by its pleiotropic functions, as it participates in diverse processes relevant for brain function, explained hereunder.

2.5.3. KL enhances synaptic plasticity

Long-term potentiation (LTP) induced by NMDARs in the hippocampus is essential for different forms of memory, like spatial, temporal, and associative [172]–[174]. When glutamate binds to NMDARs and Ca enters the cell, a complex intracellular cascade is initiated, triggering LTP, and eventually altering the synapses. Synaptic GluN2B is an NMDAR subunit with crucial functions in memory and learning, whose currents are involved in LTP [138], [175].

Transgenic mice systemically overexpressing *kl* show synaptic GluN2B enrichment in the frontal cortex and the hippocampus, as well as enhanced LTP. Thus, upregulation of GluN2B subunit mediated by KL overexpression could be the reason why *kl*-overexpressing mice have improved memory [116]. Similarly, in an AD mouse model, increased KL levels led to GluN2B enrichment in post-synaptic densities, as well as enhanced NMDAR-dependent synaptic plasticity in the hippocampus. Besides, it prevented the depletion of NMDAR subunits in the hippocampus, which could explain the improved memory and learning observed in these mice [165]. In a different study, soluble pKL (consisting of KL1+KL2 extracellular domains) administered peripherally induced cleavage of the NMDAR subunit GluN2B, enhanced NMDAR-dependent synaptic plasticity, as well as cognitive enhancement and neural resilience in young, aging, and α-synuclein transgenic mice [170].

Modulating LTP at the hippocampus influences learning and memory. Despite glutamate is the principal neurotransmitter implicated in LTP in hippocampus, this mechanism can be also modulated by other molecules such as ACh, dopamine, norepinephrine, cortisol, serotonin, and estrogens, with which KL could also interact, ultimately impacting cognition [176].

2.5.4. KL protects from oxidative stress in brain

In brain, KL reduces the oxidative stress through inhibition of the insulin/IGF-1 pathway through a mechanism previously explained (section 0). In cell cultures such as human SH-SY5Y neuroblastoma cells, rodent primary hippocampal neurons, and human oligodendrocyte cell lines, recombinant pKL treatment decreased ROS and upregulated redox systems, preventing neuronal damage caused by oxidative stress [119], [177], [178]. In this line, KL upregulation in SAMP8 mice reduced oxidative stress in brain and ameliorated memory deficits [179], [180].

2.5.5. KL is required for NPC and oligodendrocyte maturation and myelination

The decline of the hippocampal-dependent memory function is associated with decreased neural progenitor cell (NPC) proliferation and maturation, events observed in KL-deficient neurospheres. Conversely, pKL treatment enhances neural proliferation and maturation in these neurospheres. Furthermore, KL-overexpressing mice show improved hippocampal-dependent memory. Therefore, KL could protect against memory loss through regulation of postnatal neurogenesis [181].

KL is also involved in oligodendrocyte maturation and its functions, including myelination. Myelin abnormalities are associated with normal brain aging, but also with neurodegenerative diseases like multiple sclerosis. KL-deficient mice present a lower number of total and mature oligodendrocytes compared to control littermates, as well as reduced myelin protein and gene expression, and impaired myelination [112]. Damaged myelin is also observed in brain of aging rhesus monkey, in which *kl* expression is decreased and correlates with cognitive decline [133]. Conversely, pKL treatment enhanced oligodendrocyte differentiation and myelination in a human oligodendrocyte hybrid cell line and in rat primary oligodendrocyte progenitor cells. It was observed that exogenous KL

interacted in the ERK and Akt signaling pathways, decreasing proliferation and enhancing differentiation of these cells [112], [178]. Therefore, KL could be a potential therapeutic target to protect brain from age-dependent myelin changes, and to promote myelin recovery in demyelinating diseases.

2.5.6. KL reduces neuroinflammation

KL can suppress neuroinflammation by inhibiting the NLRP3/caspase-1 signaling pathway, a key event in AD [171], [182], [183].

In the APP/PS1 mouse model of AD, the high concentration of NLRP3 and active caspase-1 was reversed by the overexpression of full-length KL cDNA. Moreover, microglia transformation to the anti-inflammatory M2 type increased Aβ clearance in the brain and decreased Tau phosphorylation. KL has also shown to reduce other inflammatory markers in cell cultures. For instance, pKL pretreatment in human SH-SY5Y neuroblastoma cells exposed to Aβ reduced NF-kB, IL-1β, and TNFα. In peripheral blood mononuclear cells (PBMCs) of AD patients treated with an adenovirus expressing KL, reduced production of inflammatory cytokines and activation of the Wnt/β-catenin pathway were observed [184].

2.5.7. KL induces autophagy

Recent studies suggest that KL can induce autophagy, facilitating the clearance of toxic Aβ and Tau protein aggregates [185]. For instance, lentivirus-mediated overexpression of full-length KL induced autophagy activation in both AD mice and cultured murine microglia [161]. Conversely, *kl*-deficient mice show significant reduction of autophagy [186]. Thus, KL could be a potential target to stimulate the impaired autophagy observed in AD [159], [187].

In summary, KL is thought to counteract cognitive decline and memory deficits through different mechanisms in brain, summarized in Figure 10:

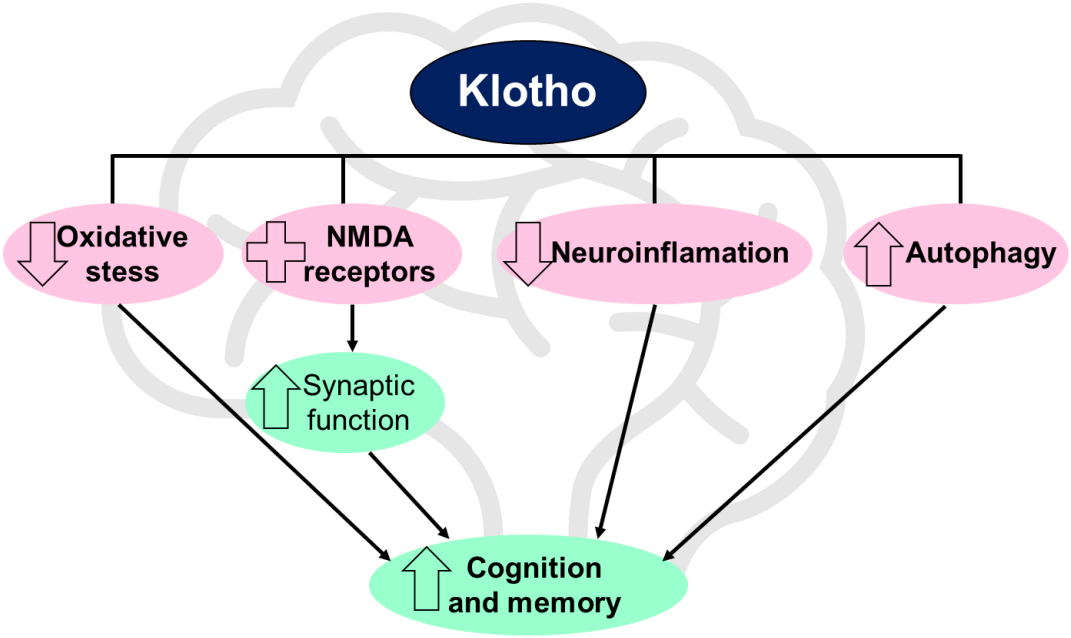

Figure 10. Summary of the principal mechanisms by which Klotho could contribute to enhance the memory and cognitive functions.

2.6. Secreted Klotho: a potential molecular target in AD

To date, therapies for AD based on selective agents have not proven effective to reverse the cognitive deficits. This might be due to the multifactorial nature of AD, in which diverse simultaneous events contribute to the pathology. Therefore, future therapeutic approaches against AD should focus on pleiotropic molecules able to mediate in different pathologic events. In this sense, KL could be a potential therapeutic target, as demonstrated by its multiple effects in the CNS, explained in the previous section.

By stimulating those processes, KL has shown to improve pathological hallmarks of AD. For instance, Aβ clearance is enhanced in AD mouse models overexpressing KL [161], [162], [171]). Mitigation of Tau pathology has also been observed in AD patients carrying the KL-VS allele in heterozygosity, which appears to increase KL protein levels. Decreased Tau-related symptoms and Tau-imaging was accompanied by reduced cognitive impairment in those patients [166]. Altogether, results from different studies indicate that KL could be a potential therapeutic target for the treatment and/or prevention of AD.

KL could also contribute to cure or prevent AD through its anti-aging properties. As previously explained, aging is the major risk factor for suffering AD [5], so leading the

patients into a healthy aging process could prevent or delay the development of AD symptoms.

However, the exact molecular and cellular pathways by which KL improves cognitive performance, as well as its involvement in AD pathology, remain to be fully understood. To date, no specific receptor for KL has been described in brain.

Another key question that remains to be elucidated is which of the KL variants (mKL, pKL or sKL) is the most relevant in the CNS and exerts the neuroprotective functions in brain. Most studies refer to “soluble” KL without making a distinction between “processed” and “secreted”. This is probably because they are usually analyzed through the common domain KL1, present in both soluble forms, so no differentiation between sKL and pKL can be made. Although, it is highly unlikely that the two isoforms have the same properties.

In a previous study, our group specifically analyzed the gene expression of sKL and mKL in brain and kidney of healthy aging and 3xTg-AD mice. In both models, they observed that each transcript decayed with age. However, sKL was almost exclusively found in brain, and had a different spatial and temporal expression profile to that of mKL [132]. In a different study, our group demonstrated that AAV-mediated expression of sKL in brain improves age-dependent cognitive impairment in mice [118]. A different group also demonstrated that AAV-mediated expression of human-sKL in hippocampus benefits memory formation in mice [169]. Taken together, these results indicate that sKL has an important role in brain, and so in the decline of cognitive capacities. Moreover, the expression of sKL and mKL seems to be differentially regulated, suggesting different functions for the resulting proteins, sKL and mKL or pKL.

The few results available in humans also point in the same direction. A study screened human cDNA libraries and 6 and 4 independent clones from the kidney and hippocampus, respectively, were isolated [127]. They found that the sKL transcript predominated over mKL in kidney and hippocampus. However, to our knowledge there is no study in which mRNA levels of the different KL isoforms have been directly quantified in human tissues.

Therefore, two lines of research emerge. On the one hand, the relevance of the secreted variant over the full-length transcript in the human brain should be confirmed. On the other hand, the potential of KL as a therapeutic target for the treatment and/or prevention of AD should be further explored.

3. Gene therapy

Gene therapy consists of transferring genetic material to a patient with the aim of treating or preventing a disease. This approach relies on the capacity of the patient's own cells to produce the therapeutic product coded on the transferred genetic material. The therapeutic effect can be achieved through different strategies [101], [188]:

- Transferring a correct copy of a gene whose mutation is causing a disease.
- Transferring a therapeutic gene whose increased expression has beneficial effects (augmentation therapy).
- Silencing the expression of a detrimental gene by transferring interference RNA or by genome editing.
- Replacing a mutated gene by its correct copy in the genome by genome-editing techniques.

When clinical research was initiated in 1990, gene therapy was directed to treat monogenic diseases by administering the correct copy of the defective gene. Today, more than 3,000 clinical trials on gene therapy are being conducted to treat a broad range of pathologies including, genetic, cardiovascular, infectious, neurological, neuromuscular, hematological, and ocular disorders, although, the vast majority of gene therapy clinical trials are directed to cancer (Figure 11). As of 2022, there are 22 gene therapies approved for clinical use [189] (Table 1).

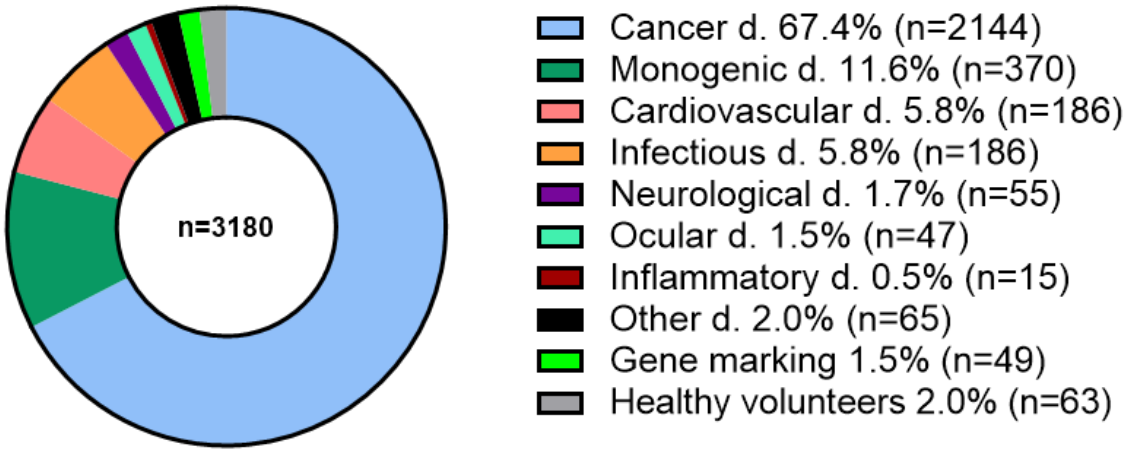

Figure 11. Indications addressed by Gene Therapy Clinical Trials. Data obtained from [189].

Table 1. Approved gene therapies as for October 2022. Adapted from [190].

Product name	Generic name	Year approved	Disease (s)	Locations approved
Gencidine	Recombinant p53 gene	2004	Head and neck cancer	China
Oncorine	E1B/E3 deficient adenovirus	2005	Head and neck cancer; nasopharyngeal cancer	China
Rexin-G	Mutant cyclin-G1 gene	2006	Solid tumors	Philippines
Neovsculgen	Vascular endotelial growth factor gene	2011	Peripheral vascular disease; limb ischemia	Russian Federation, Ukraine
Imlygic	Talimogenelaherpa repvec	2015	Melanoma	US, EU, UK, Australia
Strimvelis	Autologous CD34+ enriched cells	2016	Adenosine deaminase defieciency	EU, UK
Kymriah	Tisagenlecleucel-t	2017	Acute limphocytic leukemia; diffuse large B-cell lymphoma	US, EU, UK, Japan, Australia, Canada, South Korea
Luxturna	Voretigene neparvovec	2017	Leber's congenital amaurosis; retinitis pigmentosa	US, EU, UK, Australia, Canada, South Korea
Yescarta	Axicabtagene ciloleucel	2017	Diffuse large B-cell lymphoma; nonHodgkin's lymphoma; follicular lymphoma	US, EU, UK, Japan, Canada, China
Collategene	beperminogene perplasmid	2019	Critical limb ischemia	Japan
Zolgensma	onasemnogene abeparvovec	2019	Spinal muscular atrophy	US, EU, UK, Japan, Australia, Canada, Brazil, Israel, Taiwan, South Korea
Zynteglo	Betibeglogeneauto temcel	2019	Transfusion-dependent beta thalassemia	EU, UK
Tecartus	Brexucabtageneaut oleucel	2020	Mantel cell lymphoma; acute lymphocytic leukemia	US, EU, UK
Libmeldy	atidarsagene autotemcel	2020	Metachromatic Leukodystrophy	EU, UK
Breyanzi	Lisocabtagenemara leucel	2021	Diffuse large B-cell lymphoma; follicular lymphoma	US, Japan
Abecma	Idecabtagenevicleu cel	2021	Multiple myeloma	US, Canada, EU, UK, Japan
Delytact	Teserpaturev	2021	Malignant Glioma	Japan
Relma-cel	relmacabtagene autoleucel	2021	Diffuse large B-cellllymphoma	China
Carvykti	ciltacabtagene autoleucel	2022	Multiple myeloma	US
Upstaza	eladocagene exuparvovec	2022	Aromatic L-amino acid decarboxylase (AADC) deficiency	EU, UK
Roctavian	valoctocogene roxaparvovec	2022	Hemophilia A	EU, UK

3.1. Gene Therapy Vectors

The vehicle by which the genetic material is transferred into the cells is called a 'vector'. Gene therapy vectors can be administered either directly into the patient (*in vivo*) or in cultured cells that are then transplanted into the patient (*ex vivo*). For *ex vivo* gene therapy, usually in stem cells, it is important to use integrating vectors that allow the transferred DNA to be incorporated into the host cell genome. This way, when the cell divides, the therapeutic gene will be inherited by the daughter cells. Lentiviral vectors are commonly used for this type of *ex vivo* gene therapies. For *in vivo* gene therapy, usually targeting postmitotic cells that no longer divide, non-integrative vectors are preferred since they have less risk to induce insertional mutagenesis. Long-term expression of the transferred genetic material can be achieved by episomal stabilization of the DNA [188]. For this purpose, AAVs are the preferred vectors.

Vectors can be classified as viral and non-viral. Non-viral vectors usually consist of the DNA or RNA molecules to be transferred and a lipidic or polymeric envelope surrounding it. The advantages of non-viral vectors are lower immunogenicity than viral vectors, larger cargo capacity and simpler production processes. However, synthetic vectors show poor efficiency in transferring the genetic material into the cells *in vivo* and just provide transient expression of the transgene [191]. Conversely, viral vectors are much more efficient in transducing target cells, and so they are the most used in clinical trials despite being more immunogenic (Figure 12).

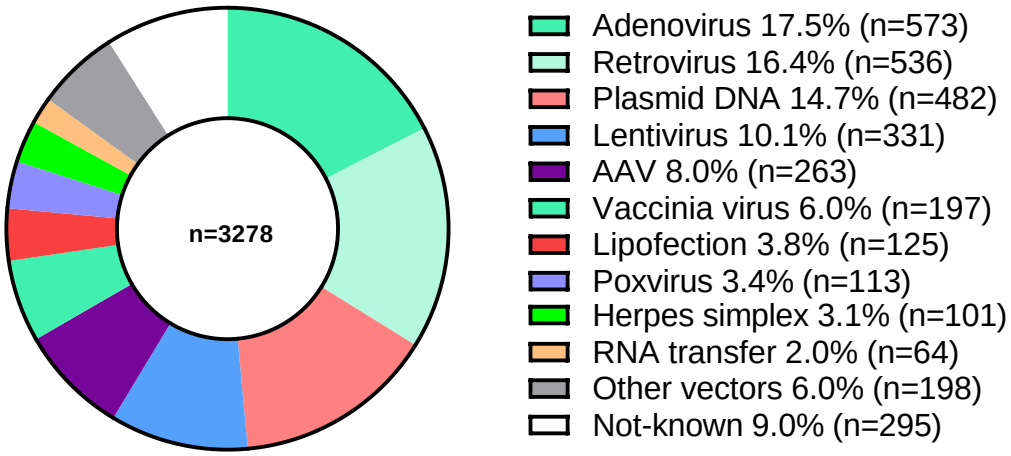

Figure 12. Vectors used for Gene Transfer in Gene Therapy Clinical Trials. Data obtained from [189].

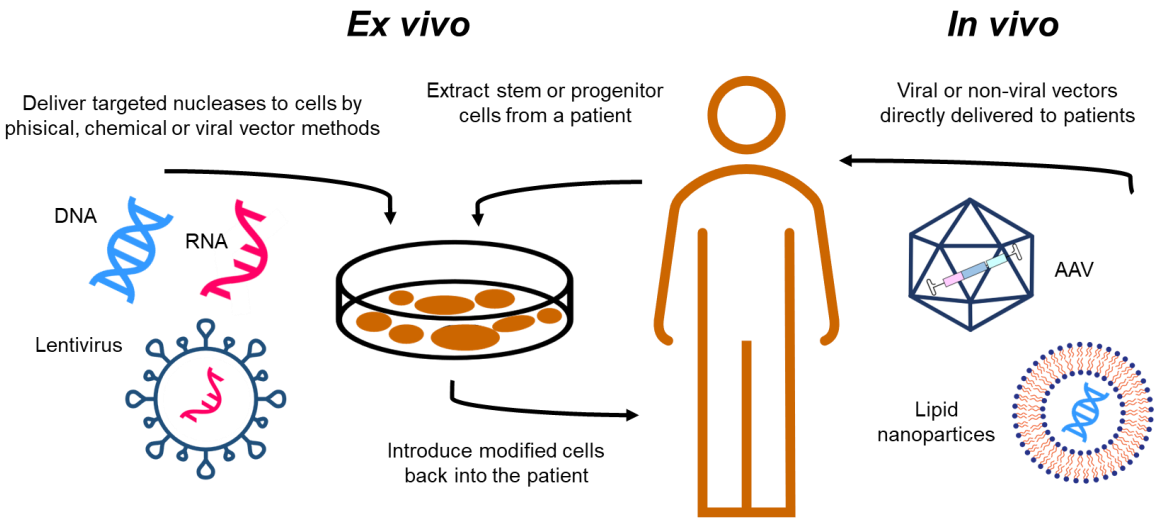

Figure 13. Types of gene therapy and most used vectors. Adapted from [101].

3.2. Viral vectors

Viruses have naturally evolved to efficiently access host cells, deliver their genome, and exploit the cell resources to express viral genes, leading to replication and generation of more viral particles. Gene therapy based on viral vectors leverages the viral infection pathway to deliver therapeutic transgenes to target cells. This is achieved through viral genome modification so that the viral genes that lead to replication and toxicity are deleted and replaced by the therapeutic gene. Therefore, recombinant viruses possess high infective capacity while lacking replicative capacity, so they are safe and efficient vectors.

There is a broad range of viral vectors with diverse properties, whose suitability will depend on the application (Table 2). The choice of a vector should also consider limitations such as immunogenicity [192], [193], carcinogenesis [193], cell tropism [194], packaging capacity and the feasibility of scaled production. An ideal viral vector should be able to specifically deliver the transgene to the organ, tissue, or cell of interest without causing off-targets and immunogenic reactions and must be produced in high titers in a reproductible manner [195]. The most used viral vectors in preclinical and clinical trials are adenovirus, lentivirus and adeno-associated virus (AAV) (Figure 12). For *in vivo* gene therapy, AAV vectors are among the most suitable ones due to their high transduction efficiency in a wide variety of tissues, stable and long-term transgene expression and low or inexistent toxicity [196]. By 2021, AAV vectors had been used in 263 clinical trials [189].

Table 2. Principal types of viral vectors used in gene therapy. Adapted from [195].

Vector	Genetic material	Capacity	Tropism	Inflammation	Vector genome	Limitations	Advantages
Enveloped							
Retrovirus	RNA	8 kb	Dividing cells only	Low	Integrated	• Only transduces dividing cells. • Integration might induce oncogenesis.	• Persistent gene transfer in dividing cells.
Lentivirus	RNA	8 kb	Broad	Low	Integrated	• Integration might induce oncogenesis.	• Persistent gene transfer in most tissues
HSH-1	dsDNA	40 kb* 150 kb**	Strong for neurons	High	Episomal	• Inflammatory • Transient transgene expression in cells other than neurons.	• Large packaging capacity. • Strong tropism for neurons.
Non-enveloped							
AAV	ssDNA	<5 kb	Broad; possible exception of haematopoietic cells	Low	Episomal (>90%) Integrated (<10%)	• Small packaging capacity.	• Non-inflammatory. • Non-pathogenic.
Adenovirus	dsDNA	8 kb* 30 kb***	Broad	High	Episomal	• Capsid mediates a potent inflammatory response.	• Extremely efficient transduction of most tissues.

*Replication defective; **Amplicon; ***Helper dependent. AAV: adeno-associated viral vector; HSV-1: herpes simplex virus-1 dsDNA: double stranded DNA; ssDNA: single stranded DNA.

3.3. AAV vectors

AAV are non-pathogenic members of the *Parvoviridae* family, *Dependoparvovirus* genus. As its name may suggest, they depend on the factors provided by a 'helper' virus to replicate. Different viruses such as herpesvirus, adenovirus, papillomavirus, baculovirus and human bocavirus-1 can act as helpers by coinfection [197]. In the absence of the helper virus, AAV can still transduce and stay in the host cell in episomal state cell for years, but they are not able to replicate and generate new AAV particles.

The first approved gene therapy product was Glybera in 2012, based on AAV-gene transfer of the human lipoprotein lipase (LPL) enzyme for the treatment of LPL deficiency [198]. Luxturna was approved (2017) to treat an inherited retinal disease [199] and Zolgensma (2019) for spinal muscular atrophy [200]. In 2022, two additional AAV-based gene therapies have been approved: Upstaza for AADC deficiency [201], and Roctavian for hemophilia A [202].

3.3.1. AAV Genome structure and engineering

The wild-type virus (wtAAV) consists of a single-stranded DNA (ssDNA) genome of 4.7 kb in a small (23-28 nm) icosahedral, non-enveloped capsid. The genome has 2 genes that generate several open reading frames (ORFs), flanked by inverted terminal repeats (ITRs). The *rep* ORF encodes proteins (Rep78, Rep68, Rep52 and Rep48) involved in the replication of the viral genome, transcription, integration into the host genome and assembly of virions. The *cap* ORF encodes 3 structural virion proteins (VP1, VP2 and VP3) that constitute the viral capsid. There is one more ORF as an alternate reading frame within the *cap* sequence that generates the assembly-activating protein (AAP) [203]. The AAP organizes the structural proteins in the nucleolus to assemble the viral capsid [204]. The ITRs are about 145 nucleotides and have a complex T-shaped structure. They are the origin of replication and act as the signals for packaging. The ITRs are the only *cis*-acting sequences required for genome replication, integration, and packaging of the recombinant genome into the capsid to produce AAV vectors.

Recombinant AAV (rAAV) can be generated by replacing the *rep* and *cap* sequences by a gene of interest (GOI) or transgene and a promoter, that will be flanked by the ITRs, constituting the 'expression cassette'. To ensure an efficient gene expression in host cells, the expression cassette cloned into rAAV should also include an appropriate enhancer and polyA sequences. The *rep* and *cap* elements are provided in *trans* during AAV production by triple transfection in a producer cell line [205]. Briefly, cells are co-transfected with 3 plasmids. One plasmid encodes the expression cassette flanked by the ITRs to be packaged in the viral capsids. Two other plasmids with no ITRs provide in *trans* the *rep* and *cap* sequences (pRepCap) and the helper genes (E1a, E1b, E2a, E4orf6 and VA; pHelper). E1a and E1b may also be provided by the producer cells, by being integrated in their genome, like in the HEK293 cell line. The resulting rAAV consist of an icosahedral viral capsid containing the expression cassette of the transgene of interest flanked by ITRs. These rAAV are not able to replicate in host cells (Figure 14). The DNA packaging capacity of rAAV is limited to the wtAAV genome size. Therefore, the expression cassette in between the ITRs should not exceed 4.4 kb including the transgene, the promoter, and regulatory sequences, or 4.7 kb including the ITRs [206].

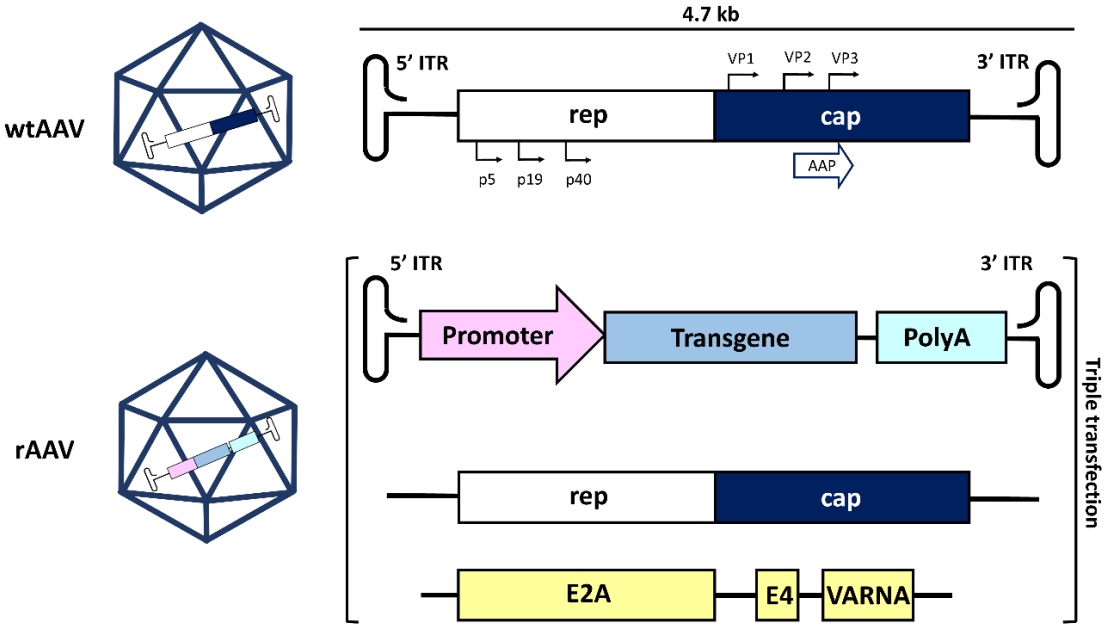

Figure 14. Genomic structure of AAV. Adapted from [203].

3.3.2. rAAV transduction mechanism

The mechanism by which AAV transduce host cells is not fully understood, and it is thought that there may be multiple transduction mechanisms depending on the AAV serotype, among other variables. It is generally accepted that AAV enters a host cell by binging to cell surface receptors and sugars on proteoglycans [207], [208] (Table 3). This binding triggers the AAV internalization by clathrin-mediated endocytosis, and the endosome containing the AAV is transported through the cytosol by the cytoskeletal network. Then, due to the low pH inside the endosome, the viral capsid undergoes a conformational change that enables endosomal escape, and the vesicle is ruptured. Following endosomal escape, the AAV travels though the cytoplasm to enter the cell nucleus, where the viral DNA is uncoated from the capsid. In the case of AAVs carrying single-stranded DNA (ssDNA) sequences (ssAAV), these must be converted to double-stranded DNA (dsDNA) to allow transcription and gene expression. The complementary strand may be synthetized either by DNA polymerases of the host cell or by annealing of the anti-sense strands that coexist in the nucleus. In the case of the self-complementary AAVs (scAAV), which are designed as double-stranded, they can directly undergo transcription. The ITRs can drive inter- and intra-molecular recombination, generating circularized viral genomes and concatemers. These episomal genomes are stable for the transgene expression and can persist in the nucleus. AAV genomes can also integrate into the host genome (Figure 15). However, since the

sequences necessary for integration (Rep78 or Rep68) are not present in rAAV, it is a very unusual event [209], [210].

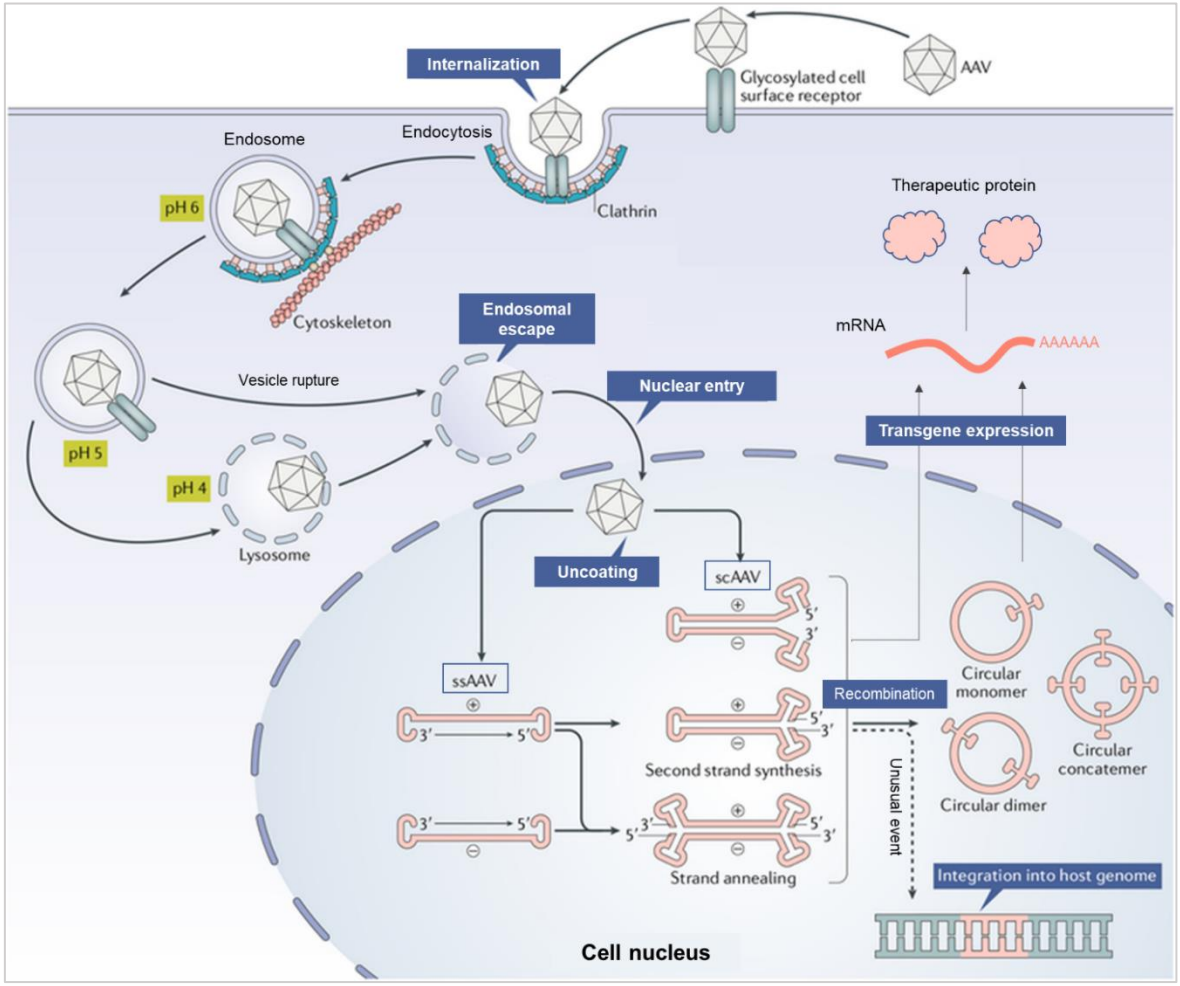

Figure 15. rAAV transduction mechanism. Adapted by permission from Springer Nature [209].

Table 3. AAV serotypes and their receptors. Adapted from [211].

AAV serotype	Origin of isolation	Primary receptor	Co-receptor	Tissue tropism	Application	Approved drug
AAV1	Monkey	Sialic acid	AAVR	Muscle CNS, Heart	Muscle diseases Heart failure AAT deficiency	None
AAV2	Human	Heparin	Integrin FGFR HGFR LamR AAVR	Liver CNS Muscle	Eye diseases Haemophilia CNS diseases AAT deficiency	Luxturna (for Leber congenital amaurosis)
AAV3	Human	Heparin	FGFR HGFR LamR AAVR	Muscle Stem cells	No trials underway	None
AAV4	Monkey	Sialic acid	Unkown	Eye CNS	Eye diseases	None
AAV5	Human	Sialic acid	PDGFR AAVR	CNS Lung Eye	Haemophilia Eye diseases AIP	None
AAV6	Human	Heparin Sialic acid	EGFR AAVR	Muscle CNS Heart Lung	Haemophilia CNS diseases	None
AAV7	Monkey	Unknown	Unknown	Muscle CNS	No trials underway	None
AAV8	Monkey	Unknown	LamR AAVR	Liver Muscle Pancreas CNS	Eye diseases Haemophilia Muscle diseases	None
AAV9	Human	Galactose	LamR AAVR	Every tissue	CNS diseases Muscle diseases	Zolgensma (for spinal muscular atrophy)
AAV10	Monkey	Unknown	Unknown	Muscle	No trials underway	None
AAV11	Monkey	Unknown	Unknown	Unknown	No trials underway	None
AAV12	Human	Unknown	Unknown	Nasal	No trials underway	None

3.3.3. AAV tropism and serotypes

The transduction effectiveness of AAVs is highly determined by the interaction between the capsid and the cell surface receptors, which leads to the AAV internalization. The specific molecules expressed on the surface of the host cell condition the binding of the virus, and so its tropism, defined as the AAV preference for a particular host tissue or cell type [196]. The tropism is also determined by the composition of the AAV capsid, as well as the combinatorial interaction with co-receptors [212].

Since the different AAV serotypes have different capsids, each AAV serotype shows a particular tissue- and cell-specific tropism profile (Table 3). To date, 13 natural serotypes (AAV1-13) and over 100 variants of AAV have been isolated from humans and from non-human primates [211].

The serotype 2 (AAV2) was the first AAV vector to be identified in 1965 and its genome was cloned into a bacterial plasmid, allowing a profound characterization [213], [214]. Consequently, rAAVs are usually produced using the ITRs and *rep* sequences of the AAV2. Using the *cap* genes from other serotypes enables capsid pseudotyping to generate rAAV with different tropisms [215], [216]. Furthermore, capsid variants can be engineered to obtain mutant rAAV with enhanced transduction and reduced immunogenicity. Recently, different strategies that have been implemented to genetically modify existing AAV capsids, such as rational design, directed evolution and computer-guided design of ancestral capsid libraries, resulting in new rAAV variants with different tropism and transduction efficiencies [211].

AAV9

The AAV9 serotype is a commonly used vector for gene transfer to the CNS, both in preclinical and clinical trials (reviewed in [217]). For instance, Zolgesma is a rAAV9-based treatment for spinal muscular atrophy, approved in 2019 [200]. AAV9 is able to transduce all major cell types in brain (neurons, microglia, astrocytes, and oligodendrocytes), and has shown higher transduction efficiency than other serotypes when injected in brain. In addition, AAV9 seems able to undergo axonal transport, leading to widespread distribution of the vector genomes to distal projection sites in the brain [218]–[220]. Furthermore, AAV9 is able to cross the BBB following intravenous administration, transducing neurons and glia within CNS [221], [222].

AAV7m8

The AAV7m8 (also referred to as AAV2-7m8 in literature) is a variant derived from the AAV2 serotype by *in vivo*-directed evolution [223]. With the purpose of isolating AAV variants with tropism for the retina, different AAV libraries were generated, one of them consisted of AAV2 capsids with a randomly inserted 7 amino acid sequence (7mer). In the AAV7m8 variant, the 7mer sequence was inserted at residue 587 of AAV2 capsid VP1, disrupting basic arginine residues implicated in AAV2 binding to its primary receptor, the heparan sulfate proteoglycan (HSPG). The AAV7m8 variant showed increased transduction efficiency in the retina of mice and primates, probably due to its reduced heparin affinity which could decrease capsid sequestration and enhance penetration through retinal layers. Besides,

the 7mer insertion could confer binding to a novel cell surface receptor or enhance intracellular viral trafficking. Be that as it may, the AAV7m8 variant has also shown high transduction efficiency in human iPSC-derived cortical and retinal neurons [224], [225] as well as human retinal organoids [226], [227].

3.3.4. Advantages, limitations, and improvements of AAVs as Gene Therapy vectors.

At present, rAAV are vectors of choice for *in vivo* gene therapy. They show unique advantages that make them superior over other vectors, although some limitations must be considered, such as:

- Safety. AAVs are naturally non-pathogenic to humans and replication-defective in the absence of a helper virus. Besides, rAAV rarely integrate in the host genome and have low immunogenicity compared to other viral vectors, probably due to their low efficiency in transducing antigen-presenting cells. Therefore, rAAV have a safe profile and present low risk to cause side effects. However, recent evidence suggests that at high doses, AAV generate hepatic toxicity, complement activation and potential neurotoxicity, although these effects seem to be dose-dependent [228]–[230].

- Long-term expression of therapeutic products. AAV genomes can form stable circular episomes in the host cell nucleus that persist in non-dividing cells for years. This results in sustained long-term expression of the therapeutic transgene after a single administration, without integrating within the host genome [196].

- Broad tropism. The existence of diverse serotypes allows a broad range of tissue- or cell-directed gene therapy in a wide variety of organs [194], [231].

- Limited transgene capacity. The low packaging capacity of rAAV capsids only allows expression cassettes smaller than 4.4 kb, limiting the sequence length of GOI and promoters. To enable the delivery of large transgenes, new approaches based on the use of dual rAAV are being developed [232] .

- Delayed transgene product. To start transgene expression, the single-stranded viral genome must be converted to double-stranded, which is considered a rate-limiting step

[233]. The use of scAAV vectors, whose genomes consist of dsDNA, can speed up this step.

- Translatability to humans. Preclinical data obtained in mice regarding rAAV serotype tropism, transduction efficiency, dose, toxicity, immune response, and therapeutic efficacy have not shown to extrapolate to humans, large animals, or even other mouse strains. The use of *in vitro* models derived from human cells, like organoids, could overcome this limitation, as they could better represent the patients' cells than animal models [234].

- Large-scale manufacturing. The AAV production through the triple transfection procedure in the HEK293 cell line is adapted for both adherence and suspension cells, reaching 10^{14} vg/L. This production rate is suitable for small number of patients, but it is not scalable to larger production batch sizes needed in advanced clinical trials. Besides, this procedure can generate empty capsids lacking the transgene that could contribute to increased toxicities. Implementing improved processes in HEK293 and other cell lines such as insect (Sf9) has recently increased the production ratio to 10^{15} vg/L [235], [236].

- Therapy cost. The high price of AAV-based gene therapy treatments, mainly due to the high manufacturing cost, makes them hardy affordable [209]. For instance, Glybera was withdrawn from the market due to its exorbitant cost (around one million dollars per treatment).

- Immunogenicity. It is commonly agreed that rAAV vectors have a low immunogenic profile compared to other viruses. Nevertheless, immune responses in human patients following rAAV gene therapy is a matter of concern (Figure 16).

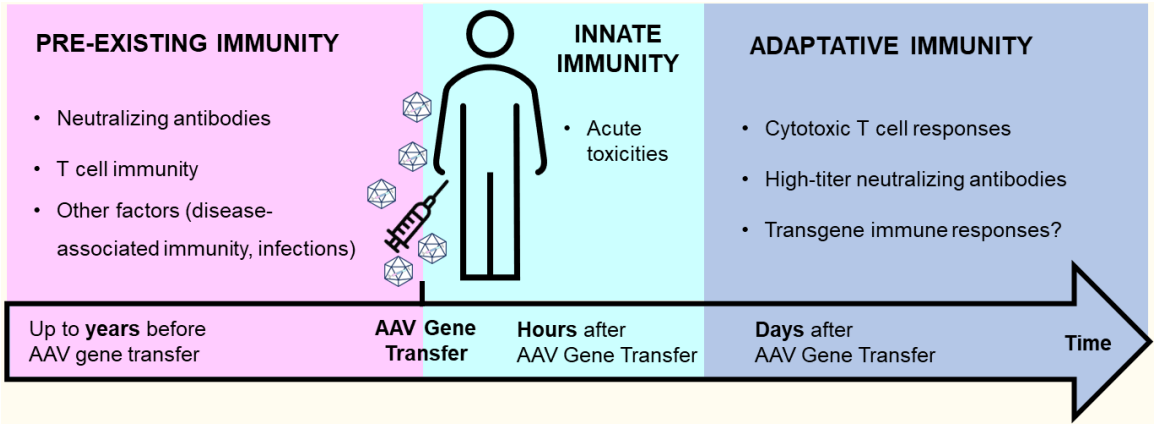

Figure 16. Types of immune response related to AAV administration. Adapted from [237].

Despite AAV are not associated to any disease in humans, neutralizing antibodies (NAbs) against nearly all AAV serotypes can be found in 30-60% of the human population due to a previous exposure from a natural infection [238]. The preexisting NAbs bind to rAAV capsids, avoiding their interaction with target cells and therefore the expression of the transgene, which limits the efficacy of the therapy. Administration of rAAV also triggers a humoral response, generating NAbs against the vector capsid. This limits the possibility of re-administration in cases in which repeated dosing is required. Currently, patients presenting NAbs against AAV are excluded from clinical trials. Some approaches to overcome the humoral immunity are transient depletion of B cells [239] and immunosuppression using rapamycin [240] to induce immune tolerance. Another approach is to re-administer a high vector dose in subjects having low titer of NAbs, although it could also trigger an anti-capsid cytotoxic T lymphocyte (CTL) response [192]. CTL-mediated cytotoxicity may lead to the elimination of transduced cells, losing the expression of the therapeutic transgene (Figure 17). However, since rAAVs are poorly immunogenic, this response does not affect efficacy below a critical dose threshold [241]. After administration, rAAV capsids may also degrade in endosomes of immune cells, exposing the viral capsid or genome to Toll-like receptors (TLR9 and TLR2). This provokes an innate immune response through the MyD88 pathway, eventually activating the adaptative immunity [242].

It must be mentioned that these immunogenic concerns mainly apply to AAV therapies directed to systemic or neuromuscular diseases, which require widespread transduction and high AAV doses (above $1x10^{14}$ vg/kg). In contrast, AAV approaches directed to brain or eye can be administered locally and require much lower doses, circumventing the immunogenic risks.

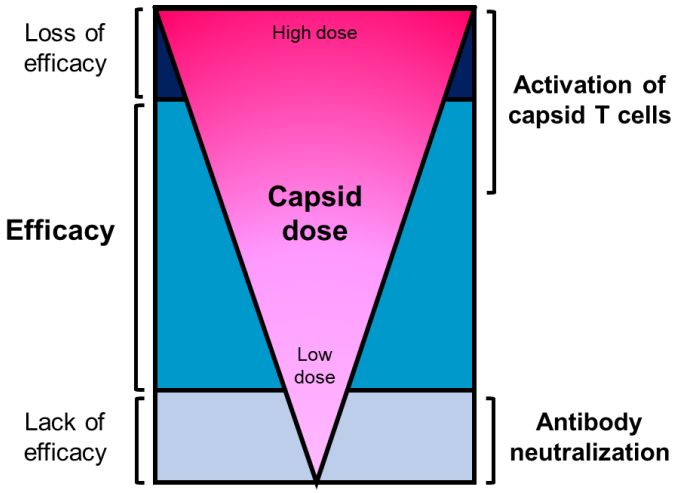

Figure 17. AAV capsid dose *vs* efficacy and immune response. Adapted from [192].

3.4. Gene Therapy for CNS disorders

Access to the CNS is limited due to the presence of the BBB, which prevents systemically administered drugs to reach therapeutic levels in brain parenchyma. This must be sometimes balanced by increasing drug dosage, which in turn increases side effects.

Direct intracerebral delivery of therapeutics is an alternative strategy for circumventing the BBB and targeting specific tissues while reducing drug dosage. In this sense, rAAV vectors are a validated tool for long-term *in vivo* expression of a therapeutic protein with just one low-dose single-infusion [243]. Besides, the low presence of NAbs in the CSF does not compromise the therapeutic efficacy of rAAV [244], [245]. Previously, direct delivery of rAAV to the brain has demonstrated to cause little or no immune response [246].

In the past years, capsid engineering has led to AAV variants with increased efficiency at crossing the BBB in the animal models tested, for instance the AAV.PHP.B and AAV-B1 [247]–[249]. The capsid variants of the PHP.B family, derived from AAV9, demonstrated great BBB permeability after systemic injection in C57BL/6J mice and allowed for broader and more uniform transduction of the CNS than intraparenchymal injections [250]. However, despite these vectors seeming promising, further characterization revealed that their increased BBB penetration did not apply to other species like non-human primates and not even to other mice strains [251]–[253] . Besides, the AAV-PHP.eB variant was no superior to AAV9 when the administration route did not require the vectors to cross the BBB [254]. Herein, direct intracerebral administration of AAV9 is still a first choice in research studies for gene transfer into the CNS.

The clinical efficacy and safety of rAAV to treat CNS disorders has been tested in clinical trials for several disorders, among others Parkinson's disease, aromatic-L-amino acid decarboxylase (AADC) deficiency, spinal muscular atrophy, and Canvan disease (reviewed in [234], [255]). To date, four phase I clinical trials have addressed AD using rAAV vectors to express different therapeutic proteins in the CNS: active telomerase (hTERT) (NCT04133454), APOE2 (NCT03634007), Brain-Derived Neurotrophic Factor (BDNF) (NCT05040217) and Nerve Growth Factor (NGF) (NCT00087789). While there is no existing treatment to cure or slow the progression of AD, AAV-based gene therapy seems a promising strategy.

4. Experimental Models of Alzheimer's Disease

The use of experimental models of AD is crucial for elucidating the mechanisms and etiology of the pathology, identifying diagnostic biomarkers and testing therapeutic strategies. An ideal model should recapitulate all aspects of the disease. Since AD is a specific pathology of humans, the most adequate system to study the disease would be the patients. However, as conducting research in the living human brain is not feasible nor ethical, several *in vivo*, *in vitro* and *in silico* systems have been developed to model AD.

4.1. *In vivo* AD models

Animal models play a crucial role in the *in vivo* study of AD pathophysiology and the development of therapies. Although a wide variety of vertebrate and non-vertebrate species have been utilized to model AD (reviewed in [256]), the mouse is the most used species, as 196 mouse models of AD existed by 2022 [257].

4.1.2. Mouse models of AD

The mouse is one of the best characterized mammal species and there is plenty of accumulated knowledge from research studies. Its small size, high birth rate, feasible maintenance in animal facilities and relative low cost, compared to other species, are some of the advantages that favor their use in research. Furthermore, they provide information about cognitive impairments and memory deficits that is not possible to obtain from other animal or cellular models [256], [258].

Mouse models of AD may be either transgenic, spontaneous, or interventional, being the transgenic the most convenient as mice do not naturally develop AD [256]. Transgenic AD mice are genetically modified to overexpress a gene. Transgenic mouse models of AD usually overexpress APP to recapitulate the Aβ plaque pathology. APP overexpression is usually induced by human transgenes harboring familial AD mutations, and/or by adding the human APP transgene. Because Tau is not naturally expressed in mice, some AD models overexpress human Tau to recapitulate the NFT pathology. A general limitation of AD mouse models is that most of them only develop either Aβ or Tau pathology, whereas AD patients present both pathological hallmarks [259]. In this sense, the 3xTg-AD model

was developed to overcome this limitation and has been widely used in research, including the present study.

The 3xTg-AD mouse model

The 3xTg-AD mouse model harbors 3 mutant genes: APP_{Swe}, $PS1M_{146V}$, and Tau_{P301L} [260]. The APP_{Swe} and $PS1M_{146V}$ are common mutations in familial AD that increase the production of Aβ, favor the Aβ42 form and promote the formation of plaque. The Tau_{P301L} mutation makes the Tau protein more prone to phosphorylation and the subsequent formation of pathological NFT.

The 3xTg-AD model shows progressive cognitive impairment and develops cognitive deficits analogous to early cognitive changes in preclinical AD patients. The first deficits observed in these mice may be detected at 3-5 months of age and are related to associative learning, followed by deficits in spatial working memory at 6 months old in the MWM task. Deficits in recognition memory are found in 9-11 months old 3xTg-AD mice [261]–[264].

Overall, the research conducted in mouse models has provided remarkable advances in the understanding of the AD pathology and the development of novel therapies. However, mouse models fail to faithfully develop clear NFTs, neurodegeneration and behavioral phenotypes observed in AD patients. The anatomical and genetic differences between the human and rodent brain, as well as the artificially induced overexpression of human proteins to mimic the disease, are some important limitations of this species as AD model [265], [266]. Because AD pathology can only be reproduced in mice by overexpressing transgenes related to familial AD, mouse models do not faithfully represent the sporadic AD developed by most of the patients.

Besides, all the promising candidate therapies for AD tested in animal models have failed in clinical trials so far [267], adding evidence to the limited translatability from *in vivo* models to human patients also observed in the development of AAV-based gene therapies for multiple diseases.

4.2. Human-derived *in vitro* models

There is increasing need for systems that better represent the molecular environment occurring during AD in a human context. In this sense, *in vitro* models derived from human cells show promise.

A technological breakthrough made it possible to obtain induced pluripotent stem cells (iPSCs) from fibroblasts of AD patients [268]. Since then, diverse two-dimensional (2D) and three-dimensional (3D) *in vitro* models derived from AD patient's iPSCs have been developed, for instance traditional 2D cell cultures, spheroids, defined matrix cultures, organoids, and human xenografts for *in vivo* analysis (reviewed in [269]). These cell cultures allow to represent not only the familiar, but also the sporadic form of AD, which affects the vast majority of AD patients and is not usually reproduced *in vivo* animal models [256].

Because AD pathogenesis is driven by non-cell autonomous processes involving different cell types and molecules that interact among them (for instance neurons, microglia, and extracellular protein aggregates), a model integrating all these factors is needed. In this sense, brain organoids have recently been developed as a promising 3D *in vitro* model to bridge the gap between *in vivo* and 2D traditional cell cultures.

4.2.1. Brain organoids

Brain organoids or 'mini brains' are 3D structures derived from iPSCs, which cultured under appropriate conditions, can self-organize and differentiate into diverse cell types present in the brain [270].

Recently, brain organoids modelling AD have been successfully generated, and can recreate the extracellular AD physiopathology, including Aβ aggregates and NFT, the effect of these deposits on cells, and cell-cell interactions in 3D [269], [271]–[273]. As a potent tool to model AD in a human-like environment, brain organoids provide a platform for basic research, drug discovery and personalized medicine, and increase the translatability of preclinical drug discovery in AD [274].

Organoids are a useful tool for gene therapy studies as well. First, they are a reliable system to test the transduction efficiency of different serotypes, which could overcome the problem associated with interspecies extrapolation [234]. Besides, they can be used for evaluating

proof-of-concept of gene therapy strategies and the therapeutic efficacy of the transgenes in a human context, which in turn may increase the translation to the clinic [275]. Moreover, the multiple applications of brain organoids allow for the reduction of the excessive use of laboratory animals in research, which entails an ethical issue and increases the cost of the studies.

Nevertheless, there are various limitations associated with the use of these *in vitro* models such as having limited life span, exhibiting non-physiological reactive changes, and presenting a fetal phenotype [234], [269]. They also lack relevant tissue components present in a complex organism such as immune and vascular system, perivascular compartment, and suitable drainage of metabolites. Thus, when organoids grow to a certain size, the diffusion of nutrients and oxygen to the center is insufficient, resulting in a necrotic core that could interfere in the AD phenotype [276], [277]. Likewise, the drugs to be tested do not penetrate to the internal parts of the organoids and accumulate in the radius at different concentrations, which interferes drug screening and therapeutical tests. In addition, the self-assembly nature of organoids and the variety of protocols used by research groups generates high heterogeneity and variability, making data comparison and reproducibility difficult to achieve [266].

4.3. Closing remarks about AD models

Although a huge amount of *in vivo* and *in vitro* models of AD are available, none of them are fully representative of the whole human AD pathophysiology [278]. Hence, the suitability of an experimental model depends on the object of study and the election requires awareness of its own limitations while making some compromises.

In this scenario, combining different types of models and integrating the results obtained could help elucidate the mechanisms of the disease and the efficacy of drug candidates. For instance, animal models are essential for studying the outcome of the therapies on memory and cognitive functions, whereas human-derived brain organoids could bring light into the molecular mechanism occurring in the human brain during AD, as well as increasing the translatability of the tested therapies.

HYPOTHESIS AND OBJECTIVES

Hypothesis

Expression of secreted Klotho in the Central Nervous System through AAV vectors could be a potential therapeutic strategy against Alzheimer's disease by counteracting the cognitive and memory deficits.

Objectives

1. To characterize the relative expression of the two Klotho transcript variants (sKL and mKL) in different areas of the human brain.

2. To assess whether the relative expression of sKL and mKL is altered during Alzheimer's disease in human patients and the 3xTg-AD mouse model.

3. To analyze changes in the levels of soluble Klotho protein in CSF of AD patients respect to cognitively healthy individuals.

4. To study the correlation of CSF KL levels with risk factors of AD (age, sex and APOE genotype) in cognitively healthy humans and AD patients.

5. To express sKL in the CNS of two mouse models of AD (3xTg-AD and APP/Tau) using AAV9 vectors and to assess the therapeutic effect on the memory and cognitive deficits.

6. To establish a protocol and an AAV capsid variant to efficiently transduce human iPSCs-derived brain organoids.

MATERIALS AND METHODS

1. MATERIALS

1. Human samples

Human biological samples were obtained from different collaborators following the guidelines of Spanish legislation on this matter (Real Decreto de Biobancos 1716/2011) and approval of the local ethics committee.

Brain

Post mortem brain specimens of human donors were provided by Dr. Isidre Ferrer from the Hospital de Bellvitge Biobanc (Barcelona, Spain). For brain areas were obtained: frontal cortex (FC), entorhinal cortex (EC), hippocampus (HC) and amygdala (AM). AD patients were diagnosed during brain autopsy in different severity stages of the disease (I to IV), according to the Braak staging criteria [61], and then classified into mild (AD I/II) and severe (AD III/IV) groups. Only individuals with no co-morbidities were selected for study. Donors with no neuropathological lesions (NNL) were used as controls. Number of samples per group detailed in Table 4. Brain specimens were stored at -80ºC. Small fragments of about 100 mg were dissected in a cold chamber (4ºC) prior to processing for analysis. White matter, blood vessels and hematomas were discarded.

Table 4. Samples of *post mortem* human brain.

		Gender (n)		Brain areas available (n)			
Diagnosis	**Average age (y/o)**	**F**	**M**	**FC**	**EC**	**HC**	**AM**
NNL	48.4	4	6	10	9	6	8
AD I/II	70.0	3	7	10	10	10	10
AD III/IV	78.4	2	8	9	10	8	9

Diagnosis according to Braak criteria. F: females, M: males. y/o: years old. n: number of samples.

Kidney

RNA samples from human kidney were provided by Dr Anna Messegué (Hospital Vall d'Hebron, Barcelona, Spain). Donors analyzed did had not been diagnosed of any pathology (n=14).

Choroid plexus

RNA samples from human choroid plexus were kindly provided by Dr Eva Carro (12 de Octubre Hospital Research Institute, Madrid, Spain). These were obtained from AD patients of stages IV-VI (Braak staging) and non demented controls. Number of samples per group detailed in Table 5.

Table 5. Samples of choroid plexus from human donors.

		Gender (n)		
Diagnosis	**Average age (y/o)**	**F**	**M**	**Total (n)**
NNL	**76.2**	**2**	**3**	**5**
AD IV-VI	**75.8**	**2**	**3**	**5**

Diagnosis according to Braak criteria. F: women, M: males. y/o: years old. n: number of samples.

Cerebrospinal fluid

CSF samples were obtained from AD patients by lumbar punction and were provided by Dr. Albert Lleó (Hospital de Sant Pau, Barcelona, Spain). The donors were classified according to the Global Deterioration Scale (GDS) into GDS-3 (MCI), GDS-4 (MD) and GDS-1 (No cognitive decline), used as controls [57]. Number of samples per group, gender and APOE genotype, detailed in Table 6.

Table 6. Samples of CSF from human donors.

			Gender (n)		APOE genotype (n)				
Diagnosis	**Average age (y/o)**	**Total (n)**	**F**	**M**	**2+3**	**3+3**	**3+4**	**4+4**	**N/C**
GDS1	65.0	14	7	7	1	8	1	0	4
GDS3	70.0	15	10	5	N/C	N/C	N/C	N/C	15
GDS4	65.5	14	9	5	2	2	4	2	4

Diagnosis according to the Global Deterioration Scale. y/o: years old. F: women, M: males. APOE genotype expressed as combination of the two alleles. 2: APOE2, 3: APOE3, 4: APOE4. N/C: non-communicated. n: number of samples.

2. Mouse models

The **3xTg-AD** colony in the UAB was stablished in 2004 from progenitors provided by Dr LaFerla Laboratory (University of California, Irvine, USA). For in vivo experiments, only female 3xTg-AD mice were used. The characterization of the endogenous KL expression

was performed using samples of female and male 3xTg-AD mice and wild type (WT) mice with genetic background C57BL/6.

The **APP/Tau** mouse model of AD was generated by Dr A. Saura's group (UAB, Barcelona, Spain). APP/Tau transgenic mice and littermate non-transgenic controls (WT) mice were obtained by crossing heterozygous $APP_{Sw,Ind}$ (line J9; C57BL/6) [279] and Tau P301S (line PS19, JAX #008169; C57BL/6) [280] mice expressing the familial AD-linked K670N/M671L and V717F *APP* and frontotemporal dementia-linked P301S *Tau* mutations, respectively. Our own colony was stablished by multiple crossings from two starting breeder couples kindly provided by Dr Saura. The offspring was genotyped by standard PCR.

3. Cell lines

The Human Embryonic Kidney 293 (HEK293) cell line is an immortalized cell line coding in its genome the E1 (early 1) region of the adenovirus, essential for initiating the viral life cycle, hence the *in vitro* production of the AAV vectors by the triple transfection method. The clone HEK293-AAV (Stratagene) was used to produce AAV vectors. The clone HEK293-QB (Q-BIOgene) was used to validate the transduction and transgene expression of the AAV generated.

4. Bacterial strains

Chemically competent *E.coli* bacteria were transformed with plasmid DNA to obtain high number of plasmid copies (strain TOP10R, Invitrogen) and to perform the homologous recombination cloning (strain BJ5183R , Stratagene).

5. Plasmid and viral vectors

The human variants of the sKL and mKL cDNA were designed by our group and ordered for the novo synthesis to (ProteoGenix). The cDNA sequence of each transgene was cloned into a plasmid vector (either pGV-CMV or pAAV-CAG), containing the promoter and the

ITRs, to be subsequently packed into AAV vectors. The mouse variants of sKL and mKL cDNA were designed by our group and ordered for the novo synthesis (Eurofins Genomics) and cloned into pGG2-CMV vectors in a previous work of our group (A. Massó, 2015). The control vectors encoding the green fluorescent protein (GFP) or a null sequence were previously generated in our laboratory and used to generate the control AAVs: pGV-CMV.eGFP and pGV-CMV.null. The following plasmid vectors were in the triple transfection to generate AAV vectors: pXX6, pRep2Cap9, pRep2Cap7m8 (Addgene). The main plasmid vectors used in this work are summarize in Table 7. The viral vectors produced from those plasmids are summarized in Table 8

Table 7. Plasmid vectors used in this work to generate AAV vectors.

Plasmid vector	Description
pGV-CMV	Plasmid encoding the CMV promoter and ITRs for AAV generation.
pEX-K4_Human-sKL	Synthetic plasmid coding the human-sKL cDNA (Eurofins Genomics).
pGV-CMV-human.sKL	Plasmid encoding the human-sKL cDNA under the control of the CMV promoter.
pGG2-CMV	Plasmid encoding the CMV promoter and ITRs for AAV generation.
pUC57-human.mKL	Synthetic plasmid coding the human-mKL cDNA (Proteogeix).
pGG2-CMV-human.mKL	Plasmid encoding the human-mKL cDNA under the control of the CMV promoter.
pAAV-CAG	Plasmid encoding the CAG promoter and ITRs for AAV generation.
pGG2-mouse.sKL	Plasmid encoding the mouse-sKL cDNA under the control of the CMV promoter.
pAAV-CAG-mouse.sKL	Plasmid encoding the mouse-sKL cDNA under the control of the CAG promoter.
pGV-CMV-null	Plasmid encoding a null sequence under the control of the CMV promoter (negative control).
pGV-CMV-eGFP	Plasmid encoding the GFP under the control of the CMV promoter (positive control).
pRep2Cap9	Plasmid coding the capsid of the AAV9 serotype for AAV9 production.
pRep2Cap7m8	Plasmid coding the capsid of the AAV7m8 variant for AAV7m8 production.
pXX6	Helper plasmid for AAV production

Table 8. AAV vectors generated for this work.

AAV vector	Abbreviation	Description
AAV9-CMV-mouse.sKL	**AAV9-CMV-sKL**	AAV9-mediated expression of mouse-sKL in mouse models.
AAV9-CMV-mouse.mKL	**AAV9-CMV-mKL**	AAV9-mediated expression of mouse-mKL in mouse models.
AAV9-CAG-mouse.sKL	**AAV9-CAG-sKL**	AAV9-mediated expression of mouse-sKL in mouse models.

AAV9-CMV-null	**AAV9-null**	Negative control for the genes overexpressed by AAV9 vectors.
AAV9-CMV-GFP	**AAV9-GFP**	AAV9-mediated expression of GFP in brain organoids. Positive control.
AAV7m8-CMV-GFP	**AAV8m8-GFP**	AAV7m8-mediated expression of GFP in brain organoids. Positive control.
AAV7m8-CMV-null	**AAV7m8-null**	Negative control for the genes overexpressed by AAV7m8 vectors.
AAV9-CMV-human.sKL		AAV9-mediated expression of human-sKL in brain organoids.
AAV9-CMV-human.mKL		AAV9-mediated expression of human-mKL in brain organoids.
AAV7m8-CMV-human.sKL		AAV7m8-mediated expression of human-sKL in brain organoids.
AAV7m8-CMV-human.mKL		AAV7m8-mediated expression of human-mKL in brain organoids.

6. Oligonucleotides

Primer pairs for transgenic mice genotyping

Transgenic mice were genotyped by standard PCR using the following pairs of primer sequences for the 3xTg-AD (Table 9) and the APP/Tau (Table 10) colonies.

Table 9. Primers sequences for 3xTg-AD mice genotyping.

Target gene	Sequences 5'-3' (Forward / Reverse)	Amplicon size (bp)
Human APP (transgene)	GCTTGCACCAGTTCTGGATGG / GAGGTATTCAGTCATGTGCT	450
Human Tau (transgene)	GAGGTATTCAGTCATGTGCT / TTCAAAGTTCACCTGATAGT	350
Actin (internal control)	CACTATTGGCAACGAGCGGTTC / ACTTGCGGTGCACGATGGAG	150

Table 10. Primers sequences for APP/Tau mice genotyping.

Target gene	Sequences 5'-3' (Forward / Reverse)	Amplicon size (bp)
Human APP (transgene)	CGTGAGTTTGTAAGTGATGCC / TCTTCTTCTTCCACCTCAGC	360
Mouse APP (internal control)	CAAATGTTGCTTGTGTGGTG / GTCAGTCGAGTGCACAGTTT	200
Human Tau (transgene)	GGCATCTCAGCAATGTCTCC / GGTATTAGCCTATGGGGGACA	450
oIMR1544 (internal control)	CAAATGTTGCTTGTCTGGTG / GTCAGTCGAGTGCACAGTTT	200

Taqman sets for gene expression analysis

Taqman sets composed of a pair of primers and a probe were used to analyze gene expression. The Taqman sets used to analyze the endogenous gene expression of secreted KL (sKL) and membrane KL (mKL) in human and mouse are detailed in Table 11 and Table

12. Taqman sets used to validate transgene expression in vivo following AAV transduction in mice (tg) detailed in Table 11.

Table 11. Sequences of Taqman sets of custom design.

Target gene	Primers FW/RV (5' – 3')	Probe (5' – 3')
Human sKL	AACTACATTCAAGTAAGTCAGC / CAGAGTGGTATCTACTAGTG	6FAM/TCAGCAGTC/ZEN/TCACCAAGCCCT/3IABkFQ
Mouse sKL	GCCTCTTGCTTCCTCACTAAG / GACTGAAGCGTTCAGGACTATG	6FAM-CAGTGTTGGGACGTTGAGCCAAAC-BHQ-1
Mouse mKL	GCCGCATTCCACACATTTC / TCCGTAATTGCCACCAAAGA	6FAM-TGCAGGGTGAATGGTATCTGAATCTGC-BHQ-1
Mouse tg-sKL	GTGTCGGCCTCTTGCTTC / TCATCAATGTATCTTATCATGTCTGCTC	6FAM/GCCGCTTCCCTTTAGTGAGGGTTAAT-BHQ-1
Mouse tg-mKL	GCCGCATTCCACACATTTC / CTGCATTCTAGTTGTGGTTTGTC	6FAM/TTAACCCTCACTAAAGGGAAGCGGC-BHQ-1
Mouse rplp0 (m36b4)	ATGGGTACAAGCGCGTCCTG / AGCCGCAAATGCAGATGGATC	6FAM/TGTGGAGACTGAGTACACCTTCCCA-BHQ-1

FW: forward, RV: reverse. tg: transgene. Human sKL TaqMan design obtained from [281] and synthesis ordered to IDT. The rest of the Taqman sets were designed by our group and synthesis ordered to Condalab.

Table 12. Taqman sets inventoried by Invitrogen (Thermo Fisher Scientific).

Target gene	Reference
Human mKL	Hs00935388_m1
Human UBE2D2	Hs00366152_m1
Human CYC1	Hs00357717_m1

2. METHODS

1. Genotyping of transgenic mice

1.1. Genomic DNA extraction

Mice were genotyped using genomic DNA extractions from tail biopsies. Tail biopsies of around 40 mg were incubated in Eppendorf tubes with 250 µL of 50 mM NaOH at 55ºC for 1-12 h. Tubes were vortexed until complete homogenization of the tissue, and then centrifuged at maximum speed for 10 min. The supernatant containing the DNA was transferred to a new tube and the debris pellet was discarded. DNA-containing fractions were stored at -20ºC until PCR genotyping.

1.2. Transgene detection by PCR

3xTg-AD mice: One single PCR reaction was performed to amplify the two transgenes transgene with the corresponding reference gene (Table 9). PCR reactions of a total volume of 23 µL contained 2 µL of genomic DNA solution, 1.25 µL primers 10uM, 0.2 µL deoxynucleotide triphosphates (dNTPs) 25mM (Fermentas), 2.5 µL Taq buffer 10x, 1 µL $MgCl_2$ 50mM (Fermentas), 0.25 µL DreamTaq Polymerase 5 U/µL (Fermentas) and sterile H2O (Braun). PCR reactions took place in a Thermal Cycler (5331 MasterCycler Gradient, Eppendorf) as follows: heating at 94ºC for 5 min followed by 40 cycles of 94ºC for 30 min, 52ºC for 30 min and 72ºC for 1 min. The reaction ended with a final step of 72ºC for 3 min and cooling at 4ºC.

APP/Tau mice: Two separate reactions were performed for each transgene with each corresponding reference gene (Table 10). PCR reactions of a total volume of 25 µL contained 2 µL of genomic DNA solution, 0.5 mM each primer, 25 mM dNTPs (Fermentas), 10x Taq buffer including MgCl2 (Fermentas), 5 U/µL DreamTaq Polymerase (Fermentas) and sterile H_2O (Braun). PCR reactions took place in a Thermal Cycler as follows: heating at 94ºC for 4 min followed by 40 cycles of 94ºC for 1 min, 60ºC for 1 min and 72ºC for 1 min. The reaction ended with a final step of 72ºC for 7 min and cooling at 4ºC.

PCR products were visualized by electrophoresis in a 2% agarose gel using 15 µL of the PCR reaction and 1.66 µL of Xylen Cyanol loading buffer. Electrophoresis was performed

at 120 V constant voltage for 1 hour. DNA amplicons were visualized using a UV transilluminator (GeneGenius BioImaging System, Syngene).

2. RNA extraction and analysis

2.1. RNA isolation

To prevent RNA degradation, RNAse-free conditions were ensured by cleaning surfaces, materials, and gloves with 70% ethanol and RNAseZap (Ambion, Waltham, USA). Filter tips, RNAse-free water and solutions were used, and samples were kept on ice to prevent RNA degradation.

To obtain RNA from cultured cells, medium was aspirated, cells were detached and washed using cold PBS, and transferred to a tube for centrifugation at 12000g for 10min at 4ºC (Eppendorf centrifuge 5415R). Supernatant was discarded, cold Qiazol (around 150 µL per 6wp well) was added to the cell pellet and homogenized by pipetting. The cell lysate was then centrifuged at 4ºC and maximum speed for 10min. The supernatant (RNA fraction) was transferred to a new tube and stored at -80ºC.

RNA from human and 3xTg-AD mice brain parenchyma was isolated using 500 µL of QIAzol Lysis Reagent (Qiagen) per 100 mg of frozen tissue sample. The tissue was homogenized using the TissueLyser (QIAgen) in the presence of grinding beads during a 6-min cycle of 50 Hz. The homogenates were then centrifuged at 12000g for 10 min at 4ºC (Eppendorf centrifuge 5415R). The supernatant was transferred int a new tube and kept at RT for 5 min. Chloroform (Panreac) was added (0.2 mL/mL Qiazol), samples were vortexed to mix the phases and incubated at RT for 3 min. After centrifugation at 12000g during 15 min at 4ºC, the aqueous phase was recovered and transferred to a new tube, where isopropanol was added (0.5 mL/mL Qiazol) and mixed. Samples were incubated for 10 min at RT and then centrifuged at 12000g during 15 min at 4ºC. Supernatant was discarded and the RNA pellet was washed using 75% ethanol (1 mL/mL Qiazol), then centrifuged at 7500g at 4ºC for 5 min. Once dried, the pellet was resuspended in 20 µL of MilliQ water, quantified and stored at -80ºC.

RNA isolation from APP/Tau mice was performed using the RNA extraction kit RNeasy Mini Kit (Qiagen) following the manufacturer instructions. Previously, the tissue was homogenized by sonication using the ultrasonic processor (Vibra-cell, Sonics & Materials

Inc) at 40 Hz and 3 pulses of 10 seconds, keeping the sample on ice during all the process to prevent RNA degradation. Once homogenized, samples were centrifuged at 12000g during 15 min at 4ºC and supernatant used for RNA isolation.

2.2. RNA quantification

The concentration of RNA samples was ascertained by measuring optical density at 260 nm using the NanoDrop-1000 spectrophotometer (Thermo Scientific). The absorbance of the RNA samples was also measured at 280 and 230 nm to assess RNA purity. An A260/A280 ratio comprised between 1.8 and 2.2 is indicative of a good purity of an RNA preparation with respect to protein or phenol contaminations. The 260/230 ratio shows the presence of unwanted organic compounds when it has value higher than 2.2. Generally acceptable 260/230 ratios are in the range from 2.0 to 2.2.

2.3. Assessment of RNA integrity

The integrity of the RNA molecules isolated was assessed by electrophoresis in denaturing TAE buffer-based agarose gel with 0.5% bleach (6% sodium hypochlorite), as described in [282]. Briefly, 1 µg of total RNA was prepared with 10x Xylen Cyanol buffer and loaded into 1% agarose gel prepared with TAE and commercial bleach. Samples were run for 1 h at 80 V constant voltage and gels were visualized using a UV transilluminator (GeneGenius BioImaging System, Syngene). The presence of the ribosomal RNA (rRNA) at the level of ~4.8 kb (28S rRNA) and ~2.0 kb (18S rRNA) without a smear between them, is indicative of good RNA integrity.

2.4. DNAse treatment and Reverse Transcription

To avoid unspecific amplification of genomic DNA during the PCR reaction, RNA samples of APP/Tau mice were treated with DNase I, RNase-free (Thermo Scientific), an endonuclease that digests single- and double-stranded DNA. 1 µg of RNA was incubated with 1U of DNAseI enzyme at 37ºC for 30 min. Then the enzyme was inactivated by heating the sample at 65ºC for 10 min in the presence of 50 mM EDTA. The purified RNA was used as a template for reverse transcription using the SensiFast cDNA synthesis kit (Bioline),

following the manufacturer's instructions. cDNA samples were obtained at a final concentration of 50 ng/µL.

2.5. Real-Time quantitative PCR (qPCR)

Specific TaqMan primer and probe sets were used to quantify the expression of different genes (Table 11, Table 12). This technology was chosen because of its increased specificity compared to the classical pair of primers. The increased specificity is achieved through the nucleic acid probe complementary to an internal segment in between the pair of primers, in the target DNA. The probe is labeled with two fluorophores in 5' and 3', whose emission spectrums overlap, resulting in "quenching" of the first fluorophore by the second. As the Taq polymerase extends the primer, its exonuclease activity degrades the probe, resulting in the release of the fluorophores, unblocking the quenching effect and allowing fluorescence. The fluorescence detected in qPCR is directly proportional to the fluorophore release, and hence to the initial amount of cDNA template. Two reference genes were targeted in each assay to ensure accurate normalization.

Each reaction consisted of 50 ng of cDNA template, 5uM Taqman probe, forward and reverse primers (5 µM each), SensiFAST Probe No-ROX One-Step Kit (Bioline) and MilliQ water to a final volume of 10 µL. Hard-Shell Rhin-Wall 384-Weel Skirted PCR (BioRad) were filled with two replicates per sample and sealed with Microseal Adhesive Seals (BioRad). Reactions were performed in the CFX384 Thermocycler (BioRad) of the Analysis and Photodocumentation Service of the UAB, using the designed program: 50ºC for 2 min and 40 cycles of 95ºC for 10min (polymerase activation and denaturation), 95ºC for 15 s (denaturation) and 1 min at 60ºC (annealing and elongation).

2.6. qPCR data analysis

From each reaction, the cycle threshold (Cq) was measured and used for gene expression quantification. Replicates having more than 1 Cq difference were discarded as outliers. The quantification of gene expression relative to two reference genes was calculated using the Hellemans' relative quantification model for normalization with multiple reference genes [283]. The relative expression of sKL *vs* mKL, was measured by calculating the relative expression ratio for every individual using the Cq measures of both genes.

3. Biochemical techniques for protein analysis

3.1. Protein extraction

Protein extracts were obtained using the *RIPA lysis buffer*. To obtain protein extracts from cell cultures, medium was aspirated, cells were washed and detached from the plate using PBS and transferred to a tube for centrifugation at 12000g for 10min at 4ºC (Eppendorf centrifuge 5415R). Supernatant was discarded, cold RIPA (around 100 µL per 6wp well) was added to the cell pellet and homogenized by pipetting. The cell lysate was then centrifuged at 4ºC and maximum speed for 10min. The supernatant (protein fraction) was transferred to a new tube and stored at -80ºC.

To obtain protein extracts from animal or human frozen tissues, these were firstly homogenized in an Eppendorf tube using cold RIPA buffer (1 mL/100 mg tissue) and an ultrasonic processor (Vibra-cell, Sonics & Materials Inc) at 40 Hz on ice. Homogenates were then centrifuged to separate cellular debris at 12000g during 15 min at 4ºC, and the supernatants (protein fraction) were stored at -20ºC.

RIPA lysis buffer: 50 mM Tris-HCl (Sigma) pH 7.4, 150 mM NaCl (Panreac), 1 mM EDTA (USB), 1 % NP-40 (Panreac), 0.25 % sodium deoxycholate (Sigma), 50 mM sodium fluoride (Sigma), 1 mM sodium ortovanadate (Sigma), 10 mM beta-glycerophosphate disodium salt hydrate (Sigma), 5 mM sodium pyrophosphate decahydrate (Sigma) and protease inhibitor cocktail (Calbiochem).

3.2. Protein quantification

Protein extracts were quantified using the *Pierce BCA Protein Assay Kit* (Thermo Scientific), based on the Biuret reaction. This consists of the reduction of Cu^{+2} to Cu^{+1} by protein in an alkaline medium and the colorimetric detection of Cu^{+1} ions using bicinchoninic acid (BCA).

The chelation of two molecules of BCA (bicinchoninic acid) with one Cu^{+1} produces a water-soluble complex (purple colored), which exhibits a strong absorbance at 562 nm. This absorbance is nearly linear with increasing protein concentrations over a range of 20-2000 µg/mL.

Protein concentrations were determined with reference to standards of a common protein: bovine serum albumin (BSA). A series of dilutions ranging ranged from 2 mg/mL to 0.625 mg/mL were prepared using BSA (supplied by the kit) and milliQ water, so a standard curve

could be later stablished through spectrophotometry. Protein samples were diluted in milliQ water 1:5 to 1:10 (depending on the sample origin) so they could fit the standards range. Duplicates of samples dilutions and standard solutions were loaded in a 96-well microplate (10 µL per well). 200 µL of working solution (supplied by the kit) was added to each well. The microplate was then incubated for 30 min at 37ºC. Absorbance at 562 nm was determined by the Absorbance Reader ELx808 (BioTek) and analyzed using the KC4 software (BioTek). The concentration of each sample was calculated by interpolating their absorbance in the obtained the standard curve.

3.3. ELISA

The levels of soluble KL protein in human CSF were measured using the commercial kit Human soluble Alpha Klotho ELISA (27998, IBL, Minneapolis, USA), following the manufacturer's instructions. CSF from human patients was diluted 1:4 in EIA buffer supplied by the kit and 100 µL per sample were loaded into each well. The assay was performed at RT following kit's instructions. The absorbance of the resulting chromogen product was measured at 450nm using the plate reader Wallac 1420 Victor 3 (PerkinElmer, Waltham, USA).

3.4. Western blot

In this work, the western blot technique was used to validate the transgene expression of the produced AAV in cultured cells. The western blot technique allows the identification of specific proteins by immunodetection after separation according to their molecular weight. The immunodetection is based on the use of antibodies conjugated to the horseradish peroxidase (HRP) enzyme and a chromogenic reagent, that is visualized in an imaging device.

Protein sample preparation

Protein extracts were diluted in milliQ water to obtain 20 to 50 µg of protein mixed with loading buffer 6x to a final volume of 30 µL. Proteins were denatured at 99ºC for 10 minutes and either stored at -20ºC or loaded into the SDS-PAGE gel.

Denaturing gel electrophoresis (SDS-PAGE)

The proteins in each sample were separated according to their molecular weight through a sodium dodecyl sulphate polyacrylamide gel electrophoresis (SDS-PAGE). SDS is an anionic detergent that denatures proteins, losing their 3D structure. Thus, when an electric field is applied, denatured proteins migrate according to their molecular weight.

Gels for SDS-PAGE were prepared using 10% Acrylamide Bis-acrylamide solution (29:1) (Amresco) in resolving gel buffer. The upper part of the gel is composed of a stacking zone of 5% acrylamide in stacking gel buffer that allows protein concentration prior to separation. For gel polymerization, ammonium persulfate (APS) 10% (Amresco) and tetramethylethylenediamine (TEMED) (Sigma), at 5:1 proportion, were added to both solutions.

The polymerized gel was placed in the electrophoresis chamber Mini Protean Tetra Cell (BioRad) and filled with Electrophoresis buffer. The protein samples and the molecular weight marker Page-Ruler Pre-stained Protein Ladder (Fermentas) were loaded into the different wells and the electrophoresis was ran in two cycles using the voltage source PowerPac Basic Power Supply (BioRad). The first cycle consisted of 90 V for 20 min to concentrate the proteins in stacking fraction of the gel, and the second of 130V for 1h30min to separate the proteins according to their molecular weight.

Resolving gel buffer: 1.5M Tris-HCl (Sigma), 0.4% SDS (USB), pH adjusted 8.8.

Stacking gel buffer: 0.5M Tris-HCl, 0.4% SDS, pH adjusted 6.8.

Loading buffer (5x): 20% glycerol (Panreac), 10% SDS, 0.32% 2-β-mercaptoethanol (Sigma), 0.02% bromophenol blue (Sigma).

Electrophoresis buffer: 25mM Tris-HCl, 192mM Glycine (Serva), 1% SDS.

Transference

Once proteins were separated in the gel, they were transferred onto a PVDF blotting membrane (Amersham Hybond P 0.2 PVDF, GE Healthcare) through a semidry transference system (Trans-Blot Semi-Dry Transfer Cell, BioRad) connected to a voltage source (BioRad).

The membrane was previously activated with methanol HPLC grade (Sigma) for 10 sec, washed in type-2 water and kept in transfer buffer. Two Whatman papers (Extra Thick Western Blotting Filter Paper, Thermo Scientific) and the gel containing the separated

proteins were wetted in transfer buffer for 15 minutes before transference. All components were placed on the transference device in this order: one Whatman paper, the activated PVDF membrane, the gel containing the separated proteins and finally the second Whatman paper. A pin was rolled after placing every layer to eliminate bubbles that could alter the electric current and the protein transference to the membrane. The transference was performed applying an electric current of 30 V for 45 min.

Transference buffer: 25mM Tris, 190mM glycine, 20% methanol.

Immunodetection

The detection of particular proteins was achieved using specific primary antibodies, followed by secondary antibodies conjugated to horseradish peroxidase (HRP). HRP is an enzyme able to cleave chemiluminescent agent, producing luminescence that is detected using an imaging device. The amount of luminescent signal is proportional to the amount of HRP present, hence to the amount of protein immunodetected. To avoid unspecific bindings of antibodies to the membrane or to other proteins, the transferred membrane was incubated in blocking solution (5% w/w BSA in TBS-T buffer), during 1 h shacking at room temperature. The blocked membraned was then incubated with the primary antibody diluted in 5 to 10 mL of blocking solution, shaking at 4ºC overnight. Then, the primary antibody was recovered, and the membrane was washed three times using TBS-T for 10 min in agitation. The rat anti-KL 2076 and rat anti-KL 234 antibodies (1:1,000) were used for the detection of KL proteins through the KL1 antigen, of both mouse and human origin. The secondary antibody was diluted in blocking solution (1:10,000) and incubated on the membrane for 1h at RT in agitation. Three more washes of 10 min with TBS-T were performed prior to immunodetection.

In order to detect the specific recognition of the protein of interest by the primary antibody, the membrane was incubated with the luminol and peroxide substrates provided in the Westar EtaC Ultra 2.0 Western-Blot kit (Cynagen), following the manufacturer's instructions. The HRP enzyme conjugated to the secondary antibody catalyzed luminol oxidation by the peroxide, and oxidized luminol emitted light that was detected through a chemiluminescence system (ChemiDoc, BioRad).

TBS buffer: 50 mM Tris (Sigma), 136 mM NaCl (Panreac), 40 mM KCl (Panreac), pH adjusted 7.5.

TBS-T buffer: 0.1% Tween-20 (Sigma) in TBS.

4. Generation of plasmid vectors for rAAV production

4.1. Restriction enzyme digestions

Plasmid DNA (1 to 2 µg) was digested using 1 to 10U of restriction enzyme (Fermentas or New England Biolabs), using 10x buffer provided by manufacturer and autoclaved milliQ wáter in a total volumen of 20µL at 37ºC, overnight.

4.2. DNA ligation reaction

Ligation reaction to clone a transgene into a receptor plasmid was performed using 10U of the T4DNA ligase and ligase buffer 10x (New England Biolabs), 10 ng of the linearized receptor vector, the equivalent molar amount of transgene sequence (1:1) and milliQ water in a final volume of 15 µL. Reactions were performed at 16ºC overnight and the ligase enzyme was finally inactivated at 65°C for 20 min.

4.3. Bacteria Transformation by Heat Shock

All the procedure was performed near the Bunsen flame to avoid contaminations. Competent bacteria stored at -80ºC in 100 µL aliquots were thawed on ice for 10 min. The plasmid DNA solution was added to the cells and kept in ice for 30 min. For the thermal shock, the mix was incubated at 42ºC for 90 s and rapidly returned to ice. 900 µL of liquid LB medium (Miller's LB Broth, Conda) without antibiotic was then added and bacteria were incubated in the shaker at 37ºC for 1 h. Then, the culture was seeded in a Petri plate (Nunc) with LB-agar (Panreac) and antibiotic. Cells were incubated at 37ºC overnight. Transformed colonies were selected and cultured in 3 mL of liquid LB medium with antibiotic at 37ºC overnight in agitation.

4.4. DNA Miniprep

DNA minipreps were performed to obtain plasmid DNA by alkaline lysis of a bacterial pre-culture. This method provides low amounts of plasmid DNA (5-15 µg) with low purity. Nevertheless, it is enough for plasmid verification through restriction-enzyme digestions prior to amplification.

The bacterial pre-culture was centrifuged at 12000g for 1min. Supernatant was discarded and cells were suspended in 200 µL of *suspension buffer* using a vortex. Then, 400 µL of *lysis solution* was added and homogenized by softly inverting the tube. It was incubated at room temperature during 5min for cell lysis and 400µL of cold *precipitation buffer* was added. It was incubated in ice for neutralizing the mix and for protein precipitation and centrifuging at 14000g for 10 min. The supernatant was recovered, and DNA was precipitated by adding 550 µL of isopropanol (Panreac). 5min later it was centrifuged at 12000g for 10 min, supernatant was discarded and the DNA pellet was washed with 500 µL of 70% ethanol. After centrifuging at 12000g for 5 min, the supernatant was discarded and the remaining ethanol was air-dried. Finally, the DNA pellet was suspended in 30 µL of milliQ water with RNAseA (QIAGEN).

Suspension buffer: 50mM Tris-HCl (Sigma) pH=8.0, 10 mM EDTA (USB), 100 mg/mL RNasaA (QIAGEN).

Lysis solution: 200 mM NaOH (Panreac), 1% (w/v) SDS (Amresco).

Precipitation buffer: 3M AcK (Sigma) pH=5.5.

4.5. DNA Maxiprep

DNA maxipreps provide large amounts of high-quality plasmid DNA (250-1000 µg), required for transfection in eukaryotic cells. For plasmid amplification, transformed bacteria were cultured in 1 mL of liquid LB with antibiotic for 16h. 100 to 1 mL of this pre-culture was inoculated into 250 mL of liquid LB with antibiotic and growth overnight at 37ºC in agitation. Plasmid DNA purification was performed using a commercial kit, either E.Z.N.A.R FastFilter Plasmid DNA Maxi Kit (Omega Bio-Tek) or PureLink HiPure Plasmid Maxiprep Kit (Invitrogen), following the manufacturer's instructions. DNA concentration is finally determined by spectrophotometry using the NanoDrop-1000.

4.6. Electrophoresis in agarose gel

Agarose 1% or 2% (w/v) gels were prepared in an Erlenmeyer flask by dissolving agarose (Seaken LE Agarose, Iberlabo) in *TAE 1x* and heating the mix in a microwave. RedSafeTM Nucleic Acid Staining Solution 20.000x (iNtRON Biotechnology) was added to the agarose solution for DNA display, as it emits green fluorescence when it binds to DNA, becoming a non-carcinogenic alternative to ethidium bromide staining. The solution was poured into

the gel tray (BioRad), and once the gel polymerized, the comb was removed. The agarose gel was covered by TAE 1x solution in the electrophoresis cuvette. Loading buffer 10x was added to the DNA samples, and each one was loaded inside a gel well. Depending on DNA fragment size, GeneRuler 1kb or 100bp (ThermoFisher Scientific) was loaded. An electric current of 80-90 V was applied for 120 min (for DNA band purification) or 60 min (for standard PCR verification), while DNA validation digestions were run at 100-120 V for 60 min (Sources of Power Pac Basic electrophoresis, BioRad). Finally, the gel was placed in the UV transiluminator (GeneGenius BioImaging System, Syngene) to display separated DNA fragments, and images were analyzed with the GeneSnap software (Syngene).

Loading buffer 10x: 50% glicerol, 100mM EDTA pH 8.0, 1% SDS and 0.1% Bromofenol Blue or Xylene Cyanol FF.

TAE 1x: 40mM Tris-acetate, pH=8; 0,1mM EDTA (Calbiochem).

4.7. DNA purification from agarose gel

DNA fragments separated by electrophoresis were purified from agarose gels using the *Wizard SV Gel and PCR Clean-Up System* (Promega) following the protocol supplied. This method is based on the ability of DNA to bind to a silica matrix. Purified DNA is finally dissolved in 30 µL of nuclease free water provided by the kit.

4.8. DNA quantification

The DNA obtained in the different procedures was quantified using the spectrophotometer NanoDrop-1000 (NanoDrop Technologies) at 260 nm wavelength. This system provides the DNA concentration in ng/µL and nucleic acid purity through the 260/280 and 260/230 ratios.

5. Generation of rAAV vectors

Viral vectors were produced, purified, and manipulated in the biosafety level 2 facilities at UAB.

5.1. rAAV vector production by triple transfection

Recombinant AAV were produced by the triple transfection method in the HEK293 producer cell line following a protocol based on [284]. Briefly, three plasmids are used to co-transfect the cells: pAAV (plasmid encoding expression cassette with the transgene of interest between the ITRs, to be packaged), pRepCap (providing in trans the rep and cap sequences, determines de serotype of the AAV) and the pXX6 (helper genes for replication). Following transfection, the DNA is replicated in the producer cells and the expression cassettes are packaged into the viral capsids. The resulting rAAV are harvested from the cell lysates 48 to 72 h later and undergo purification and quantification (titration).

At least 2 days prior to transfection, HEK293-AAV cells (Stratagene) were seeded in 15 cm-plates (Falcon) using *growth media*. 20 to 60 plates with cells at 70% confluency were used per rAAV production.

The day of transfection, the *Plasmid solution* and the Polyethylenimine *(PEI) solution* were prepared separately according to the number of plates to be transfected. Then, solutions were gently mixed and incubated for 20 min at RT to form PEI:DNA complexes. PEI is a stable cationic polymer that condenses DNA into positively charged particles that bind to anionic cell surfaces. As a consequence, the PEI:DNA complex is endocytosed by cells, the exogenous DNA is released into the cytoplasm and episomal expression of the plasmids takes place [285]. Concurrently, growth media was replaced by 12mL/plate of *transfection media*. Then, 2 mL/plate of the PEI:DNA solution were added and gently distributed through the plates. Transfected cells were incubated at 37ºC and 5% CO2. After 6h, media was replaced by fresh growth media and further incubated for 48h. Cells were harvested from the plate using a scrapper (Biologix) and centrifuged at 200g for 15 min in 50-mL tubes. Cell media were transferred to a new tube and cell pellets were resuspended in 30 mL *lysis buffer*. Cell media were stored at -20ºC and cell pellets at -80ºC until rAAV purification.

Growth media: Dulbecco's Modified Eagle's Medium (DMEM), 10% fetal bovine serum (FBS), 1% Penicillin-Streptomycin (P/S).

Plasmid solution (per 15cm-plate): 25 µg pXX6, 12.5 µg Rep2CapX and 12.5 µg pAAV in 1 mL NaCl 0.9% (Braun).

PEI solution (per 15cm-plate): 2.25 µL PEI 10 mM (PolyScience) per DNA µg in 1 mL NaCl 0.9%.

Transfection media: DMEM, 1% FBS, 1%P/S.

Lysis buffer: 50 mM Tris (Sigma), 20 mM NaCl (Panreac), 2 mM MgCl2 (Panreac).

5.2. rAAV vector purification by iodixanol gradient

The purification protocol is composed of a first phase in which viral particles in the cell pellets and in the cell media are precipitated through different procedures, respectively. In a second phase, the viral particles precipitates obtained from both sources undergo an iodixanol gradient jointly.

Cell pellets were first lysed through 3 cycles of freeze-thaw. After centrifugation at 2000g for 10 min, cell debris were discarded, and the supernatant was treated with 50 U/ml benzonase nuclease (71206–3, Merck) and incubated at 37ºC for 1 h to degrade all forms of DNA and RNA outside the viral capsids. Then it was centrifuged at 3000g for 20 min and the supernatant was collected and adjusted to 200 mM NaCl using a 5 M stock solution. To favor the virus precipitation, the clarified cell lysate was mixed with polyethylene glycol (PEG 8000; Sigma) to a final concentration of 8% and incubated at 4ºC overnight. The precipitate was centrifuged at 8000g and 4ºC for 15 min and resuspended in 5mL Lysis buffer and stored at 4ºC. Cell media were mixed with 5 M stock solution and PEG in the same proportions that the cell pellets and incubated at 4ºC overnight to precipitate the viral particles. After centrifugation at 3000g and 4ºC for 30 min, the precipitate was resuspended in 5 mL Lysis buffer and treated with benzonase in the same conditions described above. Viral precipitates from the cell pellets and media fractions were mixed prior to further purification in iodixanol gradient.

The gradient was composed of the following solutions of differential iodixanol (Axis-Shield PoC AS) concentrations: 15 % in PBSMK-NaCl, 25 % in PBSMK with 20 µL phenol red (Sigma), 40 % in PBSMK and 60 % in PBSMK with 2 µL phenol red. The gradient was set in an ultracentrifuge tube (Optiseal Polypropylene Tube, Beckman Coulter), gently adding the iodixanol solutions by layers so the density was increasing from the top to the bottom. The viral precipitate was added on the top of the gradient. Then it was ultracentrifuged at 69000 rpm using a Beckman 70Ti rotor (Beckman Coulter) at 18ºC for 1 h 30 min. Finally, the bottom of the tube was holed with a needle and the the viral fractions were recovered.

In cases in which high concentration of rAAV was needed, the viral fraction was concentrated using an Amicon Ultra-15 Centrifugal Filter Device (Millipore).

Lysis buffer: 50 mM Tris (Sigma), 20 mM NaCl (Panreac), 2 mM MgCl2 (Panreac), adjusted pH 8.5.

PBSMK: PBS, 1 mM MgCl2 (Panreac), 2.5 mM KCl (Panreac).

PBSMK-NaCl: PBSMK, 1 M NaCl.

5.3. rAAV concentration by Amicon column

To increase the AAV titer, some AAV productions were concentrated using Amicon Ultra-15 100K filter device (Millipore). First, the column was filled with 5 mL 70% ethanol and incubated for 30 min RT. Ethanol was discarded and the column was washed using 10mL of sterile PBS and centrifuged at 2600g for 2 min at RT. The AAV pool was diluted 1:4 in sterile PBS 1x and added to the upper chamber of the filter device, then centrifuged at 2.600g at RT in rounds of 1 min until the volume in the upper chamber marked 500 to 200 µL. Then the concentrated phase in the upper chamber was recovered using a pipette, aliquoted and tittered.

5.4. rAAV titration by PicoGreen

The titer of viral particles in rAAV productions was quantified after iodixanol purification through the PicoGreen method, previously described by the Viral Vector Unit of our group (UPV, UAB) [286]. It is based in the ability of PicoGreen, a fluorescent dye, to bind dsDNA in solution. Despite the rAAV genome being a ssDNA molecule, it can be quantified by binding to PicoGreen after the single-stranded genomes are released from lysed capsids and anneal.

First, 2 µL of rAAV samples were mixed with 8 µL of H2O and 10 µL of lysis buffer. To lysate the viral capsids, the mix was incubated at 70ºC for 1 h and gradually cooled down at a rate of 5ºC/min until 25ºC. In parallel, a non-lysed set of the samples compose of 2 µL of the same rAAV fractions and 8 µL of H2O and 10 µL of TE, was incubated a RT. To obtain a 6-point standard curve of known DNA concentration, one-third serial dilutions ranging from 0.16 to 40 ng were prepared using a DNA stock solution (bacteriophage λ DNA, 100 µg/mL;

Molecular Probes, Invitrogen). The standard dilutions, a blank control and all the lysed and non-lysed rAAV samples (in duplicate) were loaded in a black 96-well plate (96wp) (Nunc). Quant-iT PicoGreen dsDNA reagent (Molecular Probes, Invitrogen) was diluted 1:600 in TE and 180 µL of this solution were added to each well. The plate was incubated in the dark at RT for 5 min and then fluorescence was analyzed in a plate reader (Perkin Elmer Wallac 1420 Victor3) at 485 nm/535 nm. The fluorescence value of the blank was subtracted from each sample. Corrected data were used to make a linear regression analysis of the fluorescence measurement versus the amount of DNA. The concentration of DNA (ng/mL) for each sample was obtained by interpolation in the standard curve.

The following formula was used to convert ng/ml to viral genome per mL:

$$\textbf{\textit{rAAV viral genome}}\ \textit{(vg/mL)} = \textbf{\textit{A}}\ \textit{(ng/mL)} \cdot \textbf{\textit{1.82}} \cdot \textbf{\textit{10}}^{\textbf{\textit{12}}}\ \textit{(bp/ng)} / \textbf{\textit{B}}\ \textit{(bg/vg)}$$

A: rAAV genome concentration (ng/mL)

B: length of AAV genome (bp/vg)

Finally, the rAAV titer was calculated as the difference between the value of rAAV viral genomes from lysed samples and the rAAV viral genomes value from non-lysed samples.

Lysis buffer: 20 mM Tris pH 7.4, 200 mM NaCl, 0.2% SDS.

TE: 10 mM Tris pH 8.0, 1 mM EDTA.

5.5. *In vitro* validation of AAV vectors

The rAAV transduction and transgene expression was validated by transducing cultured HEK293-QB (Q-BIOgene). Cells growth at 60 to 80% confluency in 6-well plates (Falcon) were infected with around $5 \cdot 10^4$ vg/cell in 750 µL/well *infection media* and incubated for 72 h at 37ºC, 5% CO2. The day after transduction, 2 mL of *infection media* were added per well. 72 h after transduction, cells were harvested in PBS, centrifuged at 1000 rpm for 5 min and resuspended in either cold Qiazol or RIPA, depending on the subsequent analysis. To validate the transcription of the transgene, cells were lysed in Qiazol and processed as explained in 0 prior to PCR analysis. To validate the protein expression of the transgene, cells were lysed in RIPA as explained in 0 and the protein was detected by Western blot (0).

Infection media: DMEM + 2% FBS + 1% P/S.

6. Mice handling

The experimental procedures involving mice were conducted in the animal facilities of the UAB and approved by the Animal Experimentation Ethics Committee of UAB (number CEEAH-3427). Mice were bred in Macrolon cages, fed ad libitum with standard diet, and kept under controlled temperature (22±2ºC) and light-dark cycles (12h). All the materials used in surgical procedures were washed with water and soap and sterilized with 70% ethanol prior to use in each animal.

6.1. Anesthesia

Prior to surgery procedures, mice were anesthetized by intraperitoneal injection of 120 mg/kg of ketamine (Imalgene 50 mg/mL, Merial Laboratories) and 12 mg/kg of xylacine (Rompun, Bayer) diluted in 0.9% saline solution (B.Braun). A toe pinch was performed prior to surgical intervention to ensure the mouse was completely unconscious.

6.2. rAAV administration by stereotactic injection

rAAV were administered to the CNS of mice by unilateral intracerebroventricular (ICV) stereotaxic injection. Since the lateral ventricles are filled with CSF, and the CSF circulates all over the CNS, ICV injection guarantees the rAAV distribution to different brain areas, specially to the hippocampus.

After anesthesia, animals were placed in a stereotactic frame and the area of the injection in the head was sterilized with 70% ethanol. Using a sterile scalpel, an incision of 7-8 mm was performed in between the eyes and the base of the neck to expose the skull and locate Bregma (coordinate zero). The skull was washed using sterile NaCl 0.9% (Braun). The coordinates of the site of injection (IVC: Anteroposterior: -0.22 mm; Lateral: 1.0 mm; Depth: 2.5 mm) were located with a 10mL-Hamilton syringe attached to the stereotaxic device and a perforation in the skull was manually performed using a 27G x 1/2 needle (0.40 x 12 mm; B.Braun). The rAAV solution was contained in the Hamilton syringe according to the dose stablished in a maximum volume of 9 µL. The syringe was placed in the site of injection and the solution was administered at a speed of 0.5 µL/min using an ultra-micropump (World Precision Instruments). The syringe was kept in the injection site for 10 additional min to let the viral solution spread and prevent reflux. Then the incision was sealed using 1-2 staples

and disinfected with povidone iodine. The mouse was placed in a warming environment for recovery and monitored for at least 30 min.

6.3. Behavior tests

Male and female mice were handled tested separately.

Assessment of sensorimotor functions.

Prior to the cognitive and memory tests, sensorimotor capabilities were evaluated in all the mice by the following tests. The tail suspension test was performed to evaluate **motor and visual reflexes**. The mouse was held by his tail at 30 cm above a black flat surface during 3 s, and then it was slowly lowered onto the surface. The mouse extending the extremities as it gets closer to the surface indicates correct reflexes and scores 1, whereas the lack of reflexes scores 0. The test was performed three times and the average score above 0.6 indicated valid reflexes.

The **motor coordination and equilibrium** were assessed by the distance covered and the latency to fall off a horizontal wooden rod (1.3 cm wide) on two consecutive 20 s trials, respectively.

Prehensility and motor coordination were measured as the distance covered on the wire hang test, which consisted in allowing the animal to cling from the middle of a horizontal wire (diameter: 2 mm, length: 40 cm, divided into eight 5 cm segments) with its forepaws for two trials of 5 s and a third 60 s trial. Muscle strength was measured as the time until falling off the wire in the 60 s trial. All the apparatus was suspended 40 cm above a padded table.

Open Field

The Open Field test aims to evaluate the exploratory activity of mice in an anxiogenic environment. The apparatus consisted of a homemade square wall-enclosed area (50 × 50 × 25 cm) where the mouse was allowed to freely explore. One mouse at a time was placed in the center of the apparatus and recorded for 5 min using a digital camera (Nikon) fixed above the apparatus. Then the mouse was returned to its home cage was wiped with 70%

ethanol prior to testing the following mouse. Recorded tests were analyzed later either manually or using the Any-Maze software, depending on the experiment.

The base of the maze was segmented to examine the thigmotaxis, which is an index of angiogenic behavior based on the natural tendency of mice to remain close to the maze walls. Thigmotaxis was measured as the percent of the total test time that the mouse spent in area designed as 'exterior' versus the time percent spent in the 'center' (Figure 18).

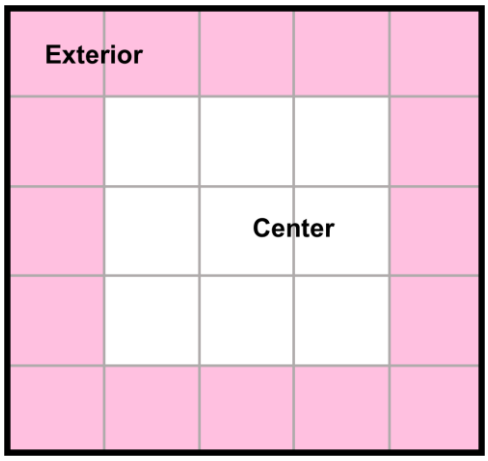

Figure 18. Open Field maze representation. The zone overlay was used to interpret thigmotaxis during the Open Field test. The Exterior area consist of the 16 outer blocks adjacent to the maze walls (identified as pink). The Center area corresponds to the 9 inner blocks (identified as white). Increasing time spent in the Exterior area is interpreted as increased thigmotaxis, hence increased anxiety-related behavior. The colors used to identify areas in this figure do not represent the actual maze (totally white).

Novel Object Recognition

The Novel Object Recognition (NOR) test evaluates the mice's ability to recognize a novel object in the environment, based on the mice's natural preference for novel objects. Three tasks (habituation, familiarization, and memory) are conducted by each mouse during 3 consecutive days using the same apparatus than in the Open Field test (50 × 50 × 25 cm arena). The day 1 (habituation), the animal was placed in the center of the empty apparatus and let explore for 5 min. In our set, this task matched with the Open Field test. The day 2 (familiarization), two identical objects (familiar) were placed in the center of the arena and each mouse was allowed to explore them during 5 min. The day 3 (memory), one of the familiar objects (F) was replaced by a novel one (N), having a distinct shape, material and color, and each mouse was allowed to explore both for 5 min (N+F) (Figure 19). The position of the novel and familiar objects was randomly assigned to each animal to avoid bias.

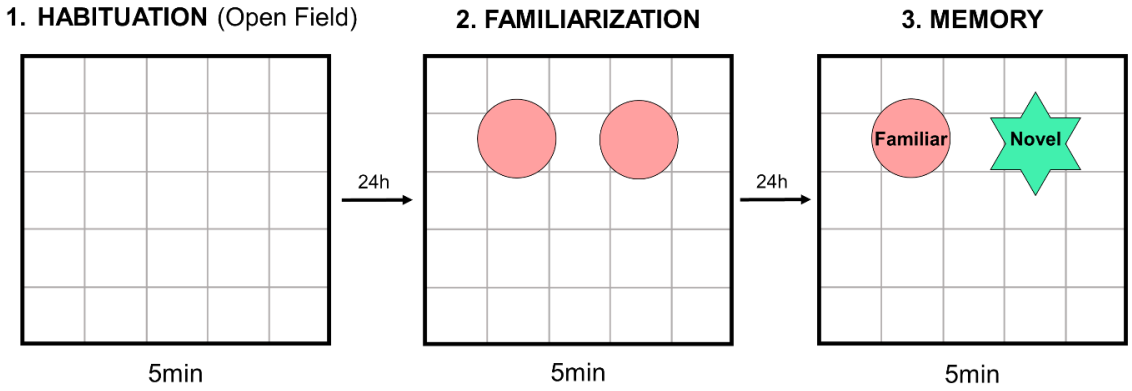

Figure 19. Schematic representation of the NOR test.

Tasks were recorded using a camera and the videos were analyzed afterwards using the Any-Maze software. Since mice show an innate exploratory behavior and natural propensity to the novelty, the NOR test allows us to evaluate the index of stimulus recognition and the short-term memory when comparing the time spent exploring the novel versus the familiar object [287]. Various parameters were measured such as mean speed, distance and time spent exploring the objects. The discrimination index, defined as the difference of time spent exploring the novel and familiar objects, divided by the total time exploring [DI=(TN-TF)/(TN+TF)], was calculated to evaluate the preference for the new object, hence the cognitive capacity. A positive DI score indicates more time spent with the novel object, a negative score indicates more time spent with the familiar object, and a zero score indicates a null preference [288]. Cognitive function may also be measured through the **Preference Index (PI),** which is a ration of the amount of time spent exploring an object over the total time spent exploring both objects [PI=TN/(TN+TF) · 100 (%)]. Therefore, a PI above 50% indicates preference for the novel object, below 50% preference for the familiar object, and 50% no preference [289].

The total time exploring both objects in the familiarization and memory assays were used as inclusion criterion, being mice exploring objects for less than 5 s excluded from the analysis. In addition, outliers were a priori defined as greater than 2 SDs above or below the mean to ensure unbiased exclusion. Only the mice that meet the inclusion criteria are considered in Results.

T-Maze

The T-maze test is based on the willingness of mice to explore new spaces and it is used to assess short-term spatial working memory. The device used consisted of a symmetrical T-shaped black maze. Two arms 25 cm long were connected at the center at 90º angle by a 30 cm arm (leg), whose extreme was the start point. The two alternative arms and the start point could be blocked with a black barrier.

In the first phase of the test (learning), one of the arms was blocked. The mouse was placed at the blocked start point during 10 s for habituation and then the barrier was opened to allow the mouse to freely explore the leg and the open arm (familiar arm) for 2 min. The blocked arm was randomly alternated for each mouse to avoid bias. Afterwards, the mouse was returned to its home cage for 2 min. In the meantime, maze was cleaned with 70% ethanol and both arms were opened. In the second phase (memory trial) both arms of the maze are accessible so the mouse could choose to explore either the familiar or the newly open arm (novel arm). Similar to the previous phase, the mouse was placed in the start point for 10 s for habituation and then allowed to freely explore the two arms for 2 min (Figure 20).

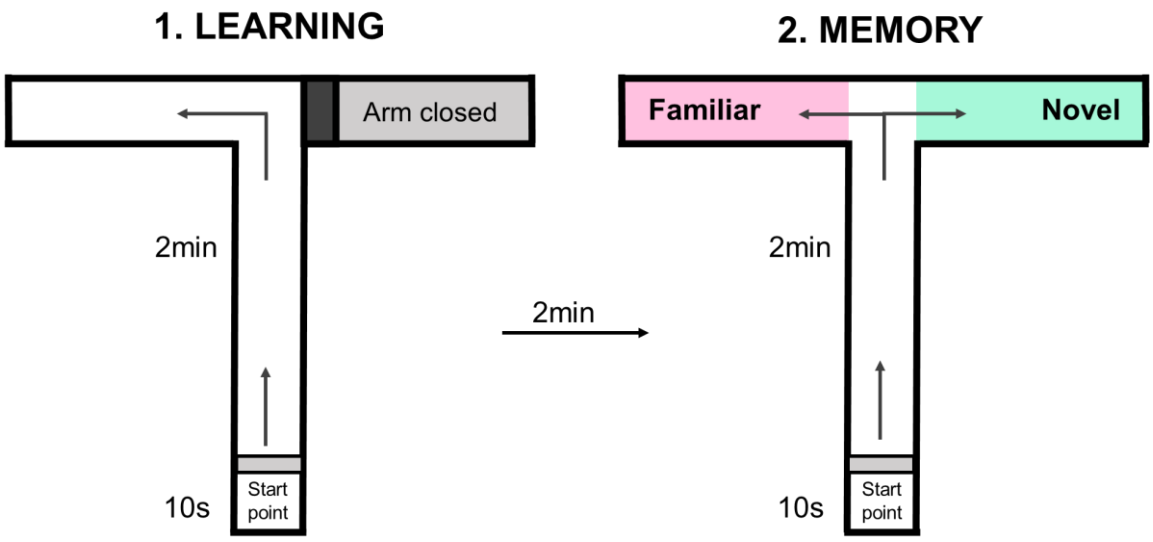

Figure 20. Schematic representation of the T-maze test.

Mice behavior was recorded, and multiple parameters were automatically measured by the Any-maze software. To ensure the reliability of the parameters measured for memory assessment, the following exclusion criteria were applied: (1) Mice not entering to the open arm at least once during the learning phase, were excluded. (2) Mice not entering to either

of the arms at least twice during the memory phase, were excluded. (3) Mice differing more than 2 times the SD of the mean of the group in any of the following parameters, were excluded of the analysis: total time exploring arms, total number of entries to either arm, and latency to reach intersection.

Morris Water Maze

The Morris Water Maze (MWM) is a widely used test to evaluate the hippocampal-dependent spatial learning and memory. The test consists of locating and reaching a platform (7 cm diameter, located 1.5 cm below the water surface) in a circular pool 120-cm diameter, 60-cm height) filled with opaque white water at 25 °C and surrounded by black curtains.

The first day (*Cue)* consisted of visual perceptual learning. Each mouse was placed in the pool filled with opaque water in which a platform was visible over the water surface using a striped flag (5 × 8 cm) as a cue. Each mice performed 4 trials of maximum 60 s on the cue day. The 4 following days (*Learning*), mice were trained to reach the hidden platform, with the help of visual cues around the pool for orientation. Training consisted of 4 trials of maximum 60s per day, for 4 days. If a mouse failed to locate the platform in 60s during any learning trial, it was placed on the platform for 10s before being removed to its home cage. Spatial learning was demonstrated by decreasing in the time (latency) to find platform and the path length (distance) to reach the platform. During the training days, the hidden platform remained located at the same point, and the mice were dropped to the pool at varied sites between trials. For assessment of spatial memory, mice underwent two probe trials 2 h and 24 h after the last training session, respectively. The probe trials consisted of 60 s with no platform in the pool. The Any-maze software allowed us to divide the pool into 4 areas (quadrants) and demarcate the target area (where the platform was located in the learning) for analysis. The *target* was defined as the zone that used to be occupied by the platform plus the surrounding area, equivalent to an extension of 0.5 times the diameter of the platform. Mice entered the pool by different sites in the 2h and in the 24h probe trials. Mice that did not reach the target during the 60 s that lasted the memory tests, were assigned the maximum value in the latency parameter (60s) (Figure 21).

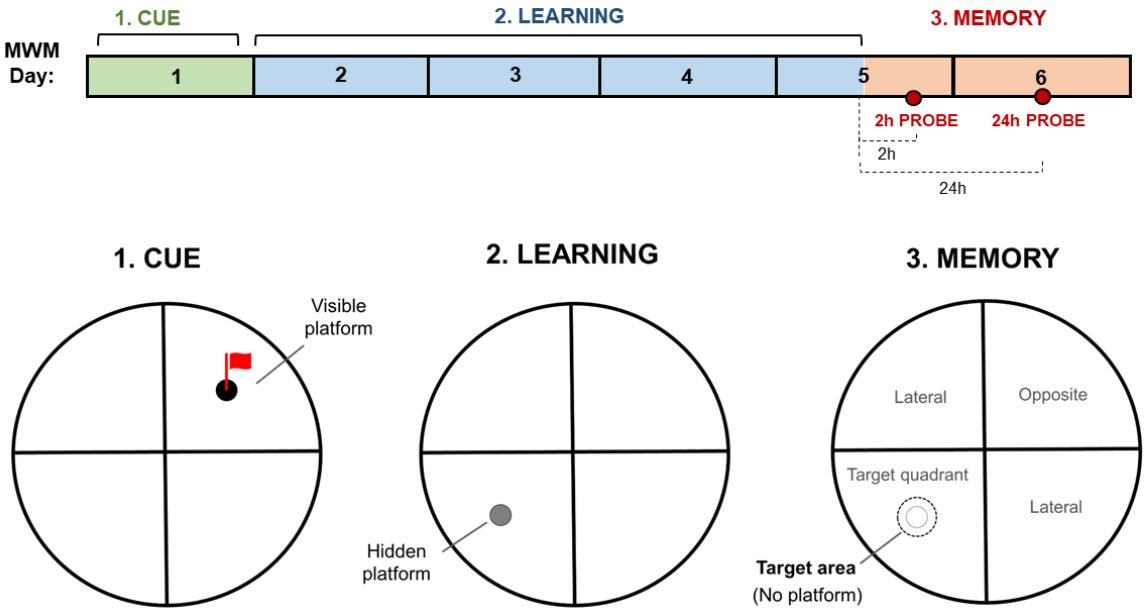

Figure 21. Timeline and schematic representation of the MWM test.

Multiple parameters such as time to reach the platform (latency), distance traveled, swimming speed, and time spent in each area were recorded and quantified using ANY-maze behavioral tracking software. Spatial memory was demonstrated by a decreased latency to reach the target area and a preference for the target quadrant, in comparison to other quadrants of the pool.

6.4. Euthanasia and sample collection

Mice were first anesthetized by inhalation of isoflurane (Isoflo, Esteve) in a closed chamber, followed by cervical dislocation and decapitation using scissors.

Liver and kidney sections were collected in Eppendorf tubes. Brain was cut in two hemispheres. One hemisphere was submerged into cold PFA 4% for subsequent fixation and immunohistochemistry analysis. The other hemisphere was dissected on a cold surface into the following brain areas: hippocampus, entorhinal cortex, frontal cortex, olfactory bulb, and cerebellum. Each area was collected in an individual tubes, flash frozen in dry ice and stored at -80ºC freezer until processing for biochemical analysis.

7. Brain organoid cultures

All the experiments concerning human brain organoids were conducted by the PhD candidate at Dr Muotri's Laboratory (University of California San Diego, USA) during a 6-month research stay.

The generation of the human brain organoids was performed by Dr Muotri's team as described in [290]. Briefly, iPSC colonies were gently dissociated using Accutase in PBS (1:1) (Life Technologies). Around 4 million cells were plated in a well of a 6-well plate and kept under suspension (so called "protocol B" in our Results section). Alternatively, around 3 million cells could be plated in an AggreWell 800 plate (StemCell) after treatment with anti-adherence rinsing solution (StemCell) (referred to as "protocol A" in Results section). After transferring cells to a 6-well plate, they were kept on a shaker under permanent rotation at 95 rpm in the incubator. For neural induction, media containing DMEM/F12, 15mM Hepes, 1× Glutamax, 1× N2 NeuroPlex (Gemini), 1× MEM-NEAA, 1µM dorsomorphin (R&D System), 10µM SB431542 (Stemgent) and 100 U/ml penicillin-streptomycin was used for 6 days. NPC proliferation was obtained in the presence of Neurobasal media supplemented with 2× Gem21 NeuroPlex, 1×NEAA, 1× Glutamax, 20ng/ml EGF and 20ng/ml bFGF. Next, cells were kept in the same media in the absence of growth factors for neuronal maturation.

7.1. AAV-Transduction of brain organoids

AAV transduction was performed in human brain organoids at 44 days post-differentiation and later. Brain organoids cultured in 6wp were spared in single wells in a 96-well plate for prior to AAV administration. In the case of the small organoids generated by "protocol B", around 10 units were spared in each well. Conditioned media was recovered from the 6-well plate, centrifuged, and stored at 4ºC in a new 50 mL tube for future media changes. AAV dilutions were prepared in a maximum of 10% PBS and fresh culture media according with the dose selected and the titer of the viral batch. 100 µL of AAV preparation was added to each well and incubated under rotation for 5-6 h. Then wells were filled with fresh and conditioned media (1:1) to the normal culture volume. After 24 h, half of the medium was replaced by fresh media. Medium was replaced with fresh and conditioned media 1:1 every 2-4 days, depending on the culture appearance. Live cell imaging for transgenic GFP

expression detection was performed every 24 h to using an EVOS Cell Imaging System (Thermo Fisher Scientific).

7.2. Immunohistochemistry of brain organoids

Brain organoids were harvested in 1.5mL tubes containing cold PFA 4% and kept at 4ºC ON for fixation. Then, PFA was replaced by sucrose 30% in PBS and kept at 4ºC for 24-48h. Fixed organoids were transferred to a plastic mold and embedded in O.C.T (Sakura) avoiding bubbles. For solidification, the molds were kept on dry ice for at least 1 h and stored at -80ºC. Organoids were sectioned in 20 µm slices using a cryostat a -20ºC. Following air dry, the slides containing the sliced samples were permeabilized 0.2 % triton X-100 in PBS for 15 min, blocked with 2% BSA (blocking solution) for 2 hours at room temperature, and incubated with primary antibodies overnight at 4°C. For GFP immunodetection, the primary antibody used was a chicken polyclonal anti-GFP (ab13970, Abcam) diluted1:1000 in blocking solution (PBS + 2% BSA). The next day, the organoid slices were washed with PBS and incubated with secondary antibodies (Goat anti-chicken 488-conjugated antibody, Life Technologies) diluted 1:1000 in blocking solution, for 1-2 hours at room temperature in the dark. The nuclei were stained using DAPI solution (1 µg/mL). In between every reagent, organoid slices were gently washed with PBS. The slides were mounted using ProLong Gold antifade reagent, incubated for at leart 48h at room temperature in the dark, and finally analyzed under a fluorescence microscope (Axio Observer Apotome, Zeiss).

8. Statistical analyses

Statistical analyses were performed using the GraphPad Prism software. Differences between two means were assessed by the t-test. Differences between more than two means were determined using either one-way ANOVA (for one variable) or two-way ANOVA (for two variables) followed by post hoc tests (indicated in figure legends). Tuckey's post hoc test was normally used to determine differences between multiple groups. Dunnet's post-hoc test was used once to determine differences between two disease groups respect to the control group. The Pearson correlation coefficient was calculated to assess the linear correlation between two continuous variables. One-sample t-test for studying the

expression ratio of sKL *vs* mKL. Comparison of proportion tests was used to compare the percentage of mice entering the novel arm first in the T-maze. In mouse studies, exclusion criteria were defined a priori to ensure unbiased exclusion of outliers (greater than 2 SDs above or below the mean). Null hypotheses were rejected at or below a p-value (p) of 0.05.

RESULTS AND DISCUSSION

CHAPTER 1

Molecular characterization of Klotho in the human CNS in health and Alzheimer's disease

RESULTS

Klotho is known to be expressed in the human kidney and brain, where it exerts important functions. However, the relative contribution of each transcript variant (sKL and mKL) in the human CNS remains to be fully determined. In this regard, we aimed to quantify the relative amount of sKL and mKL transcripts in brain areas of human donors with no neuropathological disorders. Given the relevance of KL in neurodegenerative diseases, we also quantified the gene expression of the KL variants in different stages of AD.

To further characterize the KL expression in the CNS, we analyzed the protein levels of soluble KL in CSF of healthy adults and AD patients. In addition, we studied the correlation of soluble KL levels to other clinical factors such as age, sex and APOE genotype (Figure 22).

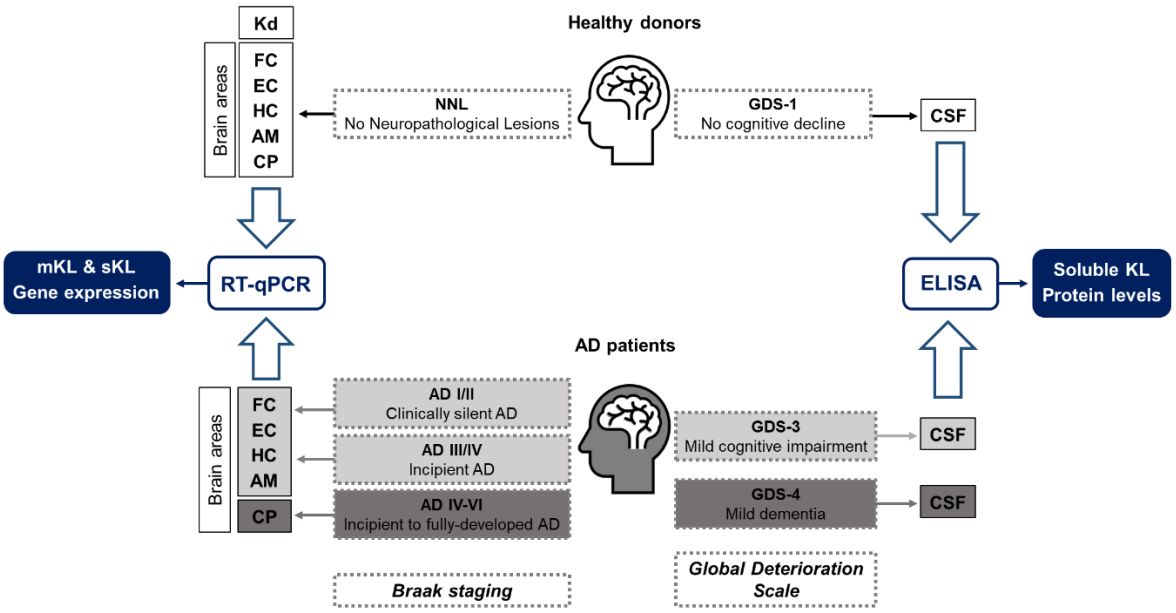

Figure 22. Experimental design for the molecular characterization of KL in the Human CNS with no pathological lesions (NNL) and AD. Kd: kidney, FC: frontal cortex, EC: entorhinal cortex, HC: hippocampus, AM: amygdala, CP: choroid plexus, CSF: cerebrospinal fluid, GDS: Global Deterioration Scale.

1. Gene expression profile of the Klotho variants in brain

The genetic expression of mKL and sKL was quantified by reverse transcription-quantitative polymerase chain reaction (RT-qPCR) using specific TaqMan sets for each transcript variant. Briefly, each TaqMan set is composed of two primers and one probe that aligns in between the cDNA region flanked by the primers, providing high specificity for each alternative mRNA. Specifically, the cDNA region targeted for the mKL transcript spanned exons 3 and 4; and the primers targeting the sKL transcript aligned exon 3 and a sequence including the intronic area specific for sKL after exon 3 and the 3' region of exon 4. This, together with the use of a probe targeting the amplified sequence, provided specificity for each transcript and avoided genomic DNA amplification.

The relative amount of sKL and mKL was calculated for each individual by the ratio sKL/mKL, taking into account: (1) the difference between the Cq's of the two transcripts, and (2) that the amplification efficiencies of the two TaqMan sets are equivalent because they all have amplification efficiencies very close to 100% [291]:

$$\text{sKL/mKL ratio} = 2^{\Delta Cq} \text{ ; where } \Delta Cq = Cq_{mKL} - Cq_{sKL}$$

In the areas in which mKL was more abundant than sKL, we calculated the inverted ratio (mKL/sKL) to obtain integer values:

$$\text{mKL/sKL ratio} = 2^{\Delta Cq} \text{ ; where } \Delta Cq = Cq_{sKL} - Cq_{mKL}$$

1.1. Relative gene expression of sKL and mKL in healthy adults and AD patients

First, we investigated the relative abundance of both mRNA transcripts in human tissues by RT-qPCR. Because the kidney is the predominant organ expressing KL [127], we analyzed the gene expression of mKL and sKL in kidney samples of healthy human donors. We detected both transcripts and confirmed that mKL was about 3-fold higher than sKL (Figure 23), as previously reported [281].

Next, we analyzed the relative expression of mKL and sKL in different brain areas of healthy adults. For the first time, the alternative sKL transcript was detected in the human frontal and entorhinal cortex, hippocampus, amygdala, and choroid plexus by RT-qPCR.

Remarkably, the sKL/mKL ratio was significantly higher than 1 in frontal cortex, entorhinal cortex, and amygdala, meaning that the sKL alternative transcript was 2.5 to 4.4-fold more abundant than mKL in these areas. In the hippocampus, the sKL transcript was also more abundant than mKL (around 4-fold on average), although no statistical significance was detected due to the low sample size (n=3). Surprisingly, in the choroid plexus, the relative amount of sKL *vs* mKL was inverted, making the mKL transcript significantly more abundant than sKL in this tissue. It should be acknowledged though, that the mKL transcript did not reach twice the levels of sKL in choroid plexus, suggesting closer expression levels of sKL and mKL in this area, in contrast with the other areas analyzed, in which sKL *vs* mKL levels differed more than 2-fold. This is also supported by the significance level of the expression ratios following One-sample t-test: p=0.0188 (#) in CP versus at least p=0.0054 (##) in the other areas.

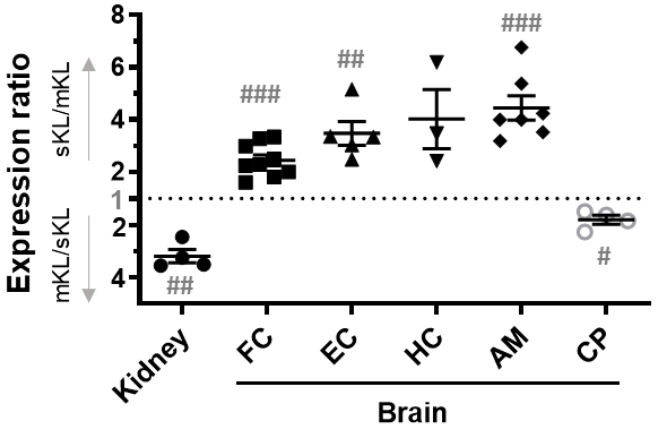

Figure 23. Gene expression ratio of sKL *vs* mKL in kidney and brain areas of humans with NNL. Individual dots represent the ratio for each subject. Mean±SEM plotted per area. The one-sample t-test was used to determine whether a mean ratio was different from 1, in which case the relative proportion of the KL variants would be different (statistical significance indicated with: #p<0.05, ## p<0.01, ###p<0.001). Sample size (n): FC: frontal cortex (9), EC: entorhinal cortex (5), HC: hippocampus (3), AM: amygdala (7). CP: choroid plexus (4).

Subsequently, we investigated the gene expression profile of the KL variants in brain of AD patients, classified *post mortem* according to the Braak criteria [61]: AD I/II (clinically silent AD patients), AD III/IV (incipient AD patients), AD IV-VI (incipient and fully developed AD patients), and donors with no neuropathological lesions (NNL) as healthy controls. It should be noted that the samples of choroid plexus (CP) were obtained from different patients than the rest of areas (FC, EC, HC and AM), and that the AD stages of the CP samples (AD IV-VI) do not match with the others (AD I/II, AD III/IV).

The transcription levels of mKL and sKL were normalized to two housekeeping genes (reference), cytochrome c1 (CYC1) and ubiquitin conjugating enzyme E2 D2 (UBE2D2), as recommended by [292]. The results did not show significant differences between disease groups in the analyzed brain areas (Figure 24). Nevertheless, some trends could be observed: sKL expression was slightly increased in hippocampus, amygdala and choroid plexus of AD patients compared to healthy donors, whereas in frontal cortex it tended to decrease (Figure 24.A). As for mKL, it showed a slight trend to decrease in frontal and entorhinal cortex of AD patients compared to NNL donors, while in hippocampus a slight decrease was only noticeable in the ADI/II patients, but not in more advance stages. In contrast, mKL expression tended to increase in amygdala and choroid plexus, especially in advanced AD stages (AD III/IV and AD IV-VI, respectively) (Figure 24.B).

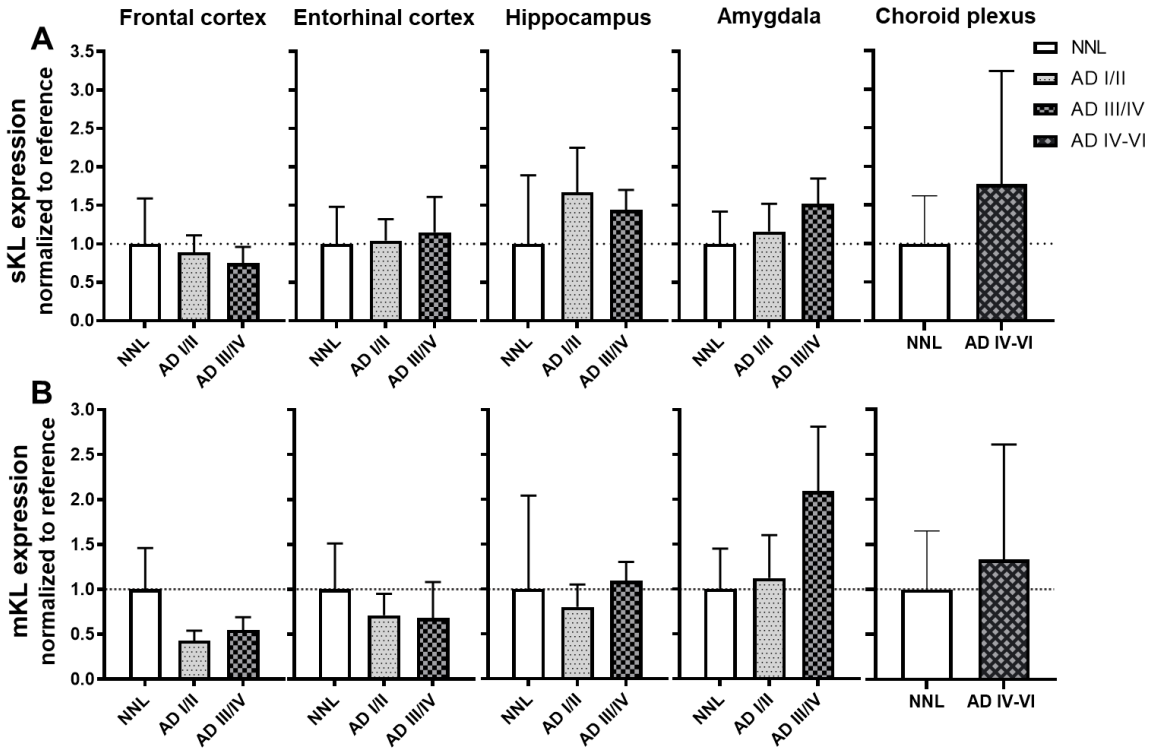

Figure 24. Gene expression levels of mKL and sKL in brain areas of adults with NNL and AD patients classified according to Braak staging criteria. The expression levels for each KL variant were normalized to two housekeeping genes used as reference (CYC1 and UBE2D2). Data represented as fold-change to NNL group plotted as Mean±SEM. Differences between three disease groups analyzed by One-way ANOVA (FC, EC HC and AM); differences between two groups analyzed by t-test (CP). Sample size per area and group (n): FC (NNL: 10, ADI/II: 10, AD III/IV: 9), EC (NNL: 8, ADI/II: 10, AD III/IV: 10), HC (NNL: 3, ADI/II: 7, AD III/IV: 6), AM (NNL: 7, ADI/II: 8, AD III/IV: 7), CP (NNL: 4, ADIV-VI: 5).

We also investigated the relative expression of sKL *vs* mKL in brain samples of AD patients. In agreement with the results in healthy individuals, mRNA levels of sKL were significantly higher than mKL in all the areas analyzed during AD pathology, with exception of choroid plexus. In this area, the mKL transcript was significantly more abundant in healthy donors; however, in AD IV-VI patients, the relative amount of sKL and mKL transcripts was similar (Figure 25). Interestingly, the sKL/mKL ratio was elevated in clinically silent AD patients (AD I/II) compared to the healthy group, especially in frontal cortex and hippocampus, two areas highly involved in the cognitive impairment associated with AD. In frontal cortex, in which sKL/mKL ratio was significantly higher in the AD I/II group, the increased relative amount of sKL may be explained by a drop in mKL, as observed in Figure 24. In hippocampus, the increased sKL/mKL ratio (Figure 25) seemed to be due to a rise in sKL expression (Figure 24), although in this area differences between groups were no significant, probably due to the low number of replicates.

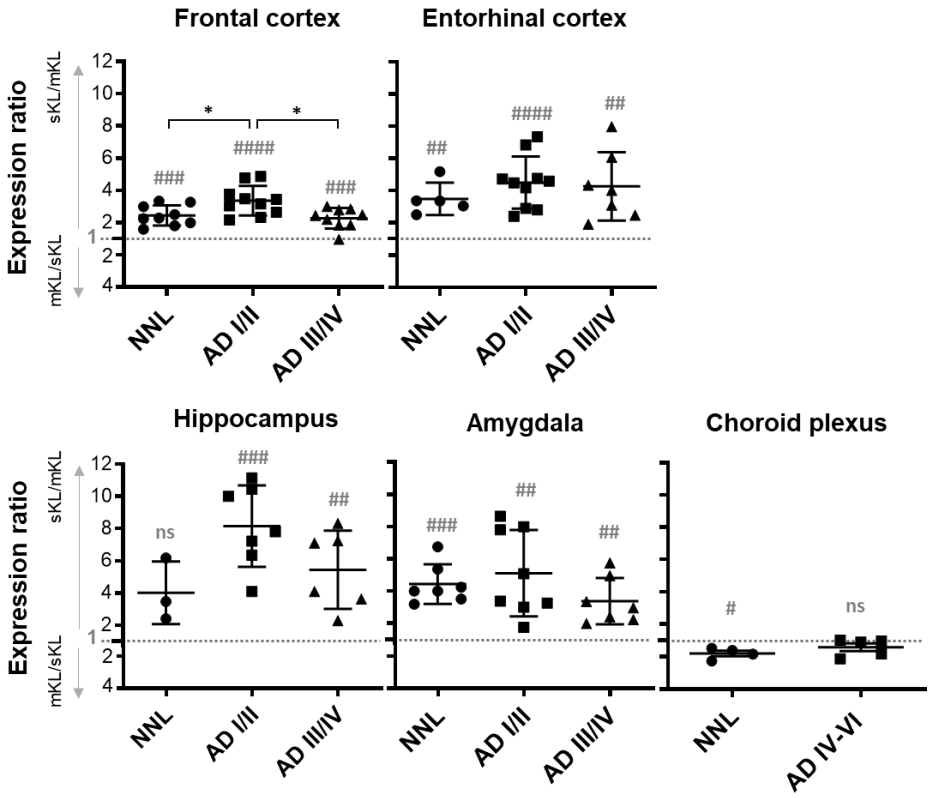

Figure 25. Gene expression ratio of sKL vs mKL in brain areas of adults with NNL and AD patients (ADI/II and AD III/IV) classified according to the Braak staging criteria. Individual dots represent the ratio for each subject, plotted as Mean±SEM. The one-sample t-test was used to determine whether a mean ratio was different from 1, in which case the relative proportion of the KL variants would be different in a particular area (statistical significance indicated with: # p<0.05, ## p<0.01, ###p<0.001). The one-way ANOVA and Tuckey post-hoc were used to detect differences in the mean ratio between groups in each area (statistical significance indicated with *p<0.05). Sample size per area and group (n): FC (NNL:9, ADI/II:10, ADIII/IV:9);

EC (NNL:5, ADI/II:10, ADIII/IV:7); HC (NNL:3, ADI/II:7, ADIII/IV:6); AM (NNL:7, ADI/II:8, ADIII/IV:7); CP (NNL:4, ADIV-VI:5).

1. 2. Relative gene expression of sKL and mKL in WT and AD mouse models

Since the mouse is one of the most used animal models in preclinical research, and the most used *in vivo* model of AD, we aimed to characterize the relative expression of the *KL* variants in this specie. Similar to the approach conducted in humans, we analyzed the genetic expression of sKL and mKL and calculated their relative abundance in kidney and brain areas of 13-month-old WT and AD model (3xTg-AD) mice.

As expected, mKL was the most abundant transcript variant in kidney, being on average over 30 times more abundant than the sKL in both WT and 3xTg-AD mice (Figure 26Figure 5. A and B, respectively), although statistical significance was not observed in this tissue due to the low sample size (n= 3 and 2, respectively). Besides, we observed that mKL was also the most abundant transcript variant with statistical significance in all the brain areas analyzed, in both WT and 3xTg-AD mice. Interestingly, this ratio was inverted to that observed in the human brain parenchyma, where we had found sKL transcript being more abundant than mKL (Figure 23, Figure 25).

In the brain of WT mice, the average mKL/sKL ratio ranged from 6.7 to 13.3, being relatively homogeneous among the different brain areas. The mKL/sKL ratio was lower in frontal cortex (6.7) and cerebellum (7.3), whereas it was more elevated in entorhinal cortex (13.3) and hippocampus (12.5), indicating that mKL was much more expressed than sKL in those areas (Figure 26.A).

In 3xTg-AD mice, the mKL/sKL ratio was higher than WT in all the areas analyzed except in frontal cortex (4.2), where it was maintained low similar to WT mice. While in entorhinal cortex and hippocampus of WT the mean ratios were homogeneous around 13, in 3xTg-AD those were above 20, indicating an increased proportion of mKL expression *vs* sKL in those areas. The cerebellum presented a high variability among the samples analyzed, with ratios ranging from 12 to 27 and a higher average than the rest of the brain areas analyzed (Figure 26.B).

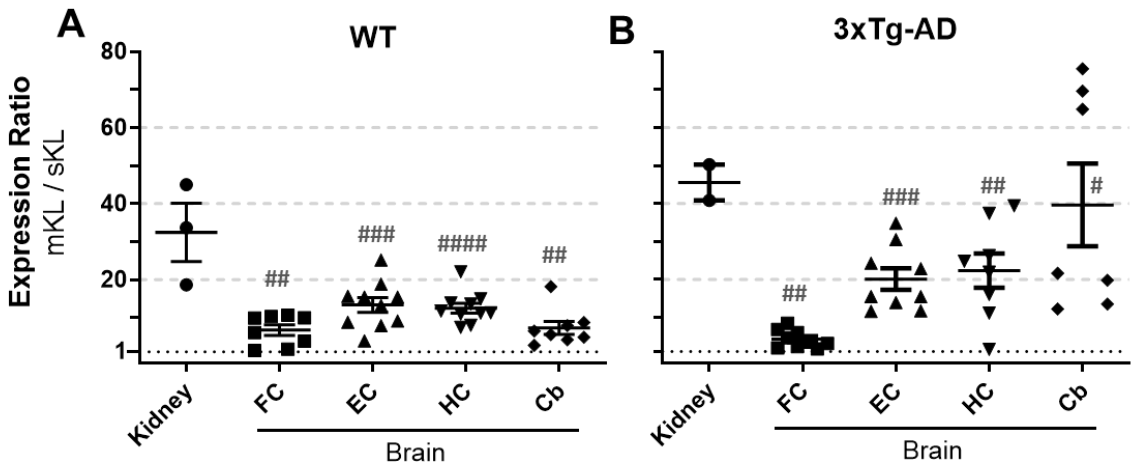

Figure 26. Relative mRNA expression ratio of mKL and sKL in mouse kidney and brain areas of (A) WT mice (WT) and (B) AD mouse model (3xTg-AD). Individual dots represent the ratio for each subject. Mean±SEM plotted per group. The one-sample t-test was used to determine whether a mean ratio was different from 1, in which case the relative proportion of the KL variants would be different in a particular area (statistical significance indicated with: # p<0.05, ## p<0.01, ###p<0.001, ####p<0.0001). FC: frontal cortex, EC: entorhinal cortex, HC: hippocampus, Cb: cerebellum. Sample size (n): WT (Kidney:3, FC:8, EC:10, HC:10, Cb:8); 3xTg-AD (Kidney:2, FC:9, EC:9, HC:8, Cb:7).

2. Protein levels of soluble Klotho in the human CSF

To further characterize the KL expression in the human CNS, we analyzed the protein levels of soluble KL in CSF obtained *in vivo* from healthy elder individuals and AD patients. CSF donors were classified according to the Global Deterioration Scale (GDS) into cognitively normal (GDS1, healthy controls), MCI and MD (GDS3 and GDS4, respectively, AD patients) [57]. The CSF donors were different from the brain tissue donors whose samples were used to analyze KL gene expression. The CSF samples were analyzed using a commercial ELISA kit that detects the KL1 domain of the KL protein. Therefore, all the soluble variants presenting this domain could be detected, including sKL and the processed KL1 and KL1+KL2 (pKL) from mKL [293] .

2.1. Quantification of the protein levels of soluble KL in CSF of AD patients and cognitively healthy adults

Quantification of the soluble Klotho concentration in the CSF samples revealed significant differences between the groups analyzed (One-way ANOVA: p=0.0272) (Figure 27). Soluble KL was significantly decreased in CSF of GDS4 AD patients (655.2 pg/mL) compared to the GDS1 controls (857.8 pg/mL) (Dunnett's post hoc p= 0.0479); whereas the GDS3 patients presented similar KL levels (829.5 pg/mL) to the cognitively healthy group.

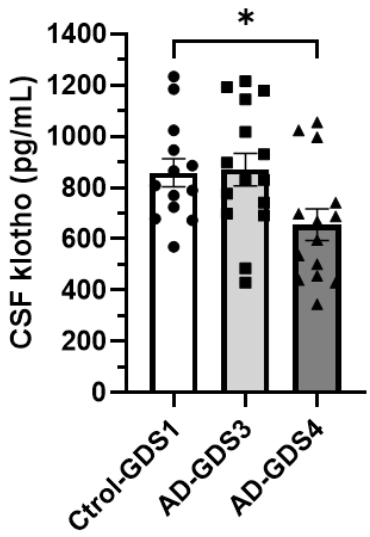

Figure 27. Quantification of soluble KL protein levels in CSF of adults with no cognitive decline (Ctrol-GDS1) and AD patients with MCI (AD-GDS3) and MD (AD-GDS4), classified according to the Global Deterioration Scale. The one-way ANOVA and Dunnett's post hoc tests were performed to detect differences between the mean of each AD group and the cognitively healthy controls (*p<0.05). Sample size (n): Ctrol-GDS1(13), AD-GDS3(15), AD-GDS4(14).

2.2. Association of soluble KL levels in CSF with sex and age in healthy adults and AD patients

We compared KL CSF concentrations between men (M) and women (F) aged 61 to 76 years old (Figure 28.A-D). Despite KL levels tended to be higher in women, we did not observe significant differences between men and women in any of the GDS groups analyzed. This result confirmed the suitability of comparing the GDS groups irrespective of the sex in our donors, as we did in our analysis to gain statistical power.

To investigate whether the levels of soluble KL in CSF vary with increasing age in elder adults, we studied the correlation between KL concentration and age in our donors, all of

them aged over 61 years old, using the Pearson correlation test. The linear regression curve presents a positive slope, indicating that CSF KL tended to increase with age in the elderly (r = 0.2966) (Figure 29.A) regardless of the GDS score, although this correlation was not statistically significant (p = 0.056).

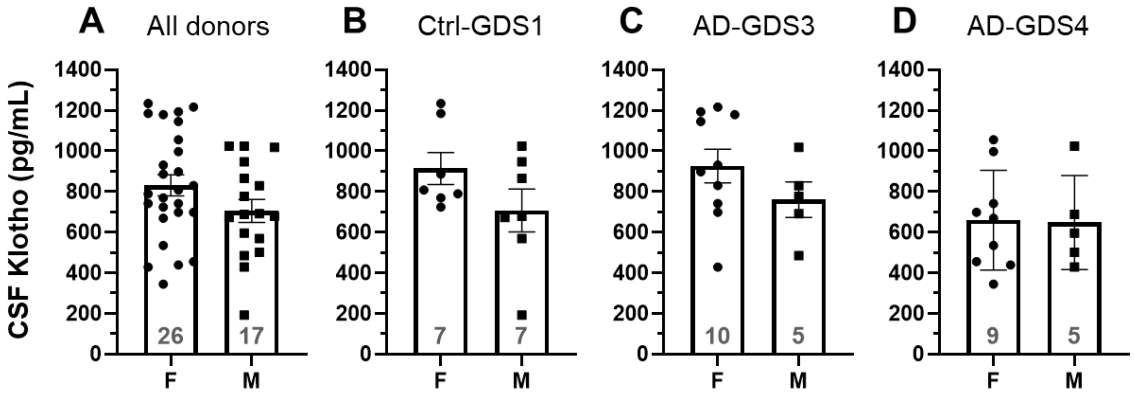

Figure 28. KL concentration in CSF of women *versus* men at different cognition status according to the Global Deterioration Scale (GDS). (A) All donors independent of disease group, (B) Ctrol-GDS-1: cognitively healthy, (C) AD-GDS3: MCI, (D) AD-GDS4 MD. F: women, M: men. Mean differences between F and M analyzed by the t- test. Mean±SEM represented. Sample size indicated within the graph bars.

Then, we analyzed whether there exists a correlation between CSF KL and age considering the AD diagnosis and the sex of our donors. In healthy adults with no cognitive impairment (GDS1), we did not observe variations of CSF KL levels with age over 61 years old (Figure 29.A). Splitting the data according to sex revealed an increasing trend of CSF KL with age in elder women, while in men tended to decrease. Nonetheless, the number of samples available was very low and those results were not statistically significant (Figure 29.C). In AD patients (GDS3 and GDS4), we observed a positive correlation of CSF KL with age that was statistically significant (r=0.4635, p=0.0113) (Figure 29.D). This correlation was stronger in men (r=0.9086, p=0.0007) than in women (r=0.3619, ns) (Figure 29.E).

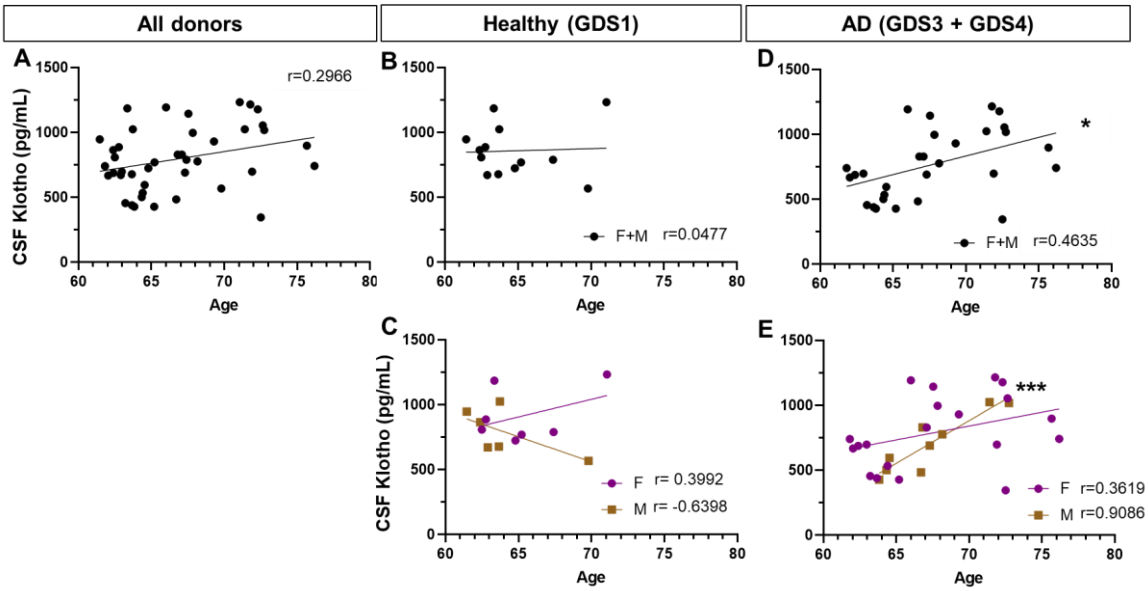

Figure 29. Correlation of CSF KL levels with age. A: all the donors with no sex nor GDS status distinction (p=0.0566); B, C: healthy subjects (GDS1); D, E: AD patients (GDS3 and GDS4). Sex distinction considered in C and E (F: females, M: males). Correlation analyzed by Pearson test (r= Pearson correlation coefficient). Statistically significant linear dependence denoted by *p < 0.05 and ***p < 0.001. Sample size (n): All donors (42); Healthy (Total:13, F:7, M:6); AD (Total:29, F:20, M:9).

2.3. Association of the soluble KL levels in CSF with APOE genotypes

Since the *APOE4* allele is the strongest genetic risk factor for developing AD [11], we next investigated the interactions between the KL levels in CSF and the APOE genotype in our donors. The APOE genotype of an individual is defined by two alleles, the most common of them being *APOE4*, *APOE2* and *APOE3*.

Interestingly, we found that individuals carrying the *APOE4* allele (either one or two copies) presented significantly lower levels of soluble KL in CSF (Mean±SEM: 540.1 ± 47.4 pg/mL) than individuals with no *APOE4* presence at all (792.5 ± 52.3 pg/mL) (p=0.0081), independent of the GDS status (Figure 30.A). Next, we examined the levels of soluble KL in CSF depending on the *APOE* genotype considering the two alleles in all the donors. We found statistically significant differences in the soluble KL levels between the different APOE genotypes regardless of the GDS stage (One-way ANOVA, p=0.0201). Individuals carrying two *APOE3* alleles in homozygosity (*3+3*) presented the highest KL concentration in CSF (831.3 ± 55.55 pg/mL), whereas the carriers of *APOE3* in heterozygosity with *APOE4* (*3+4*) presented the lowest (491.2 ± 38.31). Furthermore, there were significant differences between the carriers of the *APOE4* allele in homozygosity (*4+4*; 637.9 ± 103.0 pg/mL) *vs*

heterozygosity with allele *APOE3* (*3+4*) (Tukey *post-hoc*: p=0.0031) (Figure 30.B). Unfortunately, we could not analyze carriers of the *2+2* nor the *2+4 APOE* genotypes.

Finally, we studied whether soluble KL levels in CSF are influenced by the APOE genotype in patients with MD (AD-GDS4). No differences in the KL levels were found among our AD-GDS4 samples depending on the presence of the *APOE4* allele (Figure 30.C) nor on the *APOE* genotype (Figure 30.D). In the GDS4 group, the number of samples available was 10, so the sample size in some groups resulted in n=2, which was insufficient to detect differences. Unfortunately, we did not have at our disposal the APOE genotype of the GDS3-AD patients, so this group could not be analyzed in this regard.

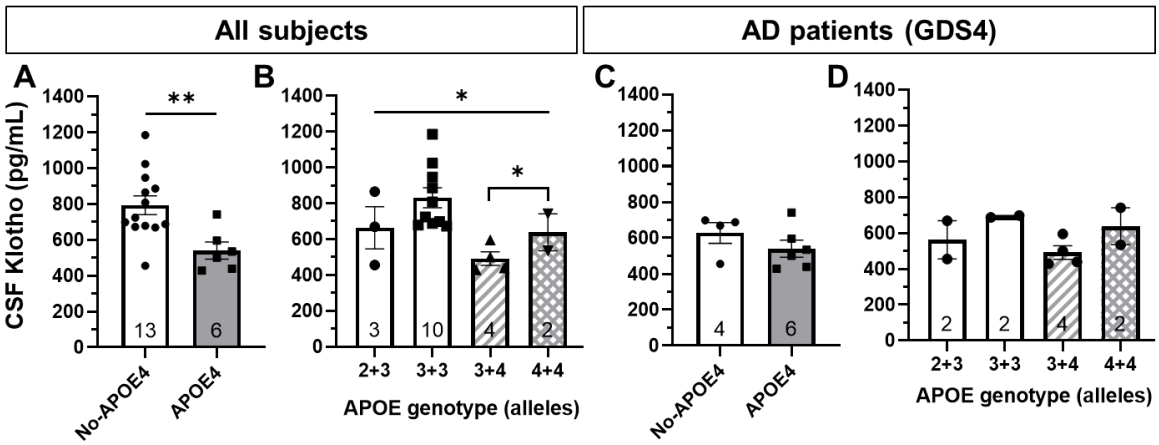

Figure 30. Levels of soluble KL in CSF of in all the subjects (A, B) and in AD-GDS4 patients (C, D), stratified by the presence of the *APOE4* allele (A, C) or the APOE genotype (B, D). No-APOE4: non-carriers of the APOE4 allele; APOE4: carriers of either one or two copies of the APOE4 allele. APOE genotype defined by the combination of two *APOE* alleles: 2=*APOE2*, 3=*APOE3*, 4=*APOE4*). Individual dots represent individual subjects. Mean±SEM is represented. Differences between two groups analyzed by t-test (A, C), and between four groups by One-way ANOVA and Tukey post hoc (B, D): *p<0.05, **p<0.01. Sample size indicated within the graph bars.

DISCUSSION

KL is known to have neuroprotective and anti-aging properties, and its deficiency in the CNS is associated with cognitive dysfunction and dementia [116], [165]. However, the role of KL in age-related neurodegenerative disorders like AD remains to be elucidated, and the relative contribution of the KL variants in the human CNS is still unknown. On this basis, the present study aimed to characterize the relative gene expression of the alternative transcript variants, sKL and mKL, in relevant regions of the human brain, both in healthy and AD conditions. Moreover, to further decipher the involvement of KL in AD, we analyzed the protein levels in human CSF and studied the correlation with other AD-related factors like aging, sex or the APOE genotype.

1. The expression profile of sKL and mKL is not homogeneous in the human brain

First, we confirmed that in humans, *KL* is predominantly expressed in the kidney, as described in other species [127], [137], and that mKL is about 3 times more abundant that sKL in this organ, in agreement with [281]. Interestingly, our gene expression analysis in different regions of the human brain revealed for the first time that the sKL transcript was significantly more abundant than mKL in the parenchymal areas: frontal cortex, entorhinal cortex, hippocampus, and amygdala. Oppositely, in the choroid plexus, mKL expression was higher than sKL.

The homology in the sKL/mKL ratio found in choroid plexus and kidney could be attributed to the analogy in cell composition, gene expression and function of these two tissues[294], [295]. The choroid plexus, located in the brain ventricles, produces the CSF and proteins that support the CNS physiology, among other important functions [296]. In this sense, similar to the kidney producing the soluble KL found in serum, the choroid plexus produces the soluble KL for the CSF [297]. Nonetheless, we cannot take for granted that the soluble KL protein present in CSF derives from the predominant transcript mKL, as other post-transcriptional and/or translational mechanisms could take place in the benefit of the sKL protein expression and/or secretion. Nowadays, the relative contribution of each KL protein variant to the CSF composition remains to be fully elucidated, since there are no available antibodies that differentiate sKL from the other soluble KL proteins derived from mKL.

Be that as it may, we demonstrated that in humans sKL is the predominant variant expressed in cortex, hippocampus and amygdala, brain regions involved in cognition,

memory, and anxiety, suggesting an important role of sKL in these neurological functions and/or neurological disorders in which those are affected, like AD. In addition, the different expression profile of the KL variants in these tissues hints towards a different role for mKL and sKL in the human CNS. In this line, Lu et al. reported that increased sKL transcript levels correlated with progression and risk of ovary cancer and increased IGF-1 expression, whereas this correlation was not observed for mKL, suggesting different functions for each KL variant [298].

In light of these findings, we do not totally agree with Mencke et al. suggesting that "the sKL transcript is not translated to protein, but instead is a target for nonsense-mediated mRNA decay (NMD) resulting in the downregulation of mKL" [281]. While this mechanism may occur in kidney during renal disease, as they report, we hypothesize a more important role for sKL in the human brain, as it is the predominant variant expressed in this organ. Nevertheless, the sKL protein has not been detected yet in the human CNS, in our judgement, due to the aforementioned technical limitations. In mice, though, the sKL protein was directly detected in brain homogenates using a new polyclonal antibody generated by our group (KL-113) in a previous work. In addition, our group found that the sKL protein was ten times more abundant in the brain than in the kidney of mice, suggesting that the two isoforms may have different functions [132].

Importantly, this was the first time that the relative expression of sKL *vs* mKL was described in the human frontal cortex, entorhinal cortex, amygdala, and choroid plexus. Previous to our work, the sKL transcript had been detected in human tissues, including kidney and hippocampus, when the *kl* gene was first identified by Matsumura et al. [127]. They reported the sKL transcript variant to be more abundant than mKL in all the tissues analyzed, including kidney, which is inconsistent with recent reports [281] and our own results. Moreover, they evaluated the sKL *vs* mKL ratio through an RNAse protection assay in clones isolated from cDNA human libraries, particularly 6 clones from kidney and 4 from hippocampus. In our view, the methodology, the source of human samples and the sample size used in our work are more robust and expected to report more accurate results. In particular, we directly obtained more than 100 RNA samples from human tissues and analyzed them by RT-qPCR using TaqMan probes, one of the most reliable technologies to quantify gene expression, besides RNA-Seq. It is worth noting as well that none of the RNA-Seq databases available are able to differentiate between expression of the full-length mKL transcript and the alternative sKL transcript [137].

2. The relative gene expression of sKL and mKL is altered during AD

In AD patients, sKL was the predominant transcript in the parenchymal brain areas analyzed, similar to the humans with no neuropathological lesions. Nonetheless, clinically silent AD patients presented an elevated sKL/mKL ratio in frontal cortex and hippocampus, two areas affected in AD pathology. These alterations at the onset of the AD pathology show parallelism with the accumulation of protein aggregates; as the Aβ plaque first appears in the isocortex, the most affected area, and NFT deposition starts in the allocortex of the medial temporal lobe, which includes the hippocampus [30]. In subsequent AD stages (AD III/IV), the expression values observed in AD I/II were not maintained nor increased, suggesting that it may exists a compensatory mechanism to recover KL expression, although the levels found in NNL were not reached. Whether *KL* dysregulation contributes to the AD onset, or on the contrary, it is a consequence of the pathology, remains unclear.

Interestingly, in the choroid plexus of AD patients, we observed similar relative expression of sKL and mKL, in contrast to healthy individuals where mKL predominated. The gene expression of both *mKL* and *sKL* increased in the choroid plexus of AD patients, although sKL increased to a higher extent, so the resulting mKL/sKL ratio was close to 1. It is worth noting that the donors of choroid plexus were at more advance stages of AD (IV-VI) than those of the parenchymal areas. Therefore, further samples of different AD stages should be analyzed to compare *kl* expression between areas and AD stages.

3. The gene expression profile of KL in brain is not uniform among species

Because the mouse is the most used animal model in preclinical research, we aimed to characterize the relative expression of sKL and mKL using a similar approach to humans. Herein, we used 13-month-old C57BL/6 (WT) and 3xTg-AD mice as models of healthy adults and AD, respectively. We analyzed the *kl* gene expression in kidney because it is the main source of KL in mouse [108]; the frontal cortex, entorhinal cortex, and hippocampus because of their role in learning and cognition, and in the cerebellum, because of the high expression of *kl* described in Purkinje cells [113].

In agreement with other studies [128], [132], mKL was the predominant transcript variant in kidney, over 30 times more abundant than sKL, both in WT and 3xTg-AD adult mice. In the mouse brain, mKL was the predominant transcript variant consistent with previous data [132], [299]. However, the differences in the relative amount of mKL *vs* sKL were less abrupt

than in kidney, ranging 6- to 12-fold depending on the brain region, in agreement with [132]. In frontal cortex and cerebellum, the relative mKL *vs* sKL expression was more homogeneous than in entorhinal cortex and hippocampus, indicating that the expression profile of the *kl* gene was not uniform throughout the mouse brain and that the two KL variants may have a different regulation and/or function, as previously suggested [132].

In the 3xTg-AD mouse model, the mKL/sKL ratio was over 20 in entorhinal cortex and hippocampus, whereas in WT it did not reach 13 in those areas. The increased proportion of mKL *vs* sKL might be due to a decreased expression of sKL in the 3xTg-AD, considering the data reported by Massó et al. [132]. This altered *kl* expression in entorhinal cortex and hippocampus may be associated to the AD pathology, as these areas are importantly affected during the disease. While the mKL/sKL ratio in frontal cortex was relatively homogeneous between 3xTg-AD and WT, in cerebellum it was highly variable for the 3xTg-AD. Since *kl* is highly expressed in the cerebellum [113], this observation could indicate a different regulation of sKL and mKL under neuropathological conditions, and/or different functions for each variant.

Consistent with previous research, this work proves that the expression profile of sKL and mKL is different in humans and mice [127], [128], indicating that the gene expression of *KL* may be differently regulated, and/or that sKL and mKL may have different functions in each species. In this regard, in rats only the mKL transcript has been detected, whose levels vary during early postnatal development in cortex and hippocampus, among other tissues [134], [300].

In a non-published study conducted in the Microcebus model (personal communication), the mKL transcript was highly predominant in kidney, same as humans and mice. In cerebral cortex though, the mKL/sKL ratio was close to 1, indicating similar expression levels of mKL and sKL in this organ, although mKL was slightly more abundant. Therefore, the relative expression of the KL variants in brain found in Microcebus (mKL/sKL around 1) are in between the values observed in mouse (mKL/sKL over 10) and humans (sKL/mKL around 2). In other words, while mKL is predominant in mouse and sKL is predominant in humans, in Microcebus both variants are expressed at a similar level. In Microcebus resembling AD pathology, both KL transcripts decreased around 3-fold in brain compared to the healthy subjects. The magnitude of the variation with AD was much higher in Microcebus than in mice and human patients. However, the mKL/sKL ratio was maintained around 1, indicating a similar sKL and mKL relative expression in cerebral cortex in this AD model.

Taken together, all these data indicate that the expression profile of *sKL* and *mKL* is not homogeneous through the different regions of the brain and among different species, and also that it is altered during AD. All this should be taken into account in studies using animal models, as the translatability of the results to humans could be compromised. In this sense, future studies involving KL should consider Microcebus as a relevant model, as the expression profile of *kl* in this specie is closer to humans than it is in mice.

To date, most of the research has been focused on the mKL variant, partly because it is the predominant variant expressed in kidney and it is highly relevant in the renal function and disease [301], but also because mKL is the most expressed variant in mouse models, in addition to the lack of antibodies that differentiate the sKL protein. However, this work reveals an important role of sKL in the human CNS, as it is the predominant variant expressed in brain regions involved in cognition and memory. In this line, sKL could also play an important role in neurological pathologies, like AD.

4. Soluble KL is decreased in CSF of Mild Dementia AD patients

In light of our previous results, we aimed to further characterize KL at the protein level in the CNS during AD. For this purpose, we analyzed the levels of soluble KL in CSF of AD patients and healthy controls. The donors had been evaluated for their cognitive performance and clinically visible symptoms and classified according to the Global Deterioration Scale (GDS) [57] .The GDS1 individuals had no cognitive decline nor memory deficits, so they were used as healthy controls. The GDS3-AD patients presented MCI, the first stage in which clinical deficits are easily identifiable, but still considered a pre-dementia stage. The GDS4-AD patients presented MD, the first of the four GDS dementia stages, in which patients present confusion, lack of concentration and memory deficits related to recent events and personal history. From the next stage (GDS5), individuals can no longer survive without assistance.

The ELISA kit used to quantify KL, detects the KL1 domain, present in all the KL variants. Therefore, in CSF we would detect ‘soluble KL’, which includes the secreted sKL and the pKL forms (KL1 and KL1+KL2) cleaved from mKL [293]. Whilst characterizing the protein profile of the KL variants in CNS was of high interest, there was no tool available for this purpose, since to our knowledge there were no existing antibodies that specifically detect the human sKL protein. Furthermore, the ELISA kit used was just validated for body fluids, so brain tissues could not be analyzed. On another note, it must be taken into account that

the age of our CSF donors was comprised between 61 and 76 years old, so the following conclusions apply to the elder population.

Remarkably, we found significantly decreased KL levels in CSF of AD patients with MD (GDS4) compared to the cognitively healthy controls (GDS1), in agreement with Semba et al [135].

Because the proteins present in the CSF are produced in the choroid plexus, we would expect that the levels of gene expression in this tissue correlate with the levels of protein in CSF. However, it must be taken into account that the donors of CSF were staged according to their cognitive status (GDS), whereas the donors of choroid plexus were classified according to neuropathological tau depositions assessed during brain autopsy (Braak staging). Besides, the AD donors of choroid plexus (AD IV-VI) were probably at a more advance stage of the disease than those of the CSF (GDS4). Herein, to study the association between CSF protein levels and choroid plexus gene expression, matching samples from the same donors should be analyzed.

Previous to our work, only Semba et al (2014) had reported decreased CSF KL levels in AD patients [135]. However, it should be noted that in that study, KL CSF levels were correlated to the Mini-Mental State Examination (MMSE) score [302] considering all the participants, independent of their AD diagnosis. While it is truth that the average MMSE score of AD patients (22.1) was lower than that of healthy adults (28.6), that correlation did not consider the AD status of the individuals analyzed.

In AD mouse models, KL protein levels in hippocampus were reported to be lower in hAPP mice than in controls [165], and our group had observed decreased sKL and mKL gene expression in the 3xTg-AD model compared to WT [132].

5. The KL CSF levels are similar in elder men and women

We did not observe significant differences in CSF KL levels in men *versus* women of advanced age. That was the reason why we did not consider the *sex* variable and analyzed men and women samples jointly to gain statistical power. Nonetheless, sex differences should be always primarily assessed in any study, especially in those involving AD, in which the incidence is higher in women [12].

Previously, Semba and colleagues reported that CSF KL concentrations are lower in females compared with males [135]. However, the age and AD status of the subjects analyzed was not considered to assess the KL levels in men vs women in that study, whereas our data refers to elder individuals. Taking this into account, and because KL is an age-related molecule, it would be interesting to study the KL levels in men vs women considering the age.

6. CSF KL levels increase with age during AD in the elderly

Since KL is known for its as anti-aging properties [303], we aimed to investigate whether KL CSF levels vary with age in elder individuals with and without AD.

In the healthy elderly, CSF KL levels were constant despite the age. However, in elder AD patients, we observed increasing CSF KL levels with age, especially in men. To our knowledge, this was the first time that KL levels in CSF were correlated with age considering the AD status in humans. In adults with normal cognition, Semba et al. reported that CSF KL levels are lower in older (average age 76) *vs* younger (average age 31) adults [135]. The old *vs* young decreased KL expression in brain is well documented in other mammal species including rhesus monkey, mouse and rat [132], [133], [304].

In 3xTg-AD mice, our group had previously reported decreased gene expression of *kl* in brain parenchyma [132]. All this does not conflict with our findings since KL in the CSF is produced in the choroid plexus, and as we observed in previous sections, *kl* expression in this tissue seems to have a different regulation than in other parenchymal regions of brain.

Taken together, our results suggest that CSF KL levels increase with age in the presence of AD pathology in elder individuals. This hypothesis would be consistent with our results of gene expression in choroid plexus, in which *kl* gene expression appeared increased in AD patients, all of them older than 70 years old and at advanced AD stage (IV-VI). The decreased CSF KL levels observed in GDS4-AD patients could be explained because in this AD group, almost the 80% of the patients were below 70 years old (n=11). Therefore, in those AD patients, decreased CSF KL levels would be associated with the presence of AD pathology, as suggested by others [135]. However, in elder population, increasing aging in the presence of AD pathology would trigger KL upregulation, probably as a neuroprotective response to counteract the neuropathological damage caused by the combination of aging and AD progression. On this basis, the increased *kl* gene expression

in choroid plexus could be a compensatory mechanism to recover the decreased KL protein levels in CSF during the AD onset.

While the age-dependent KL downregulation may be a consequence of the normal aging process, the age-dependent upregulation in choroid plexus of elder AD patients may be a neuroprotective mechanism to counteract the damage caused by the progression of the AD pathology. In support of this neuroprotective role, Chen et al. proposed that KL produced by the choroid plexus may protect myelin integrity and prevent myelin degeneration in the aging brain [112]. Nonetheless, further donors at diverse AD stages should be analyzed to properly correlate the levels of CSF KL with AD progression considering age.

In summary, our results suggest a different regulation of KL expression, both at the gene and protein level, at different stages of the AD pathology. Herein, the role of the soluble forms of KL in AD and aging should be further investigated.

7. The APOE4 allele is associated with lower KL levels in the human CSF

To further explore the role of KL in AD, we investigated the association between KL levels in CSF and the *APOE* genotype, since the *APOE4* allele is the strongest genetic risk factor for developing late onset AD [305].

A recent study reported that individuals carrying the *APOE4* allele present less risk of developing AD when they also carry the KL-VS allele in heterozygosity. This KL genotype is associated with higher levels of circulating KL protein and better cognitive function in humans [306]. Another work associated the KL-VS allele with better cognition independent of the *APOE4* allele status [116]. Taking all this data together, we would expect that increasing KL levels would be associated with less AD incidence, even in the presence of risk factors like the *APOE4* allele. Although we did not have the KL genotype of the donors at our disposal, we had obtained the actual levels of soluble KL in CSF.

Importantly, we found that the *APOE4* allele was significantly associated with lower KL levels in CSF, independent of the GDS score of the donors. Carrying one copy of the *APOE4* allele increases the risk of AD by 3-fold; and 2 copies increases it by more than 12-fold. Conversely, the *APOE2* allele is believed to provide some protection against the AD [306]. Unfortunately, we had very few samples of APOE2 carriers, as this allele is relatively rare among population. The reduced KL levels seemed to be associated to the *APOE4* in

heterozygosis with the *APOE3*, the most common allele among population that is thought to have a neutral role in the risk of AD.

To explore the relationship of KL levels with the risk of developing AD associated to the *APOE4* allele, we analyzed the CSF KL in MD patients (GDS4) stratified according to their *APOE* genotype. Unfortunately, we could not make any conclusion due to the low sample size, as we only had the *APOE* genotype of 10 AD-GDS4 patients, resulting in some groups n=2. Nonetheless, our results confirmed that the *APOE4* allele is associated with decreased CSF KL levels, although the molecular mechanisms behind the risk of developing AD remain to be elucidated. One hypothesis could be that the *APOE4* variant downregulates KL expression, resulting on decreased KL levels and decreased neuroprotection, herein favoring AD progression. Another possibility could be that KL could protect from the development of AD to a higher extent when highly expressed, for instance as a consequence of the KL-VS allele, counteracting the effects of the *APOE4* allele. As an alternative hypothesis, decreased KL levels in CSF could be a consequence of the AD pathology, in which case KL could be a diagnose biomarker of the pathology.

Further research is needed to unravel the beneficial role of KL in decrease the risk of developing AD associated to the APOE genotype. In addition, whether the *APOE4* allele in heterozygosis is associated with decreased CSF KL should be further confirmed in a more exhaustive study including larger sample sizes and individuals carrying the *APOE2* allele in heterozygosis with the *APOE4*.

8. Closing remarks

In the present study, sKL has been detected for the first time in relevant regions of the human brain, where in addition, it was the predominant variant expressed over mKL, suggesting an important role of sKL in the human CNS. Our results also suggest a different regulation for sKL and mKL in different tissues and among different species, indicating different functions for each variant and possibly a different relevance in each species. Furthermore, under AD conditions, we found altered KL expression both at the gene and protein levels, as well as a negative correlation with the *APOE4 allele*, an important risk factor of AD. Although it is not clear whether altered KL levels are a cause or a consequence of the pathology, our results point in the direction of an important role for KL in AD. The KL upregulation observed in choroid plexus during AD could be a compensation mechanism to

increase KL levels in CSF and generate neuroprotection against neuropathological symptoms. In that case, KL would be a promising therapeutic target to treat AD.

CHAPTER 2

In vivo study of AAV9-mediated sKL expression in AD mouse models

RESULTS

Based on the neuroprotective and cognition-enhancing properties of KL [116], [138], [166] and our previous results, we explored the therapeutic potential of KL to counteract cognitive deficits associated to AD in two mouse models: the 3xTg-AD and the APP/Tau. For this purpose, we overexpressed KL in the CNS using AAV vectors.

In light of our findings in human brain, we were particularly interested in the secreted isoform of the KL protein (sKL). To overexpress it in the mouse CNS, we generated an AAV9 vector encoding the cDNA of the sKL mouse variant (AAV9-sKL) and administered it to the lateral ventricle of mice brain by stereotaxic injection. A control group of mice were similarly transduced with an AAV9-null, carrying an irrelevant DNA sequence that does not generate any transcript, so these mice would experience the same anesthesia and surgical process of AAV administration without expressing any transgene.

The cognitive functions were assessed *in vivo* through different behavior and memory tests, performed at different days. Afterwards, mice were euthanized, brains were dissected, and tissues were collected for biochemical and histological analysis.

A similar experimental design was implemented for the two *in vivo* experiments using the 3xTg-AD and the APP/tau AD mouse models, with some particularities in each study further explained in the next sections.

1. *In vivo* study of AAV9-sKL gene transfer in 3xTg-AD mice

1.1. Experimental design

Originally, in this study we aimed to explore the therapeutic potential of the two KL isoforms (mKL and sKL) in 3xTg-AD mice, since the cognitive enhancing properties had not been attributed to any specific KL variant. Unfortunately, the RT-qPCR analysis of transgene expression after euthanasia revealed no AAV-mediated mKL expression in brain (data not shown), so we decided to invalidate this group and all the 3xTg-AD mice injected with the AAV9-mKL vector were excluded from the analysis.

Here, we present the effect of AAV9-mediated sKL expression in 3xTg-AD female mice. In our engineered AAV9, the expression of the sKL cDNA was under the control of the cytomegalovirus (CMV) promoter (Figure 31). At 6 months old, the AAV9 vectors were administered to every mouse at a dose of $4.7x10^{10}$ vg in a single injection to the lateral brain ventricle. Based on the titer of the AAV9 produced, this was the maximal dose that could be administered in the volume admitted in a single injection. Six months following AAV9 administration, cognitive functions were assessed by the Open filed, NOR and MWM tests. Once the behavior tests were finished, mice were euthanized, and brain tissues were collected for biochemical and histological analysis (Figure 32).

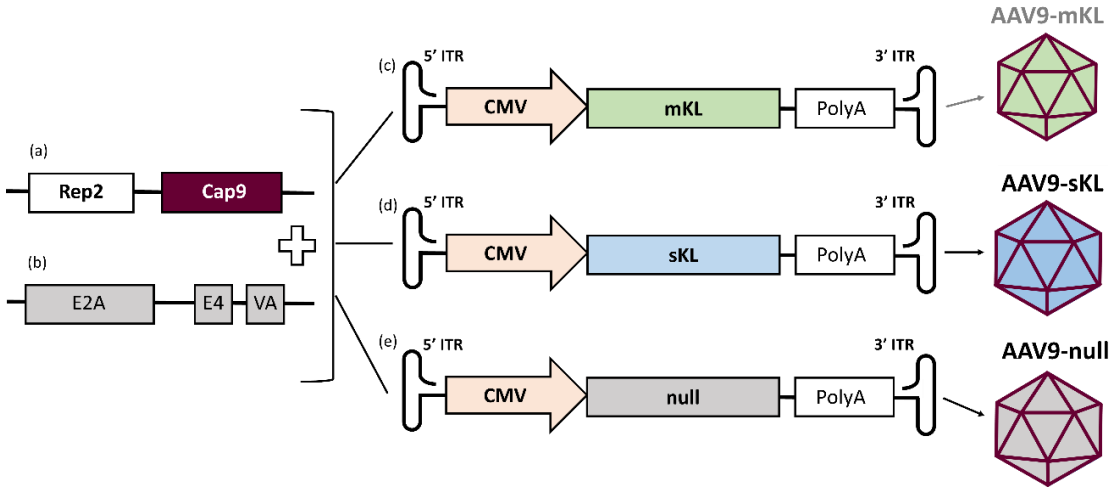

Figure 31. Genetic design of the plasmids for the production of the AAV vectors. The Rep2Cap9 (a) and the helper (b) plasmids were co-transfected into HEK293-AAV cells with the plasmid encoding the expression cassette in between the ITRs (c, d or e). Each transgene (mKL, sKL, null) was cloned under control of the CMV promoter and packaged into the AAV9 capsid (represented in purple).

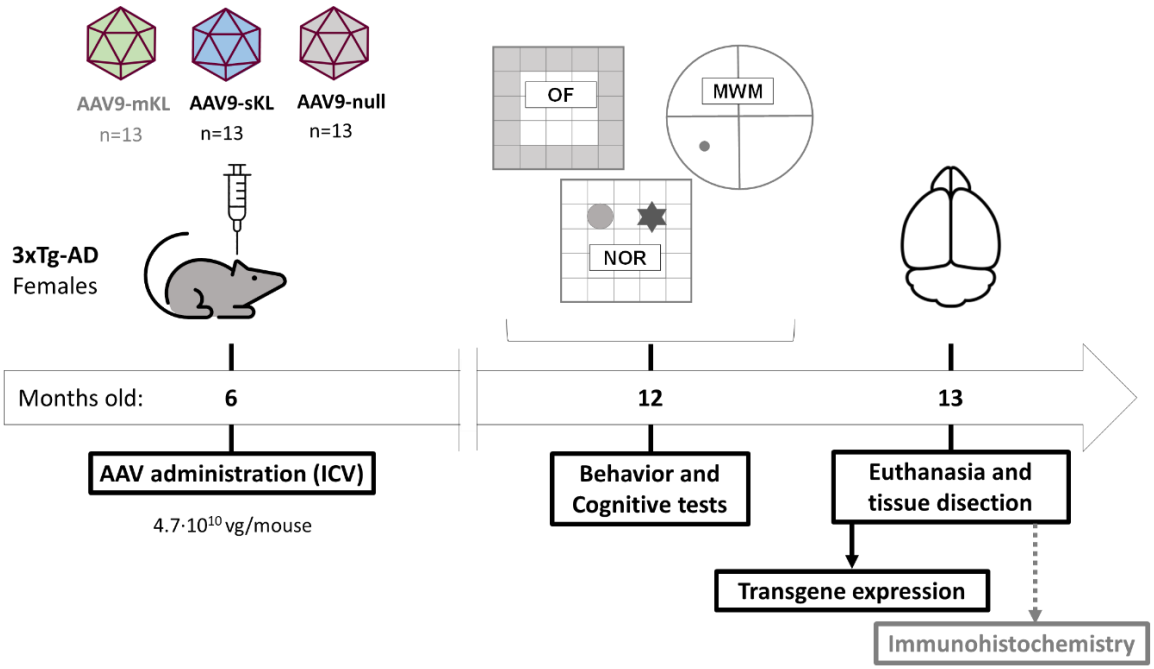

Figure 32. Experimental design of the in vivo experiment with the 3xTg-AD mouse model. Three experimental groups were stablished according to the transgene transferred I the AAV9 vectors: mKL, sKL and null sequence (control). The number of mice injected in each experimental group is indicated in the figure (n). The sample size at the end point of the experiment was reduced due to deaths during the surgical procedure and the 6 months stabling. The resulting sample size (n) of the animals tested per treatment group was: mKL=9, sKL=10, null=9.

1.2. Behavior tests

First of all, sensorimotor functions including visual and hindlimb reflexes, equilibrium and strength were assessed in all mice by different tests, explained in the Methods section. All the mice showed similar results (data not shown), indicating that sKL expression did not affect sensorimotor capabilities in 3xTg-AD mice. Therefore, we assumed that both sKL-treated and control groups presented the same physical conditions in the analysis of the subsequent behavioral tests, so any differences would be attributed to behavioral and/or cognitive functions.

1.2.1. Open Field

The Open field test was developed to study anxiety-like behavior and exploratory activity and is most often used in mice to measure general locomotor activity qualitatively and quantitatively. In this experiment, we analyzed the percentage of time immobile and thigmotaxis. Mice considered as outliers according to the criteria stablished in the Methods

sections were discarded from the presented analysis and are not represented in the following analysis.

The percentage of time immobile represents the amount of time of the test in which the mouse is motionless with signs of fear. This parameter was used as a measure of anxiety. The average time immobile was similar between both groups (p=0.92), indicating similar levels of anxiety-like behavior (Figure 33.A). The thigmotaxis is the tendency of mice to remain close to the maze walls, and it has been validated as an index of anxiogenic behavior in mice, increasing as anxiety levels rise [307]. Thigmotaxis was measured as the percent of the total test time that the mouse spent in area designed as 'exterior' *versus* the time percent spent in the 'center' (Figure 18.). The 3xTg-AD mice, both AD-null and AD-sKL, spent over the 85% of the test time in the exterior area and less than the 15% in the center. No differences were observed in the time spent in each area between the sKL and null groups (p=0.48), indicating similar levels of thigmotaxis. (Figure 33.B).

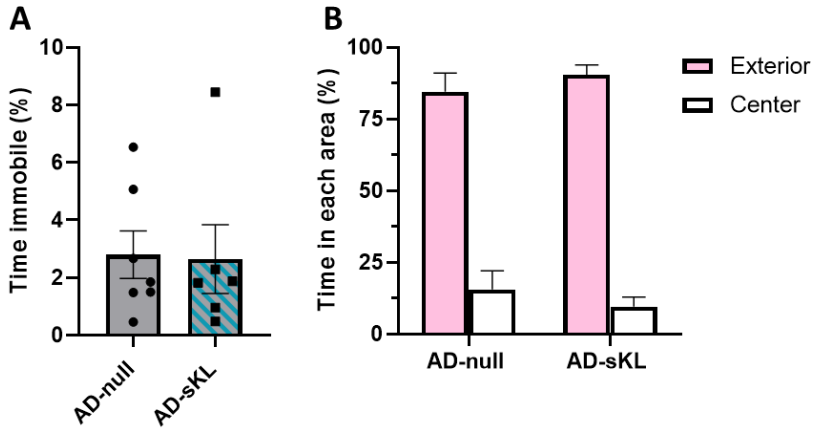

Figure 33. Parameters analyzed in the Open Field test. Percentage of time freezing during the test (A). Time spent in each area of the maze (exterior and center) (B). Differences between the sKL-treated and the null group analyzed by t-test (p<0.05). Mean±SEM represented. Sample size after removing outliers (n) in each parameter (A|B): AD-null = 7|6, AD-sKL = 6|5.

1.2.2. Novel Object Recognition

First, we measured the total time exploring objects, both in the familiarization and the memory assays, and used it as an exclusion criterion being mice exploring objects for less than 5 seconds excluded from the analysis. Only the mice that met the exploration requirement are plotted (Figure 34.A). No significant differences in the percent of time exploring objects were observed between the two groups, indicating that sKL expression did not alter the exploratory activity.

The preference index is a measure of preference for the novel object, being calculated as the percent of time that mice spent exploring the novel object out of the total time exploring objects. Both sKL-treated and control groups spent the majority if the memory test duration exploring the novel object, indicating that both groups recognized and showed preference for the novel object (Figure 34.B). No significant differences were observed between the groups in none of the NOR parameters analyzed.

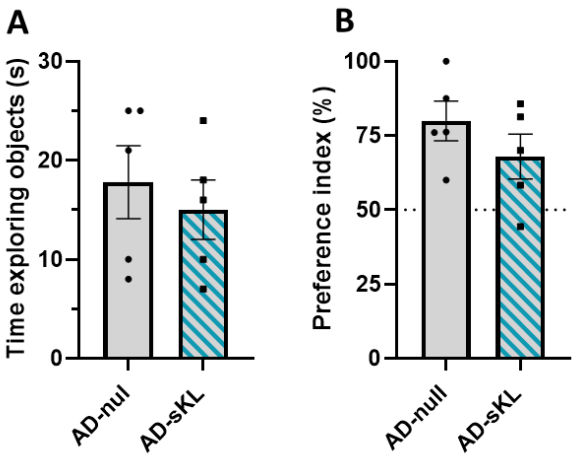

Figure 34. Parameters analyzed in the NOR test. (A) Time exploring either of the objects during the memory stage. (B) Preference index. Differences between the two groups analyzed by t-test. Mean±SEM is represented. Sample size after discarding outliers (n): AD-null=5, AD-sKL=5.

1.2.3. Morris Water Maze

During the learning phase with the hidden platform, both the latency (p=0.0045) (Figure 35.A) and the distance travelled (p=0.0003) (Figure 35.B) to reach the platform significantly decreased along the four training days in the two groups, indicating that 3xTg-AD mice learned the accurate position of the platform and developed suitable swimming approaches to reach it from random starting points within 60 s, independent of the treatment. The decrease in the latency and distance was statistically significant for the AD-sKL group on the last training day when comparing their performance with the two first days of hidden platform (day 2 vs day 5: latency p=0.0368, distance p=0.0003), suggesting an important improvement in the 3xTg-AD sKL-treated animals. The mean speed remained constant over the training days for both groups (Figure 35.C), indicating similar locomotor activity. No significant differences were found in these parameters between the two groups at any day nor at the end of the training, indicating that both AD-null and AD-sKL mice learned the task prior to the memory test.

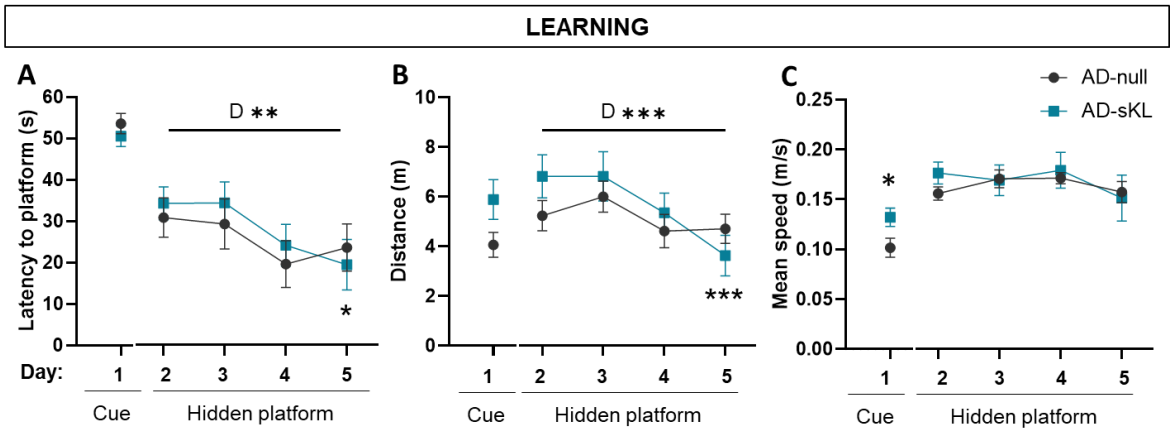

Figure 35. Learning curves in the MWM test for 3xTg-AD mice. Mean +SEM are represented. Data on day 1 (Cue) analyzed by T-test. Data on days 2-5 (Hidden platform) analyzed by 2-way ANOVA and Tuckey post-hoc (*p < 0.05, **p < 0.01, ***p < 0.001). Sample size after discarding outliers (n): AD-null=9, AD-sKL=10.

The short-term memory was tested two hours after the last training on day 5 in the so called 2 h probe trial, in which the platform was removed, and mice were recorded swimming for 60 s. The Any-maze software allowed us to segment the pool area into four quadrants (Target, Laterals and Opposite) and to demarcate the target, where the platform used to be located (Figure 21). No differences were observed in the mean speed during the 2h probe trial, indicating similar locomotor activity among the two groups (Figure 36.A). The sKL-treated mice showed lower latency to reach the platform (Figure 36.B) and higher number of entries to the target (Figure 36..C), despite differences not being statistically significant. The target quadrant of the pool was the most visited for both groups over the laterals and the opposite, as observed in the percentage of time and distance swam in this quadrant during the probe trial (Figure 36.D and E). Differences in the time and distance swam in the target versus the opposite quadrants were significantly higher for the AD-sKL group ($p < 0.0001$). It must be noted though, that the control 3xTg-AD mice also showed significant preference for the target, as observed in the higher time ($p=0.0002$) and distance swam ($p=0.0013$) in this quadrant compared to the opposite. This could indicate that the 3xTg-AD control mice could locate the platform and herein did not show profound short-term memory deficits. Although no statistically significant differences were detected between the AD-sKL and AD-null groups in the 2h probe trial, we can observe a slightly better performance in the sKL-treated mice in some of the parameters analyzed, suggesting a slight improvement in the short-term spatial memory retention following sKL-expression in 3xTg-AD mice.

The long-term memory was tested on day six, 24 hours after the last training session, in the so called 24 h probe trial. The analysis of the mean speed revealed no significant

differences in the locomotor activity between the two groups (Figure 36.F). Of note, the AD-sKL mice showed a better memory performance compared to the non-treated controls, as observed in the significantly decreased latency to reach the target ($p=0.0344$) (Figure 36.G), and the significantly higher number of entries to the target area ($p=0.0495$) (Figure 36.H). The AD-null group showed a similar percent of time and distance swam in all the quadrants, indicating no preference for any of the quadrants, which could be due to a slight long-term memory impairment (Figure 36.I,J). Conversely, sKL-treated mice showed preference for the target quadrant, being the distance swam significantly higher than the opposite ($p=0.0074$) (Figure 36.J). Taken together, these results suggest a better long-term memory in 3xTg-AD mice when overexpressing sKL.

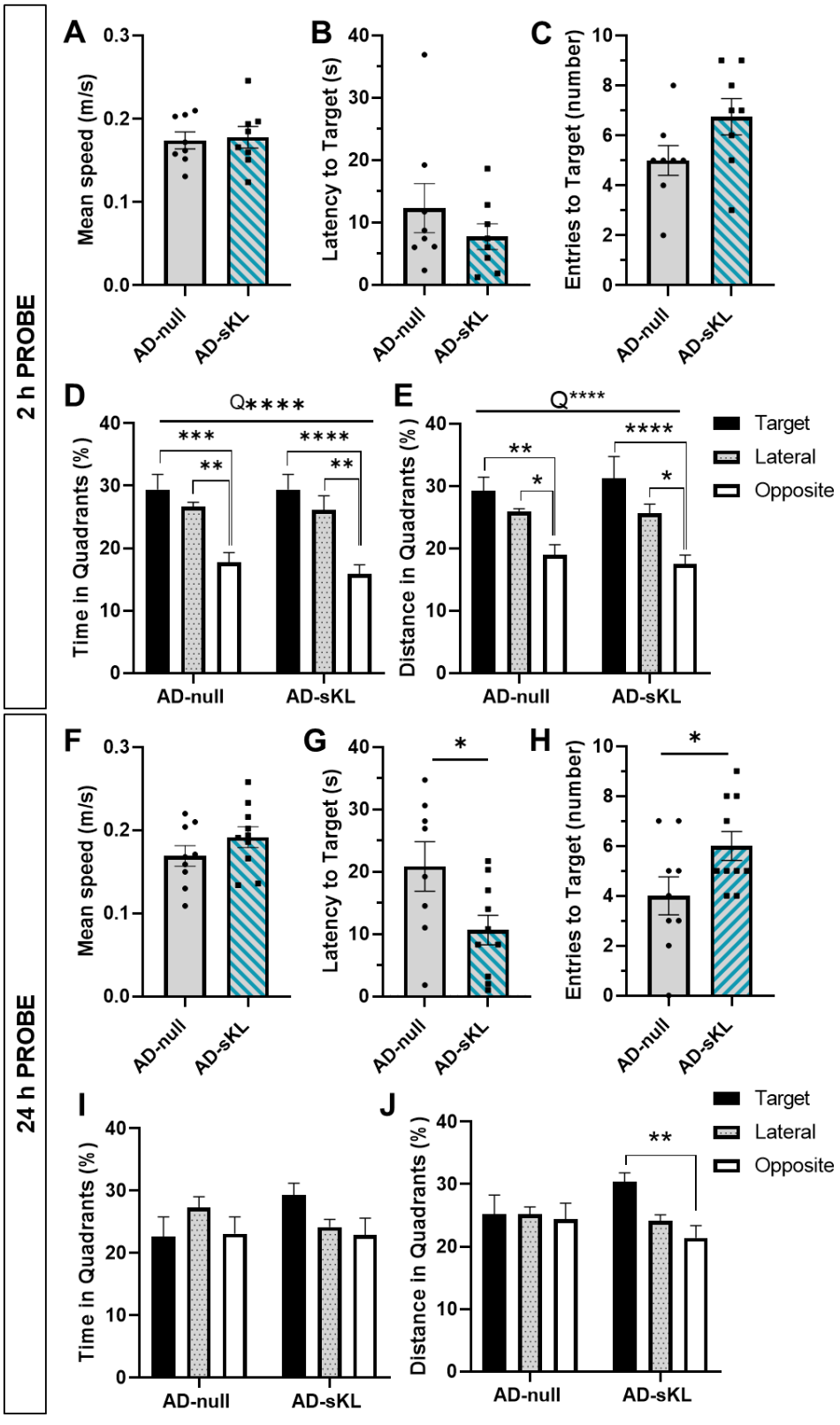

Figure 36. Parameters analyzed in the short-term (2h-probe: A-E) and long-term (24h-probe: F-J) memory tests of the MWM for 3xTg-AD mice. (A-C, F-H) Differences between experimental groups analyzed by t-test. (D, E, I, J) Differences between quadrants and experimental groups analyzed by Two-way ANOVA followed by Tuckey post-hoc (compares quadrants within groups) or Sidak pot-hoc (compares the two groups in each quadrant). *p < 0.05, **p < 0.01, ***p < 0.001, ****p < 0.0001. 'Lateral' represents the average data of the two lateral quadrants in the pool. Q: quadrant factor. Sample size after discarding outliers (n): AD-null=9, AD-sKL=9.

2. *In vivo* study of AAV9-sKL gene transfer in APP/Tau mice

2.1. Experimental design

In this study, we studied the effect of the AAV9-mediated sKL expression (AAV9-sKL) versus a negative AAV9 control encoding a null sequence (AAV9-null), in the APP/Tau AD model and WT control mice, resulting in four experimental groups (WT-null, WT-sKL, AD-null, AD-sKL).

For this experiment, the AAV9 were designed to encode the sKL cDNA under the control of the CMV enhancer fused to the chicken beta-actin (CAG) promoter (Figure 37). Besides, in the AAV production process, we concentrated the AAV preparations to obtain high AAV titers, which allowed us to administer a higher AAV dose ($1.1 \cdot 10^{11}$ vg/mouse) compared to the 3xTg-AD experiment ($4.7 \cdot 10^{10}$ vg/mouse). The AAV9 were administered to the lateral brain ventricle at 3 months of age. Learning and memory functions were assessed 4 months later by the following tests: Open Field, T-Maze, NOR and MWM. Afterwards, mice were euthanized, and brain tissues were collected for biochemical and histological analysis (Figure 38).

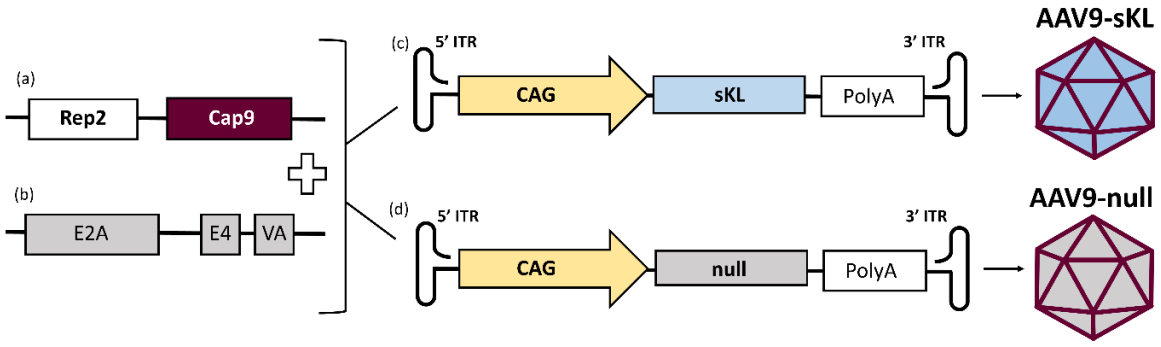

Figure 37. Genetic design of the plasmids for the production of the AAV vectors. The Rep2Cap9 (a) and the helper (b) plasmids were co-transfected into HEK293-AAV cells with the plasmid encoding the expression cassette in between the ITRs (c or d). Each transgene (sKL and null) was cloned under the control of the CAG promoter and packaged into the AAV9 capsid (represented in purple).

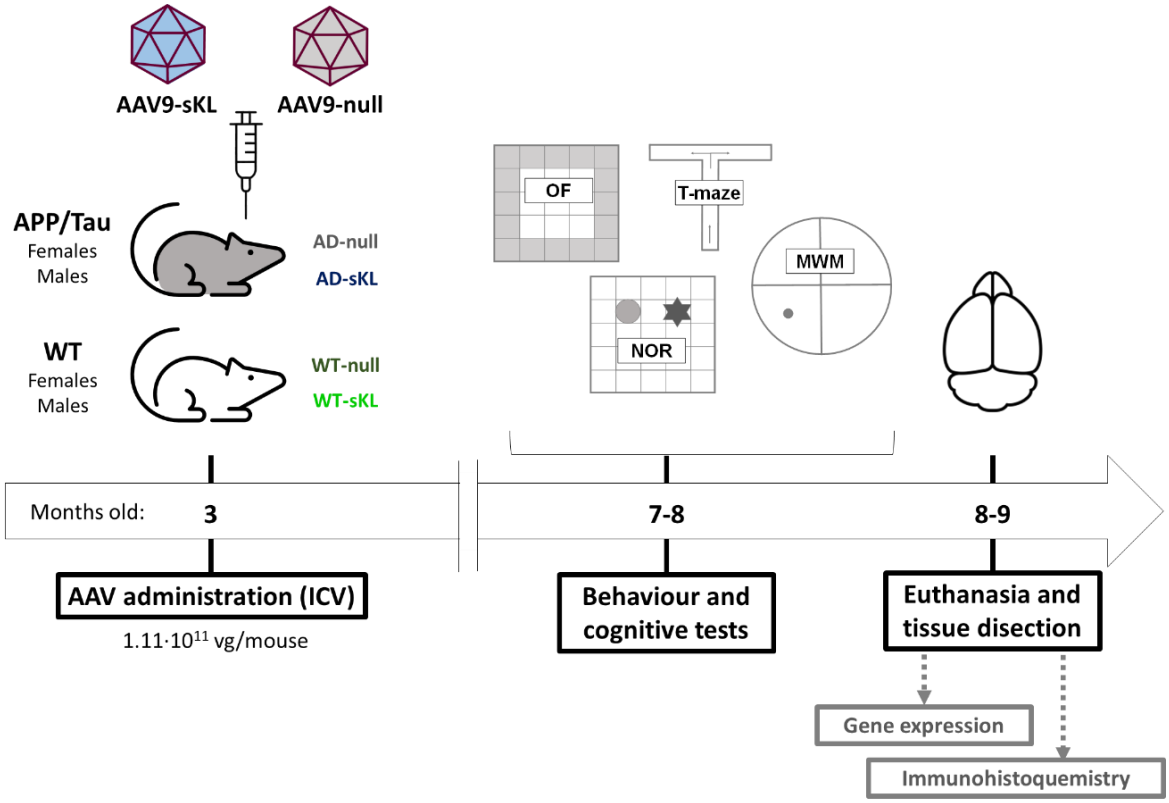

Figure 38. Experimental design of the in vivo experiment with the APP/Tau mouse model. Four experimental groups were stablished according to the genotype (APP/Tau AD or WT control) and the AAV9 treatment (sKL or null control): WT-null, WT-sKL, AD-null, AD-sKL. Females and males were analyzed separately.

The high number of mice that the experimental design required made hard to obtain enough age-matched mice. For this reason, and because testing so many mice at the same time in behavior tests was not feasible, we performed two rounds of injections in two sets of mice, born in two consecutive periods. This way, we managed to test a high number of age-matched mice at two time points, according to the age and timings stablished in the experimental design. All the conditions, including the age of the mice, the AAV vectors, the dose, the administration procedure, the behavior tests protocols, and the relative timings, were maintained in the two sets. The results in the cognitive tests indicated no differences between the same experimental groups of the two sets, confirming the suitability of analyzing them jointly to increase the sample size and gain statistical power. In the behavior studies, male and female mice were tested separately to avoid sex bias.

The total number (n) of the injected mice in the two sets is represented in Table 13. The sample size represented in each analysis is different due to the death of 3 female mice prior to the endpoint of the experiment and the exclusion of outliers according to the stablished criteria for each test (specified in Methods).

Table 13. Number of APP/Tau mice injected considering the two sets of injections.

	Sex	Females		Males		
	Treatment	**null**	**sKL**	**null**	**sKL**	Total
Set 1	WT	5	2	6	2	35
	APP/Tau	5	5	5	5	
Set 2	WT	7	6	6	7	50
	APP/Tau	7	7	5	5	
Total	**WT**	**12**	**8**	**12**	**9**	**85**
	APP/Tau	**12**	**12**	**10**	**10**	
		44		**41**		

2.2. Behavior tests.

Prior to the cognitive tests, all the mice were tested for sensorimotor functions including visual and hindlimb reflexes, equilibrium and strength as previously explained. Results indicated that there were no sensorimotor differences due to genotype (WT or APP/Tau) nor sKL expression (data not shown). Therefore, we assumed that all the experimental groups presented the same physical conditions in the analysis of the subsequent behavioral tests, so any differences would be attributed to behavioral and/or cognitive functions.

2.2.1. Open Field

The Open Field test was performed following the same set up as in the 3xTg-AD study, with the addition of the Any-maze software that allowed us to automatically measure further parameters such as the mean speed, the distance and the time moving in each area. Mice considered as outliers according to the criteria stablished in the Methods sections were discarded from the presented analysis and are not represented in the following analysis.

All the female mice presented similar mean speed and total ambulatory distance (Figure 39.A, B), indicating similar locomotor activity independent of the genotype and the sKL treatment. Consequently, the analysis of the anxiety-like behavior based on the designated areas was simplified. The percent of time immobile was around the 20% for all the groups, indicating no differences in anxiety-like behavior in terms of freezing (Figure 39.C). The percentage of time (Figure 39.D) and the distance travelled in the center (Figure 39.E) did not show differences between groups. The time spent in the exterior area was over 87% for all the female groups, whereas the time spent in the center area did not reach a 12% (Figure 39.F). This reveals a high index of thigmotaxis or wall-hugging behavior for the females in this specific animal model. No significant differences between the time spent in the exterior

nor in the center were observed between groups. Overall, the open field test revealed similar anxiety-like behavior in all the female groups, independent of genotype and sKL treatment.

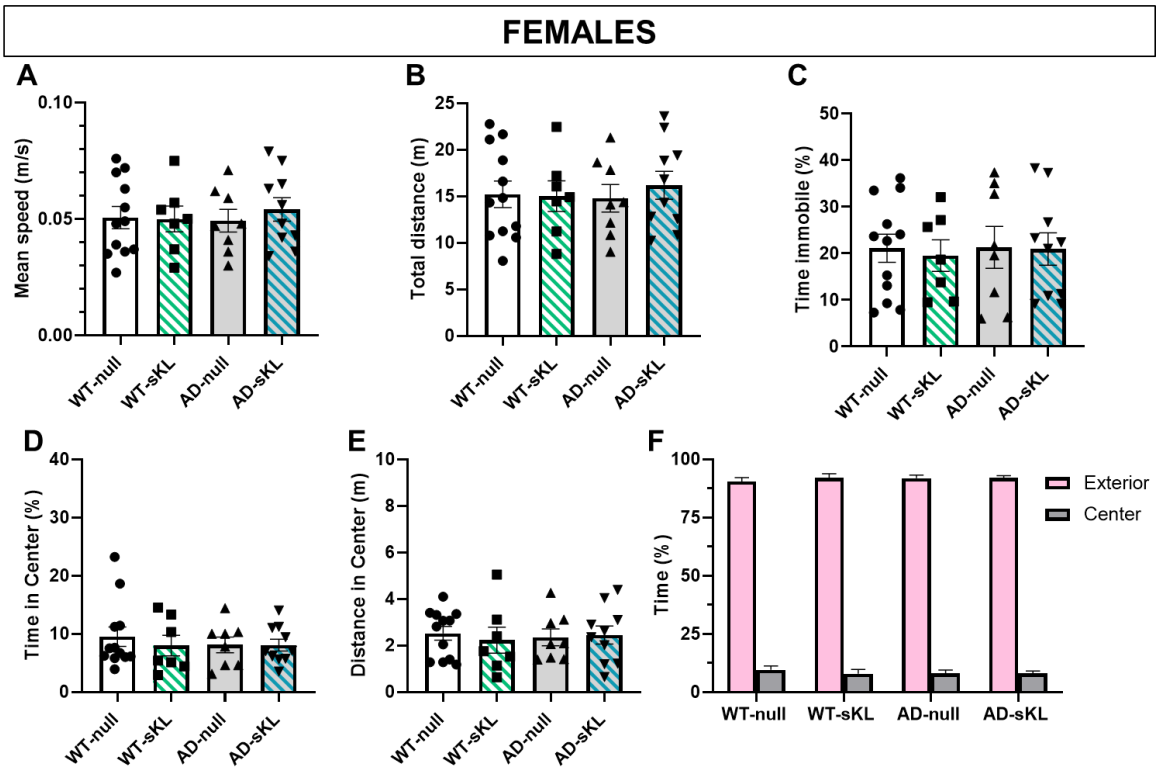

Figure 39. Parameters analyzed in the Open field test (Females). (A) Mean speed during the test for each animal. (B) Total distance travelled during the test. (C) Percentage of time immobile during the test. (D) Percentage of time spent in the center area. (E) Total distance travelled in the center area. (F) Comparison between the percentage of time spent in the exterior area versus the center. Dots represent individual mice. Bars and lines represent Mean±SEM per group. Differences between the mean of the groups analyzed by One-way ANOVA ($p<0.05$). Sample size per group after discarding outliers (n): WT-null=12, WT-sKL=7 AD-null=8, AD-sKL=10.

Male mice did not show significant differences in the mean speed and the total distance travelled (Figure 40.A, B), indicating comparable locomotor activity among the four experimental groups. The rest of the parameters analyzed (Figure 40. C, D, E), showed a high variability among males, but no significant differences in the mean were observed between the experimental groups. Similar to females, the males preferred staying in the exterior (over 75% of the time) than in the center, indicating an elevated level of thigmotaxis independent of the genotype and sKL treatment (Figure 40.F).

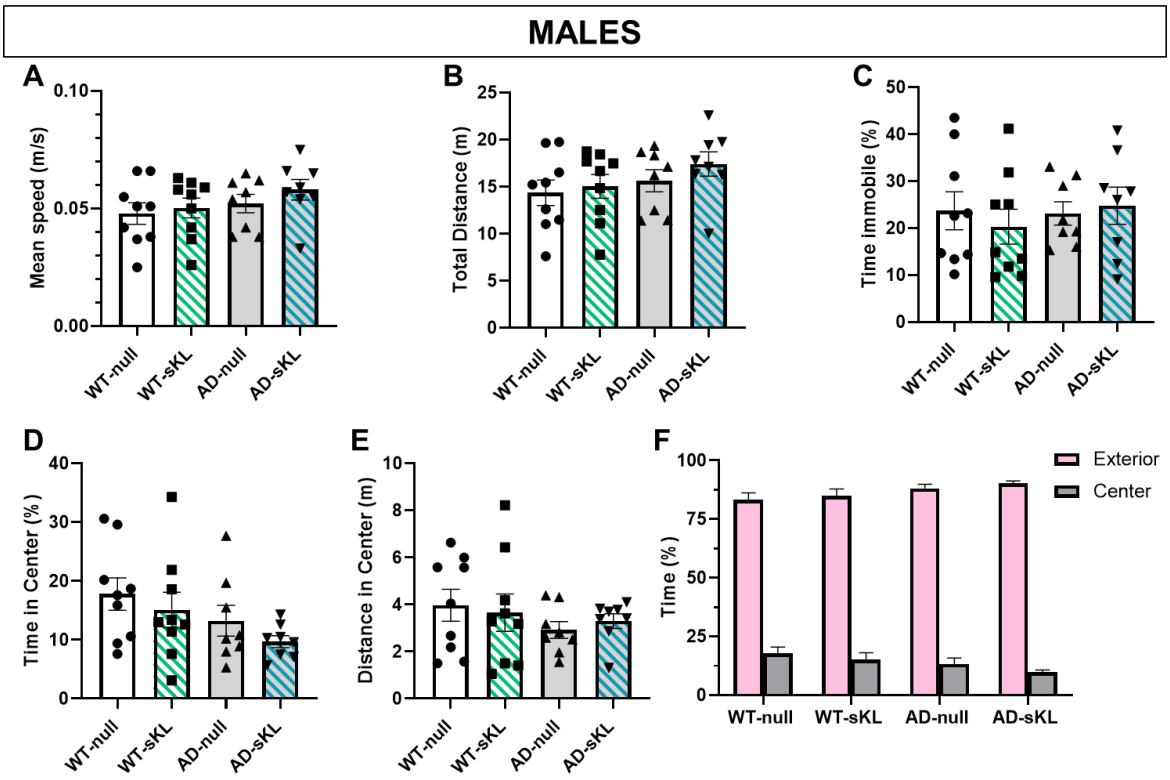

Figure 40. Parameters analyzed in the Open field test (Males). (A) Mean speed during the test for each animal. Mean per group is represented. (B) Total distance travelled during the test. (C) Percentage of time immobile during the test. (D) Percentage of time spent in the center area. (E) Total distance travelled in the center area. (F) Comparison between the percentage of time spent in the exterior area versus the center. Dots represent individual mice. Bars and lines represent Mean±SEM per group. Differences between the mean of the groups analyzed by One-way ANOVA ($p<0.05$). Sample size per group after discarding outliers (n): WT-null=9, WT-sKL=9 AD-null=8, AD-sKL=8.

Overall, both female and male mice presented a similar locomotor activity anxiety-like behavior in the open field test, independent of genotype and sKL treatment.

2.2.2. Novel Object Recognition

The Open Field test worked as a habituation step prior to the NOR task, that was subsequently performed to assess the short-term memory in mice. The protocol was similar to that performed in the 3xTg-AD study, with the addition of the Any-Maze software, that allowed us to automatically analyze further parameters. Besides, the time exploring both objects in the familiarization and memory assays was used as an inclusion criteria, being mice exploring objects for less than 5 seconds excluded from the analysis. Moreover, outliers were a priori defined as greater than 2 SDs above or below the mean to ensure

unbiased exclusion. Only the mice that met the inclusion criteria are plotted and considered in the statistical analysis below.

In the memory test, females spent similar time exploring objects independent of genotype and treatment (Figure 41Figure 40.A). The mean speed (Figure 41Figure 40.B), the total distance travelled (Figure 41Figure 40.C) and the percent of time immobile of the total test time (Figure 41Figure 40.D) did not show significant differences, indicating similar locomotor activity among all the female groups. The preference index (Figure 41.E) was slightly increased in the sKL-treated mice compared to their WT- and AD-null matching controls (a 20% and a 10%, respectively), indicating that mice overexpressing sKL showed increasing preference for the novel object than the non-treated controls, despite differences not being statistically significant (one-way ANOVA: p=0.43).

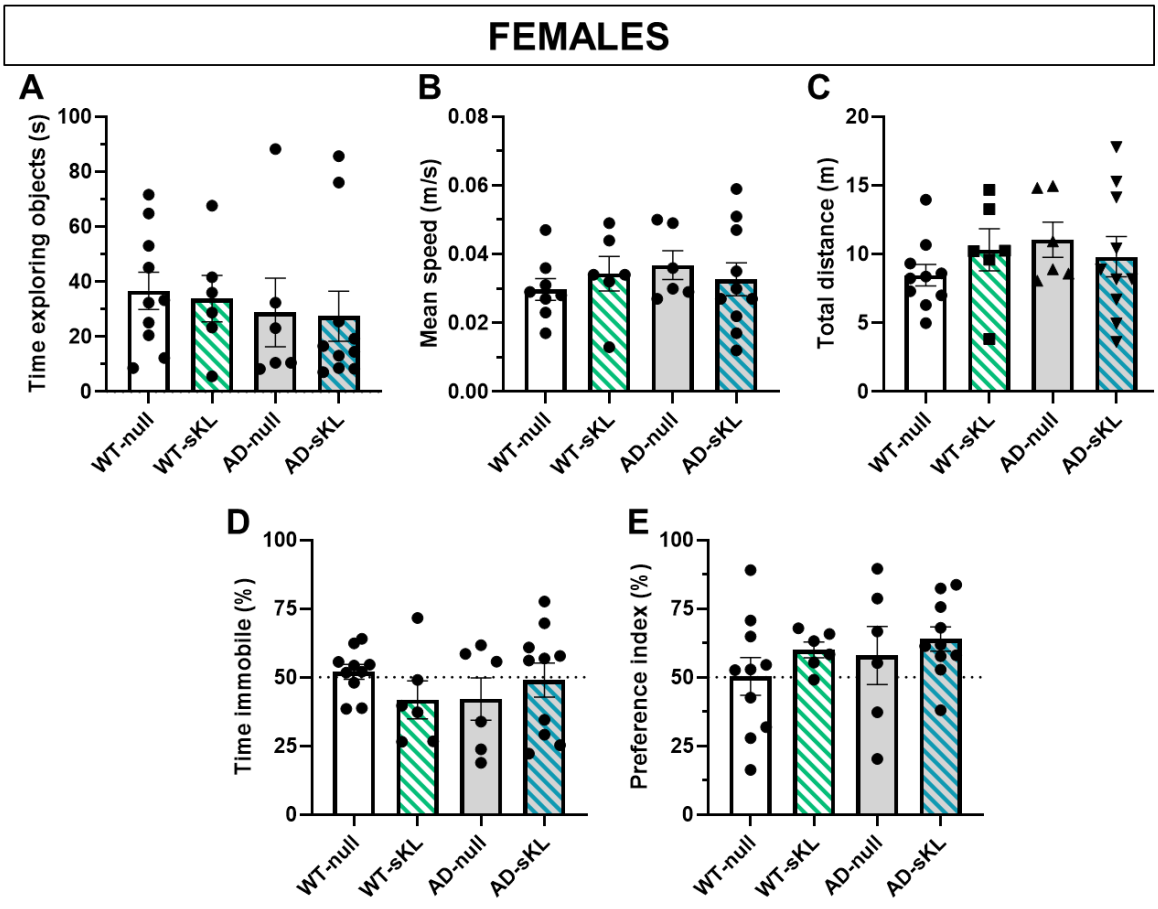

Figure 41. Parameters analyzed in the NOR memory test (females). Dots represent individual mice. Bars and lines represent Mean±SEM. Differences between groups analyzed by One-way ANOVA (ns: p>0.05). Sample size per group after discarding outliers (n): WT-null=10, WT-sKL=6, AD-null=6, AD-sKL=10.

The AD-sKL males showed higher exploratory activity than the rest of the groups during the memory test, although differences were not significant (Figure 42.A: One-way ANOVA p= 0.13). sKL-treated mice (both WT-sKL and AD-sKL) showed higher mean speed (Figure 42.B) and distance travelled (Figure 42.C) than their matched non-treated controls (AD-null and AD-null, respectively), despite differences not being statistically significant (p=0.09). Besides, sKL-treated groups spent less time immobile (38.85 and 45.39%, respectively) than the non-treated controls (both null groups above 50%) (Figure 42.D). These parameters (Figure 42.A, B, C, D) indicate a slight trend to higher locomotor activity during the NOR in male mice overexpressing sKL independent of the genotype. However, locomotor differences were not statistically significant so we assumed that those should not bias preference index. Indeed, all the male groups scored above 50% in the preference index (Figure 42.E) and no significant differences were observed between groups, indicating that no preference for the novel object independent of treatment ad genotype.

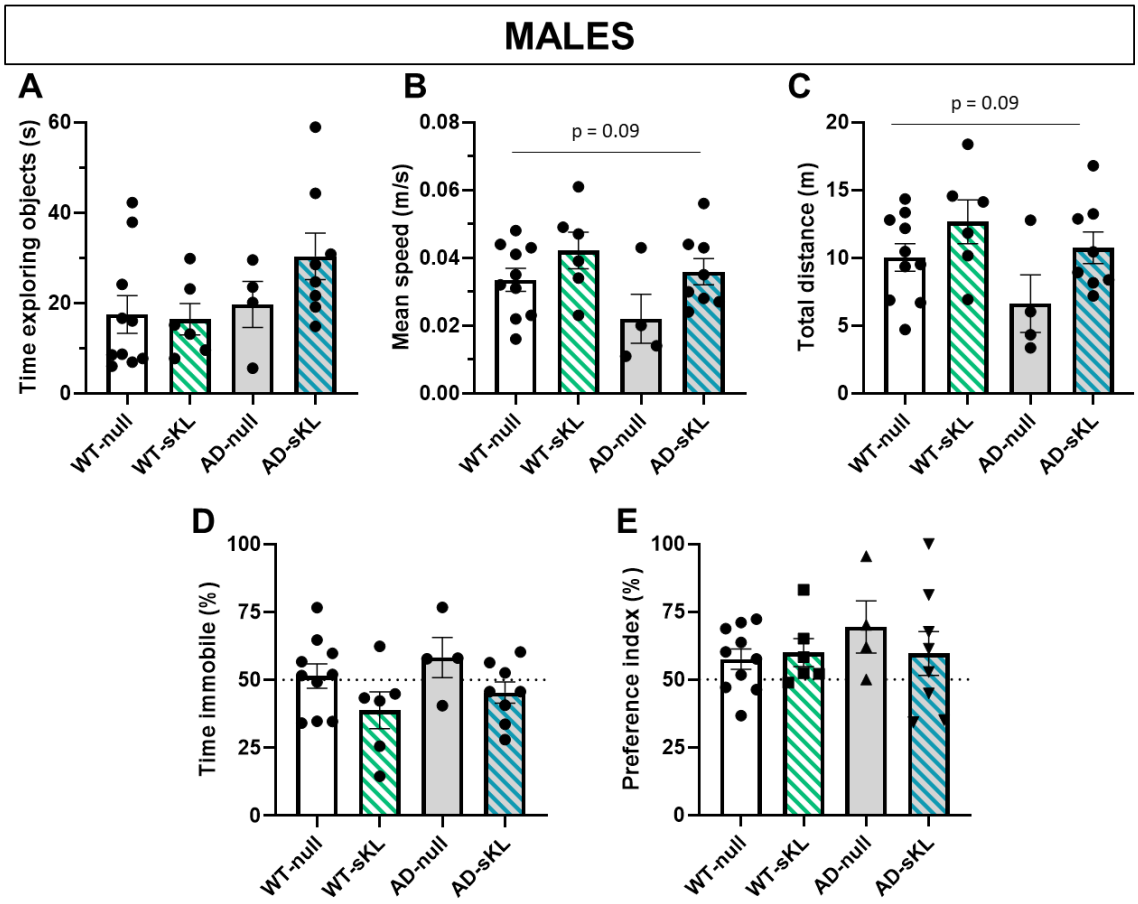

Figure 42. Parameters analyzed in the NOR memory test (Males). Dots represent individual mice. Bars and lines represent Mean±SEM. Differences between groups analyzed by One-way ANOVA (ns: p>0.05). Sample size per group (n): WT-null=10, WT-sKL=6, AD-null=4, AD-sKL=8.

2.2.3. T-Maze

Following the exclusion criteria stated in the Methods section, 8 females (WT-null: 2, WT-sKL: 1, AD-null: 2, AD-sKL: 3) and 8 males (WT-null: 1, WT-sKL: 2, AD-null: 3, AD-sKL: 2) were excluded from the present T-Maze analysis, and they are not plotted in the graphs below.

In the female mice, the time percentage exploring arms showed no differences between groups in the learning nor in the memory phases (Figure 43. A, B), indicating a similar degree of learning, motivation and willingness to explore. The AD-null group presented the lower number of entries to either arm in the memory test, whereas the AD-sKL increased the average over the rest of the groups, despite differences not being significant (Figure 43.C). Of those, the majority of entries were to the novel arm for the WT groups, as observed in the percentages over the 50%, whereas for the AD-null mice the number of entries to the novel arm was significantly lower ($p=0.0271$). Importantly, this score was recovered upon sKL treatment, as AD-sKL mice reached over 50% of visits to the novel arm on average (Figure 43.D). A similar trend was observed when analyzing the time spent in the novel arm, where AD-null mice only spent a 38%, therefore most of the time in the familiar arm. However, sKL treatment icreased the time exploring the novel arm in the AD-sKL towards the values observed in the WT groups (Figure 43.E).

When examining whether the mice entered the novel or the familiar arm first, we observed the vast majority of WT mice (over 75% of the WT-null and the totality of the WT-sKL) preferred the novel arm, whereas AD-null mice preferred the familiar arm since only 40% entered the novel arm first. Interestingly, sKL treatment also inverted this ratio in the APP/Tau females, as over the 50% of AD-sKL mice entered fist the novel arm, approximating the score to that observed in the WT groups (Figure 43.F).

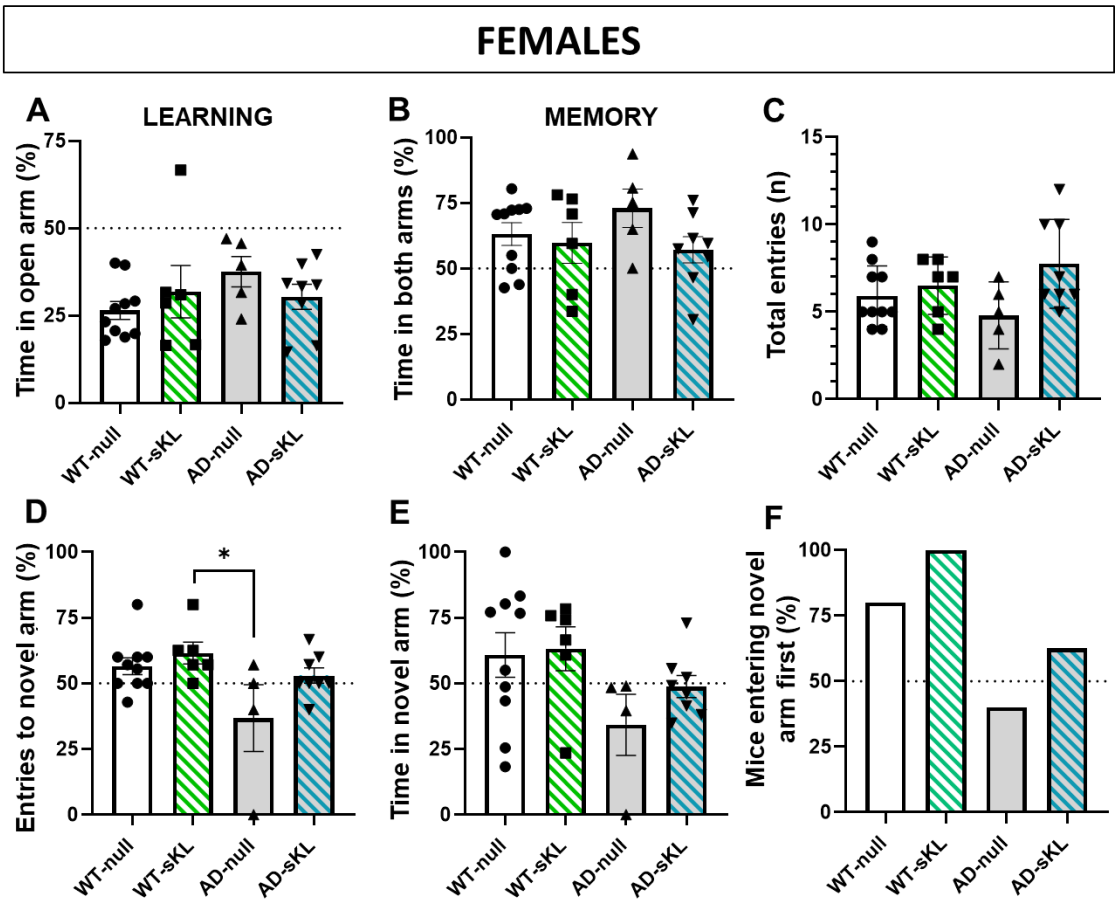

Figure 43. Parameters analyzed in the learning (A) and memory (B-F) phases of T-Maze test (females). Differences between groups analyzed by one-way ANOVA and Tuckey post-hoc in A-E; and by comparison of proportions test in F. Sample size per group (n): WT-null=10, WT-sKL=6, AD-null=4-5, AD-sKL=8.

As for males, in the learning phase, we found significant differences in the time exploring the open arm between the groups (p= 0.0398). The AD-sKL group spent more time in the open arm, suggesting higher exploratory activity (Figure 44.A). In the memory phase though, we did not observe significant differences in the time exploring (Figure 44.B) nor in the total number of entries to arms (Figure 44.C), so we assumed that all the groups presented a similar degree of motivation and willingness, allowing us to assess memory. The percentages of entries to the novel arm (Figure 44.D) and the time exploring it (Figure 44.E) were around 50% for all the groups. Analyzing the first arm entered indicated that the majority of the mice in the WT and in the AD-null groups chose the novel arm, whereas only 43% of the AD-sKL mice preferred the novel over the familiar (Figure 44.F). Altogether, these results did not show clear preference for the familiar nor the novel arm in any of the male groups analyzed, indicating a similar behavior for all of them. Therefore, this test did not reveal memory deficits in the males of the APP/Tau model.

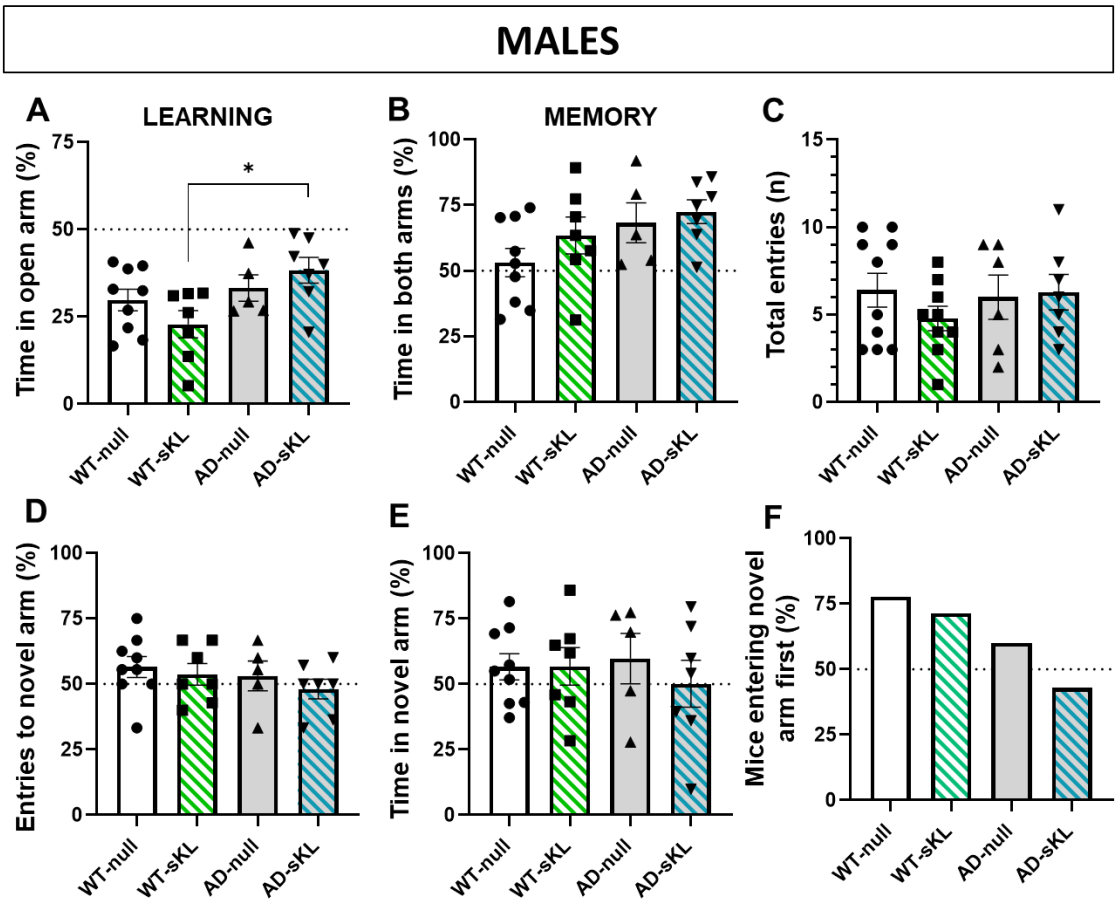

Figure 44. Parameters analyzed in the learning (A) and memory (B-F) phases of T-Maze test (males). Differences between groups analyzed by one-way ANOVA and Tuckey post-hoc in A-E; and by comparison of proportions test in F. Sample size per group (n): WT-null=9, WT-sKL=7, AD-null=5, AD-sKL=7.

2.2.4. Morris Water Maze

The MWM test was performed to assess the spatial learning and reference memory in mice following the same protocol as in the 3xTg-AD study. The protocol itself only allowed a maximum of 17 mice to be handled in a whole MWM test. The mice of each set of injections were analyzed at different time points to match the experimental design. Here we present the combined results of the two sets (total n: females=29, males=31). Females and males were tested separately in the two sets.

In the learning stage, both AD and WT females significantly decreased the latency ($p=0.0035$) (Figure 45.A) and the distance travelled to reach the platform ($p=0.0003$) (Figure 45.B) over the training days. Unexpectedly, the WT-null group increased the average latency and distance on day 5 of training despite the trend during the previous days being a decrease. This could be explained because at the beginning of the training, this group

already showed good scores at finding the platform, and even ameliorated them to a point that was hard to improve, so they might feel too self-confident to find the platform at any time. Indeed, at the beginning of the training (day 2), both WT groups showed better performance than the AD groups, as observed in the latency to reach the platform that was significantly higher in AD-null compared to WT-null (p= 0.0146) (Figure 45.A). This could suggest cognitive deficits in the females of the APP/Tau model compared to the WT controls.

Nonetheless, AD-null showed a significant improvement in both the latency and distance travelled to reach the platform on day 3 (p= 0.0417 and p= 0.0291, respectively) and day 5 (p= 0.0120 and p= 0.0159, respectively) compared to the first day of training. As a result, all the groups presented similar scores in the aforementioned parameters by the end of the training (day 5), indicating that all the mice groups learned the task and reached similar learning conditions prior to the memory tests. Moreover, the four groups showed a constant mean speed over the training days, and no significant differences were found between them (Figure 45.C).

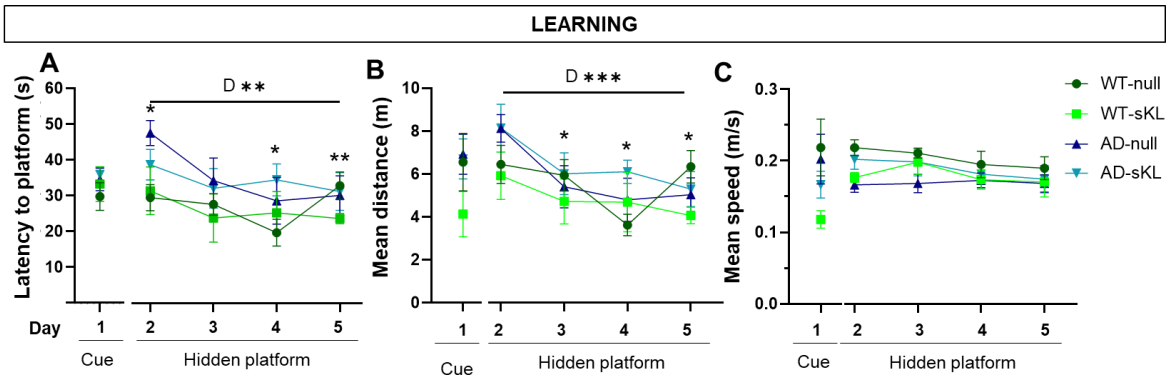

Figure 45. Learning curves in the MWM test (females). Mean±SEM represented by dots and lines, respectively. Day 1 (Cue, visible platform): Differences between groups analyzed by One-way ANOVA and Tuckey post hoc. Data on days 2-5 (hidden platform) analyzed by Two-way ANOVA and Tuckey post-hoc. Sample size after discarding outliers (n): WT-null=8. WT-sKL=5, AD-null=8, AD-sKL=9.

In memory tests, performed 2 and 24 hours after the last training trial, no significant differences were observed in any of the parameters analyzed between the female groups (Figure 46. A-J). Indeed, the non-treated APP/Tau and WT controls presented a similar performance in the memory probes, indicating that this test did not allow to detect cognitive deficits in the females of the APP/Tau model at the age analyzed.

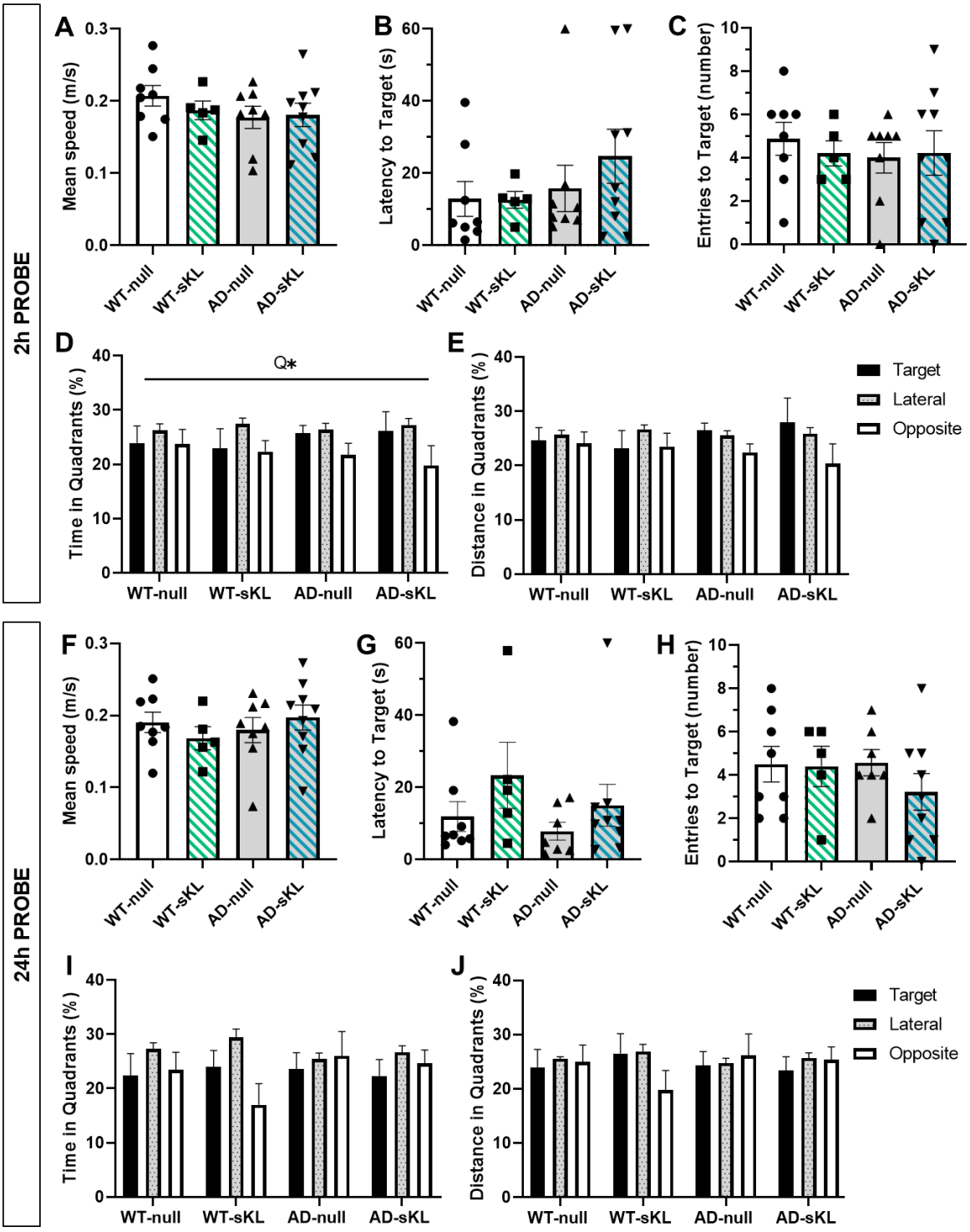

Figure 46. Parameters analyzed in the short-term (2h-probe: A-E) and long-term (24h-probe: F-J) memory tests of the MWM (females). A-C, F-H: Differences analyzed by One-way ANOVA followed by Tuckey post-hoc test. D, E, I, J: Differences analyzed by Two-way ANOVA and Tuckey post-hoc. Q: quadrant factor. GxQ: interaction between group and quadrant factors. 'Lateral' represents the average data of the two lateral quadrants in the pool. Sample size after discarding outliers (n) in each probe (2h-probe|24h-probe): WT-null= 8|8, WT-sKL= 5|5, AD-null= 8|7, AD-sKL= 9|9.

In the learning phase of the MWM, males did not show a statistically significant improvement in the parameters analyzed (Figure 47.A, B). In the case of the WT, their performance at the beginning in of the training was already good, so it hardly could be improved. As for the APP/Tau mice, in the Cue (day 1) we could observe a significantly longer latency to reach the platform compared to the WT (p=0.0263). This could indicate cognitive deficits in the APP/Tau, because the mean speed was similar for all the groups (Figure 47.D), so the decreased latency in the WT was not due to faster locomotion. In any case, during the training with the hidden platform, the APP/Tau mice learned the task as observed in the improved the latency and distance to find the platform, resulting in similar performance in all groups at the end of the training (day 5), prior to the memory tests.

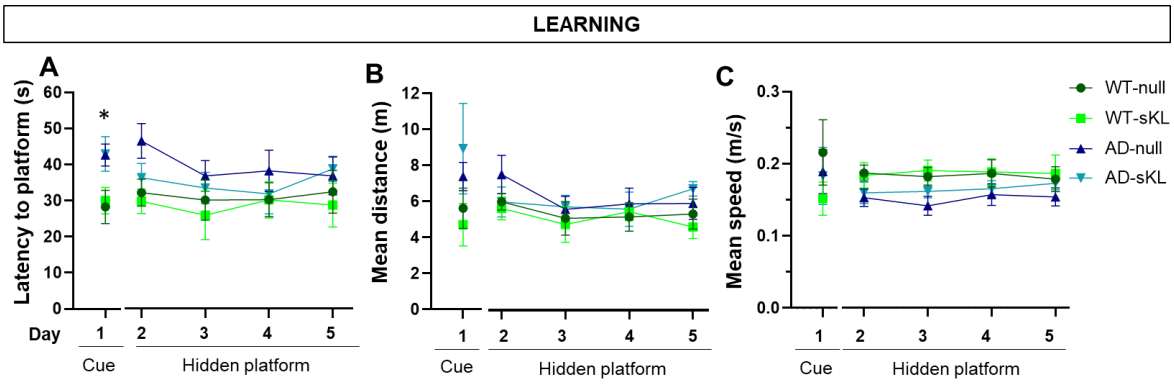

Figure 47. Learning curves in the MWM test (males). Mean±SEM represented by dots and lines, respectively. Day 1 (Cue, visible platform): Differences between groups analyzed by One-way ANOVA and Tuckey post hoc. Data on days 2-5 (hidden platform) analyzed by Two-way ANOVA and Tuckey post-hoc. Sample size after discarding outliers: WT-null=10, WT-sKL=7, AD-null=8, AD-sKL=7.

During the 2h probe trial, APP/Tau male mice presented higher latency to reach the target (Figure 48.B) and lower number of entries (Figure 48.C) compared to the WT groups, despite not being statistically significant. Following sKL treatment, we could observe an increased time in the target quadrant in AD-sKL mice and a significative reduction of the time spent in the opposite quadrant compared to the AD-null (p= 0.0365) (Figure 48.D). AD-sKL mice also swam higher distance in the target quadrant *versus* the opposite, whereas the non-treated AD-null swam more distance in the opposite quadrant (Figure 48.E). Although the 2h probe did not reveal statistically significant differences, we could observe a trend of worse short-term memory in the APP/Tau males compared to the WT, and a slight improvement following sKL treatment in the APP/Tau mice.

In the 24h probe, non-treated APP/Tau mice (AD-null) presented a significantly higher latency to reach the target than the WT-null controls (p=0.0250). This parameter was improved following sKL treatment, as AD-sKL mice showed reduced latency to reach the target compared to the non-treated AD-null (Figure 48.G). The number of entries to the target was also decreased in the APP/Tau mice compared to the WT, whereas sKL treatment seemed to recover this score, as observed in the AD-sKL group (Figure 48.H). Furthermore, the AD-sKL mice tended to increase the percentage of time and the distance swam in the target quadrant compared to the AD-null, while decreasing those parameters in the opposite quadrant, with statistical significance in the time ($p = 0.0060$) (Figure 48.I, J). Overall, the parameters analyzed in the MWM test indicate some signs of memory deficits in the males of the APP/Tau model, that are slightly improved upon sKL treatment.

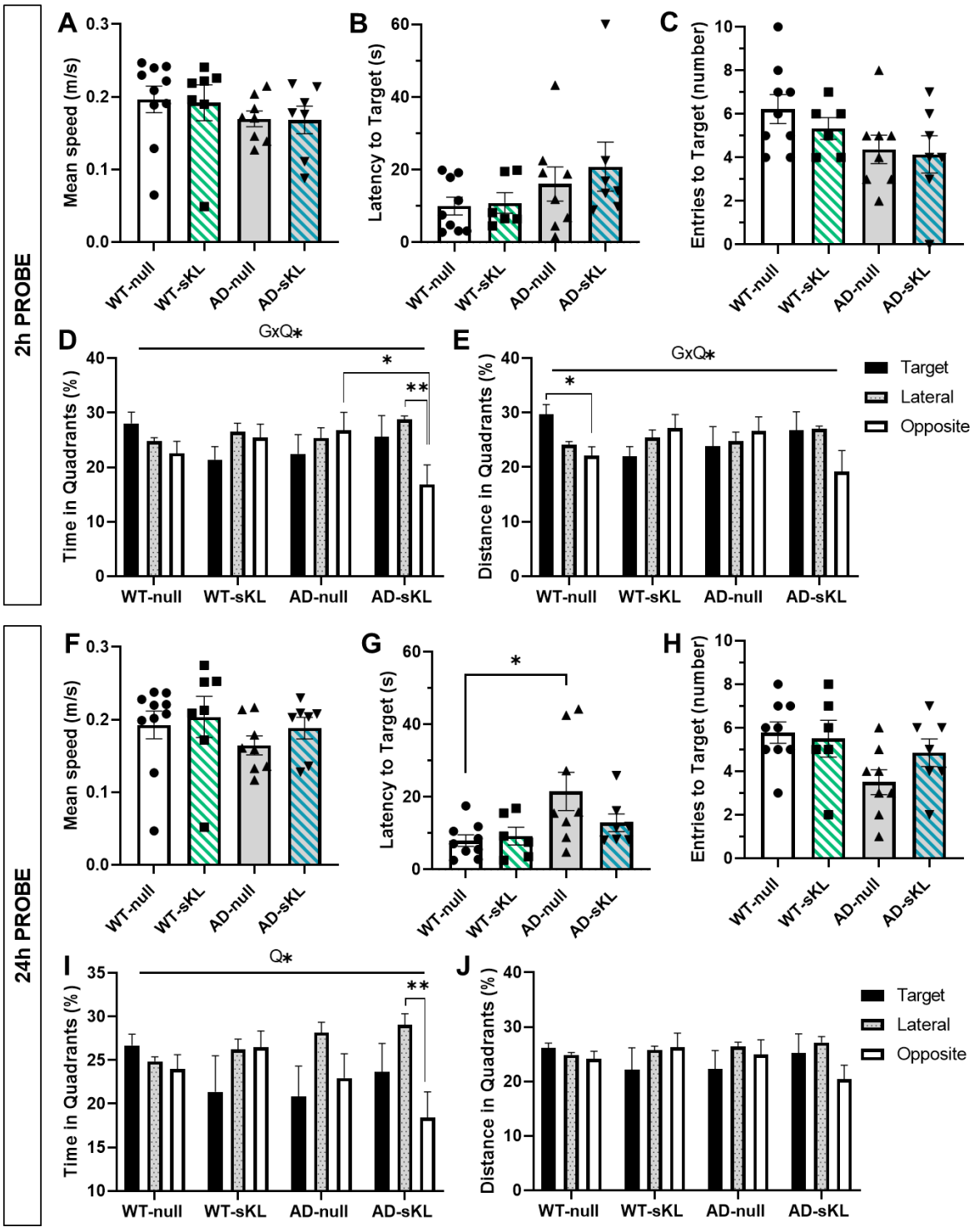

Figure 48. Parameters analyzed in the short-term (2h-probe: A-E) and long-term (24h-probe: F-J) memory tests of the MWM (males). A-C, F-H: Differences analyzed by One-way ANOVA followed by Tuckey post-hoc test. D, E, I, J: Differences analyzed by Two-way ANOVA and Tuckey post-hoc. Q: quadrant factor. GxQ: interaction between group and quadrant factors. 'Lateral' represents the average data of the two lateral quadrants in the pool. Sample size after discarding outliers (n): 2h-probe|24h-probe WT-null=9|9, WT-sKL=6|6, AD-null=8|8, AD-sKL=7|7.

DISCUSSION

Growing evidence points out to the association between altered KL expression and AD [132], [135], [162], [165], in agreement with the results presented in the previous chapter. Furthermore, KL has shown neuroprotection and cognitive enhancement in different neurodegenerative diseases, but also during healthy conditions [116], [118], [169]. Because cognitive dysfunction is a critical symptom in AD, we proposed KL expression as a therapeutic strategy.

Nowadays, the particular KL variant (secreted, membrane or processed) that mediates the cognitive enhancement remains to be determined. Most of the research has focused on the full-length form (mKL and pKL). However, our study in human samples suggests an important role for sKL in the CNS, as it is the predominant variant expressed in the human hippocampus and cortex, areas involved in memory and cognition that are affected during AD. In mice, a previous study conducted by our group found that reduced levels of sKL in hippocampus were associated with low cognitive performance, and that sKL expression in the CNS stimulated cognitive skills and protected from age-dependent cognitive decline, indicating an important role for sKL in cognitive functions in mice as well [118].

In light of these findings, we focused on the sKL variant as a therapeutic target to counteract the cognitive symptoms in AD. To explore this potential, we aimed to administer sKL in the CNS of two AD mouse models (the 3xTg-AD and the APP/Tau) and ultimately assess their cognitive performance in behavior tests. For this purpose, we generated a AAV9 vector encoding the sKL cDNA and administered it by intracerebroventricular injection (ICV) in the lateral ventricle of the mice's brain. Direct AAV injection into the brain has proven to be safe and it is widely used in most preclinical research and clinical trials targeting neurodegenerative diseases [255], [308]. The ICV injection allows the AAV vectors to be distributed in the CSF and transduce diverse brain regions that will express the transgene, including the choroid plexus, where KL is naturally expressed and released to the CSF [297]. This, together with the fact that the sKL variant is a secreted protein [128], ensures the protein distribution all over the brain in the CSF. Furthermore, the AAV9 serotype is a vector of choice in gene therapy approaches targeting the CNS due its neuronal tropism, as well as its ability to undergo axonal transport, favoring widespread transgene expression in connected regions of the brain where primary transduction is limited [219], [309]. Another advantage of our AAV-based gene therapy approach was the sustained, long-term expression of sKL in the transduced cells. In contrast, the alternative administration of

recombinant protein results in a short, temporary presence of the therapeutic protein in the organism. In particular, systemic administration of recombinant KL has showed a half-life of about 7 hours in a study conducted in mice [310].

1. Assessment of cognitive performance in 3xTg-AD mice following AAV9-sKL gene transfer

We studied the AAV9-mediated sKL expression in the 3xTg-AD mouse model, a widely used mutant mouse that was initially described to mimic the pathology observed in AD patients [311]. Our therapeutic approach aimed to prevent the cognitive decline in individuals at early AD onset, when the first neuropathological symptoms appear. Therefore, based on previous characterizations of the 3xTg-AD model [311], we administered the AAV9-sKL vectors at 6 months old, when Aβ depositions start appearing in cerebral cortex [312], but no other neuropathological symptoms are detectable. At 12 months age, neuropathology aggravates in the 3xTg-AD model, as NFTs appear in the hippocampus, Aβ accumulates in both cortex and hippocampus and there is noticeable loss of noradrenergic neurons [313]. Herein, cognitive deficits were expected in the 3xTg-AD model at 12 months old, as previously observed [314], so behavioral tests were performed at this age, with sKL being expressed in the brain for around 6 months.

First, assessment of sensorimotor capacities indicated that all mice presented similar physical conditions and correct visual and locomotor reflexes, so any differences in the subsequent behavioral tests would be attributed to the cognitive performance. Besides, we confirmed that sKL expression did not negatively affect the physical capacities, consistent with previous observations [118].

Second, the Open Field test was performed to assess anxiety-like behavior in mice based on their locomotor activity. As rodents are phylogenetically conditioned to consider open, large, brightly lit spaces as dangerous, in an open maze they tend to remain close to the walls. This behavior is known as thigmotaxis and has been validated as an index of anxiogenic behavior in mice, increasing as anxiety levels rise [307]. We observed high levels of thigmotaxis in 3xTg-AD mice, suggesting neophobia and/or anxiety-like behavior in this model in agreement with other studies [315], [316]. No differences were observed between the sKL-treated and control group, indicating that sKL expression did not alter the anxiety-like behavior in these mice. Therefore, we assumed that their performance in cognitive tests would not be conditioned by different anxiety-like behavior in the sKL-treated

and control groups. A similar conclusion was reached in a different study with mice genetically modified to overexpress *kl* [116].

Based on the innate preference of rodents to explore a novel object rather than a familiar one, we performed the NOR test [287]. The preference index did not reveal differences in the recognition memory between the sKL-treated and control 3xTg-AD mice, probably due to the low samples size after discarding outliers. Of note, further parameters should be measured to confirm the observations both in the open field and NOR tests.

Finally, the MWM test assessed the effect of sKL on the spatial learning (training) and short-term (2 h probe), long-term (24 h probe), and reference memory in 3xTg-AD mice. During all the test, the swimming speed was similar for both groups, so we assumed that the differences in the learning and memory tests would not be due the locomotor activity, but to the cognitive performance. During the training days, both sKL-treated and null-control mice decreased the latency and distance to reach the platform, indicating that 3xTg-AD mice learned the task independent of the treatment. The improvement over the days was only significant for the sKL-treated mice, suggesting a beneficial effect of sKL in the reference memory and the learning skills. At the end of the training though, similar scores indicated that both groups had learned the task prior to the memory tests. In the short- and long-term memory tests (2 and 24 h after the last training, respectively), sKL-treated mice showed lower latency and increasing number of entries to the virtual target compared to the non-treated controls. Those differences were only statistically significant in the long-term memory test (24 h probe), in which sKL-treated mice also showed preference for the target quadrant, unlike null-control mice which showed no clear preference for any quadrant. Overall, our results suggest a positive effect of sKL both in the learning and in the long-term spatial memory in 3xTg-AD mice. In agreement, improved performance in the MWM was observed in the APP/PS1 mouse model of AD following mKL expression [161], [171].

It must be acknowledged that the sKL effect observed in our study was more modest than expected, probably due to the very mild cognitive deficits in the 3xTg-AD control mice. In particular, the non-treated 3xTg-AD mice showed preference for the target quadrant in the 2 h probe trial, indicating that they were able to locate the platform in the short-term memory test. Similarly, the NOR test did not reveal short-term memory deficits in the control 3xTg-AD mice. Altogether, these observations indicate that the 3xTg-AD mice lack of profound short-term memory deficits at the age analyzed, which hinders the detection of short-term memory improvement following sKL treatment. However, in the 24h probe trial, control

3xTg-AD showed signs of long-term memory impairment as they did not show preference for any quadrant, and a positive effect could be observed in the sKL-treated mice.

Consistent with our results, another group reported that 3xTg-AD mice only showed short-term memory deficit when exposed to alcohol [317]. These and our observations differ with the initial characterization of the model, in which 3xTg-AD mice exhibited impaired short-term and long-term spatial memory in the MWM [264]. On this subject, the founder of the 3xTg-AD model and colleagues confirmed in a recent report [318] the drift in the initially described phenotype [311]. Among other factors, they attributed this drift to the segregation of alleles in the mixed strain or changes in the transgene copy number within the single site of integration [319]. Be that as it may, they confirmed that the development of the pathology has been delayed, as previously reported [312], which means that our 12-month-old 3xTg-AD females could not present the cognitive deficits initially expected for this age.

In this regard, our experiments lacked a non-transgenic control group to assess the presence of cognitive deficits in the 3xTg-AD mice in our hands. Because mice handling is limiting, we decided to focus our resources in the 3xTg-AD model by omitting a non-transgenic control group, based on preceding data. First, published studies had reported that 3xTg-AD mice performed significantly worse compared to non-transgenic mice at 12 months old [312], [314], [320]. Second, in previous assays conducted by our group, AAV-mediated expression of mKL and sKL showed similar effects in WT *vs* 3xTg-AD mice. Therefore, in order to explore the therapeutic effect of sKL and mKL on AD-related symptoms, we decided to increase the experimental groups and sample size with 3xTg-AD mice to the detriment of non-transgenic control groups. Unfortunately, the analysis of transgene expression after euthanasia revealed low or absent AAV-mediated mKL expression in mice injected with AAV9-mKL, so we eventually suppressed the mKL-treated 3xTg-AD group from the presented study, as previously mentioned. The failed AAV9-mKL transduction could be due to a defective encapsidation of the mKL expression cassette into the AAV9 particles during the vector batch production, or to a loss in the cold chain storage of the vector prior to administration, resulting in a very low infectivity ratio in that particular batch.

Another aspect that should be addressed is the exclusive use of females in the present study. Initially, our experimental design was based on a previous study conducted by our group, in which 3xTg-AD males did not exhibit AD-like pathology at 12 months old. In particular, the immunohistochemical analysis of brain revealed no presence βA depositions, and tau was only detected in some individuals. Besides, behavior tests revealed no

cognitive nor memory deficits in the 3xTg-AD male mice. Afterwards, the donating investigator communicated that male transgenic mice may not exhibit the phenotypic traits originally described [321]. In the recent aforementioned report of the colony founders, profound sex differences were characterized, with pathology only emerging in female mice, not only in the original 3xTg-AD colony but also in other groups [318]. This female sex-bias in the pathology has been explained by the authors as a consequence of the response to estrogen [318], [322], whereas other studies suggest organizational actions of sex steroid hormones during development [323].

In view of all these findings in the 3xTg-AD model, and because we observed a modest, but positive effect following our sKL gene therapy, we decided to further explore the therapeutic potential of KL in a different mouse model of AD using a similar approach with some optimizations.

2. Assessment of cognitive performance in APP/Tau mice following AAV9-sKL gene transfer

The model of choice for our next in vivo experiment was the APP/Tau, recently generated by the group of Dr Saura (UAB). The APP/Tau model was obtained by crossing of two transgenic mouse lines: the APPsw,Ind, expressing the human APP protein with the *Swedish* and *Indiana* mutations [279] and the P301Stau, expressing the human tau gene with the P301S mutation [280]. Herein, the resulting double heterozygous offspring expresses both human APP and tau, overcoming a general limitation of the available AD mouse models, since most of them only develop either plaques or tangles, while in humans both pathological hallmarks are present in AD patients [259]. This, together with their preliminary characterization of the APP/Tau phenotype (data not published), showed promise in reproducing the AD-like pathology, so we started our own APP/Tau colony and their corresponding WT controls from two breeder couples, kindly provided by Dr Saura. When the number of age-matched mice born was enough to perform an in vivo experiment, we administer our AAV9-sKL gene therapy similar to the 3xTg-AD experiment, including some variations.

First, because we aimed to optimize the *in vivo* transgene expression in this experiment, we maximized the vector dose by including a concentration step in the AAV production. Based on the AAV titer obtained, we adjusted the dose to the maximum volume admitted

by ICV injection, resulting in $1 \cdot 10^{11}$ vg/mouse, increasing the dose previously administered to 3xTg-AD mice ($4.7 \cdot 10^{10}$ vg/mouse).

Another optimization consisted of the switch of the CMV promotor by the CAG to drive the transgene expression. Despite the CMV promoter is known to provide high, rapid, and ubiquitous expression in neural cells, it is prone to silencing in some brain tissues due to methylation resulting in diminished transgene expression over time [324].

Since our experimental design required long-term transgene expression, we needed a more stable promoter. In this sense, the CAG promoter has proven to be superior to the CMV, showing sustained stable transgene expression for long periods of time [325]–[328]. Moreover, in a similar AAV-gene therapy approach to ours, the CAG promoter generated higher transgene expression than the CMV in hippocampus, a region of special interest due to its association to AD pathology [329]. However, while the CAG promoter is advantageous for its strong, ubiquitous, sustained *in vivo* expression in brain, its long size (approximately 1.7 kb) is a limitation for its use in AAV vectors with long transgenes. As the cDNA of the mKL consists of about 3 kb, cloning it in an expression under the CAG promoter resulted in an expression cassette longer than the limited capacity of the AAV genome (only allowing an expression cassette of 4.4 kb). For this reason, the present experiment could not address mKL expression under the CAG promoter following the established experimental design. Nevertheless, given the limited number of mice available, this limitation allowed us to increase the sample size of the sKL-treated groups and corresponding null controls.

The assessment of sensorimotor capacities confirmed correct visual and motor reflexes and physical conditions in all the mice independent of the genotype and sKL expression, consistent with our previous observations in 3xTg-AD mice and other studies in WT [118]. Therefore, behavioral tests would not be biased by physical capacities.

The Open Field test revealed high levels of thigmotaxis on all mice, independent of the genotype, sKL-treatment, and sex, indicating a similar anxiety-like behavior and healthy avoidance of the center in all groups. sKL expression did not affect anxiety-related behavior in WT nor APP/Tau mice, excluding bias in the performance of cognitive tests, in agreement with other studies in WT and transgenic mice overexpressing KL [116], [118].

In the NOR test, only a slight trend of improved performance was observed in females overexpressing sKL, both APP/Tau and WT. However, significant differences in the cognitive performance were not detected between WT and APP/Tau mice, both female and

male, indicating that the NOR test was not suitable to detect cognitive deficits in this model, and therefore, to assess cognition-enhancing effect of sKL could not be assessed.

The T-Maze test was added to the battery of behavior tests to assess short-term spatial and working memory by testing their ability to differentiate between the novel and familiar compartments (maze arms), as mice with healthy cognition would tend to spend more time in the novel. The results revealed preference for the familiar arm in the control APP/Tau females, suggesting that they did not remember exploring the familiar arm and explored it again, therefore indicating memory deficits. In such a way, the preference for the novel arm observed in the WT mice could be interpreted as a consequence of functional memory, because they remember the familiar arm and so they naturally choose the novel. Interestingly, sKL expression modified the behavior of the APP/Tau females towards the scores observed in the WT groups, suggesting that sKL enhanced short-term spatial and working memory in APP/Tau female mice. In agreement, improved working memory was observed in the T-maze in WT mice upon sKL expression regardless of the age [118], as well as in the similar Y-maze in young transgenic mice with systemic expression of KL [116].

In the APP/Tau male mice, however, the effect of sKL on short-term memory could not be assessed by the T-maze test, as it did not reveal a different behavior between APP/Tau- and WT- null controls. A plausible explanation is that memory deficits at this age in the males of our model are still undetectable in the T-maze. Alternatively, maybe WT mice were not able to perform the task as expected by correctly recognizing and showing preference for the novel arm. In this line, previous studies have reported that neither the T-maze nor the similar Y-maze could detect memory deficits in APP/PS1 mice at 13 months old and younger compared to non-transgenic controls [330], [331].

Finally, in the MWM, APP/Tau females presented worse abilities to find the platform compared to WT at the beginning of the training, although eventually they learned the task like WT. In the short- and long-term memory tests, APP/Tau and WT females performed similarly, indicating lack of detectable cognitive deficits in the APP/Tau females. No differences were either observed upon sKL treatment in the female groups. As for the males, the APP/Tau mice presented worse abilities to reach the platform compared to the WT at the beginning of the training, although they managed to learn the task, as observed in females. During the memory tests, some parameters indicated a worse performance in APP/Tau mice compared to WT, suggesting signs of memory deficits in the APP/Tau males. sKL-treatment slightly improved the performance during both the training and the memory

probes in APP/Tau males, although differences were only statistically significant in the time spent in target quadrant.

Overall, the MWM revealed a homogeneous performance between non-treated APP/Tau and WT controls, both in females and males, indicating lack of profound deficits in spatial learning and reference memory in this AD model at the age tested. This could explain why the effect of sKL expression in APP/Tau mice seemed modest in the MWM. A similar phenomenon could had occurred in the NOR and T-maze tests, in which a positive effect of sKL on AD-related cognitive deficits was only detectable in females.

At the beginning of this study, there was no data available regarding the AD-related cognitive deficits in 7–8-month-old APP/Tau mice, as the model was still being characterized by our collaborators. According to a personal communication, beta-amyloid depositions could not be detected in APP/Tau mice at 5-6 months old, but at 9-10 months old, some plaques were detected in cortex and hippocampus. Herein, at the age tested in our study (7–8-month-old), APP/Tau mice had not developed profound cognitive deficits yet, and it is plausible that those would be more evident at more advanced ages, given that AD is an age-related pathology. In that case, it would be interesting to further explore the therapeutic potential of sKL in APP/Tau mice at later ages.

3. Further considerations

It should be acknowledged that despite modest, sKL expression generated a beneficial effect in some cognitive and memory parameters, in both 3xTg-AD and APP/Tau mice. This is the first time that the cognition-enhancing properties of the sKL variant are assessed in these AD mouse models by AAV-based gene therapy. In aged WT mice, sKL expression had demonstrated protection against age-dependent memory deficits [118]. We did not observe a comparable effect on our sKL-treated WT mice, which in turn is not surprising because at the age tested (7-8 months old), our WT mice do not present cognitive deficits.

In other studies, expression of the full-length KL variant (mKL) ameliorated the AD-like pathology and cognitive impairment in AD mouse models such as the APP/PS1 [161], [162], [171] and the hAPP [116]. Those studies suggested that KL could ameliorate the AD-related symptoms by activating autophagy, promoting microglia transformation from the M1 type to M2 type, and regulating Aβ transporters, eventually resulting in enhanced Aβ clearance in brain [161], [162], [171], [187]. KL could also contribute to attenuate cognitive dysfunction

by reducing oxidative stress and remodeling the brain metabolome [117], [179]. In future studies, it would be interesting to assess those effects following expression of the sKL variant in AD models.

Withal, the molecular and cellular mechanism underlaying the aforementioned neuroprotective properties of KL remain to be fully elucidated. Interestingly, a recent report attributed the cognition-enhancing properties observed with mKL to its KL1 domain [117], which is the only common domain present in the sKL variant. Supporting this hypothesis, studies in WT mice have demonstrated that sKL silencing in brain results in impaired spatial learning and long-term memory [118], whereas sKL expression benefits memory formation [169].

Altogether, these data highlight the relevance of the sKL variant in the neuroprotective functions attributed to KL, and the need to further investigate its therapeutic potential against AD. Additionally, this work has evidenced some of the disadvantages regarding the use of animal models in preclinical research. First, the high variability among individuals hinders the obtention of concluding results. This was observed both in the development of cognitive deficits and the parameters analyzed in the behavior tests. Also, the AD pathology develops slowly and in an age-related fashion, so in vivo experiments take long periods of time, which in some cases are not sufficient.

Other researchers have highlighted further limitations of animals to model AD. For instance, most of the experimental models are generated by transgenic mutations to overexpress human genes associated to familiar forms of AD, but these do not represent the sporadic forms of AD, present in the 98% of the AD patients. Besides, many rodent models do not develop synaptic and neuronal loss, which are relevant pathological features observed in AD patients [332]. As a consequence, several therapies proven successful in these animal models have failed in human clinical trials [333], [334]. This low translatability is usually attributed to the limited ability of mouse models to reproduce the human aspects of AD pathology and has turned the attention towards the use of human *in vitro* models derived from cells of AD patients [335]. These are promising tools to investigate the molecular mechanism of the disease and the efficacy of new therapies in a human cellular context, which could increase translatability. Nonetheless, animal models are an indispensable resource to recapitulate the AD pathology in an organism with a complex tissue system, as well as to test the efficacy of therapeutic candidates on the memory and cognitive symptoms.

In conclusion, as the “perfect” experimental model of AD does not exist, the suitability of each model for every investigation will depend on the specific aspect of AD that aims to be addressed, while having into account the particular limitations of each model.

CHAPTER 3

Characterization and optimization of AAV-mediated gene transfer in human brain organoids

RESULTS

The development of therapies for diseases affecting the human CNS is challenging, amongst other reasons, because the translation of preclinical data obtained from traditional models to the clinic often presents unforeseen difficulties. In this context, 3D-brain organoids derived from human iPSCs could be used as a relevant model of the human brain. Furthermore, gene therapy using AAV vectors has shown promise for treating CNS diseases [217]. A wide variety of AAV serotypes with different tropism and transduction efficiency are available, so selecting the most suitable AAV capsid for transducing human brain cells is essential prior to the therapy development. For this purpose, human brain organoids are a valuable tool as they recapitulate some aspects of the human brain better than other 2D human *in vitro* cultures or animal models.

The main goals of this study were to stablish a protocol, a dose and the AAV serotype that most efficiently transduces human brain organoids. Based on their promising properties, we compared the efficiency of two AAV serotypes to transduce brain organoids: the AAV9 and the AAV7m8. The organoids used were generated following two different protocols. Briefly, the AggreWell protocol generates same-size round homogeneous organoids (A), whereas the alternative protocol (self-assembly) produces smaller brain organoids that are highly heterogeneous in size and shape (B) [336]. We used two models of neurological-disease brain organoids: one differentiated from TREX1-KO human iPSCs by “protocol A”; and other differentiated from human iPSCs SETD5-KO by “protocol B”; as well as WT brain organoids derived from human iPSCs with no genetic diseases, generated by either protocol A or B (Figure 49).

In addition to the aforementioned main goals, we also aimed to study whether the KO genotypes and/or the protocol of organoids generation influences AAV-mediated transgene expression, as well as the expression curve and peak for each AAV serotype and organoid type. Herein, we transduced mature brain organoids (from 46 to 129 days old after differentiation) with AAV7m8 and AAV9, both carrying the green fluorescent protein (GFP) transgene under the control of the CMV promotor. Live transgene expression was assessed after the day of transduction (day 0) using the fluorescence microscope EVOS to detect GFP in the surface of the live organoids in culture. An AAV9 vector coding a non-translatable null sequence (AAV-null) and non-transduced control organoids (NTC) were used as controls.

The experiments concerning human brain organoids were performed at Dr A. Muotri's laboratory (University of California San Diego, USA), except for the production of the AAV vectors.

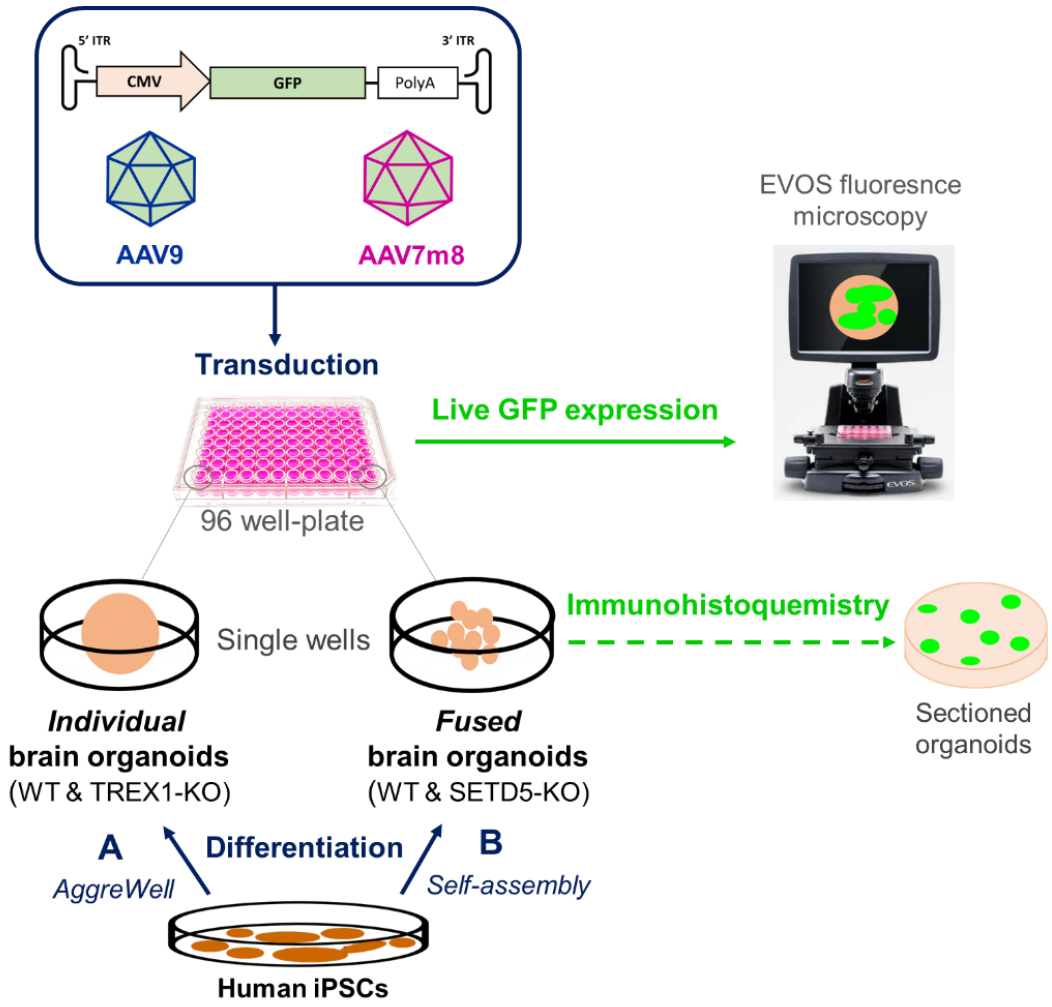

Figure 49. Experimental design for AAV-transduction of human brain organoids. AAV9 and AAV7m8 vectors were generated carrying the GFP cDNA under the CMV promotor. Brain organoids were generated from human iPSCs with different genetic background (WT, TREX-KO and SETD5-KO) by either differentiation protocol A or B. Protocol A (AggreWell) generates individual homogeneous organoids (WT and TREX-KO) that can be spared in individual wells. Protocol B (self-assembly) generates smaller and heterogeneous brain organoids that cannot be individualized (WT and SETD5-KO), so 10 organoids were spared per well and they fused. All the organoid types were transduced with AAV7m8-GFP and AAV9-GFP to compare the vectors' efficiency. Live GFP expression was detected live using the EVOS microscope. GFP expression in inner layers of the organoids was analyzed by immunohistochemistry.

1. AAV-transduction of WT and TREX1-KO individual brain organoids

Here we present the development of the AAV-transduction protocol for AggreWell-generated brain organoids. The AggreWell is a plate in which a single iPSCs suspension is added to each well. Centrifugation allows cells to evenly distribute in the microwells contained in each well, and after being incubated in rotation for 24-48 h, uniformly sized and shaped 3D organoids are generated. Hence, by this protocol, homogenous organoids in size, shape and number of cells may be generated.

In our experiments, we used AggreWell-generated brain organoids from 46 days old. At this age, these organoids had reached a size big enough to be manually spared in 96-well plates, and so they can be cultured individually before AAV transduction and afterwards. This allowed us to determine the exact AAV dose per organoid and track the transgene expression in each particular organoid every day. Hereafter, we will refer to this type of organoids as “individual organoids”.

In the experiments involving individual organoids, we used a WT cell line and a TREX1-KO cell line as a model of neurological disease, previously characterized in[290]. Briefly, the three-prime repair exonuclease 1 (TREX1) is an anti-viral enzyme that cleaves nucleic acids in the cytosol. TREX1 prevents the accumulation of the nucleic acids as well as the subsequent inflammatory response. Defective function of TREX1 triggers autoimmune diseases like Aicardi-Goutières syndrome (AGS), a neuroinflammatory disorder involving intellectual and physical problems. The TREX1-KO brain organoids used in this study recapitulate disease-relevant phenotypes of AGS, such as neural cells showing abundant extrachromosomal DNA and neurons exhibiting increased apoptosis. Besides, the TREX1-KO organoids present reduced size compared to the WT.

1.1. Dose set up for transducing individual brain organoids with AAV9 and AAV7m8 vectors.

In a first attempt to stablish a protocol for brain organoid transduction, 46-day-old AggreWell-generated organoids were individualized in 96-well plates and transduced with either AAV7m8-GFP or AAV9-GFP vectors at two different doses: $1{\cdot}10^9$ and $1{\cdot}10^{10}$ viral genomes per well (vg/well). Two organoids were transduced per AAV-condition (n=2), one of them being WT and the other TREX1-KO. The main goal of this pilot assay was to validate some protocol variables, like the plate and well type, the organoid survival after individualization, the timing of media changes and the GFP expression detection using EVOS microscope, as well as to define a valid AAV dose. That is why we used a very low organoid sample size and no comparisons between the organoid's genotypes were performed.

Transduction with the AAV7m8 variant showed higher GFP expression compared to the AAV9 at both the lower ($1{\cdot}10^9$ vg/well) and the higher ($1{\cdot}10^{10}$ vg/well) doses, as observed in the percentage of GFP-positive area of the organoids at different time points from day 5 (Figure 50.A), as well as in the accumulated GFP expression for 13 days, that was significantly higher for the AAV7m8 compared to the AAV9, at both doses (Figure 50.B).

At the lower dose ($1{\cdot}10^9$ vg/well), AAV7m8 triggered detectable GFP expression as early as day, whereas AAV9 did not produce a considerable GFP signal any day during the experiment (Figure 50.A, B, C, D). At the higher dose ($1{\cdot}10^{10}$ vg/well), the AAV7m8 generated higher GFP expression than AAV9 from day 5 (Figure 50.A, C).

At day 9 after transduction, there was a peak of transgene expression in which the AAV7m8-transduced organoids showed higher GFP signal than the AAV9 with any of the doses administered. At this time point, GFP expression was almost undetectable with AAV9 at low dose ($1{\cdot}10^9$ vg/well), whereas at the higher dose ($1{\cdot}10^{10}$ vg/well) it was detectable, although much lower than AAV7m8 (Figure 50.A and D). Consequently, in the subsequent experiments, we implemented the higher dose ($1{\cdot}10^{10}$ vg/well) to further compare the transduction efficiency of AAV7m8 *vs* AAV9.

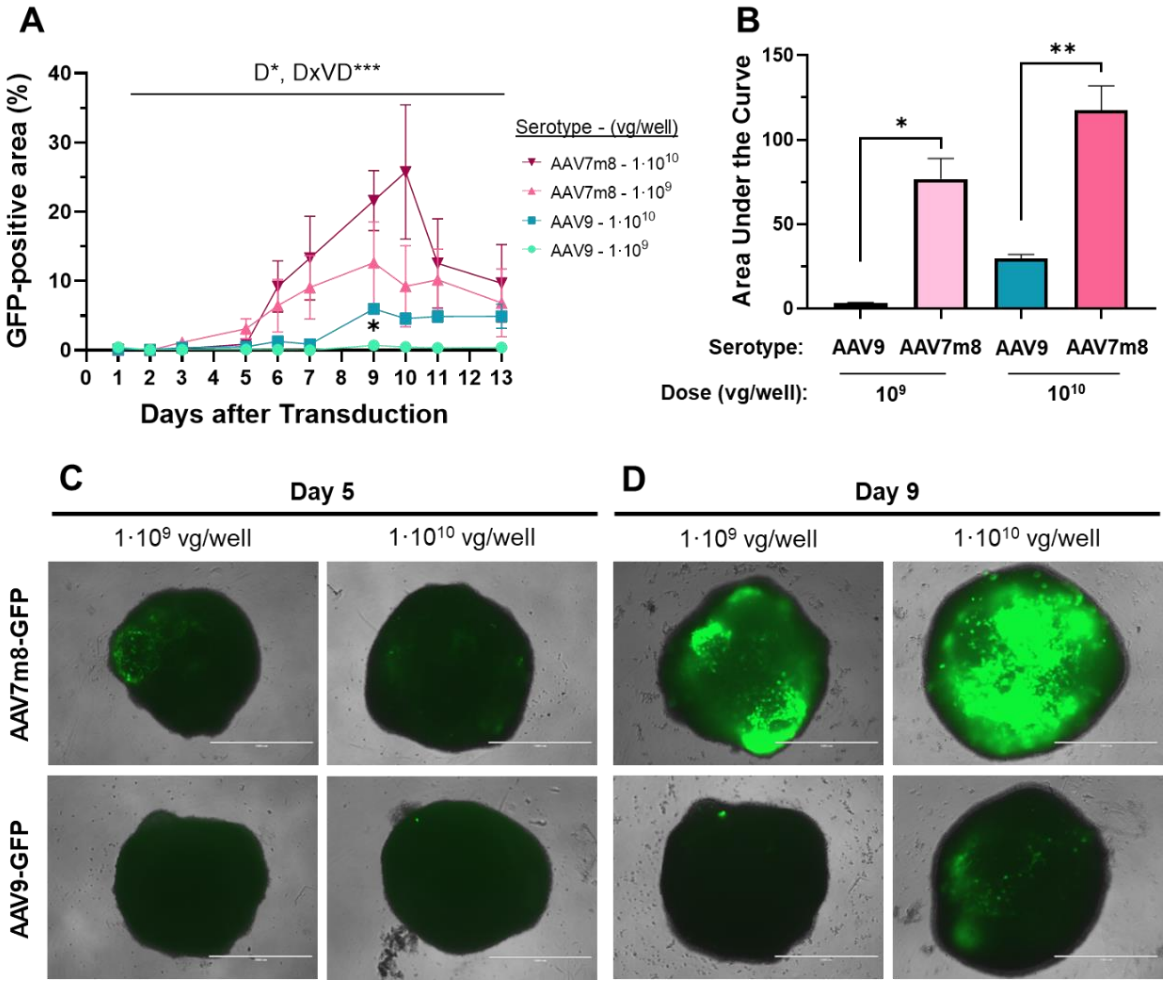

Figure 50. Dose set up for transducing individual organoids with AAV9 and AAV7m8: $1{\cdot}10^9$ vs $1{\cdot}10^{10}$ vg/well. (A) Percentage of live GFP signal on the organoids area at different time points (days after transduction). Mean±SEM are represented per AAV-condition at each time point (days after transduction). Differences between each AAV-condition at each timepoint analyzed by two-way ANOVA and Tuckey post hoc. D: variation due to the factor 'day', DV: variation due to AAV-condition (serotype and dose). DxDV: interaction between D and DV factors. (B) Accumulated GFP expression during the time course of the experiment (from day 1 to day 13 after transduction), calculated as the area under the curve from A. Mean±SEM are represented per AAV-condition. Differences analyzed by one-way ANOVA and Tuckey post hoc. (C, D) Representative images of brain organoids showing live GFP signal on days 5 and 9 after transduction, respectively. Scale bar: 1000 µm. Sample size per AAV-condition: n=2. *p<0.05, **p<0.01, ***p<0.001.

1.2. Comparing transduction efficiency of AAV9 vs AAV7m8 in individual brain organoids

Once the dose of $1 \cdot 10^{10}$ vg/well was validated with both AAV9 and AAV7m8 for transducing individual brain organoids, we aimed to further compare the transduction efficiency of both AAV serotypes using a higher number of individual brain organoids per condition (n). Thus, 54-day-old WT and TREX-KO brain organoids were transduced at a unique dose of $1 \cdot 10^{10}$ vg/well with either AAV7m8-GFP (n=4), AAV9-GFP (n=4) or AAV-null (n=2) as a negative control of GFP signal.

The AAV7m8 variant generated a significantly superior transgene expression than the AAV9, as observed in the percentage of GFP-positive area every day after transduction (Figure 51.A) and the accumulated GFP expression for 12 days (Figure 51.B). Remarkably, AAV7m8 transduction generated GFP expression as early as 1 day after transduction in WT organoids (Figure 51.C), indicating that vector entry, uncoating, transgene expression and translation took place within the first 24 hours after adding the vector to the culture media. On day 5, the AAV7m8-transduced organoids showed significant higher GFP-expressing cells than the AAV9 ($p=0.015$) (Figure 51.D). The superior transgene expression of AAV7m8 was maintained afterwards, and a peak of GFP signal was observed for both vectors on day 9 (Figure 51.A), in which AAV7m8-transduced organoids showed a GFP-positive area that was around 5-fold significantly superior to that of the AAV9 ($p= 0.0003$) (Figure 51.E). Succinctly, AAV7m8 triggered transgene expression earlier and at higher level than AAV9 at the same dose, demonstrating superior efficiency in transducing individual brain organoids, in agreement with the previous assay.

Finally, a couple of observations should be noted in this assay. First, the TREX1-KO organoids showed increasing signs of degradation starting at day 7, as they were losing their round morphology and debris was present in the media, as it can be observed on day 9 (Figure 51.E). Because this could affect the percentage of GFP-positive area used to quantify AAV efficiency, no data was considered after day 12, from which cell viability was substantially reduced. Second, it may be noticed that the percentage of GFP-positive area is around half of that observed in the previous assay using the same AAV dose. This could be due to the inter-experimental variability, and/or to the fact that organoids are older and composed by a higher number of cells, and therefore their surface is higher. In any case, this was a minor issue, as the comparison of AAV9 vs AAV7m8 was intra-experimental.

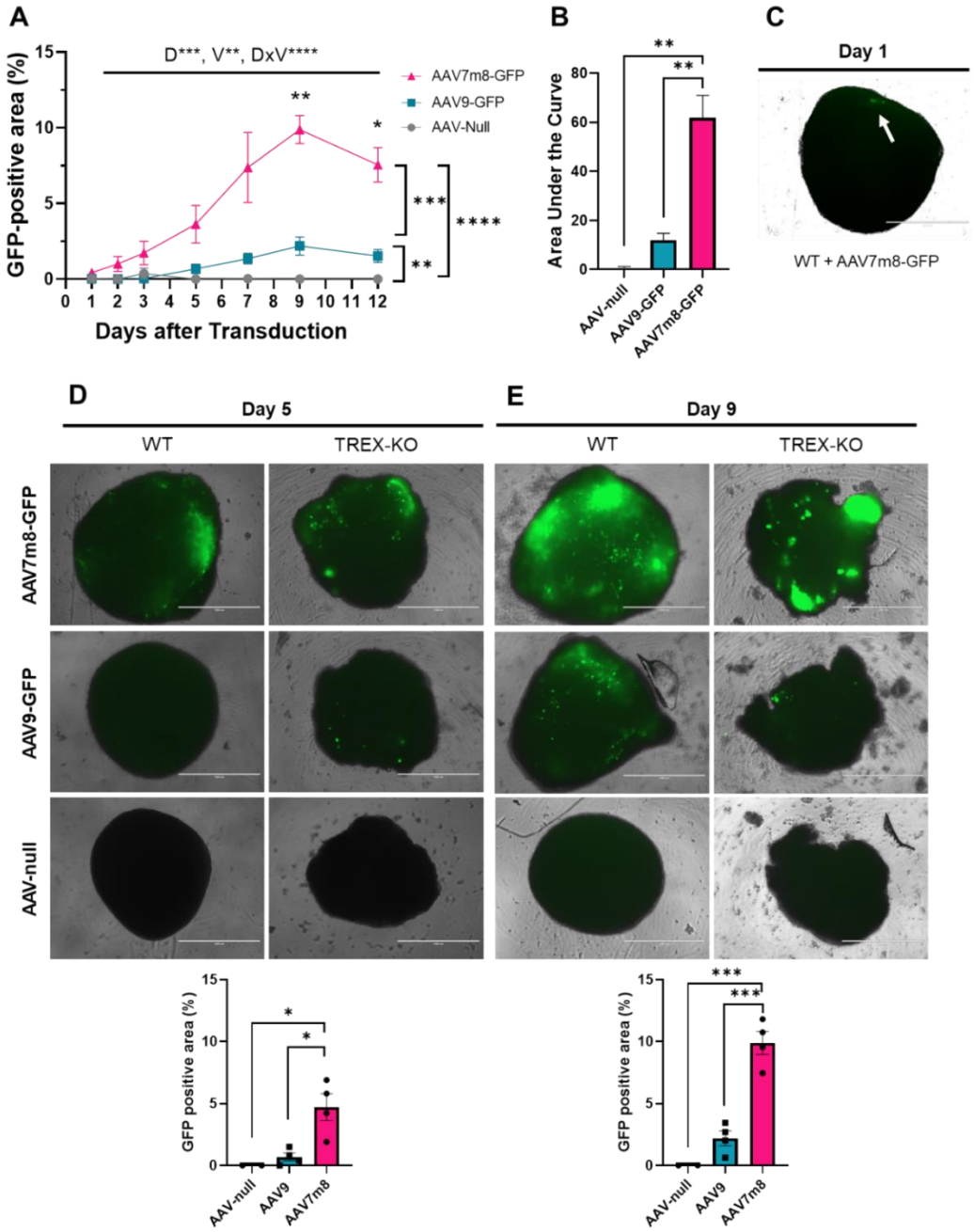

Figure 51. Comparison of AAV9 *vs* AAV7m8 transduction efficiency at $1 \cdot 10^{10}$ vg/well in individual brain organoids. A: Percentage of live GFP signal on the organoids area at different days after transduction. Differences analyzed by two-way ANOVA and Tuckey post hoc. D:variation due to the factor day, V:variation due to AAV-serotype. DxV:interaction between D and V factors. B:Accumulated GFP expression from day 1 to day 12 after transduction, calculated as the area under the curve from A. Differences analyzed by one-way ANOVA and Tuckey post hoc. C:EVOS live image of a WT brain organoid transduced with AAV7m8-GFP one after transduction showing GFP signal (white arrow). D,E:Representative EVOS images of brain organoids showing live GFP signal on days 5 and 9 after transduction. Scale bar: 1000 µm. The graphs represent de percentage of GFP-positive area on days 5 and 9 after transduction, respectively. Differences between the three AAV-conditions on each day were analyzed by one-way ANOVA and Tuckey post hoc. Mean±SEM are represented per AAV-condition. Sample size per condition (n): AAV-null=2, AAV9-GFP=4, AAV7m8-GFP=4. *p<0.05, **p<0.01, ***p<0.001, ****p<0.0001.

1.3. Protocol optimizations for AAV7m8 transduction in individual brain organoids

Once the AAV7m8 was validated as the most efficient serotype for transducing this type of brain organoids, and the dose of $1{\cdot}10^{10}$ vg/well was probed effective, some protocol innovations were implemented to increase the organoid survival and the transgene expression, including the use of conditioned media and variations in the timing of media changes after transduction.

In this assay, TREX1-KO and WT 129-day-old brain organoids were individualized in 96wp wells and transduced with AAV7m8-GFP at $1{\cdot}10^{10}$ vg/well, like in the previous assays. A total of 4 organoids, both TREX1-KO (n=2) and WT (n=2), were tracked for GFP expression after transduction. A parallel batch of non-transduced brain organoids was used as a negative control (NTC: n=4).

Comparing the GFP expression between WT and TREX1-KO organoids did not show significant differences in the accumulated GFP signal for 11 days (Figure 52.A) nor in the GFP positive area at particular time points (Figure 52.B). It should be mentioned that TREX1-KO organoids seemed to show higher percentage of GFP-positive area than the WT. This could be explained by the reduced size of the TREX1-KO compared to the WT organoids, as it can be observed in (Figure 52.B), in agreement with the previous characterization of the model.

Since the organoids' genotype did not cause a different AAV7m8-mediated transgene expression in this assay, we analyzed the WT and TREX1-KO brain organoids jointly to increase the sample size and strengthen the study of the outcome of the protocol optimizations. The GFP signal of the AAV7m8-transduced organoids was significantly higher than that of the NTC as early as at day 4 ($p=0.0286$) (Figure 52.C). Unlike in the previous experiments, the GFP signal did not decay following day 9 after transduction, but it continued increasing. Furthermore, the transgene expression was higher on the organoids' surface, reaching around the 50% of the area, whereas in the experiment previous to the protocol optimization (section 1.2), the GFP signal was around the 10% of the organoid area at the peak (on day 9) (Figure 52.A, E). In addition, organoids' viability did not seem compromised following transduction, as their morphology remained round, their size did not dramatically diminish, and no debris was observed in the media, indicating no signs of degradation (Figure 52. E, F).

In conclusion, following the optimizations of the transduction protocol, a better outcome was observed in terms of transgenic GFP expression and organoids viability.

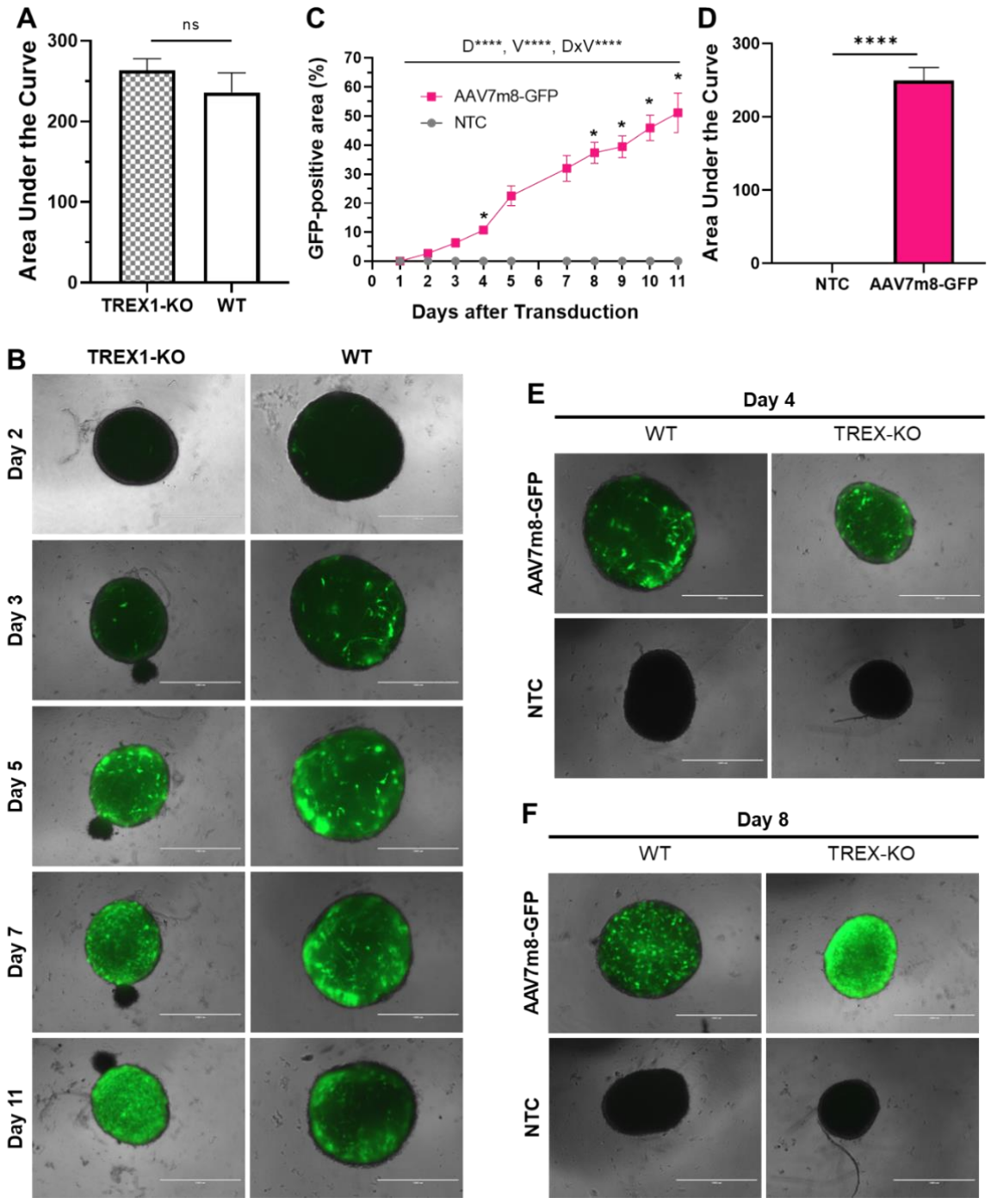

Figure 52. Transduction of individual brain organoids with AAV7m8 at $1 \cdot 10^{10}$ vg/well following protocol optimizations. A: Assessment of TREX-KO *vs* WT genotype influence on the accumulated GFP expression during the time course of the experiment (from day 1 to day 11 after transduction). Differences analyzed by t-test (ns). B: Representative EVOS images of TREX-KO and WT brain organoids showing live GFP signal at different time points after

transduction. C: Percentage of live GFP signal on the organoids area at different time points (days after transduction). Mean±SEM are represented per condition (AAV7m8-GFP and NTC) at each time point. Differences between the two conditions at each timepoint analyzed by two-way ANOVA and Sidak post hoc. D: variation due to the factor 'day', V: variation due to AAV-condition. DxV: interaction between D and V factors. D: Accumulated GFP expression (from day 1 to day 11 after transduction), calculated as the area under the curve from graph A. Mean±SEM are represented per condition. Differences analyzed by t-test. E, F: Representative EVOS images of brain organoids showing live GFP signal at days 4 and 8 after transduction, respectively. Scale bar: 1000 µm. Sample size (n): (A, B): TREX-KO=2, WT=2. (C-F): NTC=4, AAV7m8-GFP=4. *p<0.05, ****p<0.0001.

2. AAV transduction of WT and SETD5-KO self-assembled brain organoids

As an alternative to the AggreWell protocol (A), brain organoids can also be generated by spontaneous self-assembly of the iPSCs when they are cultured under rotation (B). This implies that the number of cells that get assembled is not accurately controlled, so the resulting organoids vary in number of cells and therefore in size. Briefly, these organoids, at around 50-days-old, do not present a homogeneous size, and they are so small that they cannot be individually spared in wells. Therefore, in the transduction experiments involving these self-generated organoids, we spared around 10 organoids per well in 96-well-plate wells prior to transduction. As a consequence, the AAV dose could not be stablished per individual organoid, but per well (vg/well). When various organoids are cultured in these small wells under rotation, they may fuse eventually, forming a unit that we considered an “organoid”. Herein, this type of brain organoids will be referred to as “grouped” or “fused” organoids, depending on whether they are individual units in a well or whether they are fused forming a single unit, respectively.

2.1. Dose set up for transducing fused brain organoids with AAV9 and AAV7m8 vectors

First of all, we aimed to determine an effective AAV dose for transducing small self-assembled brain organoids, so both AAV9-GFP and AAV7m8-GFP were tested at two different doses: $2.5 \cdot 10^{10}$ and $2.5 \cdot 10^{11}$ vg/well. Initially, these doses were estimated based on the results obtained in the first assays with AggreWell organoids, while considering the size and the total number of cells when transducing 10 self-assembled brain organoids per 96wp well. At the day of transduction (day 0), the 57-day-old organoids looked partially fused (Figure 53.A), as they had been spared in the 96wp wells in advance. Since this assay aimed to be a pilot experiment to adapt the transduction protocol to this type of organoids, a small sample size was used (n=1) and no statistical analysis was performed.

Transduction with the AAV9 serotype at either of the doses ($2.5 \cdot 10^{10}$ and $2.5 \cdot 10^{11}$ vg/well) generated a similar GFP expression curve (Figure 53.B) and a similar accumulated GFP expression over 16 days (Figure 53.C), indicating that 10 times more viral genomes were not worth to substantially increase the transgene expression. Therefore, the dose $2.5 \cdot 10^{10}$ vg/well was considered to be efficient enough for the AAV9.

The AAV7m8 seemed to generate a higher peak of GFP expression (on day 6) when administered at the higher dose ($2.5 \cdot 10^{11}$ vg/well), although it did not seem far higher than at the lower dose ($2.5 \cdot 10^{10}$ vg/well) (Figure 53.B). A similar trend was observed in the accumulated GFP expression over 16 days (Figure 53.C). Herein, the dose of $2.5 \cdot 10^{10}$ vg/well was considered efficient for AAV7m8, similar to the AAV9.

In addition to stablishing an effective AAV dose for transducing fused brain organoids, other observations were made following this assay. First, at day 3 after transduction, there was already a detectable GFP signal in all the conditions, being higher in the AAV7m8 transduced organoids (Figure 53.B, D). Second, at day 6, the AAV7m8-transduced organoids showed a peak of GFP expression, independent of the dose administered (Figure 53.B, E). In contrast, the expression peak of the AAV9-transduced organoids appeared later, at day 8 after transduction, and it was lower than that of the AAV7m8-transduced organoids, independent of the dose (Figure 53.B, F).

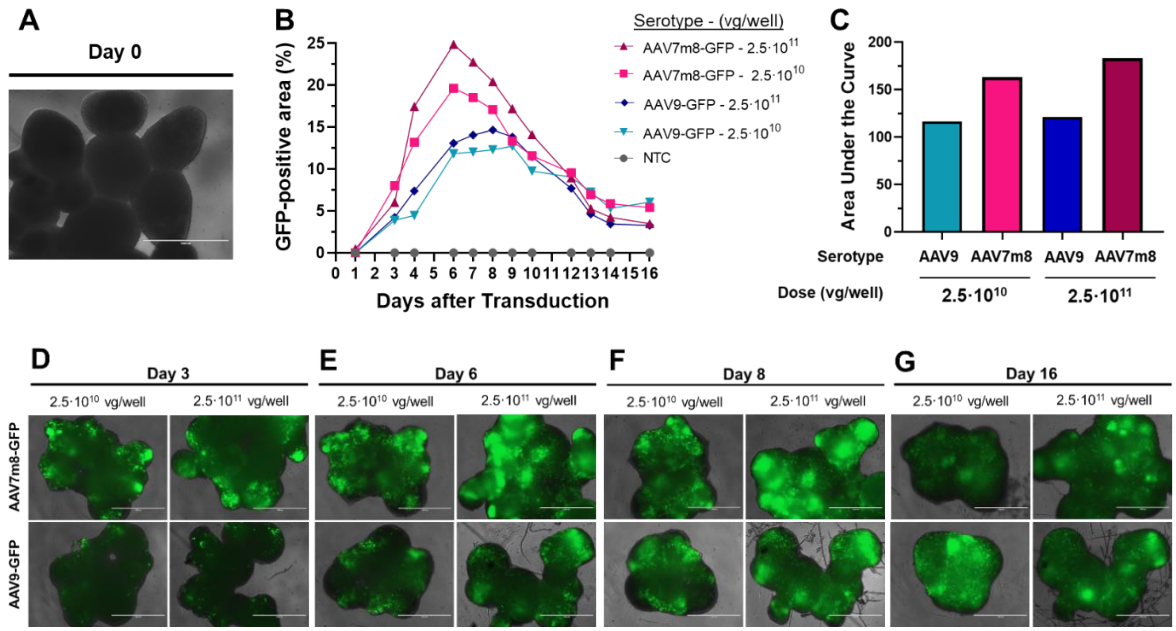

Figure 53. Dose set up for transducing self-assembled brain organoids with AAV9 and AAV7m8: $2.5 \cdot 10^{10}$ vs $2.5 \cdot 10^{11}$ vg/well. A: Representative image of one well of grouped organoids prior to transduction (day 0). B: Percentage of live GFP signal on the organoids area at different time points (days after transduction). C: Accumulated GFP expression during the time course of the experiment (from day 1 to day 16 after transduction), calculated as the area under the curve from graph B. D, E, F, G: EVOS images of brain organoids showing live GFP signal at days 3, 6, 8 and 16 after transduction. Scale bar: 1000 µm. Sample size: n=1.

In conclusion, we observed an intense and widespread GFP signal in fused brain organoids following AAV9-GFP and AAV7m8-GFP transduction at $2.5 \cdot 10^{10}$ vg/well, a dose of the same order of magnitude validated in the previous assays with AggreWell organoids ($1 \cdot 10^{10}$ vg/well). We did not observe a considerable better outcome when transducing at a dose 10 times higher ($2.5 \cdot 10^{11}$ vg/well). Therefore, we considered that the lower dose was suitable for transducing fused organoids. Besides, these results suggested that the AAV7m8 variant may be more efficient in fused organoids, based on the higher and earlier transgene expression compared to the AAV9 in spite of the dose administered, in agreement with the previous model. Nevertheless, further assays were required to confirm this observation.

2. 2. Comparing transduction efficiency of AAV9 *vs* AAV7m8 in fused brain organoids

Once the AAV dose of $2.5 \cdot 10^{10}$ vg/well was confirmed to be efficient for transducing fused brain organoids, we aimed to further compare the transduction efficiency of AAV7m8 and AAV9 in this type of brain organoids using a larger sample size. Herein, we transduced 63-day-old WT (n=4) and SETD5-KO (n=4) fused organoids with AAV7m8-GFP and AAV9-GFP and tracked the live GFP expression at different time points using the EVOS microscope. Non-transduced brain organoids (NTC) were used as a negative control of GFP signal (n=2).

In this experiment, the dose of $2.5 \cdot 10^{10}$ vg/well validated in the previous assay (section 2.1) was rounded off to $1 \cdot 10^{10}$ vg/well so it matched with the dose optimized for individual organoids (section 1.3), as we did not expect a different outcome at the same order of magnitude.

Given that SETD5-KO organoids presented signs of degradation and reduced cell viability in this experiment (Figure 54. I-J), they were analyzed separately from the WT. It should also be taken into account that the size of the fused organoids was highly heterogeneous, as previously described. This may influence the percentage of GFP positive area since the same AAV dose is used for transducing a different number of cells in each well.

In the WT fused brain organoids, the AAV7m8-GFP expression was higher at every time point after transduction, except on day 10, in which AAV9 showed an abrupt peak of GFP expression. With the data available, we could not find the reason underlaying those brusque ups and downs in the AAV9-mediated GFP expression. Further analyses using more

homogeneous brain organoids should be performed to better explain this phenomenon, including the quantification of viral genomes at different time points. The peak of AAV7m8 took place at around day 6, in which GFP signal was considerably higher than in AAV9-transduced organoids (Figure 54.A, E and F). Besides, the accumulated GFP signal over 14 days was significantly higher in the AAV7m8-transduced organoids compared to the AAV9 (Figure 54.B).

As for the SETD5-KO fused brain organoids, AAV7m8 transduction generated higher transgene expression than AAV9, as observed in the GFP-positive area at every time point after transduction (Figure 54.G) and in the accumulated GFP expression over 14 days (Figure 54.H). Like in the WT, the AAV7m8 expression peak took place at around day 6 (Figure 54.E, G), whereas AAV9 did not generate any expression peak and the GFP expression was maintained low (Figure 54.E), probably due to the reduced cell viability of the SETD5-KO organoids during this assay, as it can be observed in their degraded morphology and the presence of debris in the media (Figure 54.G-H).

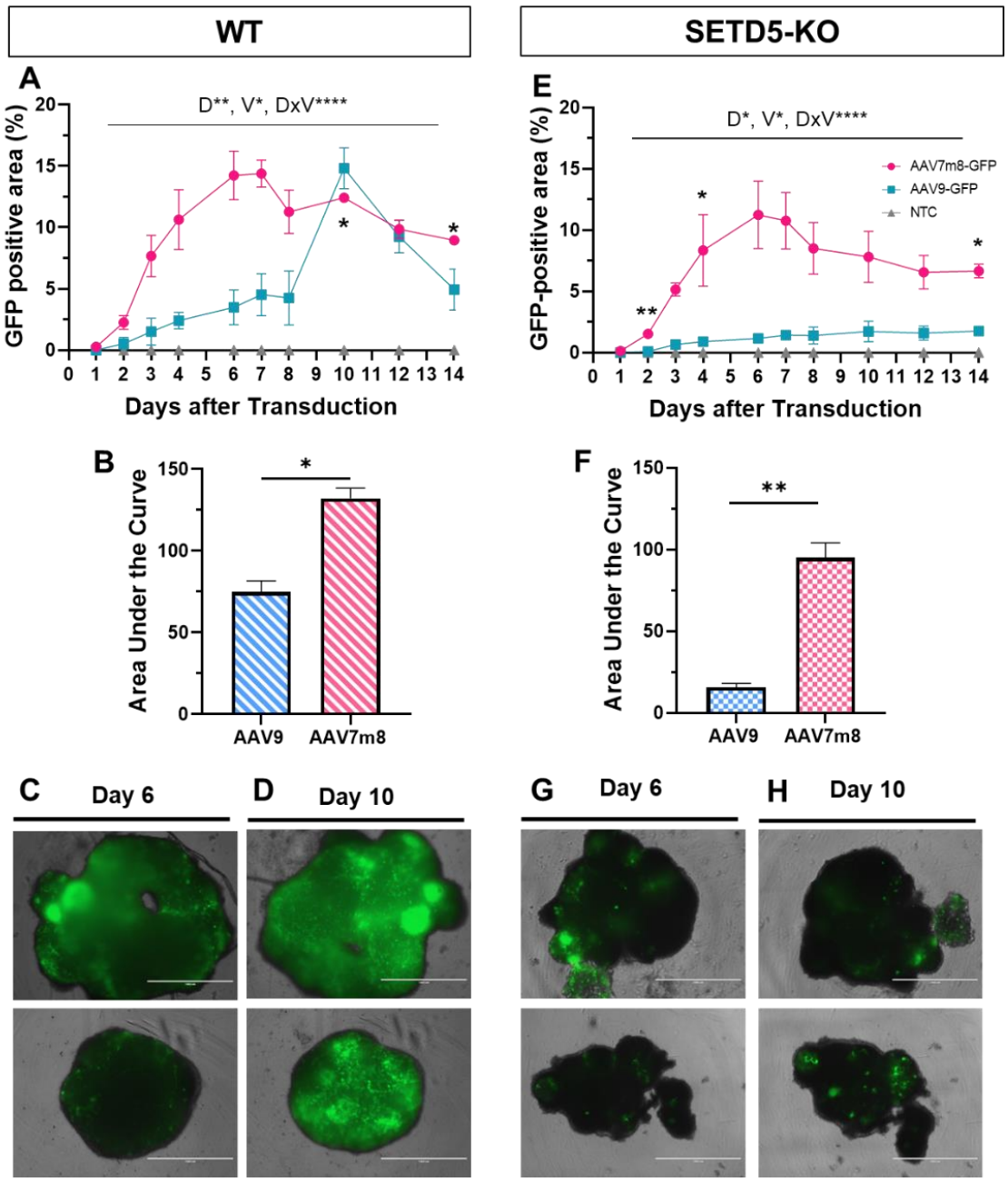

Figure 54. Comparison of the transduction efficiency of AAV9 *vs* AAV7m8 at $1 \cdot 10^{10}$ vg/well in WT (A-D) and SETD5-KO (E-H) fused brain organoids. A, E: Percentage of live GFP signal on WT organoids area at different time points (days after transduction). Mean±SEM are represented per AAV-condition (AAV7m8-GFP, AAV9-GFP and NTC) at each time point. Differences between the AAV-conditions at each timepoint analyzed by two-way ANOVA and Tuckey post hoc. D: variation due to the factor 'day', V: variation due to AAV-condition. DxV: interaction between D and V factors. B, F: Accumulated GFP expression during the time course of the experiment (from day 1 to day 14 after transduction), calculated as the area under the curve from graphs A and G, respectively. Mean±SEM are represented per AAV-condition. Differences analyzed by t-test. C-F, I-L: Representative EVOS images of the brain organoids at the expression peaks of AAV7m8 and AAV9, on day 6 and 10 after transduction, respectively. Scale bar: 1000 µm. Sample size (n): AAV7m8-GFP (WT=2, SETD5-KO=2), AAV9-GFP (WT=2, SETD5-KO=2); NTC=2. *p<0.05, **p<0.01, ***p<0.001, ****p<0.0001.

2. 3. AAV7m8 and AAV9 transduction in inner layers of brain organoids

In all the assays, the AAVs were administered to the organoids in the culture medium, so we would expect the transduced cells to be located mainly in the outer layers of the brain organoids. Thus, we used the EVOS microscope to quantify the live GFP expression in the organoids surface, as shown in the previous analyses. Nonetheless, we also aimed to investigate whether the AAVs administered to the media could trigger transgene expression in inner layers of the organoids. Hence, we performed immunohistochemistry to detect GFP in sliced organoids.

For this purpose, 63-day-old fused organoids were transduced with AAV7m8-GFP and AAV9-GFP at $1 \cdot 10^{10}$ vg/well. It is worth highlighting that the organoids used in this experiment were already fused in a single unit prior of the AAV transduction, as it can be observed in the EVOS live images (Figure 55.A). On day 22 after transduction, the organoids were fixed, sliced, and incubated with an anti-GFP antibody to immunodetect the transgenic GFP. The nuclei were dyed with DAPI (blue).

The immunofluorescence images of organoid sections showed GFP expression not only in the surface, but also in inner layers of the organoids transduced with both AAV7m8 and AAV9 vectors (Figure 55.B). Because the organoids were fused and formed a single unit prior to transduction, the central cells expressing GFP had not been transduced prior to organoids fusion. Instead, this transgene expression in inner cells implied either AAV diffusion from the media trough the external layers of the organoid to the inner cells, or retrograde transport from external projections to the internal somas, or a combination of both processes.

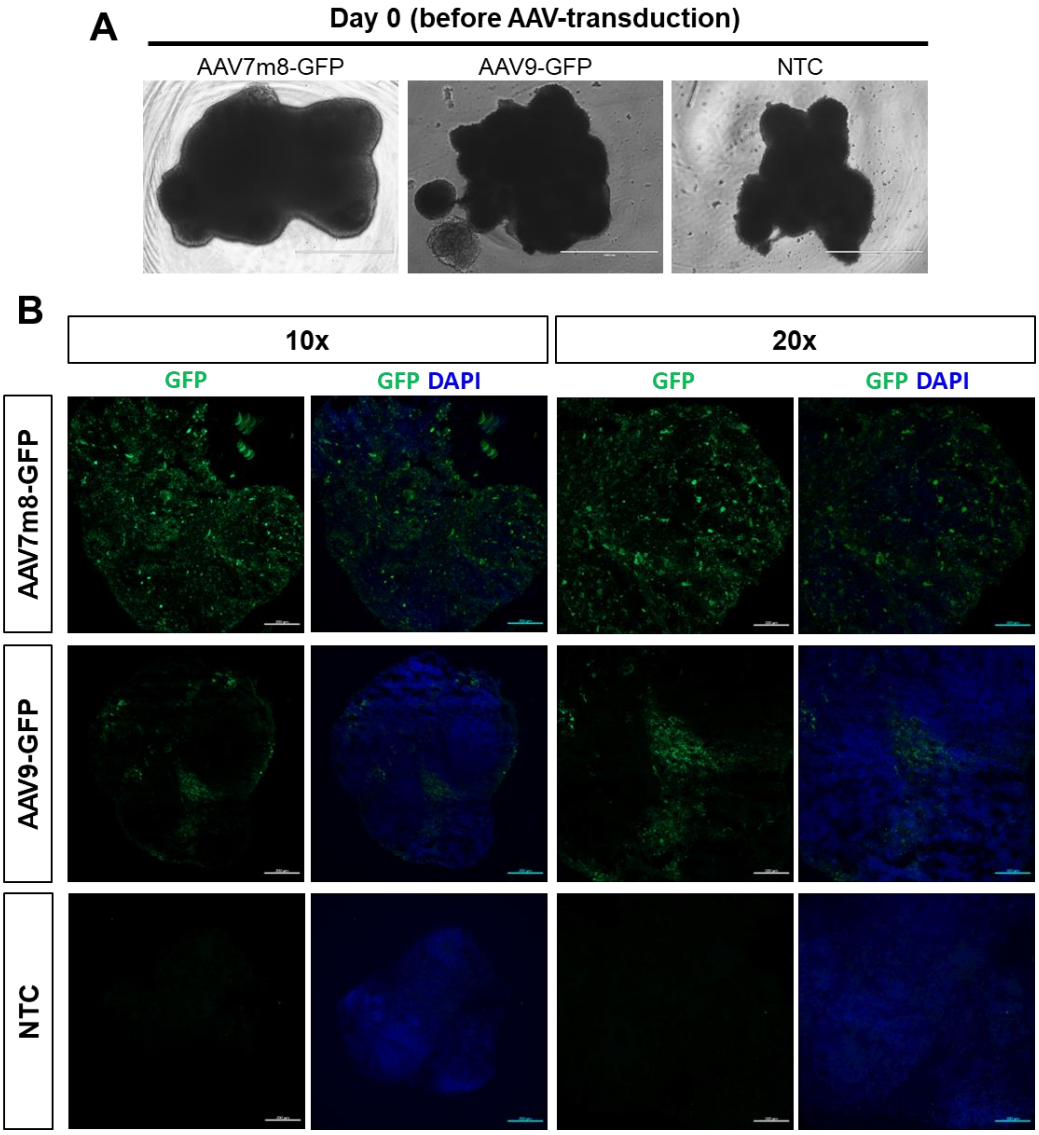

Figure 55. Transgene expression in inner layers of fussed brain organoids following transduction with AAV9 and AAV7m8 from the media. A: Representative images of the live organoids right before transduction (day 0) Scale bar: 1000 µm. B: Representative fluorescence images of immunostained sectioned organoids. Transgenic GFP was immunodetected using an anti-GFP antibody (green) and the cell nuclei were stained with DAPI (blue). Scale bar: 200 µm (10x) and 100 µm (20x).

DISCUSSION

AAV-base gene therapy has the potential to treat neurodegenerative disorders like AD, for which no treatment is yet available. However, the development of gene therapies for the human CNS is challenging due to the complexity and difficult accessibility of the brain as well as the limited translatability of traditional *in vitro* and *in vivo* CNS models to the clinic. In addition, AAV vector tropism and transduction efficiency present considerable interspecies variations, which hamper the translation of AAV-based therapies from animal models into humans. Consequently, translatable preclinical models of the human brain are urgently needed, along with AAV serotypes that efficiently transduce human brain cells.

In this context, we proposed the use of human brain organoids as a translatable and complementary model in preclinical research of AAV-gene therapy for neurological diseases. In this regard, we developed a protocol for AAV transduction in brain organoids and compared the transduction efficiency of two selected AAV serotypes: AAV9 and AAV7m8. On the one side, the AAV9 serotype has been widely used in *in vivo* gene therapy approaches for the CNS, in both preclinical and clinical trials (reviewed in [217]). The AAV9 is known to transduce all major cell types in brain (neurons, microglia, astrocytes, and oligodendrocytes), being particularly effective in driving transgene expression in cortical neurons. Moreover, its ability to undergo axonal transport leads to widespread distribution of vector genomes to distal projection sites [218]. Therefore, the AAV9 appeared a suitable serotype for transducing brain organoids, while having proved its translatability and safety *in vivo.* On the other side, the AAV7m8, a new variant derived from AAV2 [223], had demonstrated higher efficiency than other serotypes in transducing human iPSCs and iPSC-derived cortical and retinal neurons [224], [225]. Although prior to this study the AAV7m8 had not been tested for CNS transduction *in vivo* nor in brain organoids, it had showed high efficiency in retinal cells, both in organoids and animal models [226], [227], [337]. Based on this data, the AAV7m8 variant seemed a promising candidate for transducing brain organoids.

Besides, we used two types of brain organoids modelling neurological diseases, TREX1-KO [290] and SETD5-KO (Dr A. Muotri's personal communication), and their corresponding WT healthy controls, all of them derived from human iPSCs by two different methods (A and B, respectively), whose particularities were extensively explained in the previous section.

1. The AAV7m8 variant is more efficient than the AAV9 for transducing brain organoids, regardless of their morphology and genetic background

Our results revealed a higher transduction efficiency of AAV7m8 compared with AAV9 in human brain organoids. This was evidenced not only by the higher percentage of GFP expression in the organoid surface at any timepoint after transduction, but also by the accumulated GFP expression over the time course of all the experiments (from 11 to 16 days). In addition, the GFP signal was detectable earlier following AAV7m8 transduction compared to AAV9, suggesting that the AAV7m8 variant is more efficient in entering human brain cells, uncoating the capsid, escaping the endosome, and/or entering the nucleus. These downstream processes are rate-limiting steps that determine the efficiency and specificity of the different AAV serotypes, being of high relevance for *in vivo* CNS gene therapies [338], [339]. Because AAV7m8 only differs to the AAV2 serotype in a 7-amino acid insertion, it could be plausible that AV7m8 has increased efficiency in entering the cells. This would imply that various genome copies could easily enter a single cell, and if both plus and minus strands coincided, they would hybridize and form a pseudo-double DNA strand that could be immediately expressed. In that case, the delaying step of complementary-strand synthesis would not be required to start transgene expression. This would explain the detection of GFP as early as 24 h following AAV7m8 transduction at our standard dose ($1{\cdot}10^{10}$ vg/org), which was not observed with the AAV9 in any of our experiments, even at higher doses.

Another convincing explanation could be a better diffusion of the AAV7m8 through the organoid, based on the results observed in retinal gene therapy. Unlike most AAVs, the AAV2 serotype has shown ability to cross the inner limiting membrane, allowing efficient transduction of the retina after intravitreal administration. Since AAV7m8 was evolved from AAV2 to increase its efficiency to cross the inner limiting membrane [223], the high transduction efficiency of AAV7m8 observed in the brain organoids may be derived from this property, leading to an increased ability to cross the organoid structure as well.

In a recent work in which retinal organoids were transduced with the AAV7m8 variant at the same dose than ours, fluorescence was not detected until day 5 [227]. In that experiment, the reporter gene expression was driven by the CAG promoter, while we used the CMV, suggesting that the early GFP detection might be influenced by the promoter. In the CNS, the CMV promoter provides high initial neural expression that diminishes over time due to silencing in some brain tissues [324], [340]. However, since these were short-term *in vitro* approaches and both the CMV and CAG are powerful, ubiquitous, robust promoters, our

discrepancies with McClements et al. [227] might be rather explained because our ratio of infectious particles per AAV virion was superior.

Remarkably, the superior efficiency of AAV7m8 over AAV9 was consistent across our experiments with different types of brain organoids despite their size and genetic background. On one side, the results were replicated in brain organoids differentiated by alternative protocols (A and B), which involves differential morphology and size in the organoids generated. On the other side, our results were consistent in brain organoids from iPSCs of different donors (two different WT, healthy models), as well as in *knock out* models of neurological diseases (TREX1-KO and SETD5-KO). The high transduction efficiency of the AAV7m8 variant has also been reported by other groups in retinal organoids [226], [227], [337]. However, prior to this work, successful transduction of human brain organoids with the AAV7m8 variant had never been reported.

2. The morphology and size of the brain organoids influences the efficiency of AAV transduction

The levels and the onset of GFP detection was different depending on the morphology of the brain organoids transduced. Particularly, when comparing AAV7m8- *vs* AAV9-mediated GFP expression at the same dose ($1{\cdot}10^{10}$ vg/well), significant differences between the vectors were detected on day 5 in AggreWell organoids (A), whereas on day 2 in self-assembled (B) SETD5-KO organoids. This suggests that the morphology of the organoids influences the onset of transgene detection. As previously mentioned, self-assembled brain organoids (B) are much smaller than the AggreWell-generated (A), and the KO models of neurological disease are smaller than the WT. When the self-assembled brain organoids are spared in 96wp wells, they fuse and form an irregular 3D structure that is not spheric like the individual AggreWell-generated but composed of smaller spheres fused. Consequently, the organoid surface (and number of cells) in contact with the media, where the AAVs are suspended, is higher for the fused organoids than for the individual. When increasing AAV particles transduce a single cell, increasing GFP protein is accumulated, which is a requirement to detect GFP live signal in the EVOS microscope.

Therefore, this event occurs earlier in the fused brain organoids due to the relative smaller size of the spheroids and the irregular morphology of the fused units.

The influence of the organoids size on the AAV transduction efficiency was also observed in other studies with retinal organoids [227]. In any case, the exact onset of transgene expression for each AAV variant should be further determined using more homogenous brain organoids and a higher number of replicates.

3. An optimized protocol for AAV transduction and live tracking of transgene expression in human brain organoids was established

At the time these experiments were performed, there was no published protocol for AAV transduction in brain organoids. Neither there were precedents of culturing individualized brain organoids in single wells of 96-well plates, which is specially challenging due to the reduced cell viability of organoids when they are not cultured in higher densities. One study reported transduction of single brain organoids in a 96-well plate, although they were only maintained individualized for 1 hour [275].

Importantly, we managed to culture the individual brain organoids in single wells until the end point of the experiments (for 11 to 22 days, depending on the assay). This allowed us to track and quantify the live GFP expression in particular organoids daily, obtaining an expression curve of the reporter transgene for each individual. Our method provides useful data to further study the relationship between organoid size, AAV dose and transgene expression, and could contribute to the dose scalability in more complex approaches. Recently, the success of a similar approach was reported using retinal organoids, supporting the feasibility of the method despite the differences between the models [227]. In contrast, other groups have performed immunohistochemistry for transgene expression analysis, which only allows GFP quantification at a single time point for each individual organoid [275], [341]. Of note, only one of those published works used brain organoid.

One of the most relevant improvements of the protocol was the optimization of the AAV dose. To date, there is only one published work transducing human brain organoids by adding the AAV to the media [275], similar to our approach. In that work, they transduced $6 \cdot 10^{11}$ vg per organoid in a volume of 35 µL, resulting in a concentration of $1.71 \cdot 10^{10}$ vg/µL. In contrast, our dose of $1 \cdot 10^{10}$ vg per organoid was 60 times lower, and our volume of transduction (100 µL) resulted in an AAV concentration around 100-fold lower ($1 \cdot 10^{8}$ vg/µL). Another group transduced brain organoids with AAV9 at $3 \cdot 10^{10}$ vg/org by direct microinjection into the organoids. While that technique may increase the transduction

efficiency, it is a much more arduous, time-consuming, and technically limiting method compared to ours, and still, their dose was 3 times higher than ours [342].

Even though our standard dose of choice was $1{\cdot}10^{10}$ vg/org, we obtained a higher GFP expression with AAV7m8 at $1{\cdot}10^{9}$ vg/org than with ten times more of AAV9 ($1{\cdot}10^{10}$ vg/org). This not only supports the superiority of AAV7m8 over AAV9 in brain organoid transduction, but also indicates that the dose of AAV7m8 could be further reduced. The reason why we administered $1{\cdot}10^{10}$ vg/org in most of our experiments, was because we aimed to compare the AAV9 *vs* the AAV7m8, and the AAV9 did not generate any detectable transgene expression at a lower dose ($1{\cdot}10^{9}$ vg/org). An efficient AAV transduction with a reduced dose is of high relevance for the translatability of AAV-based gene therapies to the clinic. As explained in previous sections, the risk of immune responses upon AAV administration *in vivo* is highly associated to the capsid dose. Therefore, an AAV that efficiently transduces the target cells would reach therapeutic efficacy at a low dose, herein reducing the risk of an anti-capsid cytotoxic response [192]. In addition, an effectual low-dose AAV-therapy would be greatly beneficial, given the limited capacity of large-scale AAV manufacturing, as increasing number of patients could be treated from a single AAV production batch. This would accelerate the progression of clinical trials, as well as reduce the high costs of the AAV therapies derived from manufacturing [209].

Once the transduction dose was established and the AAV7m8 variant was proved more efficient in our brain organoids, we developed protocol innovations that increased the transgenic GFP expression from 10% to up to 50% in the individual organoids. Furthermore, we obtained increasing GFP signal during all the time course of the assay, pointing sustained transgene expression for at least 11 days, whereas in previous experiments GFP signal decayed after day 9. The protocol incorporated changes in the timing of media replacements after transduction and the addition of conditioned media. Those changes led to enhanced organoid fitness and viability, indicating that the increased transgene expression was directly related to the improvement of cell viability in the brain organoids.

4. AAV7m8 and AA9 generate transgene expression in inner layers of brain organoids

Because our brain organoids were transduced by adding the AAV to their culture media, we might expect that transgene expression would mainly occur in the surface of the organoids. Interestingly, immunostaining and imaging of sectioned organoids also revealed GFP expression in inner layers following transduction with both AAV9 and AAV7m8. Transgene

expression in deeper layers of brain organoids had previously been detected with the AAV9 serotype, though at a lower degree [275]. Nonetheless, this was the first time described with the AAV7m8 variant when administered in the culture media. The mechanisms underlaying transgene expression in deep layers of the organoid may be anterograde and retrograde axonal transport, previously reported for the AAV9 [343], [344]. Another possibility could be that the AAV particles diffused through the organoid and transduced cells in inner layers.

From a translational perspective, it would be interesting to investigate and exploit the mechanism by which these AAV vectors, and in particular the AAV7m8, generates transgene expression in deep layers of brain organoids, as well as comparing it to AAV2, from which AAV7m8 was evolved. This could have crucial implications for the clinical translation of AAV gene therapy for neurological disorders like AD, in which a single AAV injection should reach widespread transgene expression in deep regions of the brain

5. Further considerations and future perspectives

In summary, the present study entails a preliminary approach for the use of brain organoids as a preclinical model of AAV-based gene therapy for the CNS. We have established and optimized a protocol and a dose for brain organoid transduction, as well as identified the AAV7m8 variant as a promising candidate to target human CNS cells. Therefore, in the context of our research, the next step will be to evaluate the therapeutic effect of AAV-mediated KL expression in this model. Besides, although we managed to transduce two models of neurological diseases (TREX-KO and SETD5-KO) presenting common features with AD [290], [345], in future experiments we would use brain organoids presenting the phenotype and/or genetic background of AD. An ideal study should also incorporate brain organoids derived from diverse AD patients and healthy donors, as well as larger sample sizes, to strength the potential of our AAV-based KL gene therapy to treat AD.

From a translational perspective, we propose the AAV7m8 as a vector of choice for gene transfer to the human CNS. The increased transduction efficiency of AAV7m8 could be advantageous for reducing the dose-dependent immune response against AAV capsids observed in humans, as it could be administered at lower doses [241], [346].

Nonetheless, the mechanism underlaying the enhanced transduction properties of the AAV7m8 in human brain cells remains to be elucidated. The brain organoids used in our study are composed of different cell types (neurons, glia, and neural progenitors) [290]

whose proportion and location may be heterogeneous at different time-points and among different genotypes. Hence, the tropism of the AAV7m8 vector should be further characterized in cells of the CNS. In future experiments with brain organoids, the cell types expressing the transgene following AAV7m8 transduction could be analyzed by immunohistochemistry or flux cytometry.

This work supports the use of brain organoids to model the human CNS and to test the potential of AAV-based gene therapies, as they present a human genetic background lacking in animal models. Furthermore, genetic modification of iPSC enables the generation of patient-specific organoids, that could be of high utility for modelling neurodegenerative diseases in which human tissue is inaccessible, like AD, but also for rare diseases and personalized medicine approaches [347], [348].

Despite the numerous advantages of brain organoids, it should be acknowledged that their use for the development gene therapies against neurological diseases may present some limitations. First, although much progress is being made in the generation of more complex brain organoids, they still lack vasculature, BBB and a functional immune system. In gene therapy strategies, those features are highly relevant to predict the biodistribution and a potential immune/inflammatory response following *in vivo* delivery of gene therapy vectors [349], [350]. Second, brain organoids are far from representing the size of the human brain, making challenging the AAV dose scaling. In addition, it must be taken into account that organoids are obtained from iPSCs, so they could present a developmentally immature phenotype that may not accurately model an adult patient, like those suffering age-related disorders like AD [351], [352]. Finally, memory and cognitive decline are key symptoms of AD that cannot be evaluated using *in vitro* models. Therefore, animal models are still needed in the preclinical research of therapies against neurodegenerative diseases to study behavioral patterns and cognitive capacities. Nonetheless, the complementary use of brain organoids in preclinical research could potentially reduce the use of animal models, circumventing ethical issues, reducing costs, and accelerating the obtention of relevant results in a human context.

CONCLUSIONS

From the results obtained in the present doctoral thesis, the conclusions are the following:

1. The relative expression of the two alternative Klotho transcripts (sKL and mKL) was described for the first time in the human brain, being sKL the most expressed variant in all the parenchymal areas analyzed (frontal and entorhinal cortex, hippocampus, and amygdala), whereas in choroid plexus mKL was the predominant. The expression profile of *sKL* and *mKL* is not homogeneous through the different regions of the brain nor among different species. In the principal animal models used for neurological research (mouse, rat and Microcebus), the expression ratio of sKL *vs* mKL in brain is inverted with respect to humans, being mKL the predominant variant in those species.

2. The relative gene expression of sKL and mKL is altered in brain during Alzheimer's disease. In frontal cortex, hippocampus, and choroid plexus, sKL expression tended to increase respect to mKL in AD patients compared to healthy individuals. Conversely, in the 3xTg-AD mouse model, the altered sKL *vs* mKL ratio compared to WT seemed caused by a decreased expression of sKL respect to mKL.

3. Altered levels of soluble Klotho protein in CSF are associated with Alzheimer's disease. First, in AD patients with Mild Dementia, KL levels are significantly decreased compared to healthy adults. Second, in elder MD AD patients there is a positive correlation of KL levels with age that is not found in cognitively healthy elder individuals. Third, carriers of the APOE4 allele, the major genetic risk factor of AD, present significantly lower levels of KL in CSF. Significant differences in CSF KL levels based on sex were not found in the healthy nor in the AD groups analyzed.

4. For the first time, the ability of sKL to counteract cognitive deficits through AAV9-mediated gene therapy was tested in the 3xTg-AD and the new APP/Tau mouse models of AD. In 3xTg-AD females and APP/Tau males, sKL gene transfer tended to improve the spatial learning and the reference memory in the MWM test. APP/Tau and WT females overexpressing sKL showed improved recognition and spatial

memory in the NOR and T-maze tests. The beneficial effects of sKL on AD-related cognitive deficits were more modest than expected, probably due to the lack of profound AD symptoms in these mouse models at the age tested.

5. The AAV7m8 variant proved to be more efficient than the AAV9 serotype in transducing human iPSCs-derived brain organoids regardless of their genetic background, morphology, and differentiation method. An efficient transduction protocol and AAV dose were stablished, achieving transgene expression even in inner layers of the brain organoids with either of the serotypes tested. Human iPSCs-derived brain organoids show promise as a feasible, translatable model complementary to experimental animals in preclinical research of AAV-based gene therapy for neurological diseases.

BIBLIOGRAPHY

[1] "2022 Alzheimer's disease facts and figures," *Alzheimer's Dement.*, vol. 18, no. 4, pp. 700–789, Apr. 2022, doi: 10.1002/alz.12638.

[2] M. V. F. Silva, C. D. M. G. Loures, L. C. V. Alves, L. C. de Souza, K. B. G. Borges, and M. D. G. Carvalho, "Alzheimer's disease: risk factors and potentially protective measures," *J Biomed Sci.*, vol. 26, no. 1, May 2019, doi: 10.1186/S12929-019-0524-Y.

[3] S. Gauthier, P. Rosa-Neto, J. Morais, and C. Webster, "World Alzheimer Report 2021: Journey through the diagnosis of dementia," Sep. 2021. Accessed: Jul. 15, 2022. [Online]. Available: https://www.alzint.org/resource/world-alzheimer-report-2021/

[4] R. Brookmeyer, E. Johnson, K. Ziegler-Graham, and H. M. Arrighi, "Forecasting the global burden of Alzheimer's disease," *Alzheimer's Dement*, vol. 3, no. 3, pp. 186–191, Jul. 2007, doi: 10.1016/J.JALZ.2007.04.381.

[5] National Institute on Aging, "What Causes Alzheimer's Disease?" https://www.nia.nih.gov/health/what-causes-alzheimers-disease (accessed Jan. 04, 2023).

[6] M. Sano, J. Chen, T. Tatemichi, Y. Stern, and R. Mayeux, "Risk of dementia in first-degree relatives of patients with Alzheimer's disease and related disorders," *Arch Neurol*, vol. 48, no. 3, pp. 269–273, Mar. 1991, doi: 10.1001/archneur.1991.00530150037014.

[7] M. Kivipelto *et al.*, "Midlife vascular risk factors and Alzheimer's disease in later life: longitudinal, population-based study," *BMJ*, vol. 322, no. 7300, pp. 1447–1451, Jun. 2001, doi: 10.1136/BMJ.322.7300.1447.

[8] C. Ballard, S. Gauthier, A. Corbett, C. Brayne, D. Aarsland, and E. Jones, "Alzheimer's disease," *Lancet*, vol. 377, no. 9770, pp. 1019–1031, 2011, doi: 10.1016/S0140-6736(10)61349-9.

[9] M. Giri, M. Zhang, and Y. Lü, "Genes associated with Alzheimer's disease: an overview and current status," *Clin Interv Aging*, vol. 11, pp. 665–681, May 2016, doi: 10.2147/CIA.S105769.

[10] R. Cacace, K. Sleegers, and C. van Broeckhoven, "Molecular genetics of early-onset Alzheimer's disease revisited," *Alzheimers Dement*, vol. 12, no. 6, pp. 733–748, Jun. 2016, doi: 10.1016/J.JALZ.2016.01.012.

[11] E. H. Corder *et al.*, "Gene dose of apolipoprotein E type 4 allele and the risk of Alzheimer's disease in late onset families," *Science*, vol. 261, no. 5123, pp. 921–923, 1993, doi: 10.1126/SCIENCE.8346443.

[12] J. Viña and A. Lloret, “Why women have more Alzheimer’s disease than men: gender and mitochondrial toxicity of amyloid-beta peptide,” *J Alzheimers Dis*, vol. 20 Suppl 2, pp. S527–S533, 2010, doi: 10.3233/JAD-2010-100501.

[13] K. B. Rajan, J. Weuve, L. L. Barnes, E. A. McAninch, R. S. Wilson, and D. A. Evans, “Population estimate of people with clinical Alzheimer’s disease and mild cognitive impairment in the United States (2020-2060),” *Alzheimers Dement*, vol. 17, no. 12, pp. 1966–1975, Dec. 2021, doi: 10.1002/ALZ.12362.

[14] J. J. Ryan, L. G. Umfleet, D. S. Kreiner, A. M. Fuller, and A. M. Paolo, “Neuropsychological differences between men and women with Alzheimer’s disease,” *Int J Neurosci.*, vol. 128, no. 4, pp. 342–348, Apr. 2018, doi: 10.1080/00207454.2017.1382492.

[15] G. Chêne *et al.*, “Gender and incidence of dementia in the Framingham Heart Study from mid-adult life,” *Alzheimers Dement*, vol. 11, no. 3, pp. 310–320, Mar. 2015, doi: 10.1016/J.JALZ.2013.10.005.

[16] S. Seshadri *et al.*, “Lifetime risk of dementia and Alzheimer’s disease. The impact of mortality on risk estimates in the Framingham Study,” *Neurology*, vol. 49, no. 6, pp. 1498–1504, 1997, doi: 10.1212/WNL.49.6.1498.

[17] L. E. Hebert, P. A. Scherr, J. J. McCann, L. A. Beckett, and D. A. Evans, “Is the risk of developing Alzheimer’s disease greater for women than for men?”, *Epidemiol Rev.*, vol. 153, no. 2, pp. 132–136, Jan. 2001, doi: 10.1093/AJE/153.2.132.

[18] L. Letenneur, V. Gilleron, D. Commenges, C. Helmer, J. M. Orgogozo, and J. F. Dartigues, “Are sex and educational level independent predictors of dementia and Alzheimer’s disease? Incidence data from the PAQUID project,” *J Neurol Neurosurg Psychiatry*, vol. 66, no. 2, pp. 177–183, 1999, doi: 10.1136/JNNP.66.2.177.

[19] F. E. Matthews *et al.*, “A two decade dementia incidence comparison from the Cognitive Function and Ageing Studies I and II,” *Nat Commun.* , vol. 7, Apr. 2016, doi: 10.1038/NCOMMS11398.

[20] S. E. Tom *et al.*, “Characterization of dementia and Alzheimer’s disease in an older population: updated incidence and life expectancy with and without dementia,” *Am J Public Health*, vol. 105, no. 2, pp. 408–413, Feb. 2015, doi: 10.2105/AJPH.2014.301935.

[21] C. Kawas, S. Gray, R. Brookmeyer, J. Fozard, and A. Zonderman, “Age-specific incidence rates of Alzheimer’s disease: the Baltimore Longitudinal Study of Aging,” *Neurology*, vol. 54, no. 11, pp. 2072–2077, Jun. 2000, doi: 10.1212/WNL.54.11.2072.

[22] W. A. Rocca, “Time, Sex, Gender, History, and Dementia,” *Alzheimer Dis Assoc Disord*, vol. 31, no. 1, pp. 76–79, 2017, doi: 10.1097/WAD.0000000000000187.

[23] M. M. Mielke, M. T. Ferretti, M. F. Iulita, K. Hayden, and A. S. Khachaturian, “Sex and gender in Alzheimer’s disease - Does it matter?”, *Alzheimers Dement*, vol. 14, no. 9, pp. 1101–1103, Sep. 2018, doi: 10.1016/J.JALZ.2018.08.003.

[24] M. M. Weber, “Aloys Alzheimer, a coworker of Emil Kraepelin,” *J Psychiatr Res*, vol. 31, no. 6, pp. 635–643, 1997, doi: 10.1016/S0022-3956(97)00035-6.

[25] C. A. Ross and M. A. Poirier, “Protein aggregation and neurodegenerative disease,” *Nat Med.*, vol. 10 Suppl, no. 7, p. S10, 2004, doi: 10.1038/NM1066.

[26] D. Goldgaber, M. I. Lerman, O. W. McBride, U. Saffiotti, and D. C. Gajdusek, “Characterization and chromosomal localization of a cDNA encoding brain amyloid of Alzheimer’s disease,” *Science*, vol. 235, no. 4791, pp. 877–880, 1987, doi: 10.1126/SCIENCE.3810169.

[27] U. C. Müller and H. Zheng, “Physiological functions of APP family proteins,” *Cold Spring Harb Perspect Med*, vol. 2, no. 2, 2012, doi: 10.1101/CSHPERSPECT.A006288.

[28] M. P. Demars, A. Bartholomew, Z. Strakova, and O. Lazarov, “Soluble amyloid precursor protein: a novel proliferation factor of adult progenitor cells of ectodermal and mesodermal origin,” *Stem Cell Res Ther*, vol. 2, no. 4, 2011, doi: 10.1186/SCRT77.

[29] J. Nunan and D. H. Small, “Regulation of APP cleavage by alpha-, beta- and gamma-secretases,” *FEBS Lett*, vol. 483, no. 1, pp. 6–10, Oct. 2000, doi: 10.1016/S0014-5793(00)02076-7.

[30] A. Serrano-Pozo, M. P. Frosch, E. Masliah, and B. T. Hyman, “Neuropathological alterations in Alzheimer disease,” *Cold Spring Harb Perspect Med*, vol. 1, no. 1, Sep. 2011, doi: 10.1101/CSHPERSPECT.A006189.

[31] E. Masliah, R. D. Terry, M. Mallory, M. Alford, and L. A. Hansen, “Diffuse plaques do not accentuate synapse loss in Alzheimer’s disease.,” *Am J Pathol.*, vol. 137, no. 6, p. 1293, 1990.

[32] R. B. Knowles *et al.*, “Plaque-induced neurite abnormalities: implications for disruption of neural networks in Alzheimer’s disease,” *Proc Natl Acad Sci U S A*, vol. 96, no. 9, pp. 5274–5279, Apr. 1999, doi: 10.1073/PNAS.96.9.5274.

[33] J. A. Hardy and G. A. Higgins, “Alzheimer’s disease: the amyloid cascade hypothesis,” *Science*, vol. 256, no. 5054, pp. 184–185, 1992, doi: 10.1126/SCIENCE.1566067.

[34] G. P. Morris, I. A. Clark, and B. Vissel, “Questions concerning the role of amyloid-β in the definition, aetiology and diagnosis of Alzheimer’s disease,” *Acta Neuropathol.*, vol. 136, no. 5, pp. 663–689, Nov. 2018, doi: 10.1007/S00401-018-1918-8.

[35] M. Tolar, S. Abushakra, and M. Sabbagh, “The path forward in Alzheimer’s disease therapeutics: Reevaluating the amyloid cascade hypothesis,” *Alzheimer’s Dement.*, vol. 16, no. 11, pp. 1553–1560, Nov. 2020, doi: 10.1016/j.jalz.2019.09.075.

[36] G. Lee, R. L. Neve, and K. S. Kosik, “The microtubule binding domain of tau protein,” *Neuron*, vol. 2, no. 6, pp. 1615–1624, 1989, doi: 10.1016/0896-6273(89)90050-0.

[37] E. Kopke, Y. C. Tung, S. Shaikh, C. A. del Alonso, K. Iqbal, and I. Grundke-Iqbal, “Microtubule-associated protein tau. Abnormal phosphorylation of a non-paired helical filament pool in Alzheimer disease.,” *J Biol Chem.*, vol. 268, no. 32, pp. 24374–24384, Nov. 1993, doi: 10.1016/S0021-9258(20)80536-5.

[38] M. Butler and M. L. Shelanski, “Microheterogeneity of microtubule-associated tau proteins is due to differences in phosphorylation,” *J Neurochem*, vol. 47, no. 5, pp. 1517–1522, 1986, doi: 10.1111/J.1471-4159.1986.TB00788.X.

[39] A. Lloret, T. Fuchsberger, E. Giraldo, and J. Viña, “Molecular mechanisms linking amyloid β toxicity and Tau hyperphosphorylation in Alzheimer‘s disease,” *Free Radic Biol Med*, vol. 83, pp. 186–191, Jun. 2015, doi: 10.1016/J.FREERADBIOMED.2015.02.028.

[40] C. N. Parkhurst *et al.*, “Microglia promote learning-dependent synapse formation through brain-derived neurotrophic factor,” *Cell*, vol. 155, no. 7, pp. 1596–1609, Dec. 2013, doi: 10.1016/J.CELL.2013.11.030.

[41] C. Ising and M. T. Heneka, “Functional and structural damage of neurons by innate immune mechanisms during neurodegeneration,” *Cell Death Dis*, vol. 9, no. 2, Feb. 2018, doi: 10.1038/S41419-017-0153-X.

[42] D. v. Hansen, J. E. Hanson, and M. Sheng, “Microglia in Alzheimer’s disease,” *J Cell Biol*, vol. 217, no. 2, pp. 459–472, Feb. 2018, doi: 10.1083/JCB.201709069.

[43] M. T. Heneka *et al.*, “NLRP3 is activated in Alzheimer’s disease and contributes to pathology in APP/PS1 mice,” *Nature*, vol. 493, no. 7434, pp. 674–678, Jan. 2013, doi: 10.1038/NATURE11729.

[44] T. Goldmann, T. L. Tay, and M. Prinz, “Love and death: microglia, NLRP3 and the Alzheimer’s brain,” *Cell Res*, vol. 23, no. 5, pp. 595–596, May 2013, doi: 10.1038/CR.2013.24.

[45] M. Saresella *et al.*, “The NLRP3 and NLRP1 inflammasomes are activated in Alzheimer’s disease,” *Mol Neurodegener.*, vol. 11, no. 23, Mar. 2016, doi: 10.1186/S13024-016-0088-1.

[46] C. Ising *et al.*, “NLRP3 inflammasome activation drives tau pathology,” *Nature*, vol. 575, no. 7784, pp. 669–673, Nov. 2019, doi: 10.1038/S41586-019-1769-Z.

[47] G. C. Brown and J. J. Neher, “Microglial phagocytosis of live neurons,” *Nat Rev Neurosci.* , vol. 15, no. 4, pp. 209–216, Apr. 2014, doi: 10.1038/NRN3710.

[48] F. Giovannoni and F. J. Quintana, “The Role of Astrocytes in CNS Inflammation,” *Trends Immunol*, vol. 41, no. 9, pp. 805–819, Sep. 2020, doi: 10.1016/J.IT.2020.07.007.

[49] R. Thangavel, D. Stolmeier, X. Yang, P. Anantharam, and A. Zaheer, “Expression of glia maturation factor in neuropathological lesions of Alzheimer’s disease,” *Neuropathol Appl Neurobiol*, vol. 38, no. 6, pp. 572–581, Oct. 2012, doi: 10.1111/J.1365-2990.2011.01232.X.

[50] R. Pihlaja, J. Koistinaho, R. Kauppinen, J. Sandholm, H. Tanila, and M. Koistinaho, “Multiple cellular and molecular mechanisms are involved in human Aβ clearance by transplanted adult astrocytes,” *Glia*, vol. 59, no. 11, pp. 1643–1657, Nov. 2011, doi: 10.1002/GLIA.21212.

[51] H. Akiyama *et al.*, “Inflammation and Alzheimer’s disease,” *Neurobiol Aging*, vol. 21, no. 3, pp. 383–421, 2000, doi: 10.1016/S0197-4580(00)00124-X.

[52] M. S. Uddin *et al.*, “Autophagy and Alzheimer’s Disease: From Molecular Mechanisms to Therapeutic Implications,” *Front Aging Neurosci*, vol. 10, no. 04, Jan. 2018, doi: 10.3389/FNAGI.2018.00004.

[53] C. Z. Cai *et al.*, “Enhancing autophagy maturation with CCZ1-MON1A complex alleviates neuropathology and memory defects in Alzheimer disease models,” *Theranostics*, vol. 12, no. 4, pp. 1738–1755, Jan. 2022, doi: 10.7150/THNO.64148.

[54] G. M. McKhann *et al.*, “The diagnosis of dementia due to Alzheimer’s disease: recommendations from the National Institute on Aging-Alzheimer’s Association workgroups on diagnostic guidelines for Alzheimer’s disease,” *Alzheimers Dement*, vol. 7, no. 3, pp. 263–269, 2011, doi: 10.1016/J.JALZ.2011.03.005.

[55] M. S. Albert *et al.*, “The diagnosis of mild cognitive impairment due to Alzheimer’s disease: recommendations from the National Institute on Aging-Alzheimer’s Association workgroups on diagnostic guidelines for Alzheimer’s disease,” *Alzheimers Dement*, vol. 7, no. 3, pp. 270–279, 2011, doi: 10.1016/J.JALZ.2011.03.008.

[56] L. Vermunt *et al.*, “Duration of preclinical, prodromal, and dementia stages of Alzheimer’s disease in relation to age, sex, and APOE genotype,” *Alzheimers Dement*, vol. 15, no. 7, pp. 888–898, Jul. 2019, doi: 10.1016/J.JALZ.2019.04.001.

[57] B. Reisberg, S. H. Ferris, M. J. de Leon, and T. Crook, “The Global Deterioration Scale for assessment of primary degenerative dementia,” *Am J Psychiatry.*, vol. 139, no. 9, pp. 1136–1139, 1982, doi: 10.1176/AJP.139.9.1136.

[58] D. A. Bennett *et al.*, “Neuropathology of older persons without cognitive impairment from two community-based studies,” *Neurology*, vol. 66, no. 12, pp. 1837–1844, Jun. 2006, doi: 10.1212/01.WNL.0000219668.47116.E6.

[59] R. C. Petersen *et al.*, “Practice guideline update summary: Mild cognitive impairment: Report of the Guideline Development, Dissemination, and Implementation Subcommittee of the American Academy of Neurology,” *Neurology*, vol. 90, no. 3, pp. 126–135, Jan. 2018, doi: 10.1212/WNL.0000000000004826.

[60] A. Ward, S. Tardiff, C. Dye, and H. M. Arrighi, “Rate of conversion from prodromal Alzheimer’s disease to Alzheimer’s dementia: a systematic review of the literature,” *Dement Geriatr Cogn Dis Extra*, vol. 3, no. 1, pp. 320–332, Sep. 2013, doi: 10.1159/000354370.

[61] H. Braak and E. Braak, “Neuropathological stageing of Alzheimer-related changes,” *Acta Neuropathol.*, vol. 82, no. 4, pp. 239–259, Sep. 1991, doi: 10.1007/BF00308809.

[62] D. R. Thal, U. Rüb, M. Orantes, and H. Braak, “Phases of A beta-deposition in the human brain and its relevance for the development of AD,” *Neurology*, vol. 58, no. 12, pp. 1791–1800, Jun. 2002, doi: 10.1212/WNL.58.12.1791.

[63] D. R. Thal, E. Capetillo-Zarate, K. del Tredici, and H. Braak, “The development of amyloid beta protein deposits in the aged brain,” *Sci Aging Knowledge Environ*, vol. 2006, no. 6, 2006, doi: 10.1126/SAGEKE.2006.6.RE1.

[64] L. M. Bierer *et al.*, “Neocortical neurofibrillary tangles correlate with dementia severity in Alzheimer’s disease,” *Arch Neurol*, vol. 52, no. 1, pp. 81–88, 1995, doi: 10.1001/ARCHNEUR.1995.00540250089017.

[65] P. Giannakopoulos *et al.*, “Tangle and neuron numbers, but not amyloid load, predict cognitive status in Alzheimer’s disease,” *Neurology*, vol. 60, no. 9, pp. 1495–1500, May 2003, doi: 10.1212/01.WNL.0000063311.58879.01.

[66] S. Khan, K. H. Barve, and M. S. Kumar, “Recent Advancements in Pathogenesis, Diagnostics and Treatment of Alzheimer’s Disease,” *Curr Neuropharmacol*, vol. 18, no. 11, pp. 1106–1125, May 2020, doi: 10.2174/1570159X18666200528142429.

[67] A. J. Atkinson *et al.*, “Biomarkers and surrogate endpoints: preferred definitions and conceptual framework,” *Clin Pharmacol Ther*, vol. 69, no. 3, pp. 89–95, Jan. 2001, doi: 10.1067/MCP.2001.113989.

[68] W. M. van Oostveen and E. C. M. de Lange, “Imaging Techniques in Alzheimer’s Disease: A Review of Applications in Early Diagnosis and Longitudinal Monitoring,” *Int J Mol Sci*, vol. 22, no. 4, pp. 1–34, Feb. 2021, doi: 10.3390/IJMS22042110.

[69] R. Ossenkoppele *et al.*, “Associations between tau, Aβ, and cortical thickness with cognition in Alzheimer disease,” *Neurology*, vol. 92, no. 6, pp. e601–e612, Feb. 2019, doi: 10.1212/WNL.0000000000006875.

[70] S. Minoshima, B. Giordani, S. Berent, K. A. Frey, N. L. Foster, and D. E. Kuhl, “Metabolic reduction in the posterior cingulate cortex in very early Alzheimer’s disease,” *Ann Neurol*, vol. 42, no. 1, pp. 85–94, Jul. 1997, doi: 10.1002/ANA.410420114.

[71] A. Chandra, G. Dervenoulas, and M. Politis, “Magnetic resonance imaging in Alzheimer’s disease and mild cognitive impairment,” *J Neurol*, vol. 266, no. 6, pp. 1293–1302, Jun. 2019, doi: 10.1007/S00415-018-9016-3.

[72] Y. A. R. Mahaman *et al.*, “Biomarkers used in Alzheimer’s disease diagnosis, treatment, and prevention,” *Ageing Res Rev*, vol. 74, Feb. 2022, doi: 10.1016/J.ARR.2021.101544.

[73] I. Skoog, P. Davidsson, Ó. Aevarsson, H. Vanderstichele, E. Vanmechelen, and K. Blennow, “Cerebrospinal fluid beta-amyloid 42 is reduced before the onset of sporadic dementia: a population-based study in 85-year-olds,” *Dement Geriatr Cogn Disord*, vol. 15, no. 3, pp. 169–176, 2003, doi: 10.1159/000068478.

[74] N. Andreasen *et al.*, “Cerebrospinal fluid beta-amyloid(1-42) in Alzheimer disease: differences between early- and late-onset Alzheimer disease and stability during the course of disease,” *Arch Neurol*, vol. 56, no. 6, pp. 673–680, Jun. 1999, doi: 10.1001/ARCHNEUR.56.6.673.

[75] K. Dhiman *et al.*, “Cerebrospinal fluid neurofilament light concentration predicts brain atrophy and cognition in Alzheimer’s disease,” *Alzheimers Dement (Amst)*, vol. 12, no. 1, Feb. 2020, doi: 10.1002/DAD2.12005.

[76] N. Mattsson *et al.*, “Cerebrospinal fluid tau, neurogranin, and neurofilament light in Alzheimer’s disease,” *EMBO Mol Med*, vol. 8, no. 10, pp. 1184–1196, Oct. 2016, doi: 10.15252/EMMM.201606540.

[77] N. Andreasen, E. Vanmechelen, H. Vanderstichele, P. Davidsson, and K. Blennow, “Cerebrospinal fluid levels of total-tau, phospho-tau and A beta 42 predicts development of Alzheimer’s disease in patients with mild cognitive impairment,” *Acta Neurol Scand Suppl.*, vol. 179, pp. 47–51, 2003, doi: 10.1034/J.1600-0404.107.S179.9.X.

[78] P. Buchhave, L. Minthon, H. Zetterberg, Å. K. Wallin, K. Blennow, and O. Hansson, “Cerebrospinal fluid levels of β-amyloid 1-42, but not of tau, are fully changed already 5 to 10 years before the onset of Alzheimer dementia,” *Arch Gen Psychiatry*, vol. 69, no. 1, pp. 98–106, Jan. 2012, doi: 10.1001/ARCHGENPSYCHIATRY.2011.155.

[79] S. Janelidze *et al.*, “Plasma P-tau181 in Alzheimer’s disease: relationship to other biomarkers, differential diagnosis, neuropathology and longitudinal progression to Alzheimer’s dementia,” *Nat Med.*, vol. 26, no. 3, pp. 379–386, Mar. 2020, doi: 10.1038/S41591-020-0755-1.

[80] S. D. Pearson, D. A. Ollendorf, and J. A. Colby, “Amyloid-β positron emission tomography in the diagnostic evaluation of alzheimer disease: summary of primary findings and conclusions,” *JAMA Intern Med*, vol. 174, no. 1, pp. 133–134, Jan. 2014, doi: 10.1001/JAMAINTERNMED.2013.11711.

[81] S. Basaia *et al.*, “Automated classification of Alzheimer’s disease and mild cognitive impairment using a single MRI and deep neural networks,” *Neuroimage Clin*, vol. 21, p. 101645, Jan. 2019, doi: 10.1016/J.NICL.2018.101645.

[82] S. Janelidze *et al.*, “CSF Aβ42/Aβ40 and Aβ42/Aβ38 ratios: better diagnostic markers of Alzheimer disease,” *Ann Clin Transl Neurol*, vol. 3, no. 3, pp. 154–165, Mar. 2016, doi: 10.1002/ACN3.274.

[83] C. E. Teunissen *et al.*, “Blood-based biomarkers for Alzheimer’s disease: towards clinical implementation,” *Lancet Neurol*, vol. 21, no. 1, pp. 66–77, Jan. 2022, doi: 10.1016/S1474-4422(21)00361-6.

[84] R. J. Bateman, N. R. Barthélemy, and K. Horie, “Another step forward in blood-based diagnostics for Alzheimer’s disease,” *Nat Med.*, vol. 26, no. 3, pp. 314–316, Mar. 2020, doi: 10.1038/S41591-020-0797-4.

[85] E. H. Thijssen *et al.*, “Diagnostic value of plasma phosphorylated tau181 in Alzheimer’s disease and frontotemporal lobar degeneration,” *Nat Med.*, vol. 26, no. 3, pp. 387–397, Mar. 2020, doi: 10.1038/S41591-020-0762-2.

[86] T. West *et al.*, “A blood-based diagnostic test incorporating plasma Aβ42/40 ratio, ApoE proteotype, and age accurately identifies brain amyloid status: findings from a multi cohort validity analysis,” *Mol Neurodegener*, vol. 16, no. 1, p. 30, May 2021, doi: 10.1186/S13024-021-00451-6.

[87] Z. Breijyeh and R. Karaman, “Comprehensive Review on Alzheimer’s Disease: Causes and Treatment,” *Molecules*, vol. 25, no. 24, p. 5789, Dec. 2020, doi: 10.3390/molecules25245789.

[88] Ó. M. Bautista-Aguilera *et al.*, “Tacrines as Therapeutic Agents for Alzheimer’s Disease. V. Recent Developments,” *Chem Rec*, vol. 21, no. 1, pp. 162–174, Jan. 2021, doi: 10.1002/TCR.202000107.

[89] X. Song *et al.*, “Mechanism of NMDA receptor channel block by MK-801 and memantine,” *Nature*, vol. 556, no. 7702, pp. 515–519, Apr. 2018, doi: 10.1038/S41586-018-0039-9.

[90] J. Cummings *et al.*, “Alzheimer’s disease drug development pipeline: 2022,” *Alzheimers Dement (N Y)*, vol. 8, no. 1, p. e12295, May 2022, doi: 10.1002/trc2.12295.

[91] J. Sevigny *et al.*, “The antibody aducanumab reduces Aβ plaques in Alzheimer’s disease,” *Nature*, vol. 537, no. 7618, pp. 50–56, Aug. 2016, doi: 10.1038/NATURE19323.

[92] B. Dunn, P. Stein, and P. Cavazzoni, “Approval of Aducanumab for Alzheimer Disease-The FDA’s Perspective,” *JAMA Intern Med*, vol. 181, no. 10, pp. 1277–1278, Oct. 2021, doi: 10.1001/JAMAINTERNMED.2021.4607.

[93] “European Medicines Agency.” https://www.ema.europa.eu/en (accessed Dec. 16, 2022).

[94] M. F. Egan *et al.*, “Randomized Trial of Verubecestat for Mild-to-Moderate Alzheimer’s Disease,” *N Engl J Med*, vol. 378, no. 18, pp. 1691–1703, May 2018, doi: 10.1056/NEJMOA1706441.

[95] M. MA *et al.*, “Donanemab in early Alzheimer’s disease,” *N Engl J Med*, vol. 384, no. 18, pp. 142–143, 2021, doi: 10.1056/NEJMOA2100708.

[96] C. J. Swanson *et al.*, “A randomized, double-blind, phase 2b proof-of-concept clinical trial in early Alzheimer’s disease with lecanemab, an anti-Aβ protofibril antibody,” *Alzheimers Res Ther*, vol. 13, no. 1, Dec. 2021, doi: 10.1186/S13195-021-00813-8.

[97] S. Retout, R. Gieschke, D. Serafin, C. Weber, N. Frey, and C. Hofmann, “Disease modeling and model-based meta-analyses to define a new direction for a phase III program of gantenerumab in Alzheimer’s disease,” *Clin Pharmacol Ther*, vol. 111, no. 4, pp. 857–866, Apr. 2022, doi: 10.1002/CPT.2535.

[98] G. Klein *et al.*, “Thirty-six-month amyloid positron emission tomography results show continued reduction in amyloid burden with subcutaneous gantenerumab,” *J Prev Alzheimers Dis*, vol. 8, no. 1, pp. 3–6, Jan. 2021, doi: 10.14283/JPAD.2020.68.

[99] A. Mullard, “Anti-tau antibody failures stack up,” *Nat Rev Drug Discov.* vol. 20, no. 12, p. 888, Dec. 2021, doi: 10.1038/D41573-021-00187-4.

[100] V. K. Gribkoff and L. K. Kaczmarek, “The need for new approaches in CNS drug discovery: Why drugs have failed, and what can be done to improve outcomes,” *Neuropharmacology*, vol. 120, pp. 11–19, Jul. 2017, doi: 10.1016/j.neuropharm.2016.03.021.

[101] “U.S. Food and Drug Administration.” https://www.fda.gov/ (accessed Dec. 16, 2022).

[102] S. Ayton and A. I. Bush, “β-amyloid: The known unknowns,” *Ageing Res Rev*, vol. 65, p. 201212, Jan. 2021, doi: 10.1016/j.arr.2020.101212.

[103] K. Herrup, “The case for rejecting the amyloid cascade hypothesis,” *Nat Neurosci.* , vol. 18, no. 6, pp. 794–799, Jun. 2015, doi: 10.1038/NN.4017.

[104] E. Karran and B. de Strooper, “The amyloid cascade hypothesis: are we poised for success or failure?”, *J Neurochem*, vol. 139 Suppl 2, pp. 237–252, Oct. 2016, doi: 10.1111/JNC.13632.

[105] J. L. Cummings, G. Tong, and C. Ballard, “Treatment combinations for Alzheimer’s disease: current and future pharmacotherapy options,” *J Alzheimers Dis*, vol. 67, no. 3, pp. 779–794, 2019, doi: 10.3233/JAD-180766.

[106] V. Kheifets and S. P. Braithwaite, “Plasma-based strategies for therapeutic modulation of brain aging,” *Neurotherapeutics.*, vol. 16, no. 3, pp. 675–684, Jul. 2019, doi: 10.1007/S13311-019-00746-Z.

[107] Y. Liu *et al.*, “Application of bio-orthogonal proteome labeling to cell transplantation and heterochronic parabiosis,” *Nat Commun.*, vol. 8, no. 1, p. 643, Sep. 2017, doi: 10.1038/S41467-017-00698-Y.

[108] M. Kuro-o *et al.*, “Mutation of the mouse klotho gene leads to a syndrome resembling ageing,” *Nature*, vol. 390, no. 6655, pp. 45–51, Nov. 1997, doi: 10.1038/36285.

[109] M. Kuro-O, “Klotho,” *Pflugers Arch*, vol. 459, no. 2, pp. 333–343, Jan. 2010, doi: 10.1007/S00424-009-0722-7.

[110] H. Kurosu *et al.*, “Suppression of aging in mice by the hormone Klotho,” *Science*, vol. 309, no. 5742, pp. 1829–1833, Sep. 2005, doi: 10.1126/SCIENCE.1112766.

[111] A. Kosakai *et al.*, “Degeneration of mesencephalic dopaminergic neurons in klotho mouse related to vitamin D exposure,” *Brain Res*, vol. 1382, pp. 109–117, Mar. 2011, doi: 10.1016/J.BRAINRES.2011.01.056.

[112] C. di Chen *et al.*, “The antiaging protein Klotho enhances oligodendrocyte maturation and myelination of the CNS,” *J Neurosci*, vol. 33, no. 5, pp. 1927–1939, Jan. 2013, doi: 10.1523/JNEUROSCI.2080-12.2013.

[113] M. Shiozaki *et al.*, “Morphological and biochemical signs of age-related neurodegenerative changes in klotho mutant mice,” *Neuroscience*, vol. 152, no. 4, pp. 924–941, Apr. 2008, doi: 10.1016/J.NEUROSCIENCE.2008.01.032.

[114] A. Uchida *et al.*, “Neurofilaments of Klotho, the mutant mouse prematurely displaying symptoms resembling human aging,” *J Neurosci Res.*, vol. 64, no. 4, pp. 364–370, May 2001, doi: 10.1002/JNR.1087.

[115] T. Nagai *et al.*, “Cognition impairment in the genetic model of aging klotho gene mutant mice: a role of oxidative stress,” *The FASEB Journal*, vol. 17, no. 1, pp. 50–52, Jan. 2003, doi: 10.1096/FJ.02-0448FJE.

[116] D. B. Dubal *et al.*, “Life extension factor klotho enhances cognition,” *Cell Rep*, vol. 7, no. 4, pp. 1065–1076, May 2014, doi: 10.1016/j.celrep.2014.03.076.

[117] S. Gupta *et al.*, “KL1 domain of longevity factor Klotho mimics the metabolome of cognitive stimulation and enhances cognition in young and aging mice,” *J Neurosci.*, vol. 42, no. 19, pp. 4016–4025, May 2022, doi: 10.1523/JNEUROSCI.2458-21.2022.

[118] A. Massó, A. Sánchez, A. Bosch, L. Giménez-Llort, and M. Chillón, “Secreted αKlotho isoform protects against age-dependent memory deficits,” *Mol Psychiatry.*, vol. 23, no. 9, pp. 1937–1947, Sep. 2018, doi: 10.1038/mp.2017.211.

[119] E. Zeldich *et al.*, “The neuroprotective effect of Klotho is mediated via regulation of members of the redox system,” *J Biol Chem.*, vol. 289, no. 35, pp. 24700–24715, Aug. 2014, doi: 10.1074/JBC.M114.567321.

[120] R. K. Brobey *et al.*, “Klotho protects dopaminergic neuron oxidant-induced degeneration by modulating ASK1 and p38 MAPK signaling pathways,” *PLoS One*, vol. 10, no. 10, p. e0139914, Oct. 2015, doi: 10.1371/JOURNAL.PONE.0139914.

[121] J. M. Gaitán *et al.*, “Circulating Klotho is higher in cerebrospinal fluid than serum and elevated among KLOTHO heterozygotes in a cohort with risk for Alzheimer’s disease,” *J Alzheimers Dis.*, vol. 90, no. 4, pp. 1557–1569, Jan. 2022, doi: 10.3233/JAD-220571.

[122] D. E. Arking *et al.*, “Association of human aging with a functional variant of klotho,” *Proc Natl Acad Sci U S A*, vol. 99, no. 2, pp. 856–861, Jan. 2002, doi: 10.1073/pnas.022484299.

[123] D. E. Arking, G. Atzmon, A. Arking, N. Barzilai, and H. C. Dietz, “Association between a functional variant of the KLOTHO gene and high-density lipoprotein cholesterol, blood pressure, stroke, and longevity,” *Circ Res*, vol. 96, no. 4, pp. 412–418, Mar. 2005, doi: 10.1161/01.RES.0000157171.04054.30.

[124] J. S. Yokoyama *et al.*, “Variation in longevity gene KLOTHO is associated with greater cortical volumes,” *Ann Clin Transl Neurol*, vol. 2, no. 3, pp. 215–230, Mar. 2015, doi: 10.1002/ACN3.161.

[125] C. di Chen, S. Podvin, E. Gillespie, S. E. Leeman, and C. R. Abraham, “Insulin stimulates the cleavage and release of the extracellular domain of Klotho by ADAM10 and ADAM17,” *Proc Natl Acad Sci U S A*, vol. 104, no. 50, pp. 19796–19801, Dec. 2007, doi: 10.1073/pnas.0709805104.

[126] L. Bloch *et al.*, “Klotho is a substrate for alpha-, beta- and gamma-secretase,” *FEBS Lett*, vol. 583, no. 19, pp. 3221–3224, Oct. 2009, doi: 10.1016/J.FEBSLET.2009.09.009.

[127] Y. Matsumura, H. Aizawa, T. Shiraki-Iida, R. Nagai, M. Kuro-O, and Y. I. Nabeshima, “Identification of the human klotho gene and its two transcripts encoding membrane and secreted klotho protein,” *Biochem Biophys Res Commun*, vol. 242, no. 3, pp. 626–630, Jan. 1998, doi: 10.1006/bbrc.1997.8019.

[128] T. Shiraki-Iida *et al.*, “Structure of the mouse klotho gene and its two transcripts encoding membrane and secreted protein,” *FEBS Lett*, vol. 424, no. 1–2, pp. 6–10, Mar. 1998, doi: 10.1016/S0014-5793(98)00127-6.

[129] A. Imura *et al.*, “Secreted Klotho protein in sera and CSF: Implication for post-translational cleavage in release of Klotho protein from cell membrane,” *FEBS Lett*, vol. 565, no. 1–3, pp. 143–147, May 2004, doi: 10.1016/j.febslet.2004.03.090.

[130] M. C. Hu *et al.*, “Klotho deficiency causes vascular calcification in chronic kidney disease,” *J Am Soc Nephrol.*, vol. 22, no. 1, pp. 124–136, Jan. 2011, doi: 10.1681/ASN.2009121311.

[131] R. E. Forster *et al.*, “Vitamin D receptor controls expression of the anti-aging klotho gene in mouse and human renal cells,” *Biochem Biophys Res Commun*, vol. 414, no. 3, pp. 557–562, Oct. 2011, doi: 10.1016/J.BBRC.2011.09.117.

[132] A. Massó *et al.*, “Secreted and transmembrane αKlotho isoforms have different spatio-temporal profiles in the brain during aging and Alzheimer’s disease progression,” *PLoS One*, vol. 10, no. 11, p. e0143623, Nov. 2015, doi: 10.1371/journal.pone.0143623.

[133] J. A. Duce, S. Podvin, W. Hollander, D. Kipling, D. L. Rosene, and C. R. Abraham, “Gene profile analysis implicates Klotho as an important contributor to aging changes in brain white matter of the rhesus monkey,” *Glia*, vol. 56, no. 1, pp. 106–117, Jan. 2008, doi: 10.1002/GLIA.20593.

[134] S. M. Clinton *et al.*, “Expression of klotho mRNA and protein in rat brain parenchyma from early postnatal development into adulthood,” *Brain Res*, vol. 1527, pp. 1–14, Aug. 2013, doi: 10.1016/J.BRAINRES.2013.06.044.

[135] R. D. Semba *et al.*, “Klotho in the cerebrospinal fluid of adults with and without Alzheimer’s disease,” *Neurosci Lett*, vol. 558, pp. 37–40, Jan. 2014, doi: 10.1016/j.neulet.2013.10.058.

[136] K. Lim *et al.*, “α-Klotho expression in human tissues,” *J Clin Endocrinol Metab*, vol. 100, no. 10, pp. e1308–e1318, Oct. 2015, doi: 10.1210/JC.2015-1800.

[137] H. Olauson, R. Mencke, J. L. Hillebrands, and T. E. Larsson, “Tissue expression and source of circulating αKlotho,” *Bone*, vol. 100, pp. 19–35, Jul. 2017, doi: 10.1016/J.BONE.2017.03.043.

[138] C. R. Abraham, P. C. Mullen, T. Tucker-Zhou, C. D. Chen, and E. Zeldich, “Klotho is a neuroprotective and cognition-enhancing protein,” *Vitam Horm*, vol. 101, pp. 215–238, 2016, doi: 10.1016/BS.VH.2016.02.004.

[139] M. S. Razzaque and B. Lanske, “Hypervitaminosis D and premature aging: lessons learned from Fgf23 and Klotho mutant mice,” *Trends Mol Med*, vol. 12, no. 7, pp. 298–305, Jul. 2006, doi: 10.1016/J.MOLMED.2006.05.002.

[140] S. K. Cha, M. C. Hu, H. Kurosu, M. Kuro-O, O. Moe, and C. L. Huang, “Regulation of renal outer medullary potassium channel and renal K(+) excretion by Klotho,” *Mol Pharmacol*, vol. 76, no. 1, pp. 38–46, Jul. 2009, doi: 10.1124/MOL.109.055780.

[141] H. Kurosu *et al.*, “Regulation of fibroblast growth factor-23 signaling by klotho,” *J Biol Chem.*, vol. 281, no. 10, pp. 6120–6123, Mar. 2006, doi: 10.1074/JBC.C500457200.

[142] M. Kuro-o, “Klotho as a regulator of fibroblast growth factor signaling and phosphate/calcium metabolism,” *Curr Opin Nephrol Hypertens*, vol. 15, no. 4, pp. 437–441, Jul. 2006, doi: 10.1097/01.MNH.0000232885.81142.83.

[143] Q. Chang, S. Hoefs, A. W. van der Kemp, C. N. Topala, R. J. Bindels, and J. G. Hoenderop, “The beta-glucuronidase klotho hydrolyzes and activates the TRPV5 channel,” *Science*, vol. 310, no. 5747, pp. 490–493, Oct. 2005, doi: 10.1126/SCIENCE.1114245.

[144] S. M. Moe, “Calcium Homeostasis in Health and in Kidney Disease”, *Compr Physiol*, vol. 6, no. 4, pp. 1781–1800, Oct. 2016, doi: 10.1002/CPHY.C150052.

[145] C. B. Chiribau, L. Cheng, I. C. Cucoranu, Y. S. Yu, R. E. Clempus, and D. Sorescu, “FOXO3A regulates peroxiredoxin III expression in human cardiac fibroblasts,” *J Biol Chem.*, vol. 283, no. 13, pp. 8211–8217, Mar. 2008, doi: 10.1074/JBC.M710610200.

[146] M. Yamamoto *et al.*, “Regulation of oxidative stress by the anti-aging hormone klotho,” *J Biol Chem.*, vol. 280, no. 45, pp. 38029–38034, Nov. 2005, doi: 10.1074/JBC.M509039200.

[147] O. Altintas, S. Park, and S. J. v. Lee, “The role of insulin/IGF-1 signaling in the longevity of model invertebrates, C. elegans and D. melanogaster,” *BMB Rep*, vol. 49, no. 2, pp. 81–92, 2016, doi: 10.5483/BMBREP.2016.49.2.261.

[148] T. Utsugi *et al.*, “Decreased insulin production and increased insulin sensitivity in the klotho mutant mouse, a novel animal model for human aging,” *Metabolism*, vol. 49, no. 9, pp. 1118–1123, 2000, doi: 10.1053/META.2000.8606.

[149] Y. Wang, M. Kuro-O, and Z. Sun, “Klotho gene delivery suppresses Nox2 expression and attenuates oxidative stress in rat aortic smooth muscle cells via the cAMP-PKA pathway,” *Aging Cell*, vol. 11, no. 3, pp. 410–417, Jun. 2012, doi: 10.1111/J.1474-9726.2012.00796.X.

[150] M. Typiak and A. Piwkowska, “Antiinflammatory actions of Klotho: implications for therapy of diabetic nephropathy,” *Int J Mol Sci*, vol. 22, no. 2, p. 956, Jan. 2021, doi: 10.3390/IJMS22020956.

[151] N. Parameswaran and S. Patial, “Tumor necrosis factor-α signaling in macrophages,” *Crit Rev Eukaryot Gene Expr*, vol. 20, no. 2, pp. 87–103, 2010, doi: 10.1615/critreveukargeneexpr.v20.i2.10.

[152] M. Scheller *et al.*, “Hematopoietic stem cell and multilineage defects generated by constitutive beta-catenin activation,” *Nat Immunol.*, vol. 7, no. 10, pp. 1037–1047, Oct. 2006, doi: 10.1038/NI1387.

[153] P. Kirstetter, K. Anderson, B. T. Porse, S. E. W. Jacobsen, and C. Nerlov, “Activation of the canonical Wnt pathway leads to loss of hematopoietic stem cell repopulation and multilineage differentiation block,” *Nat Immunol.*, vol. 7, no. 10, pp. 1048–1056, Oct. 2006, doi: 10.1038/NI1381.

[154] H. Liu *et al.*, “Augmented Wnt signaling in a mammalian model of accelerated aging,” *Science*, vol. 317, no. 5839, pp. 803–806, Aug. 2007, doi: 10.1126/SCIENCE.1143578.

[155] T. C. Camilli *et al.*, “Loss of Klotho during melanoma progression leads to increased filamin cleavage, increased Wnt5A expression, and enhanced melanoma cell motility,” *Pigment Cell Melanoma Res*, vol. 24, no. 1, pp. 175–186, Feb. 2011, doi: 10.1111/J.1755-148X.2010.00792.X.

[156] J. Pan *et al.*, “Klotho, an anti-senescence related gene, is frequently inactivated through promoter hypermethylation in colorectal cancer,” *Tumour Biol*, vol. 32, no. 4, pp. 729–735, 2011, doi: 10.1007/S13277-011-0174-5.

[157] X. Tang *et al.*, “Klotho: a tumor suppressor and modulator of the Wnt/β-catenin pathway in human hepatocellular carcinoma,” *Lab Invest.*, vol. 96, no. 2, pp. 197–205, Feb. 2016, doi: 10.1038/LABINVEST.2015.86.

[158] A. Sachdeva *et al.*, “Klotho and the treatment of human malignancies,” *Cancers (Basel).*, vol. 12, no. 6, p. 1665, Jun. 2020, doi: 10.3390/cancers12061665.

[159] H. Zhou, S. Pu, H. Zhou, and Y. Guo, “Klotho as potential autophagy regulator and therapeutic target,” *Front Pharmacol.*, vol. 12, p. 755366, Oct. 2021, doi: 10.3389/fphar.2021.755366.

[160] K. Chen, X. Zhou, and Z. Sun, “Haplodeficiency of Klotho gene causes arterial stiffening via upregulation of scleraxis expression and induction of autophagy,” *Hypertension.*, vol. 66, no. 5, pp. 1006–1013, Nov. 2015, doi: 10.1161/HYPERTENSIONAHA.115.06033.

[161] C. Y. Zeng *et al.*, “Lentiviral vector-mediated overexpression of Klotho in the brain improves Alzheimer’s disease-like pathology and cognitive deficits in mice,” *Neurobiol Aging*, vol. 78, pp. 18–28, Jun. 2019, doi: 10.1016/J.NEUROBIOLAGING.2019.02.003.

[162] X. Kuang, H. J. Zhou, A. H. Thorne, X. N. Chen, L. J. Li, and J. R. Du, “Neuroprotective effect of ligustilide through induction of α-secretase processing of both APP and Klotho in a mouse model of Alzheimer’s disease,” *Front Aging Neurosci*, vol. 9, no. NOV, p. 353, Nov. 2017, doi: 10.3389/FNAGI.2017.00353/BIBTEX.

[163] M. S. Emami Aleagha *et al.*, “Decreased concentration of Klotho in the cerebrospinal fluid of patients with relapsing–remitting multiple sclerosis,” *J Neuroimmunol*, vol. 281, pp. 5–8, Apr. 2015, doi: 10.1016/J.JNEUROIM.2015.02.004.

[164] M. A. Teocchi, A. É. D. Ferreira, E. P. da Luz de Oliveira, H. Tedeschi, and L. D’Souza-Li, “Hippocampal gene expression dysregulation of Klotho, nuclear factor kappa B and tumor necrosis factor in temporal lobe epilepsy patients,” *J Neuroinflammation*, vol. 10, p. 53, May 2013, doi: 10.1186/1742-2094-10-53.

[165] D. B. Dubal *et al.*, “Life Extension Factor Klotho Prevents Mortality and Enhances Cognition in hAPP Transgenic Mice,” *Journal of Neuroscience*, vol. 35, no. 6, pp. 2358–2371, Feb. 2015, doi: 10.1523/JNEUROSCI.5791-12.2015.

[166] J. Neitzel *et al.*, “KL-VS heterozygosity is associated with lower amyloid-dependent tau accumulation and memory impairment in Alzheimer’s disease,” *Nat Commun.* , vol. 12, no. 1, Dec. 2021, doi: 10.1038/S41467-021-23755-Z.

[167] I. Driscoll *et al.*, “Age-related Tau burden and cognitive deficits are attenuated in KLOTHO KL-VS heterozygotes,” *J Alzheimers Dis.*, vol. 79, no. 3, pp. 1297–1305, Jan. 2021, doi: 10.3233/JAD-200944.

[168] B. W. Müller *et al.*, “Klotho KL-VS haplotype does not improve cognition in a population-based sample of adults age 55-87 years,” *Sci Rep.*, vol. 11, no. 1, p. 13852, Jul. 2021, doi: 10.1038/S41598-021-93211-X.

[169] D. Li, D. Jing, Z. Liu, Y. Chen, F. Huang, and T. Behnisch, “Enhanced expression of secreted α-klotho in the hippocampus alters nesting behavior and memory formation in mice,” *Front Cell Neurosci*, vol. 13, p. 133, Jan. 2019, doi: 10.3389/FNCEL.2019.00133/BIBTEX.

[170] J. Leon *et al.*, “Peripheral elevation of a Klotho fragment enhances brain function and resilience in young, aging, and α-synuclein transgenic mice,” *Cell Rep*, vol. 20, no. 6, pp. 1360–1371, Aug. 2017, doi: 10.1016/J.CELREP.2017.07.024.

[171] Y. Zhao, C. Y. Zeng, X. H. Li, T. T. Yang, X. Kuang, and J. R. Du, “Klotho overexpression improves amyloid-β clearance and cognition in the APP/PS1 mouse model of Alzheimer’s disease,” *Aging Cell*, vol. 19, no. 10, Oct. 2020, doi: 10.1111/ACEL.13239.

[172] L. Rondi-Reig, M. Libbey, H. Eichenbaum, and S. Tonegawa, “CA1-specific N-methyl-D-aspartate receptor knockout mice are deficient in solving a nonspatial transverse patterning task,” *Proc Natl Acad Sci U S A*, vol. 98, no. 6, pp. 3543–3548, Mar. 2001, doi: 10.1073/PNAS.041620798.

[173] R. G. M. Morris, E. Anderson, G. S. Lynch, and M. Baudry, “Selective impairment of learning and blockade of long-term potentiation by an N-methyl-D-aspartate receptor antagonist, AP5,” *Nature*, vol. 319, no. 6056, pp. 774–776, 1986, doi: 10.1038/319774A0.

[174] P. T. Huerta, L. D. Sun, M. A. Wilson, and S. Tonegawa, “Formation of temporal memory requires NMDA receptors within CA1 pyramidal neurons,” *Neuron*, vol. 25, no. 2, pp. 473–480, 2000, doi: 10.1016/S0896-6273(00)80909-5.

[175] C. C. Smith, L. A. Smith, T. M. Bredemann, and L. L. Mcmahon, “17β estradiol recruits GluN2B-containing NMDARs and ERK during induction of long-term potentiation at temporoammonic-CA1 synapses,” *Hippocampus*, vol. 26, no. 1, pp. 110–117, Jan. 2016, doi: 10.1002/HIPO.22495.

[176] S. J. Park *et al.*, “Inactivation of JAK2/STAT3 signaling axis and downregulation of M1 mAChR cause cognitive impairment in klotho mutant mice, a genetic model of aging,” *Neuropsychopharmacology.*, vol. 38, no. 8, pp. 1426–1437, Jul. 2013, doi: 10.1038/NPP.2013.39.

[177] M. Sedighi, T. Baluchnejadmojarad, S. Afshin-Majd, M. Amiri, M. Aminzade, and M. Roghani, “Anti-aging Klotho protects SH-SY5Y cells against amyloid β1–42 neurotoxicity: Involvement of Wnt1/pCREB/Nrf2/HO-1 signaling,” *J Mol Neurosci.*, vol. 71, no. 1, pp. 19–27, Jan. 2021, doi: 10.1007/s12031-020-01621-9.

[178] C. di Chen, H. Li, J. Liang, K. Hixson, E. Zeldich, and C. R. Abraham, “The anti-aging and tumor suppressor protein Klotho enhances differentiation of a human oligodendrocytic hybrid cell line,” *J Mol Neurosci.*, vol. 55, no. 1, pp. 76–90, Jan. 2015, doi: 10.1007/s12031-014-0336-1.

[179] X. Kuang *et al.*, “Klotho upregulation contributes to the neuroprotection of ligustilide in an Alzheimer’s disease mouse model,” *Neurobiol Aging*, vol. 35, no. 1, pp. 169–178, Jan. 2014, doi: 10.1016/J.NEUROBIOLAGING.2013.07.019.

[180] H. J. Zhou, C. Y. Zeng, T. T. Yang, F. Y. Long, X. Kuang, and J. R. Du, “Lentivirus-mediated klotho up-regulation improves aging-related memory deficits and oxidative

stress in senescence-accelerated mouse prone-8 mice," *Life Sci*, vol. 200, pp. 56–62, May 2018, doi: 10.1016/J.LFS.2018.03.027.

[181] A. M. Laszczyk *et al.*, "Klotho regulates postnatal neurogenesis and protects against age-related spatial memory loss," *Neurobiol Aging*, vol. 59, pp. 41–54, Nov. 2017, doi: 10.1016/J.NEUROBIOLAGING.2017.07.008.

[182] L. Zhu *et al.*, "Klotho controls the brain–immune system interface in the choroid plexus," *Proc Natl Acad Sci U S A*, vol. 115, no. 48, pp. e11388–e11396, Nov. 2018, doi: 10.1073/pnas.1808609115.

[183] K. Hanson, K. Fisher, and N. M. Hooper, "Exploiting the neuroprotective effects of α-klotho to tackle ageing- and neurodegeneration-related cognitive dysfunction," *Neuronal Signal*, vol. 5, no. 2, Jun. 2021, doi: 10.1042/NS20200101.

[184] B. Li *et al.*, "Mechanism of the fibroblast growth factor 23/α-Klotho axis in peripheral blood mononuclear cell inflammation in Alzheimer's disease," *Immunol Invest*, vol. 51, no. 5, pp. 1471–1484, Jul. 2022, doi: 10.1080/08820139.2021.1970180.

[185] J. Mytych, "Klotho and neurons: mutual crosstalk between autophagy, endoplasmic reticulum, and inflammatory response," *Neural Regen Res*, vol. 16, no. 8, pp. 1542–1543, Aug. 2021, doi: 10.4103/1673-5374.303014.

[186] Á. F. Fernández *et al.*, "Disruption of the beclin 1-BCL2 autophagy regulatory complex promotes longevity in mice," *Nature*, vol. 558, no. 7708, pp. 136–140, Jun. 2018, doi: 10.1038/S41586-018-0162-7.

[187] T. Y. Fung *et al.*, "Klotho an Autophagy Stimulator as a Potential Therapeutic Target for Alzheimer's Disease: A Review," *Biomedicines*, vol. 10, no. 3, Mar. 2022, doi: 10.3390/BIOMEDICINES10030705.

[188] X. M. Anguela and K. A. High, "Entering the modern era of gene therapy," *Annu Rev Med*, vol. 70, pp. 273–288, Jan. 2019, doi: 10.1146/annurev-med-012017-043332.

[189] The Journal of Gene Medicine, "Gene Therapy Clinical Trials Worlwide." https://a873679.fmphost.com/fmi/webd/GTCT (accessed Jul. 15, 2022).

[190] "Gene, Cell, & RNA Therapy Landscape Q3 2022 Quarterly Data Report," 2022. Accessed: Dec. 17, 2022. [Online]. Available: https://asgct.org/global/documents/asgct-citeline-q3-2022-report.aspx

[191] H. Yin, R. L. Kanasty, A. A. Eltoukhy, A. J. Vegas, J. R. Dorkin, and D. G. Anderson, "Non-viral vectors for gene-based therapy," *Nat Rev Genet.*, vol. 15, no. 8, pp. 541–555, 2014, doi: 10.1038/NRG3763.

[192] F. Mingozzi and K. A. High, "Immune responses to AAV vectors: overcoming barriers to successful gene therapy," *Blood*, vol. 122, no. 1, pp. 23–36, Jul. 2013, doi: 10.1182/BLOOD-2013-01-306647.

[193] C. Baum, O. Kustikova, U. Modlich, Z. Li, and B. Fehse, “Mutagenesis and oncogenesis by chromosomal insertion of gene transfer vectors,” *Hum Gene Ther*, vol. 17, no. 3, pp. 253–263, Mar. 2006, doi: 10.1089/HUM.2006.17.253.

[194] D. Brown *et al.*, “Deep Parallel Characterization of AAV Tropism and AAV-Mediated Transcriptional Changes via Single-Cell RNA Sequencing,” *Front Immunol.*, vol. 12, p. 730825, Oct. 2021, doi: 10.3389/FIMMU.2021.730825.

[195] C. E. Thomas, A. Ehrhardt, and M. A. Kay, “Progress and problems with the use of viral vectors for gene therapy,” *Nat Rev Genet.*, vol. 4, no. 5, pp. 346–358, May 2003, doi: 10.1038/NRG1066.

[196] F. Mingozzi and K. A. High, “Therapeutic in vivo gene transfer for genetic disease using AAV: progress and challenges,” *Nat Rev Genet.*, vol. 12, no. 5, pp. 341–355, May 2011, doi: 10.1038/NRG2988.

[197] A. F. Meier, C. Fraefel, and M. Seyffert, “The interplay between adeno-associated virus and its helper viruses,” *Viruses*, vol. 12, no. 6, Jun. 2020, doi: 10.3390/V12060662.

[198] S. Ylä-Herttuala, “Endgame: glybera finally recommended for approval as the first gene therapy drug in the European union,” *Mol Ther.*, vol. 20, no. 10, pp. 1831–1832, Oct. 2012, doi: 10.1038/MT.2012.194.

[199] V. Miraldi Utz, R. G. Coussa, F. Antaki, and E. I. Traboulsi, “Gene therapy for RPE65-related retinal disease,” *Ophthalmic Genet*, vol. 39, no. 6, pp. 671–677, Nov. 2018, doi: 10.1080/13816810.2018.1533027.

[200] S. M. Hoy, “Onasemnogene abeparvovec: first global approval,” *Drugs*, vol. 79, no. 11, pp. 1255–1262, Jul. 2019, doi: 10.1007/S40265-019-01162-5.

[201] S. J. Keam, “Eladocagene Exuparvovec: First approval,” *Drugs*, vol. 82, no. 13, pp. 1427–1432, Sep. 2022, doi: 10.1007/S40265-022-01775-3.

[202] H. A. Blair, “Valoctocogene Roxaparvovec: First approval,” *Drugs*, vol. 82, no. 14, pp. 1505–1510, Sep. 2022, doi: 10.1007/S40265-022-01788-Y.

[203] M. A. Kotterman, T. W. Chalberg, and D. v. Schaffer, “Viral vectors for gene therapy: translational and clinical outlook,” *Annu Rev Biomed Eng*, vol. 17, pp. 63–89, Dec. 2015, doi: 10.1146/annurev-bioeng-071813-104938.

[204] F. Sonntag *et al.*, “The assembly-activating protein promotes capsid assembly of different adeno-associated virus serotypes,” *J Virol*, vol. 85, no. 23, pp. 12686–12697, Dec. 2011, doi: 10.1128/JVI.05359-11.

[205] S. Zolotukhin *et al.*, “Production and purification of serotype 1, 2, and 5 recombinant adeno-associated viral vectors,” *Methods*, vol. 28, no. 2, pp. 158–167, 2002, doi: 10.1016/S1046-2023(02)00220-7.

[206] J. C. Grieger and R. J. Samulski, “Adeno-associated virus vectorology, manufacturing, and clinical applications,” *Methods Enzymol.*, vol. 507, pp. 229–254, 2012, doi: 10.1016/B978-0-12-386509-0.00012-0.

[207] B. R. Schultz and J. S. Chamberlain, “Recombinant adeno-associated virus transduction and integration,” *Mol Ther.*, vol. 16, no. 7, pp. 1189–1199, Jul. 2008, doi: 10.1038/MT.2008.103.

[208] M. Nonnenmacher and T. Weber, “Intracellular transport of recombinant adeno-associated virus vectors,” *Gene Ther*, vol. 19, no. 6, pp. 649–658, Jun. 2012, doi: 10.1038/GT.2012.6.

[209] D. Wang, P. W. L. Tai, and G. Gao, “Adeno-associated virus vector as a platform for gene therapy delivery,” *Nat Rev Drug Discov.* , vol. 18, no. 5, pp. 358–378, May 2019, doi: 10.1038/S41573-019-0012-9.

[210] R. H. Smith, “Adeno-associated virus integration: virus versus vector,” *Gene Ther*, vol. 15, no. 11, pp. 817–822, Jun. 2008, doi: 10.1038/GT.2008.55.

[211] C. Li and R. J. Samulski, “Engineering adeno-associated virus vectors for gene therapy,” *Nat Rev Genet.*, vol. 21, no. 4, pp. 255–272, Feb. 2020, doi: 10.1038/S41576-019-0205-4.

[212] M. Agbandje-McKenna and J. Kleinschmidt, “AAV capsid structure and cell interactions,” *Methods Mol Biol.*, vol. 807, pp. 47–92, 2011, doi: 10.1007/978-1-61779-370-7_3.

[213] R. W. Atchison, B. C. Casto, and W. M. D. Hammon, “Adenovirus-associated defective virus particles,” *Science (1979)*, vol. 149, no. 3685, pp. 754–756, Aug. 1965, doi: 10.1126/science.149.3685.754.

[214] M. D. Hoggan, N. R. Blacklow, and W. P. Rowe, “Studies of small DNA viruses found in various adenovirus preparations: physical, biological, and immunological characteristics,” *Proc Natl Acad Sci U S A*, vol. 55, no. 6, pp. 1467–1474, Jun. 1966, doi: 10.1073/pnas.55.6.1467.

[215] D. Grimm *et al.*, “In vitro and in vivo gene therapy vector evolution via multispecies interbreeding and retargeting of adeno-associated viruses,” *J Virol*, vol. 82, no. 12, pp. 5887–5911, Jun. 2008, doi: 10.1128/JVI.00254-08.

[216] J. E. Rabinowitz *et al.*, “Cross-packaging of a single adeno-associated virus (AAV) type 2 vector genome into multiple AAV serotypes enables transduction with broad specificity,” *J Virol*, vol. 76, no. 2, pp. 791–801, Jan. 2002, doi: 10.1128/jvi.76.2.791-801.2002.

[217] E. Hudry and L. H. Vandenberghe, “Therapeutic AAV gene transfer to the nervous system: A clinical reality,” *Neuron*, vol. 101, no. 5, pp. 839–862, Mar. 2019, doi: 10.1016/J.NEURON.2019.02.017.

[218] D. F. Aschauer, S. Kreuz, and S. Rumpel, “Analysis of transduction efficiency, tropism and axonal transport of AAV serotypes 1, 2, 5, 6, 8 and 9 in the mouse brain,” *PLoS One*, vol. 8, no. 9, Sep. 2013, doi: 10.1371/JOURNAL.PONE.0076310.

[219] C. N. Cearley and J. H. Wolfe, “Transduction characteristics of adeno-associated virus vectors expressing cap serotypes 7, 8, 9, and Rh10 in the mouse brain,” *Mol Ther.*, vol. 13, no. 3, pp. 528–537, Mar. 2006, doi: 10.1016/J.YMTHE.2005.11.015.

[220] C. N. Cearley and J. H. Wolfe, “A single injection of an adeno-associated virus vector into nuclei with divergent connections results in widespread vector distribution in the brain and global correction of a neurogenetic disease,” *J Neurosci.*, vol. 27, no. 37, pp. 9928–9940, Sep. 2007, doi: 10.1523/JNEUROSCI.2185-07.2007.

[221] S. J. Gray, V. Matagne, L. Bachaboina, S. Yadav, S. R. Ojeda, and R. J. Samulski, “Preclinical differences of intravascular AAV9 delivery to neurons and glia: A comparative study of adult mice and nonhuman primates,” *Mol Ther.*, vol. 19, no. 6, pp. 1058–1069, Jun. 2011, doi: 10.1038/MT.2011.72.

[222] S. Duque *et al.*, “Intravenous administration of self-complementary AAV9 enables transgene delivery to adult motor neurons,” *Mol Ther.*, vol. 17, no. 7, pp. 1187–1196, Jul. 2009, doi: 10.1038/MT.2009.71.

[223] D. Dalkara *et al.*, “In vivo-directed evolution of a new adeno-associated virus for therapeutic outer retinal gene delivery from the vitreous,” *Sci Transl Med*, vol. 5, no. 189, Jun. 2013, doi: 10.1126/scitranslmed.3005708.

[224] T. T. Duong *et al.*, “Comparative AAV-EGFP transgene expression using vector serotypes 1–9, 7M8, and 8b in human pluripotent stem cells, RPEs, and human and rat cortical neurons,” *Stem Cells Int*, vol. 2019, 2019, doi: 10.1155/2019/7281912.

[225] D. Xu *et al.*, “Overexpressing NeuroD1 reprograms Müller cells into various types of retinal neurons,” *Neural Regen Res*, vol. 18, no. 5, pp. 1124–1131, May 2023, doi: 10.4103/1673-5374.355818.

[226] M. Garita-Hernandez *et al.*, “AAV-mediated gene delivery to 3D retinal organoids derived from human induced pluripotent stem cells,” *Int J Mol Sci.*, vol. 21, no. 3, p. 994, Feb. 2020, doi: 10.3390/IJMS21030994.

[227] M. E. McClements *et al.*, “Tropism of AAV Vectors in Photoreceptor-Like Cells of Human iPSC-Derived Retinal Organoids,” *Transl Vis Sci Technol*, vol. 11, no. 4, pp. 3–3, Apr. 2022, doi: 10.1167/TVST.11.4.3.

[228] T. R. Flotte, “Revisiting the ‘New’ Inflammatory Toxicities of Adeno-Associated Virus Vectors,” *Hum Gene Ther*, vol. 31, no. 7–8, pp. 398–399, Apr. 2020, doi: 10.1089/HUM.2020.29117.TRF.

[229] D. Chand *et al.*, “Hepatotoxicity following administration of onasemnogene abeparvovec (AVXS-101) for the treatment of spinal muscular atrophy,” *J Hepatol*, vol. 74, no. 3, pp. 560–566, Mar. 2021, doi: 10.1016/J.JHEP.2020.11.001.

[230] J. Hordeaux *et al.*, “Adeno-Associated Virus-Induced Dorsal Root Ganglion Pathology,” *Hum Gene Ther*, vol. 31, no. 15–16, pp. 808–818, Aug. 2020, doi: 10.1089/HUM.2020.167.

[231] C. Zincarelli, S. Soltys, G. Rengo, and J. E. Rabinowitz, “Analysis of AAV serotypes 1-9 mediated gene expression and tropism in mice after systemic injection,” *Mol Ther*, vol. 16, no. 6, pp. 1073–1080, 2008, doi: 10.1038/MT.2008.76.

[232] M. E. McClements and R. E. MacLaren, “Adeno-associated virus (AAV) dual vector strategies for gene therapy encoding large transgenes,” *Yale J Biol Med.*, vol. 90, no. 4, pp. 611–623, Dec. 2017.

[233] F. K. Ferrari, T. Samulski, T. Shenk, R. J. Samulski, and G. T. Center, “Second-strand synthesis is a rate-limiting step for efficient transduction by recombinant adeno-associated virus vectors,” *J Virol*, vol. 70, no. 5, pp. 3227–3234, May 1996, doi: 10.1128/JVI.70.5.3227-3234.1996.

[234] E. A. Chowdhury *et al.*, “Current progress and limitations of AAV mediated delivery of protein therapeutic genes and the importance of developing quantitative pharmacokinetic/pharmacodynamic (PK/PD) models,” *Adv Drug Deliv Rev*, vol. 170, pp. 214–237, Mar. 2021, doi: 10.1016/J.ADDR.2021.01.017.

[235] R. M. Kotin and R. O. Snyder, “Manufacturing clinical grade recombinant adeno-associated virus using invertebrate cell lines,” *Hum Gene Ther*, vol. 28, no. 4, pp. 350–360, Apr. 2017, doi: 10.1089/HUM.2017.042.

[236] M. Mietzsch, H. Hering, E. M. Hammer, M. Agbandje-Mckenna, S. Zolotukhin, and R. Heilbronn, “OneBac 2.0: Sf9 cell lines for production of AAV1, AAV2, and AAV8 vectors with minimal encapsidation of foreign DNA,” *Hum Gene Ther Methods.*, vol. 28, no. 1, pp. 15–22, Feb. 2017, doi: 10.1089/HGTB.2016.164.

[237] H. C. Verdera, K. Kuranda, and F. Mingozzi, “AAV vector immunogenicity in humans: A long journey to successful gene transfer,” *Mol Ther.*, vol. 28, no. 3, pp. 723–746, Mar. 2020, doi: 10.1016/J.YMTHE.2019.12.010.

[238] R. Calcedo, L. H. Vandenberghe, G. Gao, J. Lin, and J. M. Wilson, “Worldwide epidemiology of neutralizing antibodies to adeno-associated viruses,” *J Infect Dis*, vol. 199, no. 3, pp. 381–390, Feb. 2009, doi: 10.1086/595830.

[239] M. Corti *et al.*, “Evaluation of readministration of a recombinant adeno-associated virus vector expressing acid alpha-glucosidase in Pompe disease: Preclinical to clinical planning,” *Hum Gene Ther Clin Dev*, vol. 26, no. 3, pp. 185–193, Sep. 2015, doi: 10.1089/HUMC.2015.068.

[240] A. Meliani *et al.*, “Antigen-selective modulation of AAV immunogenicity with tolerogenic rapamycin nanoparticles enables successful vector re-administration,” *Nat Commun.*, vol. 9, no. 1, pp. 1–13, Oct. 2018, doi: 10.1038/S41467-018-06621-3.

[241] F. Mingozzi *et al.*, “CD8+ T-cell responses to adeno-associated virus capsid in humans,” *Nat Med.*, vol. 13, no. 4, pp. 419–422, Mar. 2007, doi: 10.1038/NM1549.

[242] G. L. Rogers, A. T. Martino, G. v. Aslanidi, G. R. Jayandharan, A. Srivastava, and R. W. Herzog, “Innate immune responses to AAV vectors,” *Front Microbiol*, vol. 2, p. 194, Sep. 2011, doi: 10.3389/fmicb.2011.00194.

[243] P. Hadaczek, J. L. Eberling, P. Pivirotto, J. Bringas, J. Forsayeth, and K. S. Bankiewicz, “Eight years of clinical improvement in MPTP-lesioned primates after gene therapy with AAV2-hAADC,” *Mol Ther.*, vol. 18, no. 8, pp. 1458–1461, Aug. 2010, doi: 10.1038/MT.2010.106.

[244] V. Haurigot *et al.*, “Whole body correction of mucopolysaccharidosis IIIA by intracerebrospinal fluid gene therapy,” *J Clin Invest*, vol. 123, no. 8, pp. 3254–3271, Aug. 2013, doi: 10.1172/JCI66778.

[245] A. Ribera *et al.*, “Biochemical, histological and functional correction of mucopolysaccharidosis Type IIIB by intra-cerebrospinal fluid gene therapy,” *Hum Mol Genet*, vol. 24, no. 7, pp. 2078–2095, Apr. 2015, doi: 10.1093/HMG/DDU727.

[246] C. Vandamme, O. Adjali, and F. Mingozzi, “Unraveling the complex story of immune responses to AAV vectors trial after trial,” *Hum Gene Ther*, vol. 28, no. 11, pp. 1061–1074, Nov. 2017, doi: 10.1089/hum.2017.150.

[247] S. R. Choudhury *et al.*, “Widespread Central Nervous System gene transfer and silencing after systemic delivery of novel AAV-AS vector,” *Mol Ther.*, vol. 24, no. 4, pp. 726–735, Apr. 2016, doi: 10.1038/MT.2015.231.

[248] B. E. Deverman *et al.*, “Cre-dependent selection yields AAV variants for widespread gene transfer to the adult brain,” *Nat Biotechnol.*, vol. 34, no. 2, pp. 204–209, Feb. 2016, doi: 10.1038/NBT.3440.

[249] S. R. Choudhury *et al.*, “In vivo selection yields AAV-B1 capsid for Central Nervous System and muscle gene therapy,” *Mol Ther.*, vol. 24, no. 7, pp. 1247–1257, Jul. 2016, doi: 10.1038/MT.2016.84.

[250] K. Y. Chan *et al.*, “Engineered AAVs for efficient noninvasive gene delivery to the central and peripheral nervous systems,” *Nat Neurosci.*, vol. 20, no. 8, pp. 1172–1179, Jun. 2017, doi: 10.1038/NN.4593.

[251] J. Hordeaux, Q. Wang, N. Katz, E. L. Buza, P. Bell, and J. M. Wilson, “The neurotropic properties of AAV-PHP.B are limited to C57BL/6J mice,” *Mol Ther.*, vol. 26, no. 3, pp. 664–668, Mar. 2018, doi: 10.1016/J.YMTHE.2018.01.018.

[252] W. A. Liguore *et al.*, “AAV-PHP.B administration results in a differential pattern of CNS biodistribution in non-human primates compared with mice,” *Mol Ther.*, vol. 27, no. 11, pp. 2018–2037, Nov. 2019, doi: 10.1016/J.YMTHE.2019.07.017.

[253] Y. Matsuzaki *et al.*, “Intravenous administration of the adeno-associated virus-PHP.B capsid fails to upregulate transduction efficiency in the marmoset brain,” *Neurosci Lett*, vol. 665, pp. 182–188, Feb. 2018, doi: 10.1016/J.NEULET.2017.11.049.

[254] S. N. Mathiesen, J. L. Lock, L. Schoderboeck, W. C. Abraham, and S. M. Hughes, “CNS transduction benefits of AAV-PHP.eB over AAV9 are dependent on administration route and mouse strain,” *Mol Ther Methods Clin Dev.*, vol. 19, pp. 447–458, Dec. 2020, doi: 10.1016/j.omtm.2020.10.011.

[255] M. Hocquemiller, L. Giersch, M. Audrain, S. Parker, and N. Cartier, “Adeno-associated virus-based gene therapy for CNS diseases,” *Hum Gene Ther*, vol. 27, no. 7, pp. 478–496, Jul. 2016, doi: 10.1089/hum.2016.087.

[256] A. Vignon, L. Salvador-Prince, S. Lehmann, V. Perrier, and J. Torrent, “Deconstructing Alzheimer’s disease: How to bridge the gap between experimental models and the human pathology?”, *Int J Mol Sci.*, vol. 22, no. 16, p. 8769, Aug. 2021, doi: 10.3390/ijms22168769.

[257] “Alzheimer’s disease Research Models,” *ALZFORUM*. https://www.alzforum.org/research-models/alzheimers-disease (accessed Jul. 01, 2022).

[258] S. J. Webster, A. D. Bachstetter, P. T. Nelson, F. A. Schmitt, and L. J. van Eldik, “Using mice to model Alzheimer’s dementia: An overview of the clinical disease and the preclinical behavioral changes in 10 mouse models,” *Front Genet*, vol. 5, p. 88, Apr. 2014, doi: 10.3389/fgene.2014.00088.

[259] A. Myers and P. McGonigle, “Overview of transgenic mouse models for Alzheimer’s disease,” *Curr Protoc Neurosci*, vol. 89, no. 1, p. e81, Sep. 2019, doi: 10.1002/CPNS.81.

[260] S. Oddo, A. Caccamo, M. Kitazawa, B. P. Tseng, and F. M. LaFerla, “Amyloid deposition precedes tangle formation in a triple transgenic model of Alzheimer’s

disease," *Neurobiol Aging*, vol. 24, no. 8, pp. 1063–1070, Dec. 2003, doi: 10.1016/J.NEUROBIOLAGING.2003.08.012.

[261] L. K. Clinton *et al.*, "Age-dependent sexual dimorphism in cognition and stress response in the 3xTg-AD mice," *Neurobiol Dis*, vol. 28, no. 1, pp. 76–82, Oct. 2007, doi: 10.1016/J.NBD.2007.06.013.

[262] J. C. Carroll *et al.*, "Progesterone and estrogen regulate Alzheimer-like neuropathology in female 3xTg-AD mice," *J Neurosci.*, vol. 27, no. 48, pp. 13357–13365, Nov. 2007, doi: 10.1523/JNEUROSCI.2718-07.2007.

[263] R. L. Nelson *et al.*, "Prophylactic treatment with paroxetine ameliorates behavioral deficits and retards the development of amyloid and tau pathologies in 3xTgAD mice," *Exp Neurol*, vol. 205, no. 1, pp. 166–176, May 2007, doi: 10.1016/J.EXPNEUROL.2007.01.037.

[264] L. M. Billings, S. Oddo, K. N. Green, J. L. McGaugh, and F. M. LaFerla, "Intraneuronal Aβ causes the onset of early Alzheimer's disease-related cognitive deficits in transgenic mice," *Neuron*, vol. 45, no. 5, pp. 675–688, Mar. 2005, doi: 10.1016/J.NEURON.2005.01.040.

[265] E. Lauretti and D. Praticò, "Alzheimer's disease: phenotypic approaches using disease models and the targeting of tau protein," *Expert Opin Ther Targets*, vol. 24, no. 4, pp. 319–330, Apr. 2020, doi: 10.1080/14728222.2020.1737012.

[266] V. D. Ranjan, L. Qiu, E. K. Tan, L. Zeng, and Y. Zhang, "Modelling Alzheimer's disease: Insights from in vivo to in vitro three-dimensional culture platforms," *J Tissue Eng Regen Med*, vol. 12, no. 9, pp. 1944–1958, Sep. 2018, doi: 10.1002/TERM.2728.

[267] F. Panza, M. Lozupone, G. Logroscino, and B. P. Imbimbo, "A critical appraisal of amyloid-β-targeting therapies for Alzheimer disease," *Nat Rev Neurol.* , vol. 15, no. 2, pp. 73–88, Jan. 2019, doi: 10.1038/S41582-018-0116-6.

[268] K. Takahashi *et al.*, "Induction of pluripotent stem cells from adult human fibroblasts by defined factors," *Cell*, vol. 131, no. 5, pp. 861–872, Nov. 2007, doi: 10.1016/J.CELL.2007.11.019.

[269] G. Cenini *et al.*, "Dissecting Alzheimer's disease pathogenesis in human 2D and 3D models," *Mol Cell Neurosci.*, vol. 110, p. 103568, Jan. 2021, doi: 10.1016/J.MCN.2020.103568.

[270] M. A. Lancaster and J. A. Knoblich, "Generation of cerebral organoids from human pluripotent stem cells," *Nat Protoc.*, vol. 9, no. 10, pp. 2329–2340, Sep. 2014, doi: 10.1038/NPROT.2014.158.

[271] H. Wang, "Modeling neurological diseases with human brain organoids," *Front Synaptic Neurosci.*, vol. 10, p. 15, Jun. 2018, doi: 10.3389/fnsyn.2018.00015.

[272] H. Shimada *et al.*, “A next-generation iPSC-derived forebrain organoid model of tauopathy with tau fibrils by AAV-mediated gene transfer,” *Cell Rep Methods.*, vol. 2, no. 9, p. 100289, Sep. 2022, doi: 10.1016/J.CRMETH.2022.100289.

[273] W. K. Raja *et al.*, “Self-organizing 3D human neural tissue derived from induced pluripotent stem cells recapitulate Alzheimer’s disease phenotypes,” *PLoS One*, vol. 11, no. 9, Sep. 2016, doi: 10.1371/JOURNAL.PONE.0161969.

[274] G. Rossi, A. Manfrin, and M. P. Lutolf, “Progress and potential in organoid research,” *Nat Rev Genet.*, vol. 19, no. 11, pp. 671–687, Sep. 2018, doi: 10.1038/S41576-018-0051-9.

[275] J. A. Depla *et al.*, “Cerebral organoids: A human model for AAV capsid selection and therapeutic transgene efficacy in the brain,” *Mol Ther Methods Clin Dev.*, vol. 18, pp. 167–175, Sep. 2020, doi: 10.1016/J.OMTM.2020.05.028.

[276] D. Zhang, M. Pekkanen-Mattila, M. Shahsavani, A. Falk, A. I. Teixeira, and A. Herland, “A 3D Alzheimer’s disease culture model and the induction of P21-activated kinase mediated sensing in iPSC derived neurons,” *Biomaterials*, vol. 35, no. 5, pp. 1420–1428, Feb. 2014, doi: 10.1016/J.BIOMATERIALS.2013.11.028.

[277] G. Quadrato, J. Brown, and P. Arlotta, “The promises and challenges of human brain organoids as models of neuropsychiatric disease,” *Nat Med.*, vol. 22, no. 11, pp. 1220–1228, Oct. 2016, doi: 10.1038/NM.4214.

[278] S. K. Dubey *et al.*, “Recent expansions on cellular models to uncover the scientific barriers towards drug development for Alzheimer’s disease,” *Cell Mol Neurobiol.*, vol. 39, no. 2, pp. 181–209, Jan. 2019, doi: 10.1007/S10571-019-00653-Z.

[279] L. Mucke *et al.*, “High-level neuronal expression of Aβ1–42 in wild-type human amyloid protein precursor transgenic mice: synaptotoxicity without plaque formation,” *J Neurosci.*, vol. 20, no. 11, pp. 4050–4058, Jun. 2000, doi: 10.1523/JNEUROSCI.20-11-04050.2000.

[280] Y. Yoshiyama *et al.*, “Synapse loss and microglial activation precede tangles in a P301S tauopathy mouse model,” *Neuron*, vol. 53, no. 3, pp. 337–351, Feb. 2007, doi: 10.1016/J.NEURON.2007.01.010.

[281] R. Mencke *et al.*, “Human alternative Klotho mRNA is a nonsense-mediated mRNA decay target inefficiently spliced in renal disease,” *JCI Insight*, vol. 2, no. 20, p. e94375, Oct. 2017, doi: 10.1172/jci.insight.94375.

[282] P. S. Aranda, D. M. Lajoie, and C. L. Jorcyk, “Bleach gel: A simple agarose gel for analyzing RNA quality,” *Electrophoresis*, vol. 33, no. 2, pp. 366–9, Jan. 2012, doi: 10.1002/ELPS.201100335.

[283] J. Hellemans, G. Mortier, A. de Paepe, F. Speleman, and J. Vandesompele, “qBase relative quantification framework and software for management and automated analysis of real-time quantitative PCR data,” *Genome Biol*, vol. 8, no. 2, pp. 1–14, Feb. 2008, doi: 10.1186/GB-2007-8-2-R19/COMMENTS.

[284] X. Xiao, J. Li, and R. J. Samulski, “Production of high-titer recombinant adeno-associated virus vectors in the absence of helper adenovirus,” *J Virol*, vol. 72, no. 3, pp. 2224–2232, Mar. 1998, doi: 10.1128/JVI.72.3.2224-2232.1998.

[285] N. D. Sonawane, F. C. Szoka, and A. S. Verkman, “Chloride accumulation and swelling in endosomes enhances DNA transfer by polyamine-DNA polyplexes,” *J Biol Chem.*, vol. 278, no. 45, pp. 44826–44831, Nov. 2003, doi: 10.1074/JBC.M308643200.

[286] J. Piedra, M. Ontiveros, S. Miravet, C. Penalva, M. Monfar, and M. Chillon, “Development of a rapid, robust, and universal PicoGreen-based method to titer adeno-associated vectors,” *Hum Gene Ther Methods.*, vol. 26, no. 1, pp. 35–42, Feb. 2015, doi: 10.1089/hgtb.2014.120.

[287] M. G. Baxter, “‘I’ve seen it all before’ Explaining age-related impairments in object recognition. Theoretical comment on Burke et al. (2010),” *Behav Neurosci.*, vol. 124, no. 5, pp. 706–709, Oct. 2010, doi: 10.1037/A0021029.

[288] M. Antunes and G. Biala, “The novel object recognition memory: neurobiology, test procedure, and its modifications,” *Cogn Process*, vol. 13, no. 2, pp. 93–110, May 2012, doi: 10.1007/s10339-011-0430-z.

[289] R. S. Hammond, L. E. Tull, and R. W. Stackman, “On the delay-dependent involvement of the hippocampus in object recognition memory,” *Neurobiol Learn Mem*, vol. 82, no. 1, pp. 26–34, Jul. 2004, doi: 10.1016/J.NLM.2004.03.005.

[290] C. A. Thomas *et al.*, “Modeling of TREX1-dependent autoimmune disease using human stem cells highlights L1 accumulation as a source of neuroinflammation,” *Cell Stem Cell*, vol. 21, no. 3, pp. 319-331.e8, Sep. 2017, doi: 10.1016/J.STEM.2017.07.009.

[291] “Amplification efficiency of TaqMan gene expression assays,” *Applied Biosystems*. https://assets.thermofisher.com/TFS-Assets/LSG/Application-Notes/cms_040377.pdf (accessed Dec. 17, 2022).

[292] R. Rydbirk, J. Folke, K. Winge, S. Aznar, B. Pakkenberg, and T. Brudek, “Assessment of brain reference genes for RT-qPCR studies in neurodegenerative diseases,” *Sci Rep.*, vol. 6, p. 37116, Nov. 2016, doi: 10.1038/SREP37116.

[293] Y. Yamazaki *et al.*, “Establishment of sandwich ELISA for soluble alpha-Klotho measurement: Age-dependent change of soluble alpha-Klotho levels in healthy

subjects," *Biochem Biophys Res Commun*, vol. 398, no. 3, pp. 513–518, Jul. 2010, doi: 10.1016/J.BBRC.2010.06.110.

[294] B. K. Y. Bitanihirwe, P. Lizano, and T. U. W. Woo, "Deconstructing the functional neuroanatomy of the choroid plexus: an ontogenetic perspective for studying neurodevelopmental and neuropsychiatric disorders," *Molecular Psychiatry 2022 27:9*, vol. 27, no. 9, pp. 3573–3582, May 2022, doi: 10.1038/S41380-022-01623-6.

[295] R. Spector and C. Johanson, "Micronutrient and urate transport in choroid plexus and kidney: Implications for drug therapy," *Pharm Res*, vol. 23, no. 11, pp. 2515–2524, Nov. 2006, doi: 10.1007/s11095-006-9091-5.

[296] K. Kaiser and V. Bryja, "Choroid plexus: the orchestrator of long-range signalling within the CNS," *Int J Mol Sci.*, vol. 21, no. 13, p. 4760, Jul. 2020, doi: 10.3390/ijms21134760.

[297] M. M. Cararo-Lopes, C. H. Y. Mazucanti, C. Scavone, E. M. Kawamoto, and D. C. Berwick, "The relevance of α-KLOTHO to the central nervous system: Some key questions," *Ageing Res Rev*, vol. 36, pp. 137–148, Jul. 2017, doi: 10.1016/J.ARR.2017.03.003.

[298] L. Lu, D. Katsaros, A. Wiley, I. A. R. de La Longrais, M. Puopolo, and H. Yu, "Klotho expression in epithelial ovarian cancer and its association with insulin-like growth factors and disease progression," *Cancer Invest*, vol. 26, no. 2, pp. 185–192, Feb. 2008, doi: 10.1080/07357900701638343.

[299] A. Bektas, S. H. Schurman, A. A. Sharov, M. G. Carter, H. C. Dietz, and C. A. Francomano, "Klotho gene variation and expression in 20 inbred mouse strains," *Mamm Genome.*, vol. 15, no. 10, pp. 759–767, Oct. 2004, doi: 10.1007/S00335-004-2375-3.

[300] Y. Ohyama *et al.*, "Molecular cloning of rat klotho cDNA: Markedly decreased expression of klotho by acute inflammatory stress," *Biochem Biophys Res Commun*, vol. 251, no. 3, pp. 920–925, Oct. 1998, doi: 10.1006/bbrc.1998.9576.

[301] M. Kuro-o, "The Klotho proteins in health and disease," *Nat Rev Nephrol.*, vol. 15, no. 1, pp. 27–44, Nov. 2018, doi: 10.1038/S41581-018-0078-3.

[302] M. F. Folstein, S. E. Folstein, and P. R. McHugh, "'Mini-mental state': A practical method for grading the cognitive state of patients for the clinician," *J Psychiatr Res*, vol. 12, no. 3, pp. 189–198, Nov. 1975, doi: 10.1016/0022-3956(75)90026-6.

[303] J.-H. Kim, K.-H. Hwang, K.-S. Park, I. D. Kong, and S.-K. Cha, "Biological role of anti-aging protein Klotho," *J Lifestyle Med*, vol. 5, no. 1, p. 1, Mar. 2015, doi: 10.15280/JLM.2015.5.1.1.

[304] G. D. King, D. L. Rosene, and C. R. Abraham, “Promoter methylation and age-related downregulation of Klotho in rhesus monkey,” *Age (Dordr).*, vol. 34, no. 6, p. 1405, Dec. 2012, doi: 10.1007/S11357-011-9315-4.

[305] P. B. Verghese, J. M. Castellano, and D. M. Holtzman, “Apolipoprotein E in Alzheimer’s disease and other neurological disorders,” *Lancet Neurol*, vol. 10, no. 3, pp. 241–252, Mar. 2011, doi: 10.1016/S1474-4422(10)70325-2.

[306] M. E. Belloy, V. Napolioni, S. S. Han, Y. le Guen, and M. D. Greicius, “Association of Klotho-VS Heterozygosity With Risk of Alzheimer Disease in Individuals Who Carry APOE4,” *JAMA Neurol*, vol. 77, no. 7, pp. 849–862, Jul. 2020, doi: 10.1001/JAMANEUROL.2020.0414.

[307] P. Simon, R. Dupuis, and J. Costentin, “Thigmotaxis as an index of anxiety in mice. Influence of dopaminergic transmissions,” *Behav Brain Res.*, vol. 61, no. 1, pp. 59–64, Mar. 1994, doi: 10.1016/0166-4328(94)90008-6.

[308] R. Martier and P. Konstantinova, “Gene therapy for neurodegenerative diseases: slowing down the ticking clock,” *Front Neurosci*, vol. 14, p. 1002, Sep. 2020, doi: 10.3389/fnins.2020.580179.

[309] S. J. Gray, K. T. Woodard, and R. J. Samulski, “Viral vectors and delivery strategies for CNS gene therapy,” *Ther Deliv*, vol. 1, no. 4, pp. 517–534, Oct. 2010, doi: 10.4155/TDE.10.50.

[310] M. C. Hu *et al.*, “Renal production, uptake, and handling of circulating αKlotho,” *J Am Soc Nephrol.*, vol. 27, no. 1, pp. 79–90, Jan. 2016, doi: 10.1681/ASN.2014101030.

[311] S. Oddo *et al.*, “Triple-transgenic model of Alzheimer’s disease with plaques and tangles: intracellular Aβ and synaptic dysfunction,” *Neuron*, vol. 39, no. 3, pp. 409–421, Jul. 2003, doi: 10.1016/S0896-6273(03)00434-3.

[312] R. Belfiore *et al.*, “Temporal and regional progression of Alzheimer’s disease-like pathology in 3xTg-AD mice,” *Aging Cell*, vol. 18, no. 1, p. e12873, Feb. 2019, doi: 10.1111/ACEL.12873.

[313] K. F. Manaye *et al.*, “Age-related loss of noradrenergic neurons in the brains of triple transgenic mice,” *Age (Dordr).*, vol. 35, no. 1, pp. 139–147, Feb. 2013, doi: 10.1007/s11357-011-9343-0.

[314] M. Filali, R. Lalonde, P. Theriault, C. Julien, F. Calon, and E. Planel, “Cognitive and non-cognitive behaviors in the triple transgenic mouse model of Alzheimer’s disease expressing mutated APP, PS1, and Mapt (3xTg-AD),” *Behav Brain Res.*, vol. 234, no. 2, pp. 334–342, Oct. 2012, doi: 10.1016/J.BBR.2012.07.004.

[315] S. Pietropaolo, J. Feldon, and B. K. Yee, “Environmental enrichment eliminates the anxiety phenotypes in a triple transgenic mouse model of Alzheimer’s disease,” *Cogn*

Affect Behav Neurosci, vol. 14, no. 3, pp. 996–1008, Feb. 2014, doi: 10.3758/S13415-014-0253-3.

[316] L. Giménez-Llort, G. Rivera-Hernández, M. Marin-Argany, J. L. Sánchez-Quesada, and S. Villegas, "Early intervention in the 3xTg-AD mice with an amyloid β-antibody fragment ameliorates first hallmarks of Alzheimer disease," *MAbs*, vol. 5, no. 5, pp. 665–864, Sep. 2013, doi: 10.4161/mabs.25424.

[317] J. L. Hoffman *et al.*, "Alcohol drinking exacerbates neural and behavioral pathology in the 3xTg-AD mouse model of Alzheimer's disease," *Int Rev Neurobiol*, vol. 148, pp. 169–230, Jan. 2019, doi: 10.1016/BS.IRN.2019.10.017.

[318] D. I. Javonillo *et al.*, "Systematic phenotyping and characterization of the 3xTg-AD mouse model of Alzheimer's disease," *Front Neurosci*, vol. 15, p. 1829, Jan. 2022, doi: 10.3389/fnins.2021.785276.

[319] L. O. Goodwin *et al.*, "Large-scale discovery of mouse transgenic integration sites reveals frequent structural variation and insertional mutagenesis," *Genome Res*, vol. 29, no. 3, pp. 494–505, Mar. 2019, doi: 10.1101/GR.233866.117.

[320] L. Giménez-Llort *et al.*, "Modeling behavioral and neuronal symptoms of Alzheimer's disease in mice: A role for intraneuronal amyloid," *Neurosci Biobehav Rev*, vol. 31, no. 1, pp. 125–147, Jan. 2007, doi: 10.1016/J.NEUBIOREV.2006.07.007.

[321] "Strain Detail Sheet: 3xTg-AD," *Mutant Mouse Resource & Research Centers*. https://www.mmrrc.org/catalog/sds.php?mmrrc_id=34830 (accessed Nov. 15, 2022).

[322] K. R. Sadleir, W. A. Eimer, S. L. Cole, and R. Vassar, "Aβ reduction in BACE1 heterozygous null 5xFAD mice is associated with transgenic APP level," *Mol Neurodegener*, vol. 10, no. 1, pp. 1–16, Jan. 2015, doi: 10.1186/1750-1326-10-1.

[323] J. C. Carroll *et al.*, "Sex differences in β-amyloid accumulation in 3xTg-AD mice: Role of neonatal sex steroid hormone exposure," *Brain Res*, vol. 1366, pp. 233–245, Dec. 2010, doi: 10.1016/J.BRAINRES.2010.10.009.

[324] S. J. Gray *et al.*, "Optimizing promoters for recombinant adeno-associated virus-mediated gene expression in the peripheral and central nervous system using self-complementary vectors," *Hum Gene Ther*, vol. 22, no. 9, pp. 1143–1153, Sep. 2011, doi: 10.1089/hum.2010.245.

[325] N. Hitoshi, Y. Ken-ichi, and M. Jun-ichi, "Efficient selection for high-expression transfectants with a novel eukaryotic vector," *Gene*, vol. 108, no. 2, pp. 193–199, Dec. 1991, doi: 10.1016/0378-1119(91)90434-D.

[326] Y. Dou, Y. Lin, T. yun Wang, X. Y. Wang, Y. long Jia, and C. peng Zhao, “The CAG promoter maintains high-level transgene expression in HEK293 cells,” *FEBS Open Bio*, vol. 11, no. 1, pp. 95–104, Jan. 2021, doi: 10.1002/2211-5463.13029.

[327] L. Damdindorj *et al.*, “A comparative analysis of constitutive promoters located in adeno-associated viral vectors,” *PLoS One*, vol. 9, no. 8, p. e106472, Aug. 2014, doi: 10.1371/JOURNAL.PONE.0106472.

[328] R. L. Klein *et al.*, “Dose and promoter effects of adeno-associated viral vector for green fluorescent protein expression in the rat brain,” *Exp Neurol*, vol. 176, no. 1, pp. 66–74, Jul. 2002, doi: 10.1006/EXNR.2002.7942.

[329] V. Lukashchuk, K. E. Lewis, I. Coldicott, A. J. Grierson, and M. Azzouz, “AAV9-mediated central nervous system–targeted gene delivery via cisterna magna route in mice,” *Mol Ther Methods Clin Dev.*, vol. 3, p. 15055, Jan. 2016, doi: 10.1038/MTM.2015.55.

[330] T. P. O’Leary, A. T. Hussin, R. K. Gunn, and R. E. Brown, “Locomotor activity, emotionality, sensori-motor gating, learning and memory in the APPswe/PS1dE9 mouse model of Alzheimer’s disease,” *Brain Res Bull*, vol. 140, pp. 347–354, Jun. 2018, doi: 10.1016/J.BRAINRESBULL.2018.05.021.

[331] K. D. Onos *et al.*, “Enhancing face validity of mouse models of Alzheimer’s disease with natural genetic variation,” *PLoS Genet*, vol. 15, no. 5, May 2019, doi: 10.1371/JOURNAL.PGEN.1008155.

[332] E. Drummond and T. Wisniewski, “Alzheimer’s disease: experimental models and reality,” *Acta Neuropathol.*, vol. 133, no. 2, pp. 155–175, Dec. 2016, doi: 10.1007/S00401-016-1662-X.

[333] D. H. Veening-Griffioen *et al.*, “Are some animal models more equal than others? A case study on the translational value of animal models of efficacy for Alzheimer’s disease,” *Eur J Pharmacol*, vol. 859, p. 172524, Sep. 2019, doi: 10.1016/J.EJPHAR.2019.172524.

[334] P. Dallemagne and C. Rochais, “Facing the complexity of Alzheimer’s disease,” *Future Med Chem*, vol. 12, no. 3, pp. 175–177, Feb. 2020, doi: 10.4155/FMC-2019-0310.

[335] A. Banik *et al.*, “Translation of pre-clinical studies into successful clinical trials for Alzheimer’s disease: what are the roadblocks and how can they be overcome?”, *J Alzheimers Dis.*, vol. 47, no. 4, pp. 815–843, Jan. 2015, doi: 10.3233/JAD-150136.

[336] C. A. Trujillo *et al.*, “Complex oscillatory waves Emerging from cortical organoids model early human brain network development,” *Cell Stem Cell*, vol. 25, no. 4, pp. 558-569.e7, Oct. 2019, doi: 10.1016/j.stem.2019.08.002.

[337] H. Khabou *et al.*, “Noninvasive gene delivery to foveal cones for vision restoration,” *JCI Insight*, vol. 3, no. 2, Jan. 2018, doi: 10.1172/JCI.INSIGHT.96029.

[338] A. Rossi *et al.*, “Vector uncoating limits adeno-associated viral vector-mediated transduction of human dendritic cells and vector immunogenicity,” *Sci Rep.*, vol. 9, no. 1, pp. 1–14, Mar. 2019, doi: 10.1038/s41598-019-40071-1.

[339] S. Pillay and J. E. Carette, “Host determinants of adeno-associated viral vector entry,” *Curr Opin Virol*, vol. 24, pp. 124–131, Jun. 2017, doi: 10.1016/J.COVIRO.2017.06.003.

[340] T. J. McCown, X. Xiao, J. Li, G. R. Breese, and R. J. Samulski, “Differential and persistent expression patterns of CNS gene transfer by an adeno-associated virus (AAV) vector,” *Brain Res*, vol. 713, no. 1–2, pp. 99–107, Mar. 1996, doi: 10.1016/0006-8993(95)01488-8.

[341] Y. Ikeda, Z. Sun, X. Ru, L. H. Vandenberghe, and B. D. Humphreys, “Efficient gene transfer to kidney mesenchymal cells using a synthetic adeno-associated viral vector,” *J Am Soc Nephrol.*, vol. 29, no. 9, pp. 2287–2297, Sep. 2018, doi: 10.1681/ASN.2018040426.

[342] Y. L. Latour *et al.*, “Human GLB1 knockout cerebral organoids: A model system for testing AAV9-mediated GLB1 gene therapy for reducing GM1 ganglioside storage in GM1 gangliosidosis,” *Mol Genet Metab Rep*, vol. 21, p. 100513, Dec. 2019, doi: 10.1016/J.YMGMR.2019.100513.

[343] F. Green *et al.*, “Axonal transport of AAV9 in nonhuman primate brain,” *Gene Therapy 2016 23:6*, vol. 23, no. 6, pp. 520–526, Mar. 2016, doi: 10.1038/gt.2016.24.

[344] M. J. Castle, Z. T. Gershenson, A. R. Giles, E. L. F. Holzbaur, and J. H. Wolfe, “Adeno-associated virus serotypes 1, 8, and 9 share conserved mechanisms for anterograde and retrograde axonal transport,” *Hum Gene Ther*, vol. 25, no. 8, pp. 705–720, Aug. 2014, doi: 10.1089/HUM.2013.189.

[345] S. M. Moore *et al.*, “Setd5 haploinsufficiency alters neuronal network connectivity and leads to autistic-like behaviors in mice,” *Transl Psychiatry.*, vol. 9, no. 1, p. 24, Jan. 2019, doi: 10.1038/s41398-018-0344-y.

[346] C. Li *et al.*, “Neutralizing antibodies against adeno-associated virus examined prospectively in pediatric patients with hemophilia,” *Gene Ther.*, vol. 19, no. 3, pp. 288–294, Jun. 2012, doi: 10.1038/gt.2011.90.

[347] H. I. Chen, H. Song, and G. li Ming, “Applications of human brain organoids to clinical problems,” *Dev Dyn.*, vol. 248, no. 1, pp. 53–64, Jan. 2019, doi: 10.1002/DVDY.24662.

[348] J. F. Dekkers *et al.*, “A functional CFTR assay using primary cystic fibrosis intestinal organoids,” *Nat Med.*, vol. 19, no. 7, pp. 939–945, Jun. 2013, doi: 10.1038/nm.3201.

[349] P. R. Ormel *et al.*, “Microglia innately develop within cerebral organoids,” *Nat Commun.*, vol. 9, no. 1, p. 4167, Oct. 2018, doi: 10.1038/s41467-018-06684-2.

[350] M. A. Lancaster, “Brain organoids get vascularized,” *Nat Biotechnol.*, vol. 36, no. 5, pp. 407–408, May 2018, doi: 10.1038/NBT.4133.

[351] K. Togo *et al.*, “Postsynaptic structure formation of human iPS cell-derived neurons takes longer than presynaptic formation during neural differentiation in vitro,” *Mol Brain*, vol. 14, no. 1, p. 149, Dec. 2021, doi: 10.1186/S13041-021-00851-1.

[352] S. A. Nam *et al.*, “Graft immaturity and safety concerns in transplanted human kidney organoids,” *Exp Mol Med.*, vol. 51, no. 11, pp. 1–13, Nov. 2019, doi: 10.1038/s12276-019-0336-x.